2D3V Electromagnetic Particle-In-Cell Simulations of Plasmas having Kappa Velocity Distributions

by

Reginald Francis Abdul

Submitted in fulfilment of the requirements for the degree of Doctor of Philosophy in the School of Chemistry and Physics, University of KwaZulu-Natal, Westville, February 2018.

Abstract

It is now well established that the kappa distribution is a more appropriate kinetic model for space plasmas than the Maxwellian distribution. In particular it possesses a power-law tail, frequently observed in space plasmas. The research presented in this thesis outlines the development of a two-dimensional electromagnetic particle-in-cell (PIC) simulation code, designed to run on general purpose graphics processing units (GPGPUs), and presents results from simulations of waves and instabilities obtained using it. While PIC simulations are not new, the majority have focussed on the old paradigm of initial particle loadings with a Maxwellian velocity distribution, or one of its variants. Distinguishing this research from previous PIC simulations is the use of the kappa distribution for the initial particle loading. To achieve this, a fast and efficient algorithm for generating multi-dimensional kappa distributed deviates was developed.

The code is first applied to the study of waves in an electron-ion plasma, in a stable equilibrium configuration with a constant background magnetic field. Both species are modelled by isotropic (a) kappa and (b) Maxwellian velocity distributions. In each case, spectral analysis of the field fluctuations is performed, allowing mode identification. For parallel propagation, the maximum fluctuation intensities follow the dispersion relations for the L and R modes, respectively, while those at perpendicular propagation follow the dispersion relations for the X, O and electromagnetic electron and ion Bernstein waves. The variation of wave intensity for the oblique angles is also investigated. For the kappa case, this yields new and important information presently unavailable by analysis alone. The effects of the kappa distribution on wave intensity, as well as its effect on the dispersion relations of the modes is discussed in detail.

The second application is to the simulation of the electron temperature anisotropy driven whistler instability in an electron-ion plasma, where the electron species is modelled by the (a) bi-kappa and (b) bi-Maxwellian velocity distribution. For parallel propagation, the maximum field fluctuation intensities agree well with the dispersion relation for the whistler instability in a kappa plasma. While most of the wave intensity is in the parallel whistler mode, the oblique modes also contribute significantly to the overall fluctuation spectrum, but their intensities vary with angle of propagation relative to the magnetic field. The dependence of the growth rate on the index κ_e of the electron kappa distribution is discussed in detail and compared with the well known Maxwellian results. Saturation of the instability via pitch angle scattering, reducing the electron temperature anisotropy, is observed.

Preface

The work described in this thesis was carried out by the author from November 2013 to February 2018, in the School of Chemistry and Physics, University of KwaZulu-Natal, Westville, under the supervision of Professor R. L. Mace.

These studies represent original work by the author and have not otherwise been submitted in any form for a degree or diploma to another tertiary institution. Where use was made of the works of others, it has been duly acknowledged in the text.

DECLARATION 1 - PLAGIARISM

I, ... **Reginald Francis Abdul** ....., declare that

1. The research reported in this thesis, except where otherwise indicated, is my original research.

2. This thesis has not been submitted for any degree or examination at any other university.

3. This thesis does not contain other persons' data, pictures, graphs or other information, unless specifically acknowledged as being sourced from other persons.

4. This thesis does not contain other persons' writing, unless specifically acknowledged as being sourced from other researchers. Where other written sources have been quoted, then: (a) Their words have been re-written but the general information attributed to them has been referenced (b) Where their exact words have been used, then their writing has been placed in italics and inside quotation marks, and referenced.

5. This thesis does not contain text, graphics or tables copied and pasted from the Internet, unless specifically acknowledged, and the source being detailed in the dissertation and in the References sections.

Signed: .....

DECLARATION 2 - PUBLICATIONS

DETAILS OF CONTRIBUTION TO PUBLICATIONS that form part and/or include research presented in this thesis

Publication 1:

Abdul, R. F. and Mace, R. L. "One-dimensional particle-in-cell simulations of electrostatic Bernstein waves in plasmas with kappa velocity distributions". Physics of Plasmas, 22, 102107 (2015)

The development of the simulation code and numerical analysis in the above paper was done by the first author, R. F. Abdul. Both authors (R. F. Abdul and R. L. Mace) were involved in the write-up and interpretation of results.

Publication 2:

In preparation, **Abdul, R. F. and Mace, R. L. "2D3V particle-in-cell simulations of the electron temperature anisotropy driven whistler instability in plasmas having kappa velocity distributions"**.

All simulations and numerical results have been obtained. The development of the simulation code and numerical analysis was done by the first author, R. F. Abdul, under the supervision of Prof. R. L. Mace.

Signed: .....

Contents

Acknowledgements

I would like to thank my supervisor, Prof. R. L. Mace, for his guidance and advice during this research project.

I am thankful for the discussions and daily interactions with my fellow post graduate students, Farran Henning, Harry Pillay, Tamirat Gebeyehu and Francois Nsengiyumva. I would particularly like to thank Sharmini Pillay for her help and continued support over the years.

To my family, I would like to say thank you for the support, encouragements and sacrifices made to help me get this far.

The financial assistance of the National Research Foundation (NRF) towards this research is hereby acknowledged. Opinions expressed and conclusions arrived at, are those of the author and are not necessarily to be attributed to the NRF.

List of Figures

List of Tables

Chapter 1

General introduction

Owing to the ubiquitous supply of free energy sources, various types of waves can be spontaneously produced and instabilities excited in space plasmas. The interaction between waves and particles plays an important role in many space plasma phenomena. Wave-particle interaction in space is responsible for the heating and acceleration of charged particles, the precipitation of energetic electrons causing auroras, as well as the saturation of instabilities which redistributes energy in the plasma (Gendrin, 1975; Kennel and Petschek, 1966; Tsurutani and Lakhina, 1997; Summers et al., 2007). The study of plasma waves and instabilities is vital to the proper understanding of the dynamics of space plasmas and aids in the interpretation of satellite observations.

Due to the dependence of plasma micro-instabilities on the details of the particle velocity distributions, an investigation of the plasma on a kinetic level is required. Kinetic theory provides the most detailed description of the plasma. A statistical approach is taken to describe the thermal motion of the plasma particles via particle distribution functions for each species (Swanson, 2003). While the majority of studies of plasma waves are based on the assumption of plasmas in thermodynamic equilibrium, where particles are modelled by Maxwellian velocity distributions (or variants), non-thermodynamic particle distributions are often observed in space plasmas. The kappa distribution has been shown to provide a more appropriate model for these out of equilibrium velocity distributions, which we shall discuss next in Section 1.1. The study of waves propagating in plasmas having particle velocity distributions modelled by the kappa distribution will be the main focus of this thesis.

1.1 The kappa distribution

Particle collisions are infrequent in space plasmas. Many important phenomena occur on time scales shorter than the time for enough binary collisions to transpire and for the system to relax to a state of complete thermal equilibrium. The traditionally held view is that it is only in this thermal equilibrium state that the particle velocity distributions take the Maxwellian form (Pierrard and Lazar, 2010; Mace et al., 2011); however, this view is changing (see discussion below). Particle velocity distributions in space are often observed to exhibit non-Maxwellian features such as high energy tails, reflecting an abundance of high energy (superthermal) particles (Leubner, 2002; Hellberg et al., 2005; Pierrard and Lazar, 2010; Livadiotis and McComas, 2013). Traditionally, the treatment of such out of equilibrium distributions was via a sum of Maxwellians of different temperatures and number densities.

A distribution function more consistent with the observed particle velocity distributions is the kappa distribution. The kappa distribution smoothly reproduces the changeover from a Maxwellian-like core at low particle energies, to a high energy tail which decreases as a power law (Leubner, 2002). The isotropic 1D kappa distribution is given, in the commonly used form, as (Summers and Thorne, 1991)

$$f(v_x) = (\pi\kappa\theta^2)^{-1/2}\frac{\Gamma(\kappa)}{\Gamma(\kappa-1/2)}\left(1+\frac{v_x^2}{\kappa\theta^2}\right)^{-\kappa}, \tag{1.1}$$

where Γ is the gamma function, $\theta^2 = 2[(\kappa-3/2)/\kappa]v_{th}^2$ is the square of the generalised thermal speed and v_{th} is the usual thermal velocity. The parameter κ in Equation (1.1) shapes the tail of the distribution and models a wide range of power-law distributions. This enables the study of strongly non-thermal distributions which model an excess of superthermal particles (at low κ), to the Maxwellian distribution which is obtained in the limit $\kappa \to \infty$. Through the definition of θ above, a lower limit is placed on the value of κ, i.e., $\kappa = 3/2$, which arises from the physical requirement that the average particle kinetic energy not diverge (Mace et al., 1998; Hellberg et al., 2000).

Figure 1.1 compares the 1D kappa distribution given in Equation (1.1) for spectral indices $\kappa = 1.6, 3.0, 8.0$ and 20.0, displayed as the pink, cyan, blue and green curves, respectively, and the 1D Maxwellian distribution ($\kappa \to \infty$), displayed as the black curve. As illustrated in Figure 1.1, decreasing values of κ model increasingly higher numbers of high energy particles than the Maxwellian distribution. This is seen as higher values of $f(v_x)$ in the tails of the

kappa distribution compared to the Maxwellian distribution.

Initially found by Vasyliunas (1968) to adequately fit observed solar wind electron velocity distributions, the kappa distribution has since been successfully used to fit particle velocity distributions in numerous space plasma environments. Electron and ion velocity distributions modelled by the kappa distribution with $2 < \kappa < 6$ have been found in the plasma sheet (Christon et al., 1988, 1989), terrestrial magnetosphere (Gloeckler and Hamilton, 1987) as well as in the magnetospheres of other planets (Christon, 1987; Collier and Hamilton, 1995; Schippers et al., 2008), to name a few [see reviews by Livadiotis and McComas (2009), Pierrard and Lazar (2010) and Livadiotis and McComas (2013)].

While initially seen as only an empirical fit function, a number of mechanisms have been proposed for the origin of kappa distributions in space plasmas. Hasegawa et al. (1985) showed that the kappa distribution was the equilibrium velocity distribution for plasmas in a superthermal radiation field. Collier (1993) demonstrated the generation of kappa-like distributions using velocity space Lévy flights. Kappa velocity distributions in space were also proposed to form via various particle energisation processes, such as first and second order Fermi acceleration mechanisms (Parker and Tidman, 1958; Drury, 1983; Jones and Ellison, 1991; Blandford and Eichler, 1987). Furthermore, a kinetic theory was developed to show that kappa-like velocity distributions were a particular thermodynamic equilibrium state (Treumann, 1999, 2001; Treumann et al., 2004). Using Tsallis statistical mechanics (Tsallis, 1988), which provides a theoretical basis for describing and analysing systems out of equilibrium, Leubner (2002) demonstrated that the kappa distribution arises as a consequence of entropy generalisation and Livadiotis and McComas (2009, 2013) discussed at length how Tsallis statistics underpins the theory of kappa distributions. Thus, apart from the numerous observations of space plasma velocity distributions supporting its existence, the establishment of a theoretical foundation further justifies the use of the kappa distribution in the study of space plasmas. Furthermore, recent studies are beginning to challenge the view that complete thermal equilibrium implies a Maxwellian distribution, and the converse, for many particle systems whose dynamics are governed by classical physics. Some (e.g., Ryu et al. (2007); Livadiotis and McComas (2011); Yoon et al. (2012); Yoon (2014); Livadiotis (2014, 2017)) suggest that kappa-type distributions in certain instances actually replace the Maxwellian as a statistical description of the thermal equilibrium state. In other words, the Maxwellian distribution is not a unique statistical description of the thermal equilibrium state; other velocity distributions are consistent with this state also.

It is now well established that the kappa distribution is a more appropriate kinetic model for

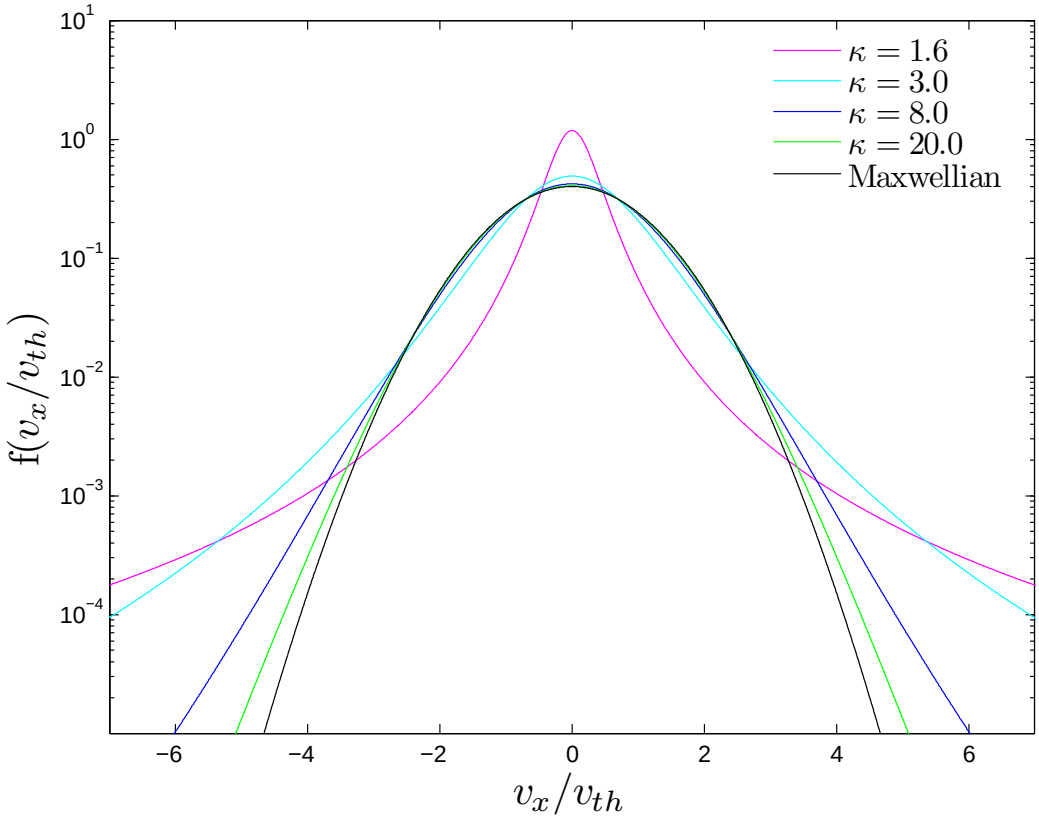

Figure 1.1: Comparison of the 1D kappa distribution, Equation (1.1), for the spectral indices $\kappa = 1.6, 3.0, 8.0, 20.0$ and the 1D Maxwellian ($\kappa = \infty$). Decreasing kappa values gives rise to a significant power law tail, where the kappa distribution approaches the Maxwellian for increasing kappa values.

space plasmas than the Maxwellian distribution (Hellberg et al., 2005), leading to a revision of kinetic theory based on plasmas close to thermodynamic equilibrium. Summers and Thorne (1991) introduced the modified plasma dispersion function Z^*_κ, analogous to the plasma dispersion function Z of Fried and Conte (1961), formalising the study of waves and instabilities in plasmas having kappa velocity distributions. The modified plasma dispersion function Z^*_κ, however, was only valid for integer κ values. Mace and Hellberg (1995) later generalised Z^*_κ and introduced the plasma dispersion function Z_κ which was valid for arbitrary real κ values. The plasma dispersion function of Mace and Hellberg (1995) relied on the well-known Gauss hypergeometric function, allowing the well-established theory of hypergeometric functions to be used to manipulate dispersion relations (Mace and Hellberg, 1995). Since magnetic fields in space plasmas introduce a preferred direction for waves to propagate, e.g., along magnetic field lines, Hellberg and Mace (2002) introduced a new plasma dispersion function $Z_{\kappa M}$. The dispersion function $Z_{\kappa M}$ was used to study waves in plasmas having velocity distributions modelled by hybrid kappa-Maxwellian distributions. The kappa-Maxwellian distribution is the product of a 1D kappa distribution which is taken along a preferred direction in space and a 2D Maxwellian distribution which is in the plane perpendicular to this direction (Cattaert et al., 2007). However, $Z_{\kappa M}$ also has general applicability, where the use of $Z_{\kappa M}$ instead of Z_κ has the advantage of yielding simpler dispersion relations (Mace and Hellberg, 2009; Mace and Sydora, 2010). With the plasma dispersion functions discussed above, the kappa distribution has been successfully used in many analytical and numerical studies of waves and instabilities in space plasmas (Hellberg et al., 2000, 2005). However, the use of kappa distributions has yet to become as widely used in the simulation studies of space plasmas.

1.2 Simulation of space plasmas

Plasma simulation provides a useful tool for the study of space plasma systems and extends the insights gained through linear theory, providing a better understanding of various space plasma phenomena (Winske and Omidi, 1996). Since simulations usually solve fundamental equations and rely on fewer assumptions than linear theory, they can provide a detailed description of complex dynamical processes in the plasma (Sydora, 1999). This is especially true in the non-linear regime of plasma wave evolution where an analytical investigation may become intractable (Matsumoto and Omura, 1984; Tajima, 1989; Dawson et al., 1993). The increased computational performance and ready availability of fast modern workstations allow for the development and execution of large-scale plasma simulations, further motivating

the use of plasma simulation studies (Liewer and Decyk, 1989; Dawson et al., 1993).

Plasma simulations can be broadly classified into two distinct model types, each providing different levels of detail and resolution of the plasma. The first type is the large scale fluid plasma model, e.g., magnetohydrodynamic (MHD) simulations (Gómez et al., 2005) and two-fluid simulations (Smith and Sakai, 2008). The second type is the small scale kinetic plasma model, e.g., particle-in-cell (PIC) simulations (Birdsall and Langdon, 1985) and Vlasov simulations (Bertrand, 2005). Hybrid simulations are also available, which model one plasma species as a fluid and the other kinetically using particle methods (Winske and Omidi, 1996).

Magnetohydrodynamic (MHD) simulations model the plasma as a continuous conducting fluid, which is described by a set of fluid equations. The fluid equations are integrated together with Maxwell's equations during the simulation, and the evolution of the plasma fluid is followed in its self-consistently created (and externally applied) electromagnetic fields (Matsumoto and Omura, 1993; Gómez et al., 2005). The fluid model is suitable for the study of slow plasma phenomena, on time scales larger than particle collision frequencies and on scale lengths larger than the collision mean free paths (Gómez et al., 2005). Thus, the fluid model is limited in its resolution of the plasma, where single particle effects and kinetic processes such as wave damping and the non-linear saturation of micro-instabilities are neglected (Winske and Omidi, 1996). The fluid model, however, provides a framework for the simulation of the long-time macroscopic, global-scale behaviour of space plasmas (Matsumoto and Omura, 1984; Gómez et al., 2005), such as simulation studies of the Earth's magnetosphere (Leboeuf et al., 1978; Ogino, 1993) and the interaction of the solar wind with the magnetosphere (Brecht et al., 1981; Ogino, 1986; Groth et al., 2000).

Kinetic simulation models provide a more fine grained resolution of the plasma, yielding a more detailed description of the plasma dynamics. The resolution of the simulation is typically set to spatial scales on the order of the Debye length and on time scales on the order of the inverse of the electron plasma frequency. Hence, kinetic simulations are usually confined to smaller scales of interest compared to the fluid model. The fine grained nature of this simulation model enables the study of plasma phenomena at the kinetic level. Kinetic simulations include particle-in-cell (PIC) and Vlasov simulations. PIC simulations employ a large number of discrete particles to represent the plasma particle velocity distribution functions in phase space (Sydora, 1999; Verboncoeur, 2005). The trajectories of the particles are then followed throughout the simulation as they interact through self-consistently created and externally applied electromagnetic fields. PIC simulations are more suited to studies where single particle effects such as wave-particle interaction, e.g., particle acceleration and

Landau damping, are important (Forslund, 1985; Matsumoto and Omura, 1993; Winske and Omidi, 1996). Multi-dimensional PIC simulations are more efficient than multi-dimensional Vlasov simulations, which solve the partial differential Vlasov equation on a phase space grid (Cheng and Knorr, 1976; Bertrand, 2005; Büchner, 2007). However, PIC simulations having too few particles in a Debye volume are subject to high levels of noise, requiring the use of higher order methods or an increase in the number of particles in a cell to yield accurate results. Vlasov simulations are free from discrete particle noise (Bertrand, 2005).

Hybrid simulations model one plasma species using PIC methods, while the other species is modelled using fluid methods (Winske, 1985; Winske and Omidi, 1996). The plasma ions are typically modelled as particles and the electrons as a charge-neutralising, massless fluid (Matsumoto and Omura, 1984; Dawson et al., 1993; Winske and Omidi, 1996). Hybrid simulations are more efficient than full PIC simulations; however, they are limited in resolution by the fluid model. Hybrid simulations are suited for the study of low frequency electromagnetic phenomena on the slower ion time scales, and for studies which are governed by ion kinetic effects, where the kinetic description of the electron species is not required (Winske and Omidi, 1993). These studies include investigations of the Earth's bow shock region (Quest, 1988; Omidi and Winske, 1990; Winske and Omidi, 1996; Burgess, 2006) and the study of electromagnetic ion cyclotron (EMIC) waves (Omura et al., 1985; Gary et al., 1994).

For the simulation code developed and described in this thesis, we have opted to use particle-in-cell (PIC) simulation methods. In Section 1.2.1, we provide a brief overview and review of the PIC simulation technique. In Chapter 2 we provide a detailed discussion of the simulation code created for this thesis.

1.2.1 Particle-in-cell (PIC) simulation

The particle-in-cell (PIC) simulation technique models the plasma as being composed of a number of particles. The simulated particles typically have a larger mass and charge than physical plasma particles and are seen to represent a collection of plasma particles (Matsumoto and Omura, 1984). PIC simulations have the ability to simulate various plasma micro-instabilities as well as the non-linear evolution of waves (Matsumoto and Omura, 1984; Birdsall and Langdon, 1985; Forslund, 1985; Tajima, 1989). During the simulation, the trajectories of the particles are tracked by numerically integrating in time the Newton-Lorentz

equations, using electromagnetic fields which are determined by solving Maxwell's equations (Hockney and Eastwood, 1981; Dawson, 1983; Matsumoto and Omura, 1984; Birdsall and Langdon, 1985; Tajima, 1989). This numerical integration places limits on the allowable time steps in the simulation to maintain numerical stability (Hockney and Eastwood, 1981; Forslund, 1985; Birdsall and Langdon, 1985), usually requiring the resolution of the electron plasma frequency and Debye length. This makes PIC simulations computationally expensive as a large number of time steps are required to produce a significant degree of plasma evolution.

While early incarnations of PIC simulations lacked sophistication, i.e., simulations were 1D electrostatic, using $10^2 - 10^3$ particles with simulations having periodic boundary conditions, good agreement between simulation results and theoretical predictions were still obtained (Langdon and Birdsall, 1970; Tajima, 1989). Buneman (1959) demonstrated the rapid dissipation of currents when entering ionised media, which was used to explain the rapid cooling in low-pressure RF discharges, and Dawson (1964) demonstrated the effects of Landau damping of electrostatic waves.

To reduce the numerical complexity of 2D simulations, the use of a mathematical grid in the PIC simulation technique was introduced (Yu et al., 1965; Hockney, 1965). Particles move freely through the grid and their charge and current densities are assigned to the grid points. The charge and current densities on the grid are then used as source terms in Maxwell's equations for the calculation of the electromagnetic fields. The direct inter-particle force calculations are disregarded in favour of forces of interaction provided by the electromagnetic fields sampled on the grid. This made simulations more efficient, since simulations have fewer grid points than particles, requiring fewer calculations per time step in order to update the particle dynamics (Dawson, 1983). A weighting scheme is needed, however, for particles to deposit charge and current density to the grid, as well as to read the electromagnetic fields from the grid points.

A natural extension of the grid was the finite-sized macro-particle techniques constructed by Birdsall and Fuss (1969) and Morse and Nielson (1969). The simulated particles are seen to have a finite size and shape $S(x)$ with the particle charge spread out over a finite region $qS(x)$, where $\int S(x) = 1$. The finite-sized particle technique is a generalisation of the point particle approach $q\delta(x)$, where particle charge density is distributed to multiple grid points instead of only one (Birdsall and Fuss, 1969; Birdsall and Langdon, 1985). The charge "clouds" are allowed to pass freely through each other, depositing charge and current density to the grid. This has the effect of reducing the high frequency fluctuations (noise) in the charge

and current densities assigned to the grid. It also smoothens out the particle interactions at small separation distances, i.e., smaller than a particle's size, when compared to the point particle approach (Langdon and Birdsall, 1970; Okuda, 1972; Birdsall, 1991). The long-range electromagnetic forces, however, remain in the simulation. The particle shapes need not be isotropic nor symmetric, but usually are, and while the use of higher order particle shapes further reduces numerical noise and artificial heating of the plasma (Peiravi, 2010), it comes at the price of an increase in the numerical complexity of the simulation.

Noise in PIC simulations arise due to the discrete particle nature of the simulation technique as well as through the use of fewer particles in a Debye volume (by many orders of magnitude) than real plasmas (Okuda, 1972; Forslund, 1985; Ueda et al., 1994; Sydora, 1999). While an increase in the number of simulated particles reduces noise, the allowable number of particles in the simulation is limited by the computational resources available (Ueda et al., 1994). PIC simulations with poor signal-to-noise ratios can produce numerical artefacts and fully developed fluctuation levels which can modify the plasma dynamics and lead to a lack of energy conservation in the simulation. Apart from the use of higher order particle and weighting schemes, various other approaches have been developed to reduce noise in simulations. Quiet start techniques (Birdsall and Langdon, 1985; Sydora, 1999) reduce noise associated with the random initialisation of the plasma particles; however, noise is only briefly reduced and is reintroduced as the simulation progresses. The δf model (Aydemir, 1994; Denton and Kotschenreuther, 1995; Sydora, 2007) separates the particle distributions into a background f_0 and perturbing part δf, where $f = f_0 + \delta f$. The simulated particles are used to represent only the perturbing part of the distribution.

With the rapid increase in the computational performance of computers, further refinements in the simulation techniques were developed (Matsuda and Okuda, 1975). Multi-dimensional simulations (Buneman et al., 1980) were run, which were also fully electromagnetic (Langdon and Dawson, 1967). Simulations which re-introduced particle collisions were developed (Burger, 1967; Birdsall, 1991) and more complex boundary conditions for simulations were used (Dum, 1984). Due to the strict time constraint of PIC simulations, large numbers of time steps are required to simulate slow-evolving plasma phenomena. Out of the need to run stable PIC simulations using larger time steps, implicit time schemes were developed (Birdsall and Langdon, 1985), as well as multi-step schemes which updated fields and particles using different time steps (Langdon and Lasinski, 1976; Matsumoto and Omura, 1984).

Simulations were also made to work on high performance and distributed memory supercomputers (Huff et al., 1982; Dawson et al., 1993). This allowed for the simulation of millions

of particles through concurrent computation of the simulation equations. In general, one of two methods are used to share the workload and allow for efficient execution of simulations on distributed memory computers. One divides the particle data among the available processors (Martino et al., 2001) and the other subdivides the simulation domain among the processors (Liewer and Decyk, 1989). Graphics processing units (GPUs) were also utilised in the parallelisation of PIC simulations, due to their high computation capabilities (Stantchev et al., 2008; Burau et al., 2010; Decyk and Singh, 2011; Abreu et al., 2011).

1.3 Thesis overview

For this thesis, we developed a 2D3V electromagnetic PIC simulation code which was made to run on general purpose graphics processing units (GPGPUs). The simulations are 2D3V in regards to the fact that the particle positions are able to vary in two dimensions, x and y, while all three components of the particle velocity vector are dynamically essential. In chapter 2, we provide a detailed discussion of the code developed for this thesis. In particular, we discuss the method that we used to initialise the particle velocities through random sampling from the kappa distribution. Next, in Chapter 3, we discuss the particle shape factors for PIC simulations and compare the effects of higher order shape factors on energy conservation in our simulations. We also compare simulation execution times for each shape factor scheme.

Chapter 4 provides results for the first of our simulation case studies. Here we apply the simulation code to the study of a quiet plasma and investigate the waves generated therein. The plasma particle velocity distributions are initialised with either isotropic kappa or isotropic Maxwellian velocity distributions. Fourier analysis of the electromagnetic fields in time is performed. A comparison between the resulting Fourier spectrum and the linear dispersion relations allows for the identification of the different plasma modes. We discuss the effects of the kappa distribution on the behaviour and dynamics of the wave modes, and also compare the intensities of the field fluctuations in each case.

In Chapter 5 we provide results from the simulation investigation of the electron temperature anisotropy driven whistler instability. For these simulations the electrons are initialised with either bi-kappa or bi-Maxwellian velocity distributions. The evolution of the whistler instability propagating in the plasma having kappa velocity distributions is discussed and compared to that for the plasma modelled by Maxwellian velocity distributions. Results are also compared to linear theory. Finally, in Chapter 6, we provide a general summary and

conclusions for this thesis.

Chapter 2

Simulation model

2.1 Introduction

Through plasma simulation we are able to probe the dynamics of large scale plasma systems, without requiring the full details of the plasma, i.e., using a reduced number of dimensions, plasma particles and smaller scale lengths compared to physical plasmas (Birdsall and Langdon, 1985; Tajima, 1989; Winske and Omidi, 1996). One of the major aims of this research project was to develop electromagnetic plasma simulation codes using the explicit particle-in-cell (PIC) simulation technique. The simulation codes were then used to investigate waves and instabilities in space plasmas, specifically, those having velocity distributions modelled by the kappa distribution. PIC simulations naturally provide a highly detailed description of the plasma physics through the evaluation of fundamental equations (Newton's and Maxwell's equations), enabling the study of macro- and micro-instabilities as well as the non-linear behaviour of plasma systems.

The code created for this thesis is 2D, in that the positions of the particles, as well as the electromagnetic fields and its sources, i.e., the charge (ρ) and current density ($\boldsymbol{J}$), are allowed to vary in both the x and y directions. All three components of the plasma particle velocities, $\boldsymbol{v} = (v_x, v_y, v_z)$, are retained, however, to adequately account for the particle motion about magnetic field lines. The simulation code was written in the C programming language and parallelised using CUDA (Compute Unified Device Architecture) C, enabling us to take advantage of the vast computing power provided by general purpose graphics processing units (GPGPUs). A more detailed discussion on GPU computing and CUDA is provided in

Section 2.2.

Particle-in-cell simulations model a plasma as being composed of particles and proceed by integrating the particle trajectories under the influence of the electromagnetic fields, which are self-consistently produced as well as externally applied (Hockney and Eastwood, 1981; Dawson, 1983; Forslund, 1985; Birdsall and Langdon, 1985; Birdsall, 1991). The electromagnetic fields in the simulation are evaluated and updated at each step by solving Maxwell's equations. A notable feature of PIC simulations is the use of a discrete spatial grid on which electric $\boldsymbol{E}$ and magnetic $\boldsymbol{B}$ fields as well as sources (ρ and $\boldsymbol{J}$) are sampled (Hockney, 1965; Birdsall and Fuss, 1969; Morse and Nielson, 1969; Langdon, 1970).

Figure 2.1 illustrates a basic layout of the simulation domain. For our 2D code, the spatial domain of the simulation is divided into cells of size Δx in the x-direction and Δy in the y-direction, with $\Delta x = \Delta y$, see Figure 2.1. The electromagnetic fields and particle charge and current densities are evaluated and stored only at the grid points, located at the cell centres, i.e., at the points (X_j, Y_k), where $X_j = j\Delta x$ and $Y_k = k\Delta y$. The particles themselves are not subject to discrete sampling and are able to move freely throughout the simulation domain, which is of size $L_x \times L_y$.

A major advantage of using the grid lies in the ability to circumvent the need to directly calculate the inter-particle forces. Instead, the particle charge ρ and current densities $\boldsymbol{J}$ are accumulated and stored at the grid points, and are then used as source terms in Maxwell's equations to evaluate the electromagnetic fields present in the plasma. The particle trajectories are then updated using an approximate force obtained by extrapolation of the electromagnetic fields at the grid points to the particle positions. Since there are usually only a few grid points involved in this interpolation, fewer calculations are needed to find the forces on each particle and to integrate the particle trajectories (Dawson, 1983; Birdsall and Langdon, 1985). This drastic reduction in computational expense makes the simulation of millions of plasma particles feasible (Hockney and Eastwood, 1981; Birdsall and Langdon, 1985; Tajima, 1989). However, the use of a spatial grid has the disadvantage of reducing the resolution of the simulation because plasma variations on scales smaller than a cell size, Δx and Δy, are not resolved (Okuda, 1972; Hockney and Eastwood, 1981; Birdsall, 1991). As mentioned, an interpolation scheme is also needed to allow information on the discrete grid, at points (X_j, Y_k), to be relayed to a particle i at continuous positions, (x_i, y_i), within the domain. This is due to the fact that the particle positions will not always coincide with the positions at which the fields are known. A set weighting scheme, which depends on the particle positions within the grid, is used to deposit charge and current density on the grid,

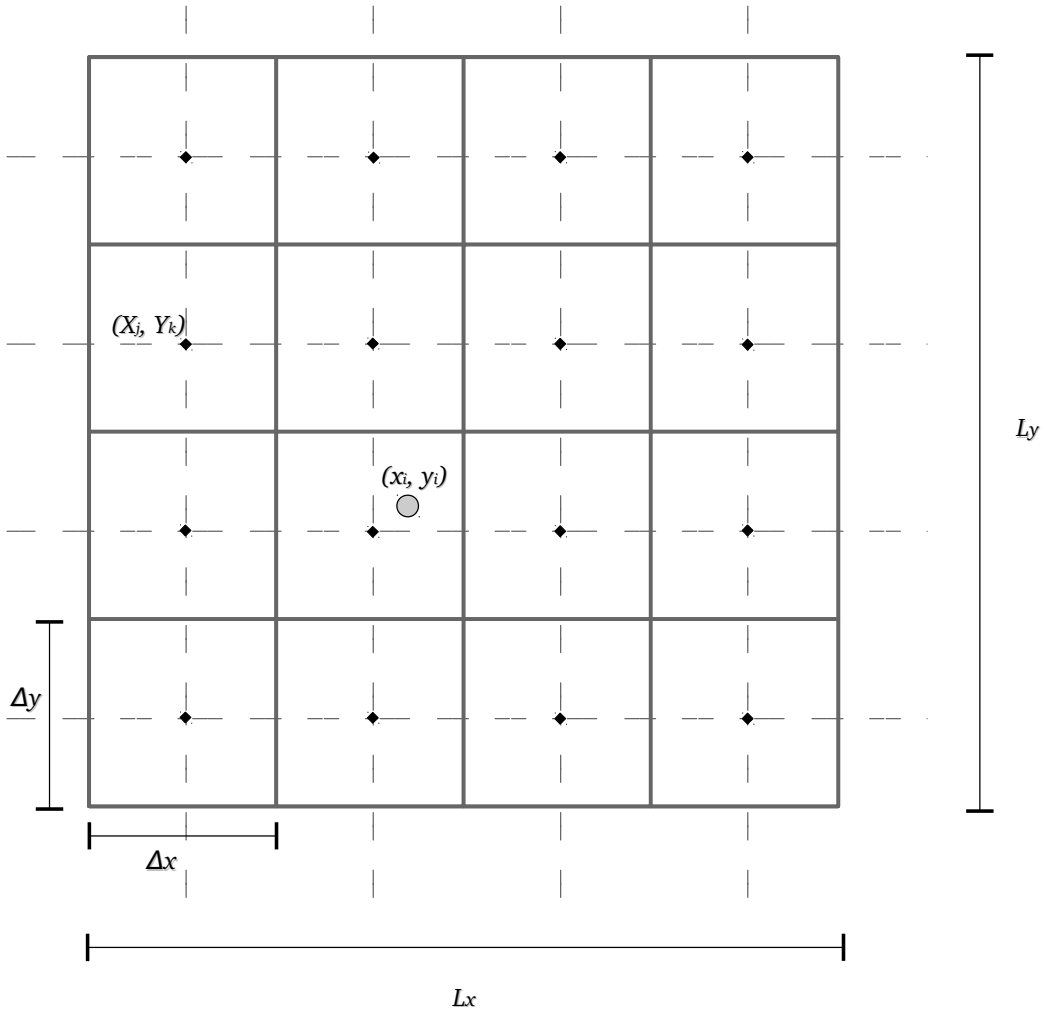

Figure 2.1: Basic layout for the 2D simulation. Each particle i in the simulation is allowed to take any position (x_i, y_i) within the simulation domain. The domain has size L_x in the x-direction and L_y in the y-direction, and is divided into cells of size Δx and Δy. The fields and particle charge and current densities are evaluated and stored only at the points (X_j, Y_k), which are located at the cell centres.

and conversely, extrapolate electromagnetic forces from grid points to particle positions.

As a consequence of the above mentioned interpolation/ extrapolation, the particles in the simulation effectively take the form of finite sized, tenuous clouds of charge, which are able to move through each other (Birdsall and Fuss, 1969; Langdon and Birdsall, 1970; Birdsall and Langdon, 1985). The size and shape of the particle cloud is influenced by the weighting scheme that is used, where higher order weighting schemes produce "fatter" plasma particles (Langdon and Birdsall, 1970; Dawson, 1983; Birdsall and Langdon, 1985; Lapenta, 2012). Higher order weighting schemes and larger particle sizes have the effect of smoothing the rapidly varying field fluctuations (noise) caused by changes in the particle number density in each cell. This smoothing of field fluctuations is beneficial, since simulations have far fewer particles in a Debye volume than real space plasmas, leading to an overemphasis of discrete particle effects (Okuda, 1972; Dawson, 1983). Large angle particle deflections (particle collisions) are also suppressed, producing a weak interaction of the simulated plasma particles at close distances while the long range, collective forces of the bulk plasma are retained (Dawson, 1983).

At the beginning of a PIC simulation, the required number of plasma particles are loaded into the simulation domain by assigning to each an initial position (x_i, y_i) within the simulation domain (the simulation box), and an initial velocity $\boldsymbol{v}_i$ sampled from a given statistical distribution. After the initialization phase, the simulation progresses through the repetition of four basic routines, over a number of time steps. These are,

- The weighting of the particle data to the grid points (X_j, Y_k), i.e., accumulating the charge ρ and current densities $\boldsymbol{J}$ on the grid, using a predefined weighting scheme.
- The full set of Maxwell's equations are numerically solved on the grid using the accumulated densities as sources.
- A second weighting is then required to extrapolate the field data on the grid to the continuous particle positions (x_i, y_i).
- The particle trajectories (positions and velocities) are then updated by solving Newton's equation with the Lorentz force.

Each of these routines will be expanded upon in the sections that follow.

2.2 Parallel computing, GPGPUs and CUDA C

Explicit particle-in-cell simulations contain strict stability constraints and require fine-grained resolution of the plasma, regardless of its relevance to the scales of interest in the problem being investigated (Dawson, 1983; Birdsall and Langdon, 1985). To obtain meaningful results in 2D PIC simulations, a large number of simulation cells and plasma particles are required to ensure acceptable statistical accuracy, necessitating increased computational performance. For this thesis we have opted to take advantage of the vast computing capabilities of general purpose graphics processing units (GPGPUs) to parallelise our simulation codes, in order to reduce execution times. Before we continue with the discussion of our PIC algorithm, we provide here a brief introduction to GPGPU computing. At the end of each of the subsequent sections describing our PIC algorithm, a description of our implementation of GPU parallelisation is also given.

Historically, increasing computational performance relied on adding processor cores or increasing the clock speed of the central processing unit (CPU) (Sanders and Kandrot, 2011). With modern devices, however, the use of these methods alone makes it intractable to extract additional performance due to hardware constraints, such as heat and power restrictions, restrictions to the physical transistor size, and limitations in the fabrication of integrated circuits (Sanders and Kandrot, 2011). Driven by the demand for high-definition 3D graphics, the programmable GPU is rapidly emerging as a viable alternative to the CPU as a source of computational growth. This is primarily due to their high computing power and capability for large scale data parallelism, as well as their relative low cost and power consumption (Decyk and Singh, 2011; Abreu et al., 2011; Kong et al., 2011; Sanders and Kandrot, 2011; Nvidia, 2015b).

The GPU is a physical co-processors to the CPU in a computer, designed and optimised for graphics workloads. Unlike the CPU, the GPU does not have a vast cache or sophisticated control flow of programs, rather having many more processing cores devoted to arithmetic operations (Nvidia, 2015a,b). This makes the GPU ideal for compute-intensive computer applications. GPUs are capable of launching thousands of lightweight threads and operate according to the single instruction multiple data (SIMD) programming model, i.e., all available processors will execute the same set of instructions using different sets of data (Nvidia, 2015b).

The GPU is made up of an array of streaming multi-processors (SMs) and an amount of

non-expandable memory (RAM) located off-chip. Each streaming multi-processor has a processing unit containing a number of processing cores, which set the allowable amount of concurrent threads, has its own local memory, and has access to shared memory and registers (Sanders and Kandrot, 2011). Memory access patterns are known to influence the efficiency of GPU applications. The basic memory layout for the GPU is as follows (Sanders and Kandrot, 2011; Kong et al., 2011),

- *Registers* have the lowest memory latency. Registers are located on-chip and are very limited. Register memory is allocated by the threads and lasts the lifetime of the executing thread.
- *Local memory* is generally 16 KB in size. This memory is created local to an executing thread and lasts the lifetime of the thread.
- *Shared memory* is generally 48 KB in size. This memory is designated on a per thread block basis (discussed later) and lasts the lifetime of the thread block. Shared memory is used to facilitate communication between a group of executing threads.
- *Global memory* is the physical RAM on the GPU board. Global memory is accessible by all threads running on the GPU as well as being accessible by the CPU. It has the highest memory latency, approximately two orders of magnitude slower than shared memory, and lasts the lifetime of the program.

The introduction of NVIDIA's CUDA (Compute Unified Device Architecture) has made GPU programming more accessible. CUDA provides a high-level, user friendly interface, allowing for the creation and execution of general purpose applications on the GPU (Stantchev et al., 2008; Decyk and Singh, 2011; Nvidia, 2015b). Programs written to run on the GPU require a native programming language, such as C, which runs on the CPU (the host) and calls the CUDA kernels, one at a time, to be executed on the GPU (the device). Programs running on the GPU are executed by sharing the computational workload among groups of executing threads, where the number of threads are specified at the beginning of the kernel launch. The executing threads are grouped together into what is known as a *thread block* and the thread blocks are arranged into a *grid*. A kernel is launched by specifying the grid layout, i.e., the number of blocks, as well as the block layout, i.e., the number of threads per block. The blocks and grid can be specified in either 1D, 2D or 3D arrays, respectively. The compute capability of the GPU describes the limits on the sizes and dimensions of the thread blocks and grids, which arise due to hardware restrictions.

Figure 2.2 illustrates a kernel launch containing 6 thread blocks (arranged as 2 rows and 3 columns), with 12 executing threads per block (arranged as 3 rows and 4 columns), for a total of 72 executing threads. Threads in different blocks are isolated and cannot directly share data or communicate with each other. When a kernel is launched, each streaming multi-processor on the GPU is assigned a thread block to execute in parallel. The threads in the block will execute the same code and share the given data (Nvidia, 2015a,b). Figure 2.3 illustrates how a CUDA kernel launched with 8 blocks will be executed on GPUs with 2 and 4 streaming multiprocessors, respectively. The thread blocks will be continually assigned to the available streaming multi-processors until all blocks that were launched have been processed. During execution of the code, the streaming multi-processors will always run 32 adjacent threads in lock-step, in what is known as a *warp*. A number of 32 thread warps are launched until the required thread count has been satisfied. A kernel launch is most efficient when all threads in the warp are active, without block divergence which is caused by threads in the block running different sets of code, e.g., running different sections of *if – else* statements (Burau et al., 2010).

GPU computing has a number of drawbacks and can add a layer of complexity to a program in order to have applications run accurately and efficiently. GPUs generally have a smaller memory space and a smaller cache than the CPU, and communication between the CPU and GPU is slow. Memory access bottlenecks are a major source of computational inefficiency in GPU applications (Decyk and Singh, 2011; Sanders and Kandrot, 2011). Memory in the GPU has high latency. Memory latency describes the number of clock cycles taken to load data from, or to write data to memory, i.e., it is the time interval between initiating a request for a byte of data in memory and the moment it is retrieved (Sanders and Kandrot, 2011). Higher latency signifies a larger number of clock cycles. The high memory latency in the GPU is, however, hidden by high memory bandwidth and increased computation. Thus, a high number of arithmetic operations, relative to memory access operations, is required for efficient GPU computation (Stantchev et al., 2008; Nvidia, 2015b).

The particle-in-cell algorithm contains data-independent, compute intensive, operations which allows simulators to take advantage of the GPU's performance capabilities (Stantchev et al., 2008; Decyk and Singh, 2011). The use of GPGPUs in large scale, multi-dimensional PIC simulations is still relatively new and a variety of approaches have been developed to tackle different aspects of the code. Stantchev et al. (2008) developed an early version of PIC codes running on the GPU, which focussed on porting only the particle-to-grid step to the GPU, which they argued dominates the execution time. Stantchev et al. (2008) observed decreased execution times over equivalently optimised CPU only codes, with runs of varying numbers

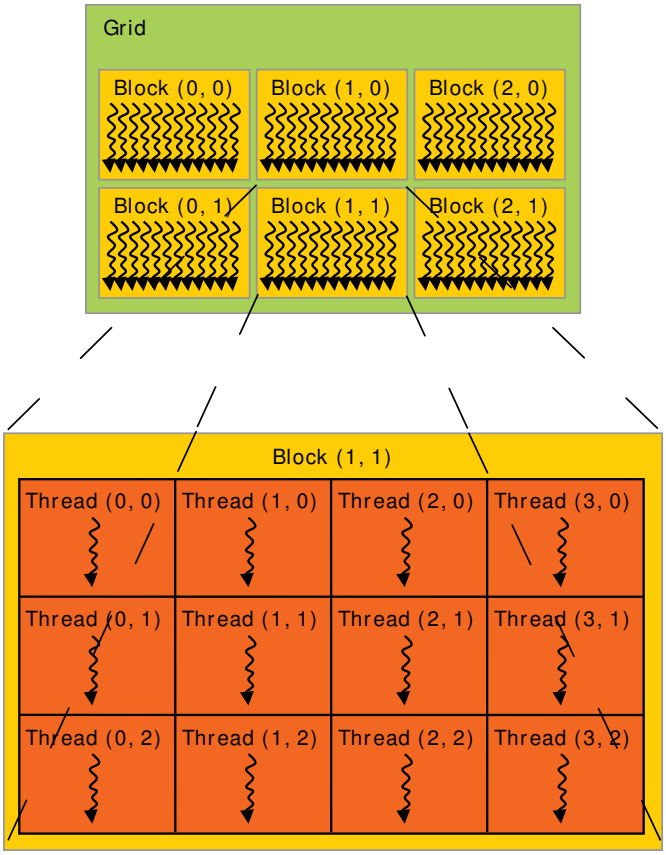

Figure 2.2: A kernel launch employing a grid layout using 6 blocks, arranged as 2 rows and 3 columns. The thread block layout has 12 threads per block, arranged as 3 rows and 4 columns. This figure is reproduced from Nvidia (2015b).

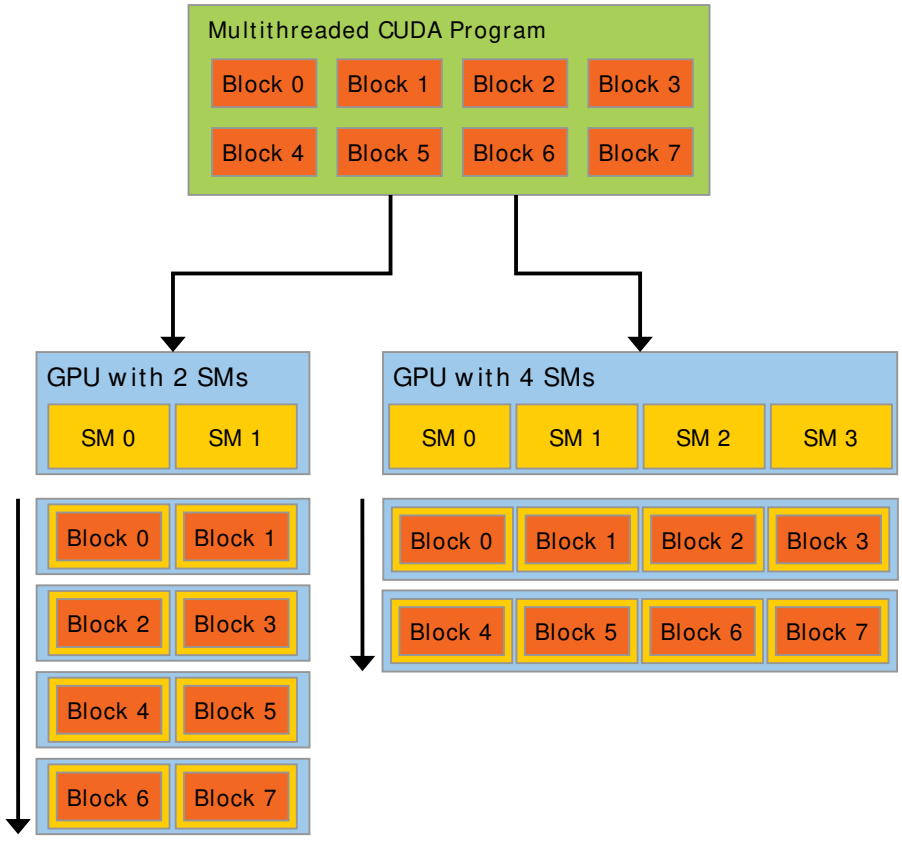

Figure 2.3: The execution of a multi-threaded CUDA application employing 8 blocks, being executed on a GPU with 2 and 4 streaming multi-processors (SMs), respectively. This figure is reproduced from Nvidia (2015b).

of particles per cell. Efficient memory management was used in the simulations of Stantchev et al. (2008), as well as the use of particle data structures which optimised the reading of particle data on the GPU. Burau et al. (2010) created the code PIConGPU, which can be scaled to run on GPU clusters and employed the message passing interface (MPI) to allow communication between cluster nodes. The PIConGPU code uses particle linked-lists to optimise memory access on the GPU and interleaves memory copies between host and device with computation on the GPU. Burau et al. (2010) were able to run numerically stable PIC simulations of laser wakefield acceleration on varying numbers of GPUs using different GPU node layouts.

Decyk and Singh (2011) provided an overview of GPU based PIC algorithms and discussed their implementation of a 2D electrostatic PIC code. The simulations performed by Decyk and Singh (2011) were observed to run 15 to 25 times faster on the GPU, compared to a similar code running only on the CPU. Kong et al. (2011) developed a 2D relativistic, electromagnetic PIC code for the GPU, using a charge conserving current deposit scheme. Kong et al. (2011) implemented a thread racing technique to resolve write conflicts in their simulations, instead of using CUDA's atomic operations. They also developed a parallel particle sort, which took advantage of fast on-chip shared memory, to sort their particle arrays. Kong et al. (2011) observed execution times of 27-81 times faster than single threaded CPU codes, depending on the simulated plasma temperature. Kong et al. (2011) also observed that differences between results obtained on the CPU (using double precision) and on the GPU (using single precision) were only of a magnitude on the order of single precision round-off error. Abreu et al. (2011) developed 2D PIC codes running on the GPU which employed direct, simultaneous visualization of simulation results, such as particle trajectories. The rendering of the simulation results was found not to slow down computation significantly, and an overall decrease in execution times was still observed when compared to CPU codes running on a single core. Chen et al. (2012) developed a hybrid CPU-GPU version of a 1D implicit PIC algorithm, where they implemented their novel charge conserving particle updating step on the GPU. The simulations of Chen et al. (2012) used a mixed precision scheme, where double precision was used for the CPU side of the code and single precision for the GPU code. Chen et al. (2012) sorted particles according to their positions and velocities, in order to manage memory more efficiently, and to aid in load balancing. No loss in accuracy was observed in results due to their mixed precision scheme. Chen et al. (2012) also observed a speed up by a factor of 100 over a CPU only code.

In the codes developed for this thesis, all particle and field data is stored in global memory of the GPU and the simulations run entirely on the GPU. This method was chosen due to the

high latency in copying data between the GPU and CPU. However, since the GPU cannot access the host file system, simulation data is transferred to the CPU when outputs need to be written to file. All simulations performed for this thesis were run on a single NVIDIA Tesla C2075 GPU, using compute capability 2.1. The simulation code was written in the C programming language and employed CUDA C for device kernels.

2.3 Loading particles into the simulation domain

To create a multi-species plasma in particle-in-cell (PIC) simulations, computer memory is allocated for every plasma particle and each particle is assigned initial values. In our simulations, each particle species is assigned a charge q_α, mass m_α and a plasma oscillation frequency $\omega_{p\alpha}$, where α denotes the particle species. The plasma particles are then loaded into phase space by assigning to each a random position (x, y) within the simulation domain as well as a random velocity (v_x, v_y, v_z). Our simulations allow the plasma species to have one of two initial states. Each species is initially modelled by either a Maxwellian velocity distribution, describing an equilibrium state, or a kappa velocity distribution, describing a non-thermal, metastable state. In this section we discuss the methods used to initialise the particle velocities, through random sampling from the relevant statistical distributions, starting with the Maxwellian distribution.

2.3.1 The Maxwellian distribution

The Maxwellian distribution is typically used to model the velocity distribution of space plasmas which are in, or near, a thermal equilibrium state. The majority of PIC simulations and analytical work has focussed on the old paradigm of using the Maxwellian distribution, or one of its variants, such as the drifting Maxwellian or bi-Maxwellian, to model plasma velocity distributions in space. We have used the Maxwellian distribution in our simulations to verify the correctness of our codes by comparing outputs to well known results. The results from the Maxwellian simulations also provide a point of reference when investigating the effects of non-thermal distributions on the behaviour of waves in space plasmas.

The 3D Maxwellian distribution is given by (Ishihara, 1971)

$$f(\boldsymbol{v}) = \left(\frac{1}{2\pi v_{th}^2}\right)^{3/2} \exp\left[-\frac{1}{2}\frac{\boldsymbol{v}^2}{v_{th}^2}\right], \tag{2.1}$$

where $v_{th} = (T/m)^{1/2}$ is the thermal velocity of the plasma particles. We measure particle temperature in units of energy, thus, here and throughout this thesis, we omit the Boltzmann constant when temperatures appear.

Particle velocities are assigned by generating random deviates sampled from the 3D Maxwellian distribution, Equation (2.1). To generate random deviates following the Maxwellian distribution, we employ the popular Box-Muller transform (Box and Muller, 1958; Press et al., 2007).

The Box-Muller transform describes a transformation method for sampling from the 1D standard Normal distribution, i.e., a normal distribution with 0 mean and unit standard deviation. The transformation works by taking two random deviates, u_1 and u_2, uniformly distributed on the interval [0, 1], and creates a pair of standard normal distributed random deviates, n_1 and n_2, using the transformation equations

$$n_1 = \sqrt{-2 \ln u_1}\, \cos(2\pi u_2), \tag{2.2}$$

$$n_2 = \sqrt{-2 \ln u_1}\, \sin(2\pi u_2). \tag{2.3}$$

The random samples from the standard normal distribution $n_{1,2}$ can then be converted to samples from an arbitrary drifting Maxwellian velocity distribution, by simply multiplying the deviates by the species thermal velocity v_{th}, and adding the species drift v_d, i.e.,

$$v_{1,2} = v_d + v_{th} n_{1,2}. \tag{2.4}$$

Equations (2.2) to (2.4) are used to sample from the 1D Maxwellian; however, a 3D velocity distribution is required for our simulations. The Maxwellian distribution is a factorisable statistical distribution, i.e., $f(v_x, v_y, v_z) = g(v_x)g(v_y)g(v_z)$, where g represents a 1D Maxwellian

$$f(v_x) = \left(\frac{1}{2\pi v_{th}^2}\right)^{1/2} \exp\left[-\frac{1}{2}\frac{{v_x}^2}{v_{th}^2}\right]. \tag{2.5}$$

Hence, it is sufficient to find the product of three independent 1D Maxwellian distributions (one for each dimension) to produce the 3D Maxwellian distribution required in our simulations.

2.3.2 The kappa distribution

The kappa distribution is increasingly being recognised to more accurately model observed space plasma velocity distributions than the Maxwellian distribution (Vasyliunas, 1968; Maksimovic et al., 1997; Treumann et al., 2004; Livadiotis and McComas, 2009), hence the reason for its use in our simulations. The kappa distribution has a power-law tail and models a greater abundance of high energy (or superthermal) particles, compared to a Maxwellian distribution with an identical number and energy density. The isotropic 3D kappa distribution, in the form given by (Summers and Thorne, 1991), is

$$f(\boldsymbol{v}) = (\pi\kappa\theta^2)^{-3/2}\frac{\Gamma(\kappa+1)}{\Gamma(\kappa-1/2)}\left(1+\frac{\boldsymbol{v^2}}{\kappa\theta^2}\right)^{-(\kappa+1)}, \tag{2.6}$$

where $\theta^2 = 2[(\kappa-3/2)/\kappa](T/m) = 2[(\kappa-3/2)/\kappa]v_{th}^2$ is the square of the generalised thermal speed and Γ is the gamma function. The parameter κ allows for a range of power laws and shapes the tail of the distribution. Low κ values produce a hard, strongly accelerated distribution with an abundance of high energy particles. Conversely, large κ values diminish the tail population and the special case of a Maxwellian distribution is attained at $\kappa \to \infty$.

While standard and efficient algorithms exist to accurately sample from the Maxwellian distribution, none are available for the kappa distribution. Rejection sampling can be utilised, as was used in the simulations performed by Lu et al. (2010) and Koen et al. (2012) to sample deviates from a 1D kappa distribution. Rejection sampling, however, can lead to considerable computational waste by rejecting many of the generated samples. This is especially true for multi-dimensional distributions. Leitner et al. (2011), on the other hand, extended the concept of the Galton board to produce kappa-like statistical distributions.

Recently, a fast and efficient method for sampling from the 1D kappa distribution was discussed by Abdul and Mace (2014). This method utilised deviates from the closely related Student t distribution (Press et al., 2007), where the equivalence of the kappa and Student t distributions was demonstrated by making various variable identifications. This method was found to accurately model the 1D kappa distribution [see Abdul and Mace (2014)].

Unlike the Maxwellian distribution, the kappa distribution is not factorisable. This is due to the non-extensive entropy from which it originates (Livadiotis and McComas, 2009). Hence, unlike in the Maxwellian case, a 3D kappa distribution cannot be accurately modelled from the product of three 1D kappa distributions. This is illustrated in Figures 2.4 and 2.5, which compares the surface iso-contours of an isotropic 3D kappa distribution to a distribution created from the product of three 1D kappa distributions, respectively. The isotropic kappa distribution, Figure 2.4, is clearly not reproduced by the product distribution in Figure 2.5. The iso-contours of Figure 2.4 form concentric spheres while those of Figure 2.5 are anisotropic and are more star shaped. Hence, the distribution in Figure 2.5 does not produce the required densities of the isotropic kappa distribution throughout the domain, and is not a monotonic function of kinetic energy. The anisotropic behaviour of the distribution in Figure 2.5 will lead to changes in the probabilities of various micro-physical processes in the plasma, producing and enhancing artificial instabilities.

To produce the desired 3D kappa loadings required for this thesis, we generalised the method of Abdul and Mace (2014). We use random deviates from the multi-dimensional Student t distribution to produce deviates following the 3D kappa distribution.

The Student t distribution is a statistical distribution akin to the kappa distribution, with a p-dimensional form given by (Kotz and Nadarajah, 2004; Shaw and Lee, 2008)

$$f(\boldsymbol{x}) = \frac{1}{(\pi\nu)^{p/2}\sqrt{|\boldsymbol{R}|}} \frac{\Gamma[(\nu+p)/2]}{\Gamma(\nu/2)} \left[1 + \frac{(\boldsymbol{x}-\boldsymbol{\mu})^T \boldsymbol{R}^{-1} (\boldsymbol{x}-\boldsymbol{\mu})}{\nu}\right]^{-(\nu+p)/2}, \tag{2.7}$$

where ν is the number of degrees of freedom (or shape parameter), $\boldsymbol{\mu}$ is the mean vector and $\boldsymbol{R}$ is the covariance matrix. Similar to the kappa distribution, the Student t has a significant power-law tail at small values of ν, where the power-law tail decays more rapidly as ν increases, producing the normal distribution at $\nu \to \infty$. The 3D Student t distribution is obtained by setting $p = 3$ and $\boldsymbol{R} = \sigma^2 \boldsymbol{I}$, where $\boldsymbol{I}$ is the identity matrix and σ^2 is the scaling parameter. This yields

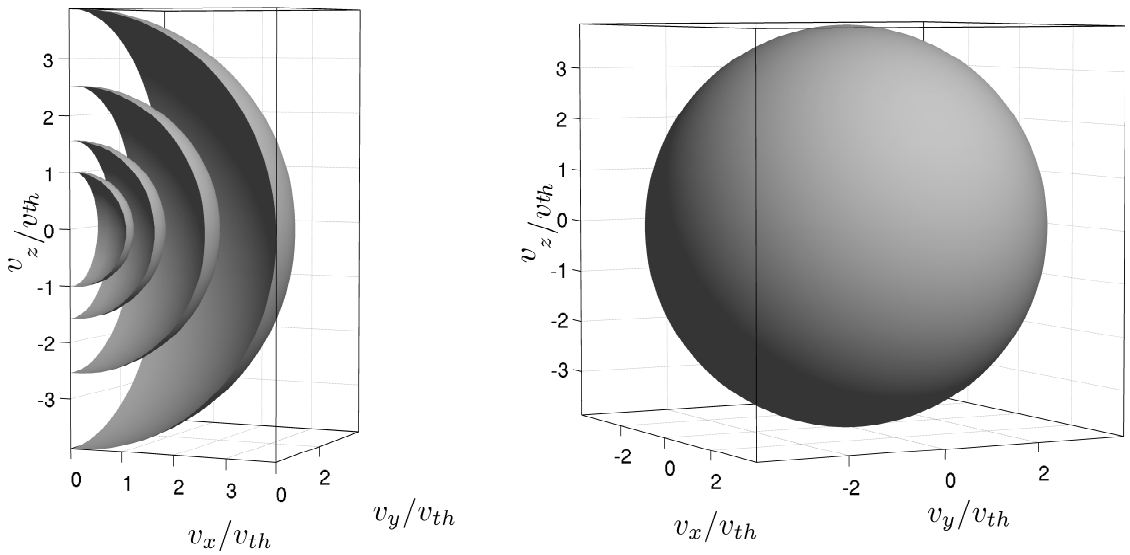

Figure 2.4: The surface iso-contours for the 3D isotropic kappa distribution, Equation (2.6).

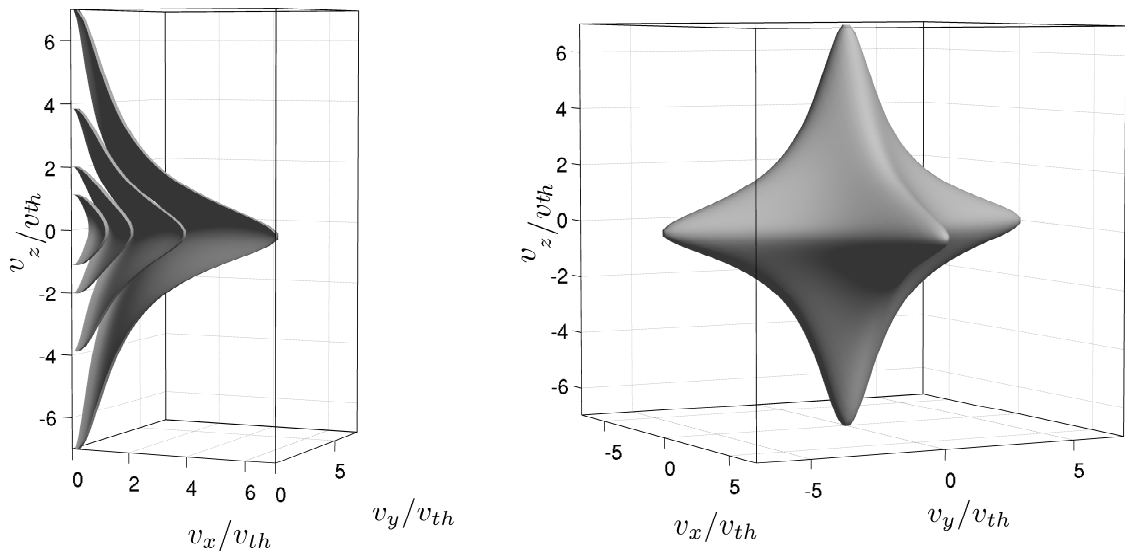

Figure 2.5: The surface iso-contours for a distribution made up from the product of three 1D kappa distributions.

$$f(\boldsymbol{x}) = \frac{1}{(\pi\nu\sigma^2)^{3/2}} \frac{\Gamma[(\nu+3)/2]}{\Gamma(\nu/2)} \left[1 + \frac{(\boldsymbol{x}-\boldsymbol{\mu})^2}{\nu\sigma^2}\right]^{-(\nu+3)/2}. \tag{2.8}$$

The 3D Student t distribution, Equation (2.8), reduces to the 3D kappa distribution, Equation (2.6), by setting $\boldsymbol{\mu}_i = 0$, and defining ν and σ^2 in the Student t distribution, respectively, as (Abdul and Mace, 2014)

$$\nu = 2\kappa - 1, \tag{2.9}$$

$$\sigma^2 = \frac{\kappa\theta^2}{2\kappa - 1}. \tag{2.10}$$

Hence, by using the variable identifications in Equations (2.9) and (2.10), the known transformation equation used for sampling from a multi-dimensional Student t distribution (Hofert, 2013) can be used to generate deviates following the kappa distribution (Abdul and Mace, 2014).

Random deviates sampled from a 3D Student t distribution, $\boldsymbol{S} = (S_x, S_y, S_z)$, are produced by transforming random standard normal deviates, $\boldsymbol{n} = (n_x, n_y, n_z)$, and chi-squared random deviates, χ^2, using the transformation equation (Kotz and Nadarajah, 2004; Shaw and Lee, 2008; Hofert, 2013)

$$\boldsymbol{S} = \boldsymbol{\mu} + \sigma\sqrt{(\nu/\chi^2_\nu)}\boldsymbol{n}. \tag{2.11}$$

By substituting Equations (2.9) and (2.10) into Equation (2.11), Equation (2.11) can be used to generate random deviates following the 3D kappa distribution. This method is accurate, easy to implement and avoids the computational waste produced through Accept-Reject sampling.

The plasma initialisation phase is performed entirely on the CPU in our simulation code. After the plasma particles have been assigned initial values, the plasma data is transferred to global memory on the GPU. Since the GPU is optimised for single precision variables, and calculations, as opposed to the double precision on the CPU (Burau et al., 2010; Chen et al., 2012; Nvidia, 2015a), all variables in our simulation code are stored in single precision

floating point format, where applicable. The particle positions (x, y) in our codes are stored as two single precision floats, for x and y, respectively, which represent the position given with reference to the cell boundary, i.e., (x, y) only take the values $0 \rightarrow 1$. An integer value is also assigned to each particle, which indicates the cell in which the particle lies (Decyk and Singh, 2011; Abreu et al., 2011). This method has the benefit of providing greater precision in calculations involving the particle positions, such as the accumulation of densities on the grid, as well as aiding in the sorting of the particle arrays. The sorting of the plasma particle data is discussed in the next section.

2.4 Sorting of the particle arrays

Memory access patterns are known to play a major role in the performance of GPU applications (Nvidia, 2015a). This is due to the manner in which threads read in data from global memory. Data is transferred in 128 byte chunks of contiguous memory. Several 128 byte chunks are transferred until the data requirement has been fulfilled. Hence, the most efficient data read is one which requires the lowest number of 128 byte data chunks, i.e., having adjacent threads in a warp request data stored in adjacent memory locations. This yields stride 1 memory access, also known as data coalescing (Sanders and Kandrot, 2011; Nvidia, 2015b,a). Having adjacent threads in the warp requesting data from random memory locations will require many, expensive global memory requests (128 bytes at a time) and the memory latency here can counter the gains of high arithmetic throughput (Decyk and Singh, 2011).

For PIC simulations, this requires that the particle data be sorted according to cells, before being processed on the GPU. This ensures that adjacent threads will read data from adjacent memory locations when cell data is being processed. This can best be understood by considering the weighting step. When looping through a randomised particle array, adjacent particles will provide density information to different (random) grid locations, requiring multiple reads/ writes to global memory. However, by having the particle arrays sorted by cells, adjacent particles (adjacent threads) will provide density information to nearby grid points, requiring fewer memory queries. Furthermore, during the particle update step, a single read of the relevant grid data is required to update all the particles within a cell. The order of the particles within a cell is not important, hence, a full particle sort by position is not required, which reduces sorting times, i.e., particles belonging to the same cell are grouped together, in any order. Also, only a small number of particles are expected to leave a given cell each time

step, due to simulations restricting the distance plasma particles can travel per time step, thus, further reducing the cost to keep the particle data sorted throughout the simulation run.

To sort the particle data in our simulations, we implemented the sort offered by the THRUST library (Nvidia, 2015d). THRUST is a template library offering an interface to a collection of parallel primitives (Nvidia, 2015a,d). The sorting algorithm is based on the radix sort and is quick and easy to implement in the code. In our simulations, we specify the position of a particle i as a pair of distances (x_i, y_i) from the cell edge (in the range [0, 1]) and use an integer c_i to represent the cell in which the particle is contained. The particle data in our simulations is arranged and stored in a single linear array, i.e., the cell index c takes on the values $c_i = 1, 2, ..., N_x N_y$, where N_x and N_y are the number of cells in the x- and y-directions, respectively. During the sort, the integer array, c_i, is sorted in ascending order and the particle data is reordered accordingly. The extra memory, added complexity and computation required to implement the particle sort is known to be overcome by the gains in efficiency, brought about by data coalescing and reducing global memory queries (Decyk and Singh, 2011; Abreu et al., 2011; Kong et al., 2011).

2.5 Weighting scheme

As mentioned, the PIC simulation technique models a plasma as being composed of a number of discrete particles, and tracks their trajectories in phase space (Sydora, 1999; Verboncoeur, 2005). The particle trajectories are not governed by direct particle-particle interactions, but rather by the interaction of the plasma particles with the electromagnetic fields, which are calculated and stored on a mathematical grid.

Since the particles move freely through the grid, the positions of the particles (x_i, y_i) will not always coincide with the positions (X_j, Y_k) at which the electromagnetic fields are known. Therefore, a weighting scheme must be used to evaluate fields at the particle positions and to deposit particle charge and current densities to the nearby grid points. In this section we discuss the weighting scheme used in our simulations to allow particles to accumulate charge and current density on the grid, as well as to allow the electromagnetic forces to be found at the particle positions.

The weighting functions used in PIC simulations are generally chosen from the family of

B-splines, of different orders (Hockney and Eastwood, 1981; Birdsall and Langdon, 1985; Haugbølle et al., 2013). In Chapter 3, a comparison of the four lowest order B-splines is given, and their effects on the noise and energy conservation in our simulations are discussed. Based on the results found in Chapter 3, we have opted to use the Triangular Shaped Cloud (quadratic spline) scheme for the simulations presented in this thesis.

For simplicity, we shall initially limit our discussion to the 1D quadratic spline. During the density accumulation step, this spline will distribute the particle data, i.e., the charge and current densities associated with a particle, to the three nearest grid points. For a 1D system, this is achieved using the function $W(x)$, which is (Hockney and Eastwood, 1981; Haugbølle et al., 2013)

$$W(x) = \begin{cases} \frac{3}{4} - \left(\frac{x}{\Delta x}\right)^2 & \text{, if } |x| < \frac{\Delta x}{2} \\ \frac{1}{2}\left(\frac{3}{2} - \left|\frac{x}{\Delta x}\right|\right)^2 & \text{, if } \frac{\Delta x}{2} \leq |x| < \frac{3\Delta x}{2} \\ 0 & \text{, otherwise.} \end{cases} \tag{2.12}$$

The weighting to a grid point located at X_j is found by evaluating $W(X_j - x_i)$, where x_i is the position of the particle. The function $W(x)$ in Equation (2.12) is centred on the position of the particle x_i, and is approximately Gaussian in shape, three cells wide at its base (see Figure 2.6). The Fourier representation of Equation (2.12) is also approximately Gaussian in shape and is given by (Birdsall and Langdon, 1985)

$$W_k(k) = \left(\frac{\sin\left(\frac{k\Delta x}{2}\right)}{\frac{k\Delta x}{2}} \right)^3 . \tag{2.13}$$

The weighting functions used in PIC simulations have associated particle shape functions $S(x)$ (Dawson, 1962; Birdsall and Langdon, 1985; Haugbølle et al., 2013). As its name suggests, the Triangular Shaped Cloud scheme produces triangular shaped particle clouds which are two cells wide in a 1D system, and have unit area. An alternate view to the use of the weighting function given in Equation (2.12), is seen as the area of overlap of a particle cloud, of unit density, with the boundaries of the surrounding cells (see Figure 2.7), i.e., the weighting to grid point X_j is

$$W(X_j - x_i) = \int_{X_j - \Delta x/2}^{X_j + \Delta x/2} dx S(x - x_i).$$

For the 2D simulations presented in this thesis, we employ symmetric particle shapes. Thus, the weighting function for our 2D system becomes $W_{2D}(\boldsymbol{r}) = W(x)W(y)$, where W is defined in Equation (2.12). The particle information is now distributed to the nine surrounding grid points.

A second (reverse) weighting step is required in PIC simulations, to ascertain the electromagnetic forces at the particle positions, using the electromagnetic fields from the surrounding cells. To avoid particle self-force and conserve particle momentum, we use the same weighting scheme as before (Hockney and Eastwood, 1981). Hence, for our 2D simulations, the plasma particles are acted upon by electromagnetic fields which are determined by the weighted sum of the fields from the nine surrounding grid points.

To perform the density accumulation on the GPU, we assign each simulation cell to a thread block and have the threads process the particles in the cell. Since the particle data is sorted by cells, each thread in the block can read all particle data in a coalesced manner and update the densities of the same set of grid points. We follow Decyk and Singh (2011) and create nine local shared memory variables per thread block, and use them to store the weightings during the particle processing. A loop through the particle data is performed, accumulating densities in the shared memory variables. After all particles in the cell have been processed, the shared memory variables are used to update the appropriate grid locations in global memory. This reduces execution times by decreasing the number of global memory reads, since global memory access is slower than shared memory.

A data hazard exists in the parallelisation of the weighting phase in the simulation. Since particles weight to the nine surrounding cells, an overlap can occur and multiple thread blocks can attempt to update the densities at the same location in global memory. When multiple threads attempt to write to the same memory location on the GPU, one thread is allowed to update the data point, while all other data is neglected. To avoid write conflicts we use CUDA atomic operations to update the density variables. Here each memory write is uninterrupted, i.e., memory is locked until the operation completes, and all threads writing to the same data point are queued.

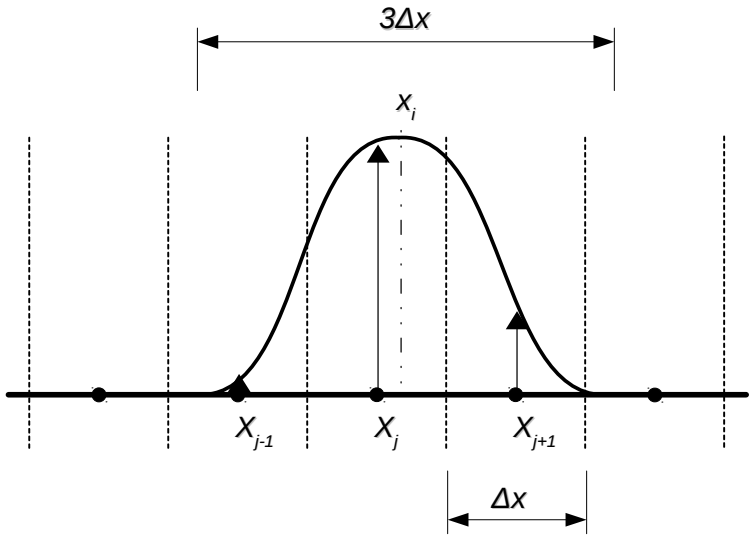

Figure 2.6: The weighting function $W(x)$ defined in Equation (2.12). The function is approximately Gaussian in shape and is three cells wide. Particle data is distributed among the three nearest grid points, with the weighting to each of the three grid points found by evaluating $W(X_{j-1} - x_i)$, $W(X_j - x_i)$ and $W(X_{j+1} - x_i)$, where x_i is the particle position.

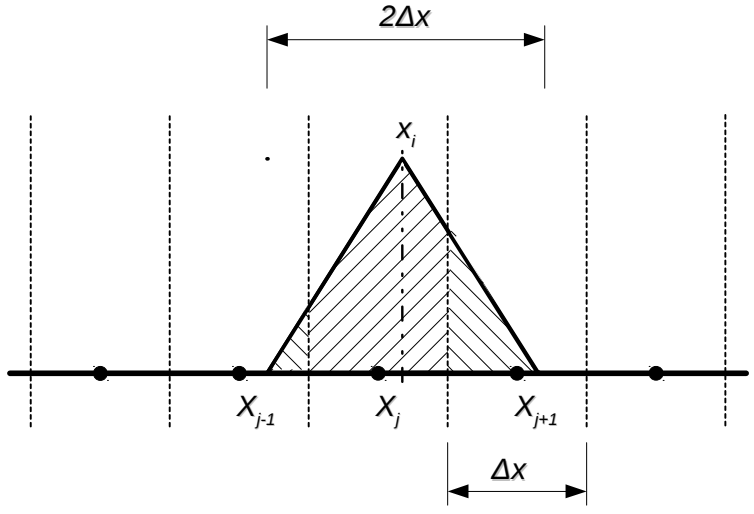

Figure 2.7: The particle cloud for the Triangular Shaped Cloud scheme, which is triangular in shape and 2 cells wide at its base. The weighting to each of the cells is seen here as the area of overlap between the particle cloud and the cell boundaries.

2.6 Updating the electromagnetic fields

Following the density accumulation step (outlined in the previous section), Maxwell's equations are solved on the grid using the accumulated charge, ρ, and current density, $\boldsymbol{J}$, as the source terms. In this section we outline the method used to solve Maxwell's equations and update the electromagnetic fields in our simulations.

The full set of Maxwell's equations, in S.I. units, are

$$\begin{aligned}
\boldsymbol{\nabla}\cdot\boldsymbol{E}(\boldsymbol{r},t) &= \frac{\rho(\boldsymbol{r},t)}{\epsilon_0}, && (2.14)\\
\boldsymbol{\nabla}\cdot\boldsymbol{B}(\boldsymbol{r},t) &= 0, && (2.15)\\
\boldsymbol{\nabla}\times\boldsymbol{E}(\boldsymbol{r},t) &= -\frac{\partial\boldsymbol{B}(\boldsymbol{r},t)}{\partial t}, && (2.16)\\
\boldsymbol{\nabla}\times\boldsymbol{B}(\boldsymbol{r},t) &= \mu_0\boldsymbol{J}(\boldsymbol{r},t)+\frac{1}{c^2}\frac{\partial\boldsymbol{E}(\boldsymbol{r},t)}{\partial t}, && (2.17)
\end{aligned}$$

where $\boldsymbol{r}=(x,y)$ in our 2D system, ϵ_0 and μ_0 are the permittivity and permeability of free space, respectively, and c is the speed of light. We employ periodic boundaries for fields and sources in all of our simulations, hence, Fourier techniques (Cooley and Turkey, 1965) are implemented in the evaluation of Maxwell's equations. The accumulated densities are Fourier transformed each time step, yielding $\rho(\boldsymbol{k},t)$ and $\boldsymbol{J}(\boldsymbol{k},t)$, and we evaluate the Fourier space form of Maxwell's equations, which are given by

$$\begin{aligned}
i\boldsymbol{k}\cdot\boldsymbol{E}(\boldsymbol{k},t) &= \frac{\rho(\boldsymbol{k},t)}{\epsilon_0}, && (2.18)\\
i\boldsymbol{k}\cdot\boldsymbol{B}(\boldsymbol{k},t) &= 0, && (2.19)\\
i\boldsymbol{k}\times\boldsymbol{E}(\boldsymbol{k},t) &= -\frac{\partial\boldsymbol{B}(\boldsymbol{k},t)}{\partial t}, && (2.20)\\
i\boldsymbol{k}\times\boldsymbol{B}(\boldsymbol{k},t) &= \mu_0\boldsymbol{J}(\boldsymbol{k},t)+\frac{1}{c^2}\frac{\partial\boldsymbol{E}(\boldsymbol{k},t)}{\partial t}. && (2.21)
\end{aligned}$$

For our simulations, we set $\epsilon_0=1$. This arises as a result of the normalised set of units we employ in our simulations. The values of μ_0 and c are arbitrarily chosen, while satisfying

$$\frac{1}{\epsilon_0 \mu_0} = c^2. \tag{2.22}$$

To aid in evaluation of Equations (2.18) to (2.21), it is useful to decompose the electromagnetic fields and sources into longitudinal (L) and transverse (T) components, which are taken with respect to $\boldsymbol{k}$ (Dawson, 1983; Sydora, 1999). For vector quantity $\boldsymbol{A}$, the longitudinal and transverse components are defined as (Sydora, 1999)

$$\boldsymbol{A}(\boldsymbol{k}, t) = \boldsymbol{A}_L(\boldsymbol{k}, t) + \boldsymbol{A}_T(\boldsymbol{k}, t), \tag{2.23}$$

where

$$\boldsymbol{k} \times \boldsymbol{A}_L(\boldsymbol{k}, t) = 0, \tag{2.24}$$

$$\boldsymbol{k} \cdot \boldsymbol{A}_T(\boldsymbol{k}, t) = 0. \tag{2.25}$$

Also, by definition

$$\boldsymbol{A}_L(\boldsymbol{k}, t) = \frac{\boldsymbol{k}(\boldsymbol{k} \cdot \boldsymbol{A}(\boldsymbol{k}, t))}{k^2}, \tag{2.26}$$

$$\boldsymbol{A}_T(\boldsymbol{k}, t) = \boldsymbol{A}(\boldsymbol{k}, t) - \boldsymbol{A}_L(\boldsymbol{k}, t). \tag{2.27}$$

It is clear from Equations (2.19) and (2.25), that the magnetic field has only a transverse component. The longitudinal component of the electric field is calculated using Equations (2.18) and (2.26), and is given by (Sydora, 1999)

$$\boldsymbol{E}_L(\boldsymbol{k}, t) = \frac{-i\boldsymbol{k}\rho(\boldsymbol{k}, t)}{\epsilon_0 k^2}. \tag{2.28}$$

Equations (2.20) and (2.21) are used to calculate the transverse components of the magnetic and electric fields, respectively, and can be written as

$$\frac{\partial \boldsymbol{B}_T(\boldsymbol{k},t)}{\partial t} = -i\boldsymbol{k} \times \boldsymbol{E}_T(\boldsymbol{k},t), \tag{2.29}$$

$$\frac{\partial \boldsymbol{E}_T(\boldsymbol{k},t)}{\partial t} = -\frac{1}{\epsilon_0}\boldsymbol{J}_T(\boldsymbol{k},t) + ic^2\boldsymbol{k} \times \boldsymbol{B}_T(\boldsymbol{k},t), \tag{2.30}$$

where the continuity equation, $\partial\rho(\boldsymbol{k},t)/\partial t + i\boldsymbol{k}\cdot\boldsymbol{J}(\boldsymbol{k},t) = 0$, was used to obtain Equation (2.30). Finite difference techniques are employed to approximate the derivatives and solve for the transverse fields in Equations (2.29) and (2.30). Furthermore, the electric and magnetic fields are staggered in time, such that the electric field is evaluated at half integer time steps, $(n+1/2)\Delta t$, which we express as the superscript $(n+1/2)$. The magnetic field is evaluated at the full integer time steps, $n\Delta t$, which we express as the superscript (n). Thus, the transverse fields are updated using the centred difference equations (Sydora, 1999)

$$\boldsymbol{E}_T^{n+1/2}(\boldsymbol{k}) = \boldsymbol{E}_T^{n-1/2}(\boldsymbol{k}) - \frac{\Delta t}{\epsilon_0}\boldsymbol{J}_T^n(\boldsymbol{k}) + ic^2\Delta t\boldsymbol{k} \times \boldsymbol{B}_T^n(\boldsymbol{k}), \tag{2.31}$$

$$\boldsymbol{B}_T^{n+1}(\boldsymbol{k}) = \boldsymbol{B}_T^n(\boldsymbol{k}) - i\Delta t\boldsymbol{k} \times \boldsymbol{E}_T^{n+1/2}(\boldsymbol{k}). \tag{2.32}$$

Equation (2.28) can be rewritten, denoting the appropriate time steps, as

$$\boldsymbol{E}_L^{n+1/2}(\boldsymbol{k},t) = \frac{-i\boldsymbol{k}\rho^{n+1/2}(\boldsymbol{k},t)}{\epsilon_0 k^2}. \tag{2.33}$$

As a consequence of the time staggering described above, a similar time staggering of the particle positions $\boldsymbol{r}$ and velocities $\boldsymbol{v}$ is used. This also has the advantage of allowing the leap-frog technique to be used to update the particle positions using its velocities. This is described in Section 2.7.

In our simulations, the particle position $\boldsymbol{r}$, charge density ρ and electric fields $\boldsymbol{E}$ are all evaluated at the half integer time steps $(n+1/2)\Delta t$. The particle velocity $\boldsymbol{v}$, current density $\boldsymbol{J}$ and magnetic fields B are evaluated at integer time steps $n\Delta t$.

Since finite difference techniques are employed in our simulations, the centred difference form of the gradient operator in Fourier space ($\boldsymbol{\nabla} \rightarrow i\boldsymbol{k}$ and $\nabla^2 \rightarrow -k^2$) needs to be used. By

adopting the convention that primed variables denote simulation values, the continuous space vector operator $i\boldsymbol{k}$ has a finite difference form $i\boldsymbol{k}^{'}$ defined as (Birdsall and Langdon, 1985; Tajima, 1989)

$$ik_x^{'} = ik_x \left[\frac{\sin(k_x \Delta x)}{k_x \Delta x}\right], \quad \text{and} \quad ik_y^{'} = ik_y \left[\frac{\sin(k_y \Delta y)}{k_y \Delta y}\right], \tag{2.34}$$

while k^2 has finite difference form $K^{'2}$ given by (Birdsall and Langdon, 1985; Tajima, 1989)

$$K_x^{'2} = k_x^2 \left[\frac{\sin(k_x \Delta x/2)}{k_x \Delta x/2}\right]^2, \quad \text{and} \quad K_y^{'2} = k_y^2 \left[\frac{\sin(k_y \Delta y/2)}{k_y \Delta y/2}\right]^2. \tag{2.35}$$

A derivation of Equations (2.34) and (2.35) is provided in Appendix A. After the field values at the grid points have been computed using Equations (2.31) to (2.33), the longitudinal and transverse components of the electric field are combined and the total electromagnetic force at the particle positions can be found.

To perform the field update step on the GPU, we assign a row of grid points to each thread block, and adjacent threads in the block are tasked with the calculation of consecutive electromagnetic Fourier modes, i.e, consecutive threads will calculate the electromagnetic fields at consecutive grid points. No data dependencies occur during this step and the field calculations proceed in parallel. We employ the cuFFT library (Nvidia, 2015c), provided by CUDA, to perform the Fourier transforms on the GPU. The cuFFT library is easy to implement and is modelled after the Fastest Fourier Transform in the West (FFTW), a popular and efficient FFT algorithm.

2.7 Particle updating

The equations governing the motion of the simulated particles are evaluated at each time step and the particle dynamics are updated. In this section we discuss the methods used to update the particle dynamics, i.e., updating the position, $\boldsymbol{r} = (x, y)$, and velocity, $\boldsymbol{v} = (v_x, v_y, v_z)$, of each particle. After the electromagnetic fields in the simulation are found for the current time step (see Section 2.6), the electromagnetic force on the particles is found from the field values, interpolated from the surrounding cells (see Section 2.5). The particle dynamics are

updated in our simulations by evaluating

$$\frac{d\boldsymbol{r}(t)}{dt} = \boldsymbol{v}(t), \tag{2.36}$$

$$\frac{m\boldsymbol{v}(t)}{dt} = q\left[\boldsymbol{E}(r(t),t) + \boldsymbol{v}(t) \times \boldsymbol{B}(r(t),t)\right], \tag{2.37}$$

where $\boldsymbol{E}$ and $\boldsymbol{B}$ are the electric and magnetic field values at the particle position (x, y), interpolated from the grid. As mentioned in Section 2.6, we employ a time staggering of simulation quantities which allows the leap-frog method to be used to update a particle's position using it's calculated velocity (Birdsall and Langdon, 1985). The electric field $\boldsymbol{E}$ and the particle positions $\boldsymbol{r}$ are evaluated at half integer time steps, which we denote with superscript $n+1/2$. The magnetic field, along with particle velocities are evaluated at integer time steps, denoted by the superscript $n+1$.

We employ finite difference techniques to evaluate Equations (2.36) and (2.37), where the centred difference form of Equations (2.36) and (2.37), denoting the appropriate time steps, is given by (Sydora, 1999)

$$\boldsymbol{r}^{n+1/2} = \boldsymbol{r}^{n-1/2} + \Delta t \boldsymbol{v}^{n} \tag{2.38}$$

$$\frac{\boldsymbol{v}^{n+1} - \boldsymbol{v}^{n}}{\Delta t} = \frac{q}{m}\left[\boldsymbol{E}^{n+1/2} + \boldsymbol{v}^{n+1/2} \times \boldsymbol{B}^{n+1/2}\right], \tag{2.39}$$

where the values $\boldsymbol{v}^{n+1/2}$ and $\boldsymbol{B}^{n+1/2}$ are approximated by $\boldsymbol{v}^{n+1/2} = (\boldsymbol{v}^{n} + \boldsymbol{v}^{n+1})/2$ and $\boldsymbol{B}^{n+1/2} = (\boldsymbol{B}^{n} + \boldsymbol{B}^{n+1})/2$, respectively (Birdsall and Langdon, 1985; Sydora, 1999).

We use the leap-frog technique to solve Newton's equation and update the particle positions. The leap-frog technique is second order accurate as well as time centred, permitting a good balance between accuracy, stability and computational expense (Dawson, 1983; Birdsall and Langdon, 1985). The particle positions in our simulations are updated via Equation (2.38).

With $\boldsymbol{v}^{n+1/2}$ defined as $1/2(\boldsymbol{v}^{n} + \boldsymbol{v}^{n+1})$, Equation (2.39) is an implicit relation for $\boldsymbol{v}^{n+1}$. We use the Boris method (Boris, 1970) to solve it. The Boris method is time centred and second order accurate, and solves Equation (2.39) by decoupling the contributions from the electric

and magnetic fields (Boris, 1970; Dawson, 1983; Birdsall and Langdon, 1985). The separation of the electric and magnetic force components in Equation (2.39) is achieved by defining the intermediate velocities $\boldsymbol{v}^-$ and $\boldsymbol{v}^+$ via

$$\boldsymbol{v}^n = \boldsymbol{v}^- - \frac{q\boldsymbol{E}^{n+1/2}}{m}\frac{\Delta t}{2}, \tag{2.40}$$

$$\boldsymbol{v}^{n+1} = \boldsymbol{v}^+ + \frac{q\boldsymbol{E}^{n+1/2}}{m}\frac{\Delta t}{2}. \tag{2.41}$$

Substituting Equations (2.40) and (2.41) into Equation (2.39) yields

$$\frac{\boldsymbol{v}^+ - \boldsymbol{v}^-}{\Delta t} = \frac{q}{2m}(\boldsymbol{v}^+ + \boldsymbol{v}^-) \times \boldsymbol{B}^{n+1/2}, \tag{2.42}$$

which contains no explicit mention of the electric field. Equations (2.40) to (2.42), therefore, describe the decoupled electric and magnetic forces on a charged particle. Equations (2.40) and (2.41) describe an acceleration of the charged particle by the electric field. On the other hand, Equation (2.42) describes a rotation of the particle momentum about an axis parallel to $\boldsymbol{B}$, by an angle $\phi = -2\tan(qB\Delta t/2m)$ (Dawson, 1983; Birdsall and Langdon, 1985; Sydora, 1999). To perform the rotation defined in Equation (2.42), the following definitions are used

$$\boldsymbol{v}' = \boldsymbol{v}^- + \boldsymbol{v}^- \times \boldsymbol{t}, \tag{2.43}$$

$$\boldsymbol{v}^+ = \boldsymbol{v}^- + \boldsymbol{v}' \times \boldsymbol{s}, \tag{2.44}$$

where $\boldsymbol{v}'$ describes some intermediate velocity, and $\boldsymbol{t}$ and $\boldsymbol{s}$ are respectively defined by (Birdsall and Langdon, 1985)

$$\boldsymbol{t} = \frac{q\boldsymbol{B}^n\Delta t}{2m}, \tag{2.45}$$

$$\boldsymbol{s} = \frac{2\boldsymbol{t}}{(1+t^2)}. \tag{2.46}$$

Hence, the full method used to evaluate Equation (2.39), and update a particle's velocity using the Boris method, is given by the following series of steps,

- The particle is initially accelerated by the electric field for half of a time step using Equation (2.40), i.e., $\boldsymbol{v}^n \rightarrow \boldsymbol{v}^-$.
- A rotation of the new particle velocity ($\boldsymbol{v}^-$) by the magnetic field is performed using Equations (2.43) and (2.44), i.e., $\boldsymbol{v}^- \rightarrow \boldsymbol{v}^+$.
- Finally, the particle is accelerated for another half of the time step, using Equation (2.41), and the updated particle velocity is found, i.e., $\boldsymbol{v}^+ \rightarrow \boldsymbol{v}^{n+1}$.

There are no data dependencies in the particle push step and each particle's position and velocity can be updated independently, in parallel. We assign a simulation cell to a thread block in the GPU and have the threads update the dynamics of all of the particles within the cell. Since the particle data in our simulations is sorted by cell, processing the particles is done in a coalesced fashion. A single read of the relevant grid (field) data is required per thread block, to update the dynamics of all particles within the cell. This has the advantage of reducing execution times by minimising global memory reads.

2.8 Stability of the numerical schemes

Particle-in-cell simulations employ a discretisation of space, through the use of a spatial grid having cell sizes Δx by Δy, and a discretisation of time, by taking a finite time step Δt. Through the improper choice of $\Delta x, \Delta y$ and Δt, artefacts can arise in the numerical schemes used to update the fields and particle dynamics, affecting both the accuracy and stability of the simulation. These artefacts arise as a result of the aliasing of the plasma dynamics and produce non-physical instabilities, and the unbounded, artificial heating of the plasma (Verboncoeur, 2005). In this section we discuss the impact the choices of $\Delta x, \Delta y$ and Δt have on the stability of the simulation run. The computer round-off errors, i.e., errors in calculations caused by the finite word-length of variables stored in the computer's memory, are usually not a major source of inaccuracies in PIC simulations (Hockney and Eastwood, 1981).

The choice of cell size, Δx and Δy, determines the resolution of the plasma by the simulation. Variation in the plasma on scales smaller than the cell size is less well resolved. It is this

loss of information which leads to aliasing of the Fourier modes in the simulation, and the formation and growth of a numeric effect know as the finite grid instability. The finite grid instability causes the artificial, unbounded heating of the plasma [see Birdsall and Langdon (1985, ch. 8) and Verboncoeur (2005)]. The order of the interpolation scheme used in the simulation is known to influence this aliasing, where the effects of aliasing are reduced for higher order weighting schemes. In the general case, the finite grid instability is known to be negligible when the cell size is restricted to (Matsumoto and Omura, 1984; Birdsall and Langdon, 1985; Ueda et al., 1994; Verboncoeur, 2005; Lapenta, 2012)

$$\Delta x < 2\lambda_{De}, \tag{2.47}$$

where $\lambda_{De} = (\epsilon_0 T_e / n_{0e} e^2)^{1/2}$ is the electron Debye length. While the Debye length is usually orders of magnitude smaller than the scales of interest under investigation, explicit PIC simulations require strict adherence to this stability condition (Verboncoeur, 2005).

The choice of time step, Δt, directly affects the stability of the leap-frog scheme used to solve Newton's equation and update the particle positions (discussed in Section 2.7). The restriction on the time step that is required to maintain stability in the leap-frog scheme can be found by analysing the dynamics of particles in simple harmonic motion (Birdsall and Langdon, 1985; Verboncoeur, 2005). A 1D simple harmonic oscillator is governed by the equation

$$\frac{d^2x(t)}{dt^2} = -\omega_0^2 x(t), \tag{2.48}$$

where ω_0 is the natural frequency of the system and $x(t)$ is the displacement of the particle from equilibrium, at time t. We now adopt the convention, $x^n \equiv x(n\Delta t)$, to denote the displacement at a particular time. This allows us to write the centred difference approximation to Equation (2.48) as

$$\frac{x^{n+1} - 2x^n + x^{n-1}}{(\Delta t)^2} = -\omega_0^2 x^n. \tag{2.49}$$

We now assume solutions of the form

$$x^n = Ae^{-i\omega n\Delta t}, \tag{2.50}$$

where A is an amplitude and ω is an unknown angular frequency. Substituting Equation (2.50) into Equation (2.49) and simplifying the result, yields

$$\frac{e^{-i\omega\Delta t} - 2 + e^{+i\omega\Delta t}}{\Delta t^2} = -\omega_0^2. \tag{2.51}$$

After some simple algebra, we obtain the result

$$\frac{\omega\Delta t}{2} = \pm \sin^{-1}\left(\frac{\omega_0\Delta t}{2}\right), \tag{2.52}$$

where the following identities were used to obtain Equation (2.52)

$$\begin{aligned} \cos(\theta) &= \frac{\exp(i\theta) + \exp(-i\theta)}{2}, \\ \sin^2(\theta) &= \frac{1 - \cos(2\theta)}{2}. \end{aligned}$$

The value of $\sin^{-1}(x)$ in Equation (2.52) can be approximated, for $x^2 < 1$, using (Gradshteyn and Ryzhik, 2007)

$$\sin^{-1}(x) = x + \frac{1}{2 \cdot 3}x^3 + \frac{1 \cdot 3}{2 \cdot 4 \cdot 5}x^5 + ..., \tag{2.53}$$

thus Equation (2.52) becomes

$$\frac{\omega\Delta t}{2} = \pm\left[\frac{\omega_0\Delta t}{2} + \frac{1}{6}\left(\frac{\omega_0\Delta t}{2}\right)^3 + \frac{3}{40}\left(\frac{\omega_0\Delta t}{2}\right)^5 + ...\right]. \tag{2.54}$$

For the case $\left|\frac{\omega_0\Delta t}{2}\right| \ll 1$, the series can be truncated to

$$\begin{aligned} \frac{\omega\Delta t}{2} &\simeq \pm\frac{\omega_0\Delta t}{2} \\ \omega &\simeq \pm\omega_0. \end{aligned} \tag{2.55}$$

Here ω is purely real and $\omega \simeq \pm\omega_0$, as desired. For the case $\omega_0\Delta t/2 > 1$, it is clear that Equation (2.52) predicts complex values of ω, for which Equation (2.50) will be either growing or decaying exponentially with time. This is inconsistent with the simple harmonic model and indicates instability in the numerical scheme. We can infer that for the leap frog scheme to be numerically stable, we require a time step defined by

$$\omega_p\Delta t < 2, \tag{2.56}$$

where ω_p is the highest natural frequency of the plasma (Hockney and Eastwood, 1981; Birdsall and Langdon, 1985). In practice, the value

$$\omega_p\Delta t \leq 0.5 \tag{2.57}$$

is commonly used for reasonable accuracy and stability (Hockney and Eastwood, 1981; Winske and Omidi, 1996). Since the electron plasma frequency is usually the highest natural frequency of the plasma, for stability in the leap-frog scheme, Equation (2.57) stipulates that Δt should be chosen such that Langmuir waves are resolved (Verboncoeur, 2005).

The codes developed for this thesis are fully electromagnetic, requiring the solution of the full set of Maxwell's equations. This places a further restriction on the choices of Δx, Δy and Δt in the simulation. This restriction arises as a consequence of the numerical schemes used to solve Maxwell's equations (see Section 2.6). To analyse the stability of the schemes

used to solve Maxwell's equations in our simulations, we examine the propagation of plane electromagnetic waves in a vacuum (Sydora, 1999).

As discussed in Section 2.6, Maxwell's equations are solved in Fourier space by first separating the electromagnetic fields into longitudinal (L) and transverse (T) components. The transverse components of the fields are then staggered in time and are governed by the equations (see Section 2.6)

$$\boldsymbol{E}_T^{n+1/2}(\boldsymbol{k}) = \boldsymbol{E}_T^{n-1/2}(\boldsymbol{k}) - \frac{\Delta t}{\epsilon_0}\boldsymbol{J}_T^n(\boldsymbol{k}) + ic^2\Delta t\boldsymbol{k}\times\boldsymbol{B}_T^n(\boldsymbol{k}), \tag{2.58}$$

$$\boldsymbol{B}_T^{n+1}(\boldsymbol{k}) = \boldsymbol{B}_T^n(\boldsymbol{k}) - i\Delta t\boldsymbol{k}\times\boldsymbol{E}_T^{n+1/2}(\boldsymbol{k}), \tag{2.59}$$

where the superscripts denote the time steps and $\boldsymbol{J}_T = 0$ in a vacuum. To proceed with the stability analysis, we assume the fields have the harmonic form given by,

$$\boldsymbol{E}_T^{n+1/2}(\boldsymbol{k}) = \boldsymbol{E}_0(\boldsymbol{k})e^{-i\omega(n+1/2)\Delta t}, \tag{2.60}$$

$$\boldsymbol{B}_T^{n}(\boldsymbol{k}) = \boldsymbol{B}_0(\boldsymbol{k})e^{-i\omega n\Delta t}. \tag{2.61}$$

Substituting the fields defined in Equations (2.60) and (2.61) into the finite difference Equations (2.58) and (2.59), yields (Sydora, 1999)

$$c^2k^2 = \frac{\sin^2(\omega\Delta t/2)}{(\Delta t/2)^2}. \tag{2.62}$$

Equation (2.62) is only satisfied for real frequency, ω, if

$$ck\Delta t < 2. \tag{2.63}$$

The condition expressed in Equation (2.63) can be written in the alternate form, for a 2D system (Verboncoeur, 2005), as

$$(c\Delta t)^2 < \left(\frac{1}{\Delta x^2} + \frac{1}{\Delta y^2}\right)^{-1}, \tag{2.64}$$

and is known as the Courant-Friedrichs-Levy (CFL) condition. The CFL condition is equivalent to the requirement that the simulation resolve light waves in the plasma (Sydora, 1999) and limits the distance a particle can move each time step, i.e., particles cannot move more than a cell size per time step.

In our simulations, values for Δx, Δy and Δt are chosen to strictly adhere to all of the above mentioned stability conditions, Equations (2.47), (2.57) and (2.64).

2.8.1 Filtering

Due to the discrete nature of PIC simulations, statistical noise remains a persistent problem (Morse and Nielson, 1971; Verboncoeur, 2005). Simulations adhering to all stability conditions can still be subjected to high noise levels. The fluctuation levels of the noise can exceed that of the waves under investigation, obscuring the plasma dynamics and creating numerical artefacts such as heating.

The use of higher order particle shapes/ weighting schemes and the filtering of the high frequency, short wavelength modes, has long been employed in PIC simulations to control noise and stabilize simulations (Birdsall and Langdon, 1985; Xue et al., 2013; May et al., 2014). By applying a Fourier space low pass filter to the particle densities, we truncate the number of physical modes, $\boldsymbol{k}$, resolved in the simulation, by attenuating the short wavelength fluctuations. Since these high frequency modes will generally interact weakly with the plasma, their exclusion is not deleterious to simulation accuracy (Dawson, 1983).

In our simulations, to suppress the high frequency modes, a low pass filter is applied to the particle densities. We employ the commonly used, exponential filter in Fourier space (Godfrey, 1974; Peiravi, 2010; Xue et al., 2013; May et al., 2014), which is

$$S_{filter}(\boldsymbol{k}) = e^{-(\boldsymbol{k}a)^2/2}, \tag{2.65}$$

where a is usually the size of the particle.

Chapter 3

Impact of the particle shape factor

3.1 Discussion of B-splines

As discussed in Section 2.5, particle-in-cell (PIC) simulations use discrete particles to model the statistical distribution of the plasma in phase space (Sydora, 1999; Verboncoeur, 2005). The particles in PIC simulations are regarded as finite sized clouds of charge which move freely throughout the simulation domain, depositing charge and current density to the grid. A weighting step is required in PIC simulations, which defines the interaction between fields located at discrete points, and the particles which can take on any position within the simulation domain. PIC simulations typically employ weighting schemes defined by the family of B-splines (Haugbølle et al., 2013).

In the code developed for this thesis, we have opted to use the third order B-spline. In this chapter, we discuss the reasoning for this choice of weighting scheme. We first give an overview of the functions defined by the family of B-splines, and then discuss results of PIC simulations obtained using each function. In particular, we focus on the impact each spline has on energy conservation in our simulations.

Below, we shall discuss the four lowest order B-splines. For simplicity, we limit our discussion of the functions to 1D systems. The first four B-splines are defined as follows:

The **Zeroth order B-spline** corresponds to the nearest grid point (NGP) scheme. In this scheme the plasma particles are treated as point particles and the weighting of all the particle

data is to a single cell, i.e., the cell in which the particle is contained. The weighting function $W_0(x)$ for this scheme is square in shape, one cell size (Δx) wide, and is defined as

$$W_0(x) = \begin{cases} 1 & \text{, if } |x| < \dfrac{\Delta x}{2} \\ 0 & \text{, otherwise.} \end{cases} \tag{3.1}$$

The **First order B-spline** (linear spline) corresponds to the cloud-in-cell (CIC) scheme. The particle cloud in this scheme is regarded as being square in shape, one cell wide. The particle data here is shared between the two nearest grid points. The weighting function $W_1(x)$ for this scheme is triangular in shape, two cells wide at its base, and is

$$W_1(x) = \begin{cases} 1 - \left|\dfrac{x}{\Delta x}\right| & \text{, if } |x| < \Delta x \\ 0 & \text{, otherwise.} \end{cases} \tag{3.2}$$

The **Second order B-spline** (quadratic spline) corresponds to the triangular shaped cloud (TSC) scheme. As its name suggests, the particle clouds are regarded as being triangular in shape, two cells wide at the base, and the particle data is shared among the three nearest grid points. The weighting function $W_2(x)$ for the quadratic spline is approximately Gaussian in shape and is three cells wide. The weighting function here, is defined by

$$W_2(x) = \begin{cases} \dfrac{3}{4} - \left(\dfrac{x}{\Delta x}\right)^2 & \text{, if } |x| < \dfrac{\Delta x}{2} \\ \dfrac{1}{2}\left(\dfrac{3}{2} - \left|\dfrac{x}{\Delta x}\right|\right)^2 & \text{, if } \dfrac{\Delta x}{2} \leq |x| < \dfrac{3\Delta x}{2} \\ 0 & \text{, otherwise.} \end{cases} \tag{3.3}$$

The **Third order B-spline** (cubic spline) corresponds to the piecewise cubic spline (PCS) scheme. The particle clouds in this scheme are approximately Gaussian in shape, three cells wide, with the particle data being divided among the four nearest grid points. The weighting function $W_3(x)$ for the cubic spline is also approximately Gaussian in shape, four cells wide, and is given by

$$W_3(x) = \begin{cases} \frac{1}{6}\left(4 - 6\left(\frac{x}{\Delta x}\right)^2 + 3\left|\left(\frac{x}{\Delta x}\right)\right|^3\right) & \text{, if } 0 \leq |x| < \Delta x \\ \frac{1}{6}\left(2 - \left|\frac{x}{\Delta x}\right|\right)^3 & \text{, if } \Delta x \leq |x| \leq 2\Delta x \\ 0 & \text{, otherwise.} \end{cases} \tag{3.4}$$

As discussed in Section 2.5, the weighting to a grid point located at X_j is found by evaluating the function $W_n(X_j - x_i)$, where x_i is the position of the particle. The weighting functions defined in Equations (3.2) to (3.4) are produced by taking the convolution of the top-hat function (zeroth order spline) with the spline from the previous order (Hockney and Eastwood, 1981; May et al., 2014), i.e., $W_3(x) = W_0(x) * W_2(x)$. The above weighting functions have a series of Fourier transforms modelled by the sinc function, where the Fourier representation of Equations (3.1) to (3.4), is given by (Birdsall and Langdon, 1985; May et al., 2014)

$$W_n(k) = \left(\frac{\sin\left(\frac{k\Delta x}{2}\right)}{\frac{k\Delta x}{2}}\right)^{n+1} , \tag{3.5}$$

where n is the order of the weighting scheme, i.e., $n = 0, 1, 2, 3$ for Equations (3.1) to (3.4), respectively. Figure 3.1 displays the four lowest order B-splines, defined in Equations (3.1) to (3.4), for a particle located at $x_i = X_j$. Figure 3.2 illustrates their Fourier representation, Equation (3.5).

As seen in Figure 3.1, increasing the order of the spline results in weighting functions which are wider and smoother. The functions progress from square shaped (blue coloured plot in Figure 3.1), which has sharp edges and weights to a single cell, to Gaussian shaped (red coloured plot in Figure 3.1), which has rounder edges and weights to four cells. Thus, the fluctuations in charge and current density produced by particles moving in and out of the cells will decrease as the order of the spline increases, reducing noise in the simulation. The Fourier representation of the weighting functions, Figure 3.2, indicates that the functions act as low-pass filters, attenuating the higher order modes. This attenuation increases as the order of the interpolation increases. The use of higher the order splines is also known to reduce the aliasing of the Fourier modes in the simulation, reducing artificial grid effects (Dawson, 1983; Birdsall and Langdon, 1985; May et al., 2014)

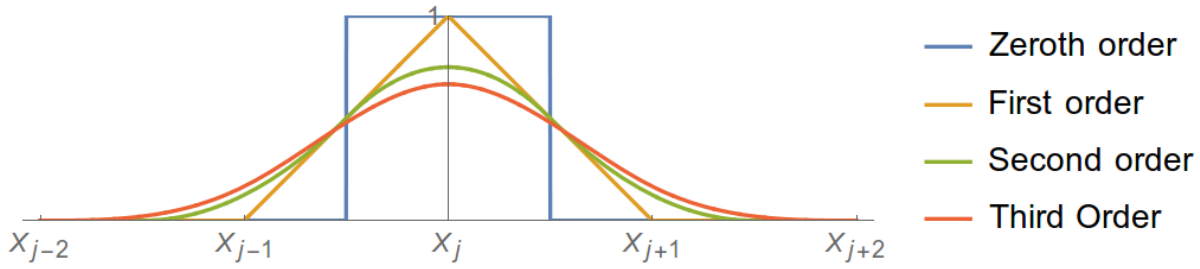

Figure 3.1: The weighting functions defined in Equations (3.1) to (3.4), respectively.

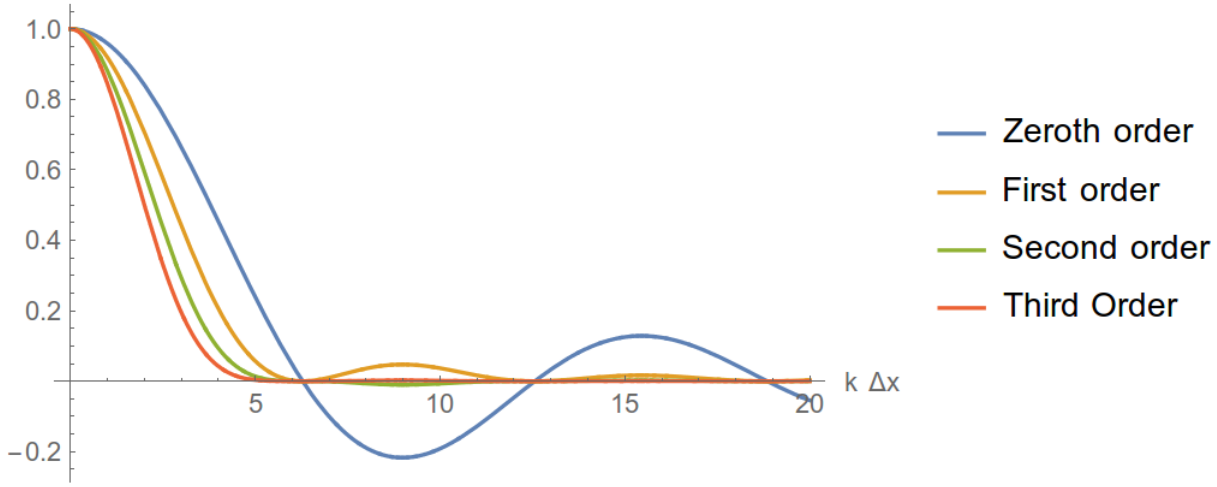

Figure 3.2: The Fourier representation of the weighting functions, given by Equation (3.5)

	Number of particles per cell, per species
Run 1	16
Run 2	32
Run 3	128

Table 3.1: An overview of the three simulation runs performed to investigate the impact of the weighting schemes on the energy conservation in our simulations.

3.2 PIC simulations: linear, quadratic and cubic splines

To investigate the impact of each weighting scheme on our simulation results, we ran 2D3V electromagnetic simulations for a stable electron-ion plasma, and briefly discuss the results next. Three simulations were run for each of the weighting schemes defined above. Since the nearest grid point (NGP) scheme is rarely used in PIC simulations, due to its poor noise properties, results using the NGP weighting were not obtained, i.e., we only obtained results using the cloud-in-cell (CIC), triangular shaped cloud (TSC) and piecewise cubic spline (PCS) schemes.

In each simulation run, we used a different number of particles per cell, per species. In simulation Run 1, results were obtained for each of the weighting schemes using 16 particles per cell, per species. For Run 2, the number of particles was increased to 32 particles per cell, per species. Finally, in Run 3, we used 128 particles per cell, per species. The simulation runs are given in Table 3.1.

Our simulation parameters are normalised with respect to the electron species. We set the ion-electron mass ratio as $m_i/m_e = 100$ and set the temperatures as $T_i = T_e$, where subscripts i and e denote the electron and ion species, respectively. In all simulation runs we used a simulation domain size defined by $L_x = L_y = 320\lambda_{De}$, with a cell size defined by $\Delta x = \Delta y = \lambda_{De}$. The particle species were modelled by isotropic Maxwellian velocity distributions in all simulations performed for this chapter.

We set the speed of light in our simulations to $c/v_{the} = 16$. The simulations are evolved up to a time corresponding to $\omega_{pe}t = 2000$, with a time step defined by $\omega_{pe}\Delta t = 0.02$. The plasma was immersed in a constant, uniform magnetic field $\boldsymbol{B}_0$, which was directed along the x-axis. The strength of the magnetic field results in an electron cyclotron frequency of $\omega_{ce}/\omega_{pe} = 0.23$.

In our discussion of the results from the simulations, we will focus primarily on the total energy in the system, i.e., the sum of particle and field energies. Since we are simulating an isolated plasma system, the total energy should remain constant. Deviations in the total energy will indicate the degree to which the simulation fails to reproduce the underlying physics. Due to the discrete nature of PIC simulations, however, fluctuations in the total energy are expected.

Figures 3.3 to 3.5 compare the temporal evolution of the total energy for each simulation from Runs 1 to 3, respectively. In each of the plots in Figures 3.3 to 3.5, the left-hand panel illustrates the results using the 2D CIC scheme (first order spline), the middle panel illustrates the results using the 2D TSC scheme (second order spline) and the right-hand panel illustrates results using the 2D PCS scheme (third order spline). Energies in our simulations are expressed in terms of the electron thermal energy T_e.

In Figure 3.3, we display the time evolution of the total energy in the simulations performed for Run 1, i.e., those having 16 particles per cell, per species. For the CIC simulation (left-hand panel of Figure 3.3), we observe an average peak-to-peak fluctuation level of $E_{\text{peak-to-peak}} \approx 6T_e$. The simulation using the CIC scheme is also observed to gain a small amount of energy as the simulation progresses. We measure the change in energy as the difference between the final and initial energies. For the CIC simulation, total energy increases by $\Delta E_{\text{tot}} = E_{\text{tot}}(\omega_{pe}t = 2000) - E_{\text{tot}}(\omega_{pe}t = 0) \approx 20T_e$. While this indicates a weakness of the plasma model, the deviation is very small, approximately 0.007 % of the initial energy, which is calculated using $[E_{\text{tot}}(\omega_{pe}t = 2000) - E_{\text{tot}}(\omega_{pe}t = 0)]/E_{tot}(\omega_{pe}t = 0) \times 100$.

As seen in the middle panel of Figure 3.3, the average peak-to-peak fluctuation level in the simulation using the TSC scheme is $E_{\text{peak-to-peak}} \approx 6T_e$, which is similar to that observed for the simulation using the CIC scheme. However, a smaller change in the total energy is observed, where energy decreases by $\Delta E_{\text{tot}} \approx 5T_e$. This should be compared to the change in energy observed when using the CIC scheme, which was $\Delta E_{\text{tot}} \approx 20T_e$.

Finally, for the simulation using the PSC scheme in Run 1, shown in the right-hand panel of Figure 3.3, we again observe a peak-to-peak fluctuation in the total energy given by $E_{\text{peak-to-peak}} \approx 6T_e$. A comparison of all of the panels in Figure 3.3, reveals that the change in total energy in the PSC simulation was the smallest of the three cases, i.e., decreasing by $\Delta E_{\text{tot}} \approx 4T_e$. This confirms that higher order weighting schemes improve energy conservation in the system.

The results obtained for the simulations of Run 2, i.e. those having 32 particles per cell, per species, are displayed in Figure 3.4. As before, all simulations here exhibit the same average peak-to-peak fluctuation in the total energy, regardless of weighting scheme. However, an increase in the number of particles per cell is observed to yield a smaller peak-to-peak fluctuation in total energy, i.e., $E_{\text{peak-to-peak}} \approx 4T_e$, compared to the simulations from Run 1. This is due to the reduction in the density fluctuations associated with a single particle moving in and out of a cell containing twice the number of particles as before. Comparing the panels of Figure 3.4 reveals a decrease in the change in total energy as the order of the weighting scheme increases, as expected. For the CIC simulation, the total energy displayed in the left-hand panel is seen to increase by $\Delta E_{\text{tot}} \approx 11T_e$, which is about half the amount that was observed in the corresponding simulation from run 1. Similarly, the TSC simulation in Run 2, showed a decrease in total energy of $\Delta E_{\text{tot}} \approx 3T_e$ and the PCS decreased by $\Delta E_{\text{tot}} \approx 2T_e$, both being smaller than their Run 1 counterparts.

Figure 3.5 displays the results from the simulations of Run 3, where the trend of decreasing peak-to-peak fluctuation levels with increasing number of particles per cell is observed. The peak-to-peak fluctuation levels for the simulations from Run 3 are observed in Figure 3.5 to be $E_{\text{peak-to-peak}} \approx 2T_e$. The deviation in the total energy for each scheme here is also observed to be lowest of the three runs. Total energy is observed to increase by $\Delta E_{\text{tot}} \approx 2T_e$ for the CIC simulation, while remaining approximately constant for the TSC and PCS simulations, respectively [compare panels in Figure 3.5].

It is clear from Figures 3.3 to 3.5, discussed above, that the order of the weighting scheme affects the conservation of energy in the simulations. An increase in the order of the weighting scheme reduces artificial instabilities and grid effects, providing a more accurate description of the plasma. However, we observed that changing the order of the weighting does not affect the peak-to-peak fluctuation levels of the total energy, as much as changing the number of particles used in the simulation does.

While increasing the order of the weighting reduces noise, it comes at the expense of an increase in the number of operations performed per particle, per time step. For our 2D system, the CIC scheme will divide the particle densities among 4 cells, the TSC scheme among 9 cells and the PCS scheme among 16 cells. In Figure 3.6 we display the execution times for each of the simulations discussed above. As expected, increasing the order of the weighting scheme increases the execution time of the simulations. The TSC scheme is observed to run for approximately 1.4 times longer than the CIC scheme on average. On the other hand, the PCS scheme, on average, runs for approximately 1.8 times longer than the

CIC scheme. Also seen in Figure 3.6, the differences between the execution times of each scheme increases as the number of particles increases.

The allowable number of particles used in our simulations is limited by the finite non-expandable memory on the GPU. Using higher order methods allows us to be able to exchange an increase in the number of operations performed, for the use of a lower number of particles per cell, to obtain more accurate results. This is best illustrated by comparing the right-hand panel of Figure 3.4 with the left-hand panel of 3.5, where we observe that energy is conserved to a similar magnitude. In other words, the total energy is seen to change by $\Delta E_{\text{tot}} \approx 2T_e$ using the PCS scheme with 32 particles per cell, per species (see right-hand plot of Figure 3.4), or by using the CIC scheme with 128 particles per cell, per species (see left-hand plot of Figure 3.5). To balance accuracy and execution times, we have opted to use the TSC scheme in all of the simulations performed for this thesis.

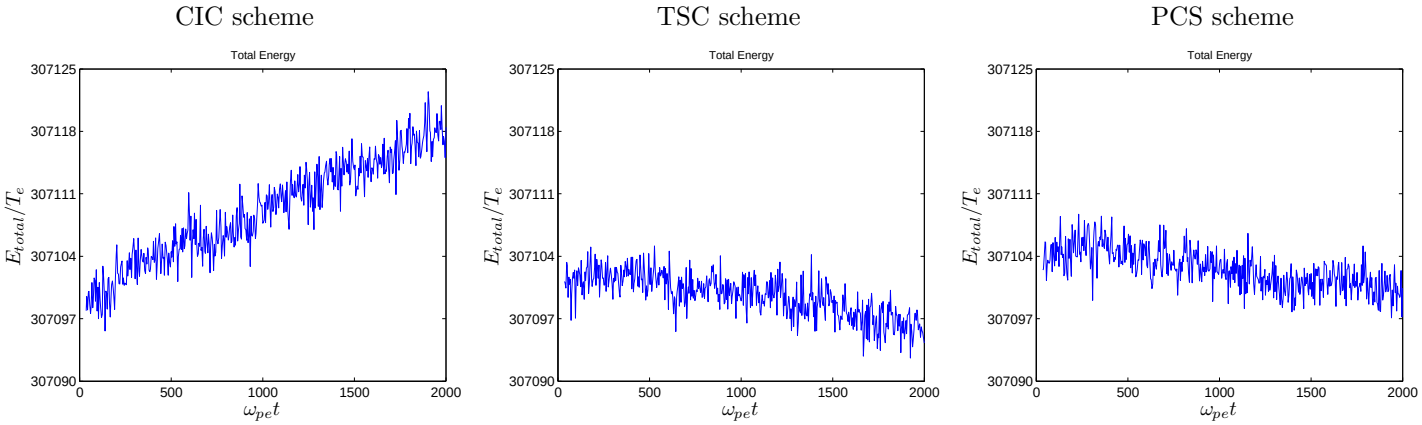

Figure 3.3: Simulation results from Run 1, i.e., those having 16 particles per cell, per species.

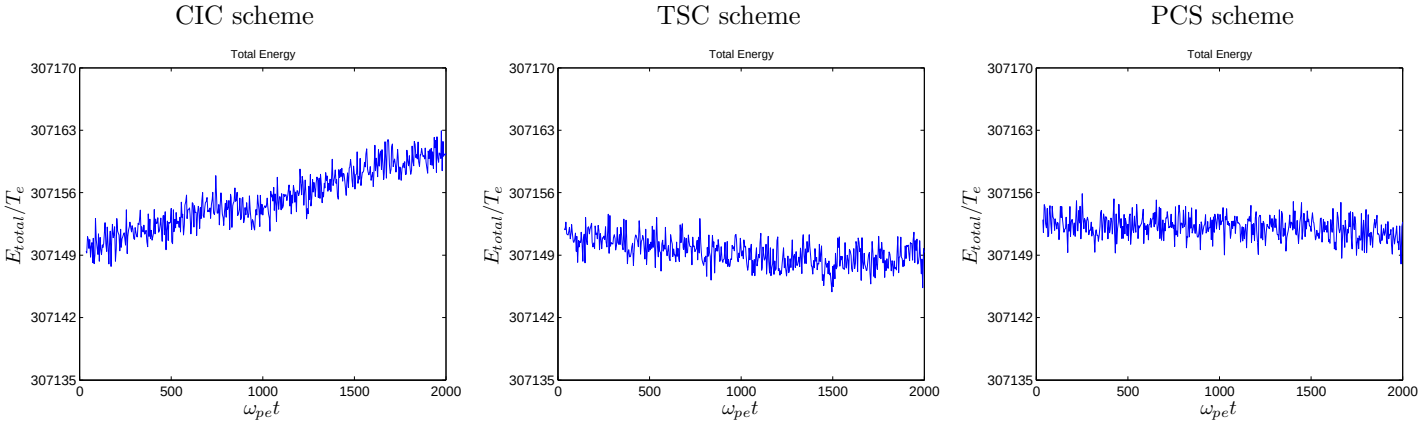

Figure 3.4: Simulation results from Run 2, i.e., those having 32 particles per cell, per species.

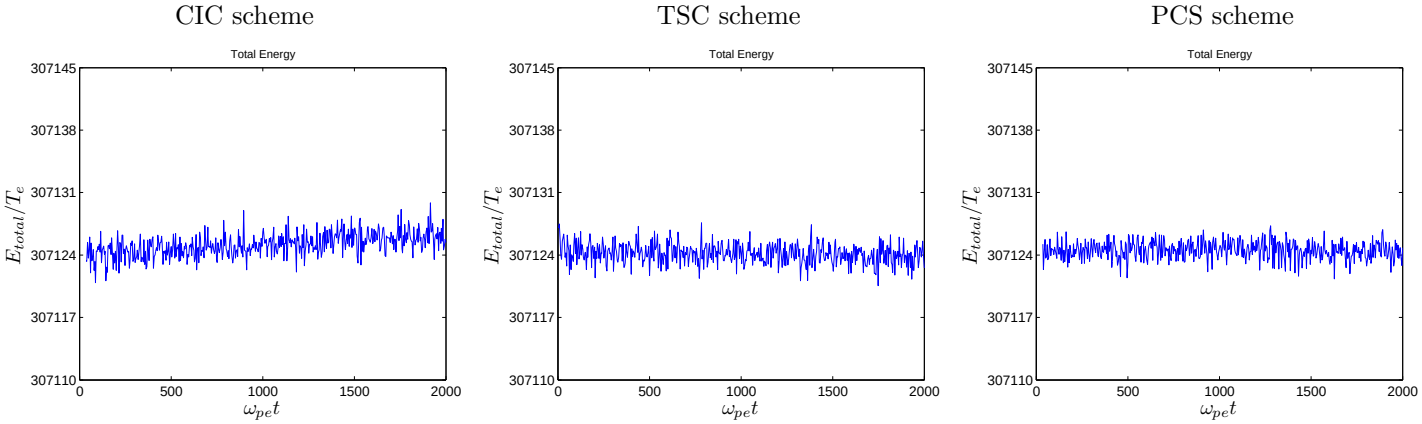

Figure 3.5: Simulation results from Run 3, i.e., those having 128 particles per cell, per species.

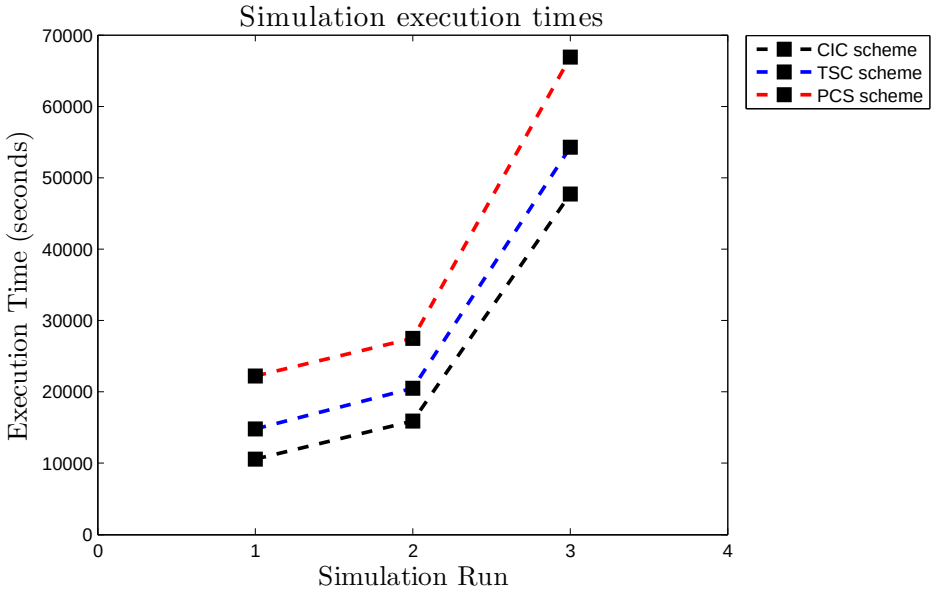

Figure 3.6: The execution times for each of the simulations from Run 1 to 3.

Chapter 4

Simulation study of stable plasma waves

As an initial case study, we apply the 2D3V electromagnetic particle-in-cell (PIC) simulation code developed and reported on in this thesis to the investigation of stable plasma waves propagating in an electron-ion plasma. The simulations are 2D3V in regards to the fact that the particle positions are allowed to vary in only two spatial dimensions, x and y, while all three components of the particle velocity vector are dynamically essential, i.e., $\boldsymbol{v} = (v_x, v_y, v_z)$. No sources of free energy are present in the plasma to drive instabilities. Waves in the simulations are formed through the random thermal motion of the particles in the magnetic field. The initial velocity distributions of the plasma species are modelled by (a) isotropic kappa distributions and (b) isotropic Maxwellian distributions. Results of simulations using initial kappa loadings are compared to those using initial Maxwellian loadings and the effect of superthermal particle populations on the behaviour of the plasma waves is discussed.

4.1 Introduction

A charged particle in the presence of an electric field $\boldsymbol{E}$ and magnetic field $\boldsymbol{B}$ experiences a force described by the Lorentz force equation (Chen, 1984)

$$\boldsymbol{F} = q[\boldsymbol{E} + \boldsymbol{v} \times \boldsymbol{B}], \tag{4.1}$$

where q is the charge of the particle and $\boldsymbol{v}$ is the particle velocity vector. The presence of the magnetic field restricts the motion of the charged plasma particles. Charged particles are able to move freely along the magnetic field since the term $\boldsymbol{v} \times \boldsymbol{B}$ in Equation (4.1) will be zero; however, particles cannot move freely across the magnetic field and will instead perform gyrations about the field lines. Thus, the dynamics of the plasma will be different in the directions parallel and perpendicular to the magnetic field, producing dissimilar wave modes.

Plasma dispersion relations characterise the propagation properties of waves in the plasma, relating the wave frequency ω to the wave vector $\boldsymbol{k}$. The frequencies ω and wave numbers k satisfying the dispersion relation describe the wave modes supported by the plasma. A number of different wave modes are supported by magnetised plasmas. A brief overview of these waves are given in Sections 4.1.1 and 4.1.2, for waves propagating parallel and perpendicularly to a static, uniform magnetic field $\boldsymbol{B}_0$, respectively, in a plasma composed of an electron and singly charged ion species. A discussion of the dispersion relations for waves propagating in magnetised plasmas having kappa velocity distributions is given in Section 4.2.

4.1.1 Parallel propagating waves

The principal electromagnetic waves propagating exactly parallel to a uniform, constant magnetic field $\boldsymbol{B}_0$ are the R- and L-modes (Chen, 1984). These are circularly polarised waves, where polarisation is given with respect to the ambient magnetic field (Tsurutani and Lakhina, 1997). During propagation of the waves, the perpendicular component of the electric field vector rotates about the magnetic field lines (Chen, 1984; Treumann and Baumjohann, 1997; Gurnett and Bhattacharjee, 2005). For the R-mode, the perpendicular component of the electric field rotates in the direction that electrons gyrate about the magnetic field, i.e., they are right-hand circularly polarised. For the L-mode, the direction of rotation corresponds to the direction that ions gyrate about the magnetic field, i.e., they are left-hand circularly polarised (Chen, 1984; Treumann and Baumjohann, 1997; Gurnett and Bhattacharjee, 2005). The cold plasma dispersion relations for the R- and L-modes are (Nicholson, 1983; Chen, 1984)

$$\frac{k^2c^2}{\omega^2} = 1 - \frac{\omega_{pe}^2/\omega^2}{1 - \omega_{ce}/\omega}, \tag{4.2}$$

for the R-mode, and

$$\frac{k^2c^2}{\omega^2} = 1 - \frac{\omega_{pe}^2/\omega^2}{1 + \omega_{ce}/\omega}, \tag{4.3}$$

for the L-mode, where $\omega_{pe} = (n_{0e}e^2/\epsilon_0 m_e)^{1/2}$ and $|\omega_{ce}| = |-eB_0/m_e|$, are the electron plasma and cyclotron frequencies, respectively, and c is the speed of light. The R-mode has two regions of propagation, separated by a stop band between its resonance and cut-off frequencies [see Chen (1984), ch. 4]. At a resonance, the index of refraction $n = kc/\omega$ becomes infinite, i.e., the wavelength becomes zero. At a cut-off, the index of refraction goes to zero, i.e., the wavelength becomes infinite. As seen in Equation (4.2), as $\omega \to \omega_{ce}$, the index of refraction $n = kc/\omega$ becomes infinite. Since the R-mode rotates in the same sense as electrons, when the wave frequency ω approaches the electron cyclotron frequency ω_{ce}, the wave and electrons approach cyclotron resonance. At cyclotron resonance $\omega = \omega_{ce}$, the R-mode loses energy by continually accelerating the electrons and the wave does not propagate. The R-mode has a cut-off at the right-hand cut-off frequency ω_R (Nicholson, 1983; Chen, 1984), defined as

$$\omega_R = \frac{1}{2}[\omega_{ce} + (\omega_{ce}^2 + 4\omega_{pe}^2)^{1/2}]. \tag{4.4}$$

R-mode waves propagating at frequencies below the electron cyclotron frequency ω_{ce} are known as whistler waves (Tsurutani and Lakhina, 1997). Whistler waves are governed by electron dynamics and occur in a diverse range of space plasma conditions. These waves are destabilised by anisotropic electron velocity distributions, such as electron beams, loss cones, rings and temperature anisotropies (Kennel and Petschek, 1966; Stenzel, 1999). Whistlers play a key role in a variety of space plasma phenomena (Kennel and Petschek, 1966; Gary et al., 1994; Watt et al., 2012). The resonant wave-particle interaction between whistler waves and energetic electrons scatters the electron pitch angles and can precipitate electrons into the ionosphere, producing aurora (Ossakow et al., 1972a; Tsurutani and Lakhina, 1997). In Chapter 5 we provide a more detailed discussion of whistler waves and present simulation results of the electron temperature anisotropy driven whistler instability.

Since ions rotate in the same sense as the electric field for the L-mode, cyclotron resonance occurs between the L-mode and the ions at $\omega = \omega_{ci}$. The L-mode has a cut-off at the left-hand cut-off frequency ω_L (Nicholson, 1983), defined as

$$\omega_L = \frac{1}{2}[-\omega_{ce} + (\omega_{ce}^2 + 4\omega_{pe}^2)^{1/2}]. \tag{4.5}$$

Analogous to the R-mode wave propagating at frequencies below ω_{ce}, L-mode waves propagating at frequencies below the local ion cyclotron frequency ω_{ci} are another parallel propagating electromagnetic wave important to a number of magnetospheric phenomena (Tsurutani and Lakhina, 1997). These waves are known as electromagnetic ion cyclotron (EMIC) waves and are generated in the magnetosphere by resonant wave-particle interaction with anisotropic ring current ions (Mauk and McPherron, 1980; Erlandson and Ukhorskiy, 2001). EMIC waves are typically driven by temperature anisotropies in the ion species. These waves resonantly interact with ring current ions and relativistic electrons in the radiation belts. The resonant EMIC wave-particle interaction alters particle energies and scatters pitch angles, contributing to the precipitation loss of particles from the magnetosphere (Summers and Thorne, 2003; Summers et al., 2007; Albert and Bortnik, 2009).

Many studies of the parallel propagating whistler waves (Gary et al., 1994; Stenzel, 1999; Schriver et al., 2010), and EMIC waves (Gendrin, 1975; Anderson and Fuselier, 1994; Silin et al., 2011) have focussed on investigating the propagation properties of these waves in plasmas having Maxwellian velocity distributions (or variants). However, a number of authors have considered the behaviour of both the whistler waves (Mace, 1998; Xioa et al., 2006; Mace and Sydora, 2010) and EMIC waves (Xue et al., 1996; Mace et al., 2011; Zhou et al., 2013) propagating in plasmas having kappa velocity distributions. These studies were motivated by the increasing acceptance that the kappa distribution provides a more realistic kinetic model for space plasma velocity distributions than the Maxwellian distribution, in various space plasma environments. The high energy tail of the kappa distribution is known to alter the statistics of micro-physical processes in the plasma such as Landau damping (Thorne and Summers, 1991) and cyclotron damping (Mace and Sydora, 2010), and can change the dispersive properties of the plasma waves (Hellberg et al., 2000, 2005). Results of analytical and numerical studies of both the whistler wave (R-mode) and EMIC wave (L-mode) have shown that the kappa distribution affects the dispersion relations of the modes as well as the growth rates of the unstable waves (Mace and Sydora, 2010; Mace et al., 2011; Eliasson and Lazar, 2015). While we only consider stable waves in this chapter, the above studies indicate that the use of the Maxwellian plasma model may yield inconsistent predictions and incorrect conclusions being drawn for the behaviour of waves in space plasmas.

4.1.2 Perpendicularly propagating waves

For wave propagation perpendicular to the ambient magnetic field, there are the X- and O-modes. The O-mode (ordinary wave) is a linearly polarised wave. During propagation of the O-mode, the fluctuating electric field is directed perpendicular to the wave vector $\boldsymbol{k}$ and parallel to $\boldsymbol{B}_0$ (Chen, 1984). Hence, the ordinary wave is unaffected by the magnetic field. The cold plasma dispersion relation for the O-mode is (Nicholson, 1983)

$$\omega^2 = \omega_{pe}^2 + k^2 c^2. \tag{4.6}$$

The X-mode (extraordinary wave) is an elliptically polarised wave. The fluctuating electric field of the X-mode has components directed parallel and perpendicular to the wave vector $\boldsymbol{k}$. Thus, the X-mode is partly longitudinal and partly transverse. The cold plasma dispersion relation for the X-mode is (Nicholson, 1983)

$$\frac{k^2 c^2}{\omega^2} = 1 - \frac{\omega_{pe}^2}{\omega^2}\left(\frac{\omega^2 - \omega_{pe}^2}{\omega^2 - \omega_{uh}^2}\right), \tag{4.7}$$

where $\omega_{uh}^2 = \omega_{pe}^2 + \omega_{ce}^2$ is known as the upper hybrid frequency. Similar to the parallel propagating R- and L-modes discussed in Section 4.1.1, the dispersion diagrams for the perpendicularly propagating X- and O-modes are separated into regions of propagation and non-propagation [see Chen (1984), Ch. 4]. As seen in Equation (4.6) for the O-mode, a cut-off occurs at $\omega = \omega_{pe}$, at which point the index of refraction, $n = kc/\omega$, goes to zero. The X-mode has a resonance, i.e., the index of refraction n becomes infinite, at the upper hybrid frequency $\omega = \omega_{uh}$, as is seen in Equation (4.7). Furthermore, the X-mode has two cut-off frequencies. These cut-offs are at the same right- and left-hand cut-off frequencies, ω_R and ω_L, defined in Equations (4.4) and (4.5), respectively, and can be obtained by setting the index of refraction, $n = kc/\omega$, to zero in Equation (4.7) and simplifying the result.

Other wave modes propagating perpendicularly to the magnetic field $\boldsymbol{B}_0$ are the Bernstein waves (Bernstein, 1958), which arise due to finite Larmor orbit effects introduced by the charged particles performing gyrations about the magnetic field lines (Swanson, 2003). These are purely kinetic plasma waves, i.e., they have no counterpart in the fluid model. Hence, the dispersion relations of the Bernstein waves are sensitive to the details of the particle velocity distributions (Fredricks, 1968; Tataronis and Crawford, 1970; Mace, 2003). Two types of

Bernstein waves can propagate in an electron-ion plasma. These are the electron and ion Bernstein waves, which exhibit qualitatively similar behaviour; however, due to the difference in masses and mobilities of the electrons and ions, they occupy different frequency ranges (Fredricks, 1968; Crawford, 1965).

Electron Bernstein waves have frequencies in excess of the electron cyclotron frequency, ω_{ce}, and propagate between harmonics of the electron cyclotron frequency. On the other hand, for singly charged ions, the ion Bernstein waves have frequencies in excess of the ion cyclotron frequency, ω_{ci}, and propagate between harmonics of ω_{ci}. The electron Bernstein waves are governed by the electron dynamics, while the ion Bernstein waves are governed primarily by the ion dynamics with the electrons contributing a first order effect in the form of additional screening (Ichimaru, 1973).

Electron Bernstein waves are frequently observed in planetary magnetospheres under the guise of the naturally occurring electrostatic plasma emissions known as banded emissions (Kennel and Ashour-Abdalla, 1982); however, alternate interpretations of banded emissions also exist (Benson et al., 2001). Banded emissions occur at frequencies between harmonics of the electron cyclotron frequency, ω_{ce}, and are primarily observed near the magnetic equator of planets, suggestive of wave propagation perpendicular to the magnetic field. On the other hand, in plasmas with low proton beta, $\beta_p \ll 1$, the Ion Bernstein instability is believed to be responsible for the enhanced magnetic and electric field fluctuations observed near the equatorial plane of the terrestrial magnetosphere (Janhunen et al., 2003; Gary et al., 2010), at frequencies between harmonics of the ion cyclotron frequency ω_{ci}. Both electron and ion Bernstein waves are stable for isotropic Maxwellian, as well as for isotropic kappa velocity distributions (Fredricks, 1968; Tataronis and Crawford, 1970; Mace, 2003, 2004; Nsengiyumva et al., 2013), where the condition for instability requires a distribution function to satisfy $\partial f(v_\perp)/\partial v_\perp > 0$ (Tataronis and Crawford, 1970). Studies which incorporate electromagnetic effects have shown that the Bernstein waves (both electron and ion types) are approximately electrostatic at small wavelengths, or at large wave numbers, while becoming significantly electromagnetic at larger wavelengths (Fredricks, 1968; Mace, 2004; Nsengiyumva et al., 2013). Furthermore, the electromagnetic electron Bernstein wave propagating in the upper hybrid frequency band is known to couple to the low frequency X-mode in both Maxwellian and kappa plasmas (Puri et al., 1973; Mace, 2004).

Motivated by the frequent observations of kappa velocity distributions in space plasmas, analytical and numerical studies have been conducted to investigate the effect of kappa distributions on the behaviour of Bernstein waves. These include investigations of both

electron Bernstein (Mace, 2003, 2004; Henning et al., 2011) as well as ion Bernstein waves (Nsengiyumva et al., 2013). The dispersion relations were found to depend significantly on the electron spectral index κ_e for the electron Bernstein waves, and on the ion spectral index κ_i for the ion Bernstein waves. For the case of electrostatic waves, these results were confirmed by 1D3V particle-in-cell (PIC) simulations of electrostatic electron and ion Bernstein waves performed by Abdul and Mace (2014). We defer a more detailed discussion of the effects of the kappa distribution on the Bernstein wave dispersion relations to later, in Section 4.3.2.

Viñas et al. (2005) proposed that the changes in the dispersive characteristics of electron Bernstein waves can be used as a reverse diagnostic, and can provide details of the electron velocity distribution. For the electron Bernstein waves propagating with frequencies at, and above the upper hybrid frequency, the points of vanishing group velocity are known to be important to the interpretation of long duration plasma wave echoes (resonances), observed during magnetospheric sounding experiments (Dougherty and Monaghan, 1966). These points were shown by Mace (2003, 2004) to experience a shift to lower frequencies and larger wave numbers as the spectral index of the electron species, κ_e, decreases. Based on this, Viñas et al. (2005) proposed that the analysis of plasma wave echoes, i.e., Q_n resonances, can be exploited to provide insights into the local electron velocity distributions and can indicate the presence of superthermal particle populations [see also Benson et al. (2013)].

An analogous reverse diagnostic for ion velocity distributions was proposed by Nsengiyumva et al. (2013), based on the investigation of ion Bernstein waves. In plasmas modelled by Maxwellian velocity distributions, mode coupling is observed between the ion Bernstein wave propagating in the lower hybrid frequency band and the waves in the adjacent harmonic bands directly above. This occurs in plasmas with sufficiently large ω_{pi}/ω_{ci} (Fredricks, 1968; Nsengiyumva et al., 2013). Here, the ion Bernstein wave appears at a continuous range of frequencies from the lower hybrid branch, cutting across numerous ion cyclotron harmonics above. This coupling was found by Nsengiyumva et al. (2013) to be reduced for decreasing ion spectral indices κ_i, producing stop bands in the dispersion relations for the ion Bernstein waves. Nsengiyumva et al. (2013) suggested that the observation of stop bands in the propagation of ion Bernstein waves, at frequencies in the vicinity of the lower hybrid frequency, can indicate the presence of ion velocity distributions of the kappa type, with low spectral indices. Conversely, continuous propagation over several ion cyclotron harmonics indicates Maxwellian velocity distributions instead. However, it should be noted that results of Nsengiyumva et al. (2013) showed that the ion Bernstein dispersion relations exhibited quasi-Maxwellian behaviour for kappa values as low as $\kappa_i = 4$.

As mentioned previously, the kappa distribution provides a more appropriate model for space plasma velocity distributions, and many analytical studies have been conducted to investigate the effects of superthermal particle populations on the behaviour of plasma waves. The use of kappa distributions, however, is yet to become as widespread in the simulation studies of waves in space plasmas. Since the assumptions and simplifications inherent in linear theory allows for the study of only a small window of plasma wave dynamics, the non-linear character of plasma simulation makes it an essential tool for the study of waves in space plasmas. Simulations are known to extend linear theory, providing insights into the plasma dynamics which cannot be obtained through linear analysis alone. Presented in this chapter are results of 2D3V electromagnetic PIC simulations of stable waves propagating in plasmas modelled by both kappa and Maxwellian velocity distributions.

4.2 Theory

4.2.1 Dispersion relations: Plasmas modelled by kappa velocity distributions

In this section we briefly discuss the dispersion relations for waves propagating in plasmas having kappa velocity distributions. Further details can be found in Mace (1996) and Mace (2004).

The homogeneous wave equation for a collisionless plasma immersed in a uniform, constant magnetic field $\boldsymbol{B}_0$, after taking the Fourier-Laplace transform, is given in cartesian tensor notation as (Melrose, 1986)

$$\Lambda_{ij}(\boldsymbol{k},\omega)E_j(\boldsymbol{k},\omega) = 0, \tag{4.8}$$

where $\boldsymbol{k}$ and ω are the wave vector and angular frequency, and $\Lambda_{ij}(\boldsymbol{k},\omega)$ is the Maxwell tensor given by

$$\Lambda_{ij}(\boldsymbol{k},\omega) = \frac{c^2}{\omega^2}(k_i k_j - k^2\delta_{ij}) + K_{ij}(\boldsymbol{k},\omega). \tag{4.9}$$

In Equation (4.9) above, K_{ij} is the dielectric tensor and δ_{ij} is the Kronecker delta tensor (Mace, 2004). The dispersion relations for electromagnetic waves in the plasma is found through non-trivial solutions of the wave equation given in Equation (4.8), which requires

$$\det \Lambda(\boldsymbol{k}, \omega) = 0. \tag{4.10}$$

The dielectric tensor elements for a non-relativistic, magnetised plasma modelled by isotropic kappa velocity distributions was derived by Mace (1996) for arbitrary real κ values. These dielectric tensor elements can be written in the form (Mace, 1996)

$$\begin{aligned} K_{ij}(\boldsymbol{k}, \omega) =& \delta_{ij} + i \sum_{\alpha} \frac{\omega_p^2}{\omega \omega_c} \frac{1}{2^{\kappa-3/2} \Gamma\left(\kappa - \frac{1}{2}\right)} \\ & \times \int_0^{\infty} d\xi e^{i\omega\xi/\omega_c} [S_{ij} \zeta^{\kappa-1/2} K_{\kappa-1/2}(\zeta) - T_{ij} \zeta^{\kappa-3/2} K_{\kappa-3/2}(\zeta)], \end{aligned} \tag{4.11}$$

where ω_p and ω_c are the usual plasma frequency and unsigned cyclotron frequencies, respectively. In Equation (4.11) above, as well as in the equations that follow, the subscript α denoting the particle species is omitted for brevity; however, all quantities relevant to the plasma species are understood to implicitly have this subscript. The tensors S and T are defined by (Mace, 1996, 2004)

$$(S_{ij}) = \begin{pmatrix} \cos\xi & \epsilon \sin\xi & 0 \\ -\epsilon \sin\xi & \cos\xi & 0 \\ 0 & 0 & 1 \end{pmatrix}, \tag{4.12}$$

and

$$(T_{ij}) = 2\left(\kappa - \frac{3}{2}\right) \frac{v_{th}^2}{\omega_c^2} \begin{pmatrix} k_\perp^2 \sin^2\xi & \epsilon k_\perp^2 \sin\xi(1-\cos\xi) & k_\perp k_\parallel \xi \sin\xi \\ -\epsilon k_\perp^2 \sin\xi(1-\cos\xi) & -k_\perp^2(1-\cos\xi)^2 & -\epsilon k_\perp k_\parallel \xi(1-\cos\xi) \\ k_\perp k_\parallel \xi \sin\xi & \epsilon k_\perp k_\parallel \xi(1-\cos\xi) & k_\parallel^2 \xi^2 \end{pmatrix}, \tag{4.13}$$

where $\epsilon = q/|q|$ defines the sign of the species charge and

$$\zeta = 2\left(\kappa - \frac{3}{2}\right)^{1/2}\left[\frac{k_\perp^2 v_{th}^2}{\omega_c^2}(1-\cos\,\xi) + \frac{1}{2}\frac{k_\parallel^2 v_{th}^2}{\omega_c^2}\xi^2\right]^{1/2}. \tag{4.14}$$

We next consider the limiting cases for waves propagating parallel ($k_\perp = 0$) and perpendicular ($k_\parallel = 0$) to the magnetic field $\boldsymbol{B}_0$, and provide the respective dispersion relations for electromagnetic waves in plasmas modelled by kappa velocity distributions.

Parallel propagation

In addition to calculating the dielectric tensor elements discussed above, Mace (1996) also derived the dispersion relations for the limiting case of waves propagating parallel to the magnetic field $\boldsymbol{B}_0$, i.e., where $k_\perp = 0$. In this subsection we shall provide the dispersion relation for the parallel propagating right-hand and left-hand circularly polarised waves. For the case of parallel propagation, Mace (1996) derived a simplified form of Equation (4.11) given by

$$K_{i,j}(k_\parallel,\omega) = \delta_{i,j} + \sum_\alpha \frac{\omega_p^2}{\omega k_\parallel \theta}\frac{(\kappa-1)^{3/2}}{\kappa^{1/2}(\kappa-3/2)}R_{i,j}(k_\parallel,\omega), \tag{4.15}$$

where $\theta = [(2\kappa-3)/\kappa]^{1/2}(T/m)^{1/2}$ is the generalised thermal speed defined for the kappa velocity distribution and the components of R_{ij} are (Mace, 1996)

$$
\begin{aligned}
R_{11} &= \frac{1}{2}\left\{ Z_{\kappa-1}\left[\left(\frac{\kappa-1}{\kappa}\right)^{1/2}\frac{\omega+\epsilon\omega_c}{k\theta}\right] + Z_{\kappa-1}\left[\left(\frac{\kappa-1}{\kappa}\right)^{1/2}\frac{\omega-\epsilon\omega_c}{k\theta}\right]\right\}, \\
R_{12} &= \frac{i}{2}\left\{ Z_{\kappa-1}\left[\left(\frac{\kappa-1}{\kappa}\right)^{1/2}\frac{\omega-\epsilon\omega_c}{k\theta}\right] - Z_{\kappa-1}\left[\left(\frac{\kappa-1}{\kappa}\right)^{1/2}\frac{\omega+\epsilon\omega_c}{k\theta}\right]\right\}, \\
R_{13} &= 0, \\
R_{12} &= -R_{21}, \qquad R_{22} = R_{11}, \qquad R_{23} = 0, \\
R_{13} &= 0, \qquad R_{32} = 0, \\
R_{33} &= 2\frac{\omega}{k\theta}\frac{\kappa-3/2}{(\kappa-1)^{3/2}}\left[\frac{\kappa-1/2}{\kappa^{1/2}} + \kappa^{1/2}\frac{\omega}{k\theta}Z_\kappa\left(\frac{\omega}{k\theta}\right)\right].
\end{aligned} \tag{4.16}
$$

The plasma dispersion function Z_κ introduced by Mace and Hellberg (1995) for arbitrary real kappa values, can be written in a form employing the Gauss hypergeometric function ${}_2F_1[a,b;c;z]$ as

$$
Z(\zeta) = \frac{i(\kappa+1/2)(\kappa-1/2)}{\kappa^{3/2}(\kappa+1)}{}_2F_1[1, 2\kappa+2; \kappa+2; 1/2(1-\zeta/i\kappa^{1/2})]. \tag{4.17}
$$

Mace (1996) showed that for wave vector $\boldsymbol{k} = \pm k\boldsymbol{e}_z$, where $k = ||\boldsymbol{k}||$, the dispersion relations for the L- and R-modes can be obtained by projecting the tensor Λ_{ij} in Equation (4.9), onto the following unimodular polarization vectors

$$
\boldsymbol{e}_L = 2^{-1/2}(\boldsymbol{e}_x - i\boldsymbol{e}_y) \qquad \text{and} \qquad \boldsymbol{e}_R = 2^{-1/2}(\boldsymbol{e}_x + i\boldsymbol{e}_y). \tag{4.18}
$$

The dispersion relations for the L- and R-modes will then satisfy

$$
\Lambda^L(\boldsymbol{k},\omega) = \Lambda_{ij}(\boldsymbol{k},\omega)e^*_{Li}e_{Lj} = 0, \qquad \text{and} \qquad \Lambda^R(\boldsymbol{k},\omega) = \Lambda_{ij}(\boldsymbol{k},\omega)e^*_{Ri}e_{Rj} = 0, \tag{4.19}
$$

where the superscript $*$ denotes a complex conjugation. The final form of the dispersion relation is [see Mace (1996)]

$$\frac{k^2c^2}{\omega^2} = 1 + \sum_{\alpha} \frac{\omega_p^2}{\omega k \theta} \left(\frac{\kappa}{\kappa - 3/2} \right) \left(\frac{\kappa - 1}{\kappa} \right)^{3/2} Z_{\kappa} \left[\left(\frac{\kappa - 1}{\kappa} \right)^{1/2} \frac{\omega \mp \epsilon \omega_c}{k\theta} \right], \tag{4.20}$$

where the minus sign $(-)$ in Equation (4.20) provides the dispersion relation for the L-mode, and the plus sign $(+)$ gives the dispersion relation for the R-mode.

Perpendicular propagation

We next consider the case of waves propagating perpendicularly to the magnetic field $\boldsymbol{B}_0$, i.e., where $k_{\parallel} = 0$. The determinant in Equation (4.10) for the case of perpendicular propagation splits into two factors. One factor yields the dispersion relation for the ordinary mode, which is

$$K_{33} - \frac{c^2k^2}{\omega^2} = 0, \tag{4.21}$$

and the other yields the dispersion relation for the extraordinary mode, given as

$$K_{11} \left(K_{22} - \frac{k_{\perp}^2 c^2}{\omega^2} \right) - K_{12}K_{21} = 0. \tag{4.22}$$

Mace (2004) derived expressions to solve Equation (4.22) and investigated generalised Bernstein modes propagating in plasmas having kappa velocity distributions. The dielectric tensor elements in Equation (4.22) can be written as (Mace, 2004)

$$\begin{aligned}
K_{11}(k_{\perp}, \omega) &= 1 + \sum_{\alpha} \left\{ \frac{1}{k^2\lambda_{\kappa}^2} - \frac{1}{2^{\kappa - 1/2}\Gamma\left(\kappa - 1/2\right)} \frac{\omega_p^2}{\omega_c^2 \lambda'} \frac{\omega}{\omega_c} \csc\left(\pi\omega/\omega_c\right) U_{\kappa+1/2,\kappa+1/2} \left(\frac{\omega}{\omega_c}, \lambda' \right) \right\}, \\
K_{12}(k_{\perp}, \omega) &= i \sum_{\alpha} \epsilon \frac{\omega_p^2}{\omega_c^2 \lambda'} \frac{1}{2^{\kappa+1/2}\Gamma\left(\kappa - 1/2\right)} \csc\left(\pi\omega/\omega_c\right) U_{\kappa+3/2,\kappa-1/2} \left(\frac{\omega}{\omega_c}, \lambda' \right), \\
K_{21}(k_{\perp}, \omega) &= -K_{12}(k_{\perp}, \omega), \\
K_{22}(k_{\perp}, \omega) &= K_{11}(k_{\perp}, \omega) - \sum_{\alpha} \frac{\omega_p^2}{\omega \omega_c} \frac{1}{2^{\kappa - 3/2}\Gamma\left(\kappa - 1/2\right)} \csc\left(\pi\omega/\omega_c\right) U_{\kappa+1/2,\kappa-3/2} \left(\frac{\omega}{\omega_c}, \lambda' \right),
\end{aligned} \tag{4.23}$$

where $\lambda^{'} = k_{\perp}^2 v_{th}^2/\omega_c^2$ and the Debye length λ_κ in a plasma having kappa velocity distributions is

$$\lambda_\kappa = \left[\frac{(\kappa - 3/2)}{(\kappa - 1/2)}\frac{\epsilon_0 T}{n_0 q^2}\right]^{1/2}. \tag{4.24}$$

The function $U_{\mu,\nu}(z,\lambda)$ appearing in the dielectric tensor elements given in Equation(4.23) yields expressions for K_{ij} in terms of generalised hypergeometric functions, and is

$$\begin{aligned} U_{\mu,\nu}(z,\lambda) = 2^{\mu-1}\pi^{3/2}\,\csc(\nu\pi)\Bigg[&\frac{\Gamma\left(\frac{1}{2}\mu - \frac{1}{2}\nu + \frac{1}{2}\right)\Gamma\left(\frac{1}{2}\mu - \frac{1}{2}\nu + 1\right)}{\Gamma(1-\nu)\Gamma\left(\frac{1}{2}\mu - \frac{1}{2}\nu + \frac{1}{2} + z\right)\Gamma\left(\frac{1}{2}\mu - \frac{1}{2}\nu + 1 - z\right)}\,(2\lambda)^{\mu/2-\nu/2} \\ &{}_2F_3\left[\frac{1}{2}\mu - \frac{1}{2}\nu + \frac{1}{2}, \frac{1}{2}\mu - \frac{1}{2}\nu + 1; 1-\nu, \frac{1}{2}\mu - \frac{1}{2}\nu + 1 + z, \frac{1}{2}\mu - \frac{1}{2}\nu + 1 - z; 2\lambda\right] \\ &- \frac{\Gamma\left(\frac{1}{2}\mu + \frac{1}{2}\nu + \frac{1}{2}\right)\Gamma\left(\frac{1}{2}\mu + \frac{1}{2}\nu + 1\right)}{\Gamma(1+\nu)\Gamma\left(\frac{1}{2}\mu + \frac{1}{2}\nu + 1 + z\right)\Gamma\left(\frac{1}{2}\mu + \frac{1}{2}\nu + 1 - z\right)}\,(2\lambda)^{\mu/2+\nu/2} \\ &{}_2F_3\left[\frac{1}{2}\mu + \frac{1}{2}\nu + \frac{1}{2}, \frac{1}{2}\mu + \frac{1}{2}\nu + 1; 1+\nu, \frac{1}{2}\mu + \frac{1}{2}\nu + 1 + z, \frac{1}{2}\mu + \frac{1}{2}\nu + 1 - z; 2\lambda\right]\Bigg] \end{aligned} \tag{4.25}$$

Mace (2004) provided useful identities which were used to derive expressions for the dielectric tensor elements in Equation (4.23). By using the equations given in Appendix B and C of Mace (2004), the dielectric tensor element K_{33} is

$$K_{33}(k_\perp,\omega) = 1 - \sum_\alpha \frac{\omega_p^2}{\omega_c^2}\frac{\omega_c}{\omega}\frac{1}{2^{\kappa-3/2}\Gamma(\kappa - 1/2)}\,\csc\,(\pi\omega/\omega_c)U_{\kappa-1/2,\kappa-1/2}\left(\frac{\omega}{\omega_c}, \lambda^{'}\right). \tag{4.26}$$

By substituting the expressions for the dielectric tensor elements of Equations (4.23) and (4.26), in Equations (4.21) and (4.22), we obtain the dispersion relations for the ordinary and extraordinary modes propagating in kappa plasmas.

4.2.2 Dispersion relations: Cold plasmas

There is no well established theory for waves propagating at oblique angles in plasmas modelled by kappa velocity distributions. Hence, we use the cold plasma dispersion relations as a rough guide for identifying the oblique modes in our simulation results. In this subsection we provide the dispersion relations for waves propagating at arbitrary angles in a cold plasma with an externally applied static, uniform magnetic field $\boldsymbol{B}_0$. The discussion of the cold plasma dispersion relations given below follows that of Stix (1992) and Gurnett and Bhattacharjee (2005).

The wave equation can be written in the alternate form (Stix, 1992; Gurnett and Bhattacharjee, 2005),

$$\boldsymbol{k} \times (\boldsymbol{k} \times \boldsymbol{E}) + \frac{\omega^2}{c^2} \boldsymbol{K} \cdot \boldsymbol{E} = 0, \tag{4.27}$$

or, by employing the definition of the index of refraction $\boldsymbol{n} = \boldsymbol{k}c/\omega$, can be written in the form,

$$\boldsymbol{n} \times (\boldsymbol{n} \times \boldsymbol{E}) + \boldsymbol{K} \cdot \boldsymbol{E} = 0. \tag{4.28}$$

For a cold plasma, the dielectric tensor K_{ij} is given by (Stix, 1992; Gurnett and Bhattacharjee, 2005),

$$K_{ij} = \begin{pmatrix} S & -iD & 0 \\ iD & S & 0 \\ 0 & 0 & P \end{pmatrix}, \tag{4.29}$$

where S, D and P are defined as,

$$S = \frac{1}{2}(R+L) \tag{4.30}$$

$$D = \frac{1}{2}(R-L) \tag{4.31}$$

$$P = 1 - \sum_{\alpha} \frac{\omega_p^2}{\omega^2}. \tag{4.32}$$

The quantity R in Equations (4.30) and (4.31) is associated with the right-hand polarised mode, and L is associated with the left-hand polarised mode. R and L are defined, respectively, as,

$$R = 1 - \sum_{\alpha} \frac{\omega_p^2}{\omega(\omega+\omega_c)} \tag{4.33}$$

$$L = 1 - \sum_{\alpha} \frac{\omega_p^2}{\omega(\omega-\omega_c)}. \tag{4.34}$$

Using ϕ to denote the angle between $\boldsymbol{n}$ and the magnetic field $\boldsymbol{B}_0$, and assuming $\boldsymbol{n}$ is in the x, z plane, Equation (4.28) can then be written as (Stix, 1992; Gurnett and Bhattacharjee, 2005),

$$\begin{pmatrix} S - n^2\cos^2\phi & -iD & n^2\cos\phi\sin\phi \\ iD & S - n^2 & 0 \\ n^2\cos\phi\sin\phi & 0 & P - n^2\sin^2\phi \end{pmatrix} \begin{pmatrix} E_x \\ E_y \\ E_z \end{pmatrix} = 0. \tag{4.35}$$

By Equation (4.10), the dispersion relation is obtained only if the determinant of the matrix in Equation (4.35) is zero. The resulting cold plasma dispersion relation is given by (Stix, 1992; Gurnett and Bhattacharjee, 2005),

$$D(\boldsymbol{n}, \omega) = An^4 - Bn^2 + C = 0, \tag{4.36}$$

where

$$A = S \sin^2\phi + P \cos^2\phi, \tag{4.37}$$

$$B = RL \sin^2\phi + PS(1 + \cos^2\phi), \tag{4.38}$$

$$C = PRL. \tag{4.39}$$

4.3 PIC simulations

4.3.1 Simulation model

In this section we shall present results from 2D3V electromagnetic particle-in-cell (PIC) simulations of a stable electron-ion plasma, i.e., there are no sources of free energy in the system to drive instabilities. The plasma is immersed in a uniform, static magnetic field $\boldsymbol{B}_0$ which is directed along the $x-$axis. Since we do not confine wave propagation to a single direction in space, we are able to study waves propagating parallel and perpendicular to $\boldsymbol{B}_0$, as well as those propagating at oblique angles.

Three simulations are run. In the first, both plasma species are modelled by isotropic kappa velocity distributions with $\kappa_i = \kappa_e = 2$, representing a strongly non-thermal plasma [subscripts denote the ion (i) and electron (e) species]. A second simulation is run which models a moderately non-thermal plasma in which both plasma species have isotropic kappa velocity distributions with $\kappa_i = \kappa_e = 4$. In the final simulation, an isotropic Maxwellian velocity distribution is used to model the plasma species, representing a plasma in thermodynamic equilibrium. Results from each simulation are analysed and compared. Table 4.1 provides an overview of the simulation run parameters.

The ion species is singly charged, and in all simulations a reduced ion-electron mass ratio of $m_i/m_e = 100$ is used. This mass ratio allows the dynamics of both plasma species to be tracked within the same simulation run, while still providing sufficient separation of the electron and ion time scales. As a consequence of the ion-electron mass ratio, both the high frequency electron Bernstein waves and low frequency ion Bernstein waves are resolved in our simulations. In all simulations, both plasma species are stationary and in thermal equilibrium, i.e., $T_i = T_e$. Table 4.2 provides a summary of the plasma species parameters used for the simulations.

All parameters in our simulations are expressed with respect to those from the electron species. Time scales are expressed in terms of the reciprocal of the electron plasma frequency, i.e., $t^{'} = \omega_{pe}t$, where the primed value denotes the simulation parameter and the unprimed variable denotes an ordinary S.I. value. Length scales are given in terms of the Debye length as $x^{'} = x/\lambda_{De}$. Consequently, velocities are expressed as $\boldsymbol{v}^{'} = \boldsymbol{v}/v_{th,e}$, where the electron thermal velocity is $v_{th,e} = (T_e/m_e)^{1/2} = \lambda_{De}\omega_{pe}$.

A time step defined by $\omega_{pe}\Delta t = 0.05$ is used in all simulations and the simulations are evolved up to time $\omega_{pe}t = 7000$. The domain of the simulation is square, and has size $L_x = L_y = 448\lambda_{De}$ with cells of size $\Delta x = \Delta y = \lambda_{De}$. We employ periodic boundary conditions for fields and particles, and all simulations are initialised with 320 particles per cell, per species, i.e., we use 64 225 280 particles per species. The strength of the background magnetic field $\boldsymbol{B}_0$ produces an electron cyclotron frequency of $\omega_{ce}/\omega_{pe} = 0.25$.

Spectral analysis of the electromagnetic field (wave) intensities, as a function of ω/ω_{ce} and $|k|c/\omega_{pe}$, is carried out for each simulation and results are illustrated in Figures 4.6 to 4.8 (discussed later). In each case, a comparison is made between regions of high wave intensity and the linear dispersion relations of Section 4.2. For the simulation parameters used here, the maximum Fourier mode resolved in our simulations corresponds to the wave number $2\pi/\Delta x = 3.14|k|\lambda_{De} = 31.4|k|c/\omega_{pe}$.

The spectral analysis carried out for the electromagnetic fields, displayed in Figures 4.6 to 4.8, is only for the wave number range $0 \leq |k|c/\omega_{pe} \leq 5$. Initial simulations (not presented here) employed the Fourier space, low pass filter described in Section 2.8.1 to suppress fluctuations at wave numbers $|k|c/\omega_{pe} \geq 15$. However, the effect of strict filtering of the Fourier modes was found to change the dispersion behaviour of the plasma waves in our simulations. As a result, for the simulations presented here, we apply only moderate filtering of the Fourier modes, i.e., wave numbers $|k|c/\omega_{pe} \leq 25$ are retained in the simulations.

Simulation overview	
Domain size	$L_x = 448\lambda_{De}$, $L_y = 448\lambda_{De}$
Cell size	$\Delta x = \lambda_{De}$, $\Delta y = \lambda_{De}$
Time step	$\omega_{pe}\Delta t = 0.05$
Number of time steps	140, 000
Run 1 velocity distribution	Isotropic kappa with $\kappa_{i,e} = 2$
Run 2 velocity distribution	Isotropic kappa with $\kappa_{i,e} = 3$
Run 3 velocity distribution	Isotropic Maxwellian

Table 4.1: An overview of the 2D3V electromagnetic PIC simulations performed for the stable electron-ion plasma. Three simulations are run. Run 1 models a plasma with isotropic kappa velocity distributions with $\kappa_{i,e} = 2$. Run 2 models a plasma having kappa velocity distributions with $\kappa_{i,e} = 4$, and Run 3 models a plasma having Maxwellian velocity distributions.

Electron species	**Ion species**
64,225,280 particles	64,225,280 particles
$\omega_{pe} = 1.0$	$\omega_{pi}/\omega_{pe} = 0.1$
$\omega_{ce}/\omega_{pe} = 0.25$	$\omega_{ci}/\omega_{pe} = 0.0025$
$q/m_e = -1.0$	$q/m_i = 0.01$
$v_{th,e} = 1.0$	$v_{th,i}/v_{th,e} = 0.1$

Table 4.2: The plasma species parameters used in all simulations of the stable electron-ion plasma.

4.3.2 Simulation Results

In this chapter, we investigate the effects the high energy tail of the kappa distribution has on the behaviour of stable waves in a magnetised plasma. The plasma species are initialised with either 3D isotropic kappa velocity distributions (a metastable state), or 3D isotropic Maxwellian velocity distributions (a thermodynamic equilibrium state), using the methods outlined in Section 2.3. As discussed in Section 2.3, the 3D isotropic kappa distribution can be written in the form (Summers and Thorne, 1991)

$$f(\boldsymbol{v}) = (\pi\kappa\theta^2)^{-3/2}\frac{\Gamma(\kappa+1)}{\Gamma(\kappa-1/2)}\left(1+\frac{\boldsymbol{v}^2}{\kappa\theta^2}\right)^{-(\kappa+1)}, \tag{4.40}$$

where the square of the generalised thermal speed is $\theta^2 = 2[(\kappa-3/2)/\kappa]v_{th}^2$, v_{th} is the usual thermal velocity and κ shapes the tail of the distribution. On the other hand, the 3D isotropic Maxwellian distribution is (Ishihara, 1971)

$$f(\boldsymbol{v}) = (2\pi v_{th}^2)^{-3/2}\ \exp\ \left[-\frac{1}{2}\frac{\boldsymbol{v}^2}{v_{th}^2}\right]. \tag{4.41}$$

Figure 4.1 compares slices, in the v_x direction, through the distribution functions given in Equations (4.40) and (4.41). The curves displayed in panel (a) of Figure 4.1 are obtained using parameters relating to the electron species, while panel (b) of Figure 4.1 illustrates curves obtained using parameters relating to the ion species. In both cases, pink and green curves represent a slice through Equation (4.40) with $\kappa = 2$ and $\kappa = 4$, respectively, and black curves represent a slice through Equation (4.41). As seen in both panels of Figure 4.1, decreasing values of κ produce a harder tail of the distribution function, i.e., models an increasing number of high energy particles. The dashed horizontal lines in both panels of Figure 4.1 are the values of $f(\boldsymbol{v}/v_{th,e})$ at which the surface iso-contours of Figures 4.2 to 4.4 are displayed. Figures 4.2 to 4.4 are discussed later. The surface iso-contours for the electron species are measured at values marked by the dashed horizontal lines shown in Figure 4.1 (a), i.e., at $f(\boldsymbol{v}/v_{th,e}) = 0.03, 0.003, 0.0001$ and 0.00001. The ion surface iso-contours are measured at the values marked by the dashed lines in Figure 4.1 (b), i.e., at $f(\boldsymbol{v}/v_{th,e}) = 30, 3, 0.1$ and 0.01.

Figures 4.2 to 4.4 compare the measured surface iso-contours obtained for the particle initial

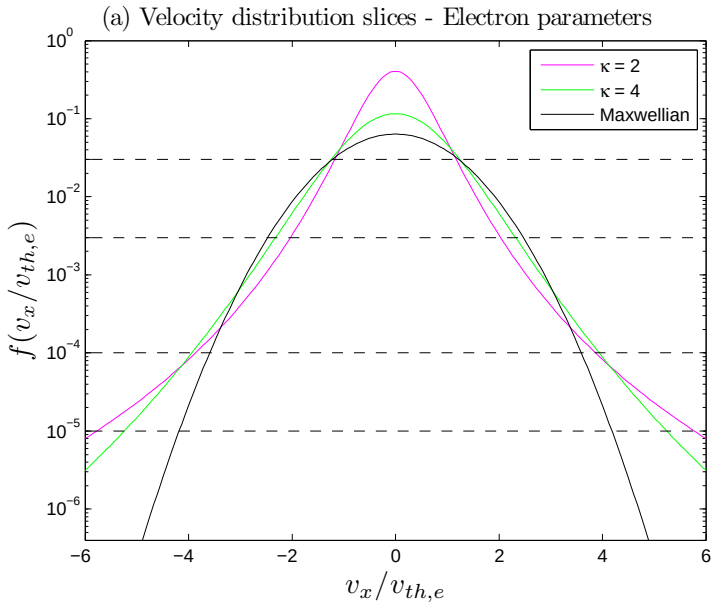

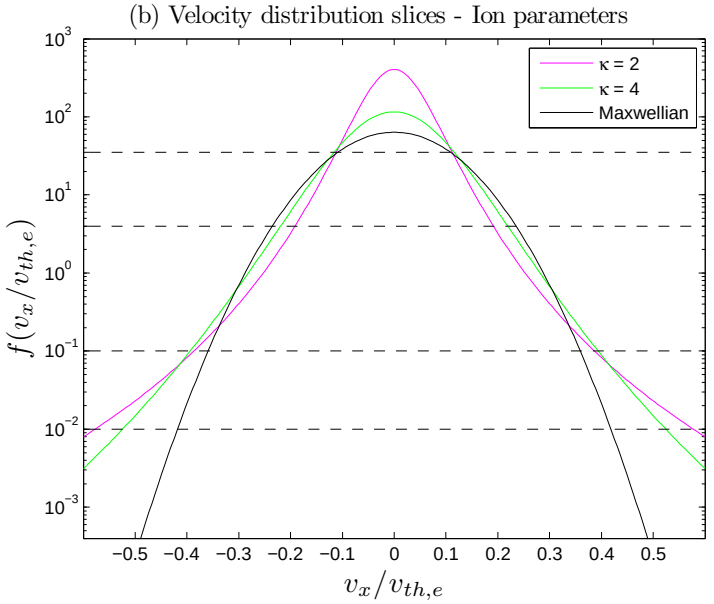

Figure 4.1: Slices through the distribution functions given by Equations (4.40) and (4.41) in the v_x direction. In panel (a), parameters relating to the electron species are used, and in panel (b) parameters for the ions species are used. The pink curves represent a slice through Equation (4.40) with $\kappa = 2$, green curves represent a slice through Equation (4.40) with $\kappa = 4$ and the black curves represent a slice through Equation (4.41). The dashed horizontal lines correspond to the surface iso-contours displayed in Figures 4.2 to 4.4.

velocity distributions in each simulation (displayed in blue) and the surface iso-contours of the relevant theoretical 3D distribution functions (displayed in grey) which were used to model the plasma. Figure 4.2 presents results from simulation Run 1 ($\kappa_{i,e} = 2$ case), Figure 4.3 presents results from Run 2 ($\kappa_{i,e} = 4$ case) and Figure 4.4 presents results from Run 3 (Maxwellian case). In each figure, panel (a) illustrates the surface iso-contours for the electron species at the values $f(\boldsymbol{v}/v_{th,e}) = 0.03, 0.003, 0.0001$ and 0.00001, while panel (b) displays those for the ion species at the values $f(\boldsymbol{v}/v_{th,e}) = 30, 3, 0.1$ and 0.01. Since isotropic distributions were used in our simulations, the surface iso-contours form concentric spheres in all cases.

As seen in Figure 4.2 (a) for the $\kappa_{i,e} = 2$ case, the surface iso-contours measured from the electron initial velocity distribution in the simulation (blue colour) coincide with those of Equation (4.40) (grey colour), when using electron parameters with $\kappa = 2$ in Equation (4.40). This is also true for the ion species displayed in panel (b), which is compared to Equation (4.40) using ion parameters.

Likewise, a comparison is made between the measured particle velocity distributions and Equation (4.40) for the $\kappa_{i,e} = 4$ case (Figure 4.3), and Equation (4.41) for the Maxwellian case (Figure 4.4). As observed in Figures 4.3 and 4.4, good agreement is seen between the measured electron and ion velocity distributions and their respective 3D distribution functions. This agreement for all cases serves to validate the particle velocity loading algorithms used in our simulation code, which was outlined in Section 2.3.

Figure 4.5 displays slices through the electron velocity distribution in the v_x-, v_y- and v_z-directions, for (a) the $\kappa_{i,e} = 2$ case, (b) the $\kappa_{i,e} = 4$ case and (c) the Maxwellian case. In each of the panels of Figure 4.5, a comparison is made between the electron initial velocity distribution (black curve) and the electron velocity distribution measured at the end of the simulation (red curve).

The plasma configuration used in the simulations performed and described in this section produce stable plasma waves, i.e., the back reaction of growing unstable waves on the resonant components of the particle distribution functions is not expected. However, for the $\kappa_{i,e} = 2$ case displayed in panel (a) of Figure 4.5, the electron velocity distribution changes from its initial loading. Specifically, the slices in the v_x-, v_y- and v_z-directions indicate a slight reduction in the number of high energy electrons, i.e., those with velocities $|v_{x,y,z}/v_{th,e}| > 2.5$, during the simulation for Run 1. As a result of the reduction in high energy particles, a slight broadening in the distribution slices at $|v_{x,y,z}/v_{th,e}| < 2.5$ is also observed in Figure 4.5 (a).

(a) Surface iso-contours for the electron initial velocity distribution having $\kappa_e = 2$

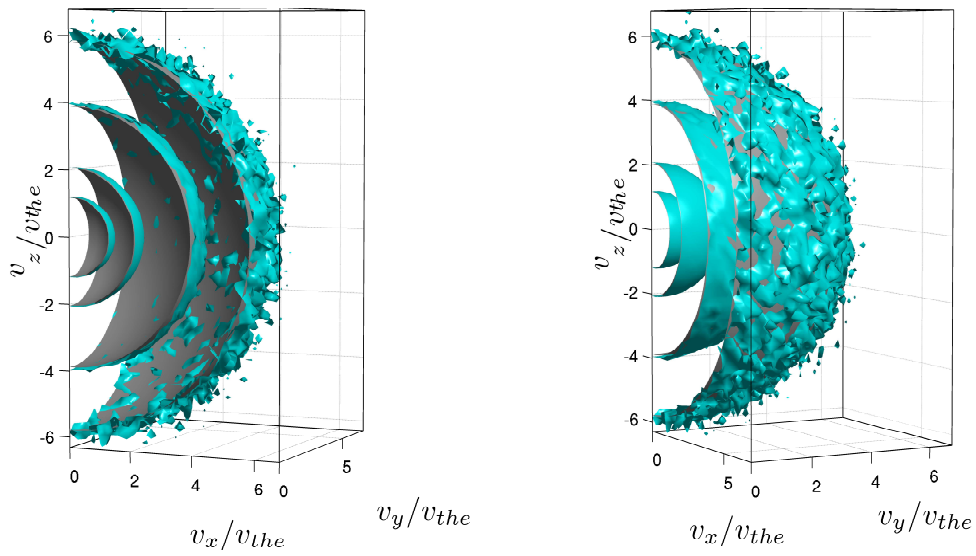

(b) Surface iso-contours for the ion initial velocity distribution having $\kappa_i = 2$

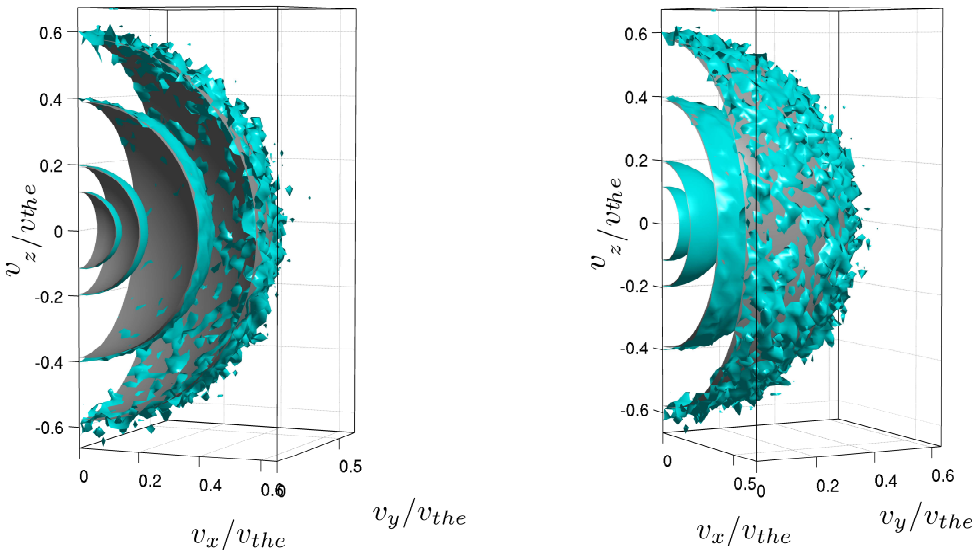

Figure 4.2: Surface iso-contours for (a) the electron initial velocity distribution and (b) the ion initial velocity distribution in the $\kappa_{e,i} = 2$ simulation. In panels (a) and (b), the blue color represents surface iso-contours measured from the simulated particle velocity distributions and the grey colour represents the surface iso-contours from the 3D kappa distribution, Equation (4.40), using the relevant particle parameters.

(a) Surface iso-contours for the electron initial velocity distribution having $\kappa_e = 4$

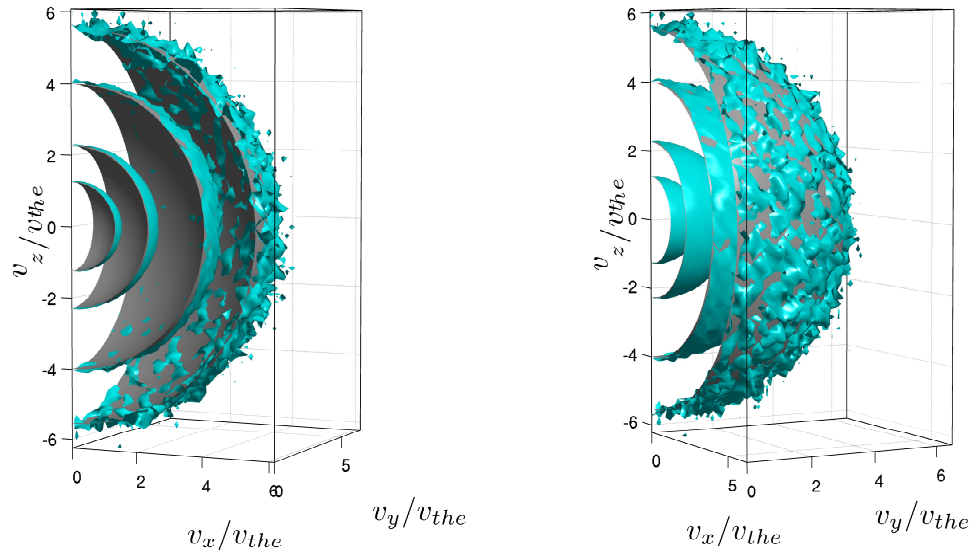

(b) Surface iso-contours for the ion initial velocity distribution having $\kappa_i = 4$

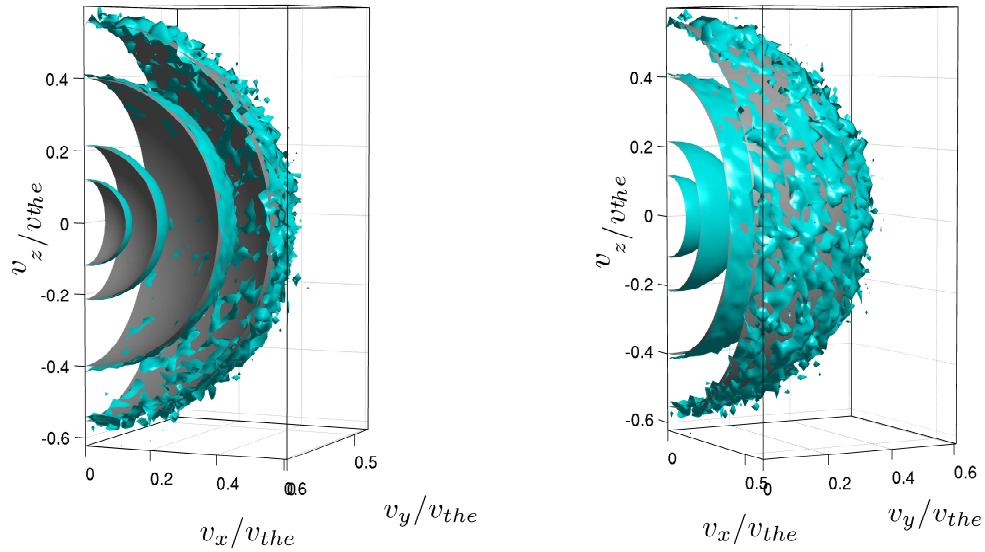

Figure 4.3: Surface iso-contours for (a) the electron initial velocity distribution and (b) the ion initial velocity distribution in the $\kappa_{e,i} = 4$ simulation. In panels (a) and (b), the blue color represents surface iso-contours measured from the simulated particle velocity distributions and the grey colour represents the surface iso-contours from the 3D kappa distribution, Equation (4.40), using the relevant particle parameters.

(a) Surface iso-contours for the electron initial velocity distribution (Maxwellian case)

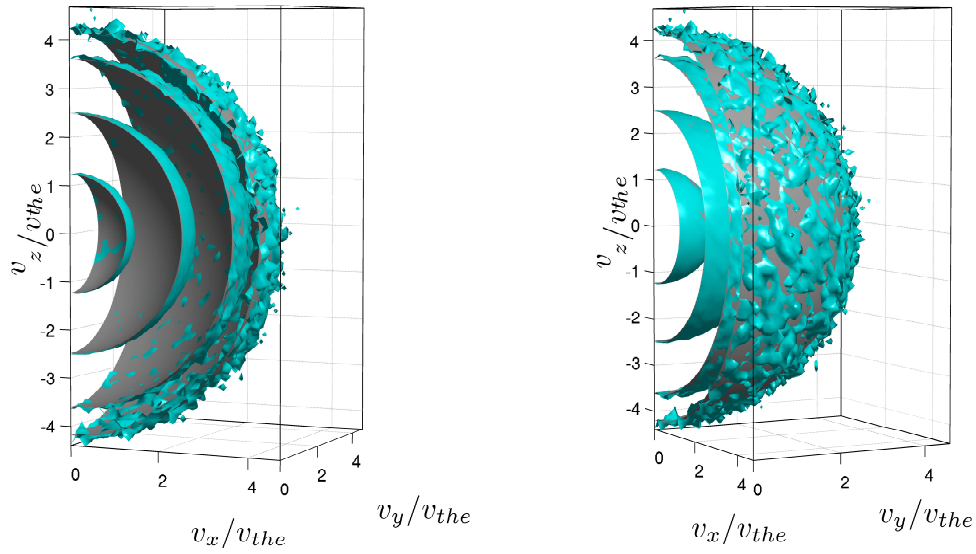

(b) Surface iso-contours for the ion initial velocity distribution (Maxwellian case)

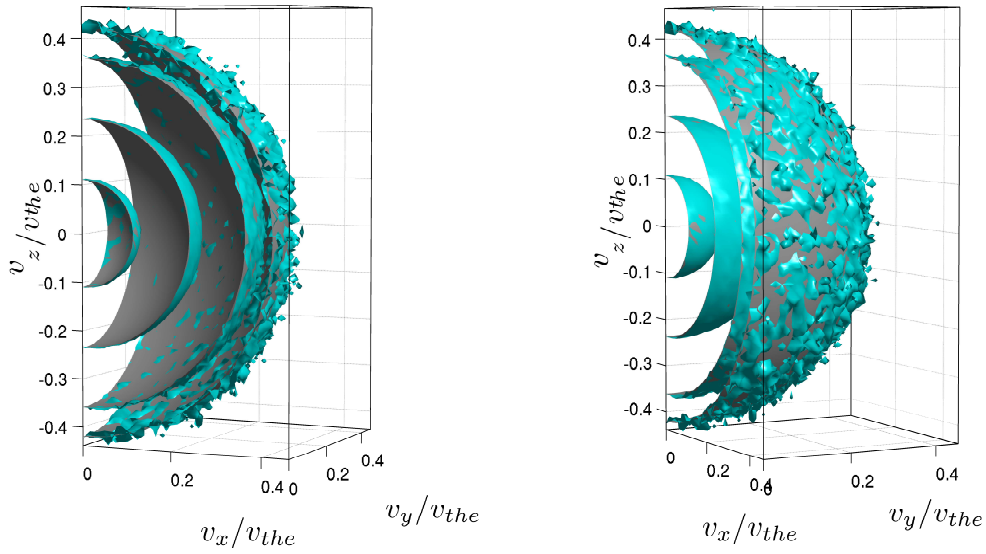

Figure 4.4: Surface iso-contours for (a) the electron initial velocity distribution and (b) the ion initial velocity distribution in the Maxwellian simulation. In panels (a) and (b), the blue color represents surface iso-contours measured from the simulated particle velocity distributions and the grey colour represents the surface iso-contours from the 3D Maxwellian distribution, Equation (4.41), using the relevant particle parameters.

This indicates a thermalisation of the electron species.

Panel (b) of Figure 4.5, i.e., the $\kappa_{i,e} = 4$ case, illustrates a similar reduction in the number of high energy electrons with velocities $|v_{x,y,z}/v_{th,e}| > 2.5$. For the Maxwellian case displayed in Figure 4.5 (c), however, the slices though the electron initial and final velocity distributions are identical, as expected for a stable plasma.

We note that the kappa distribution is known to model a metastable plasma state, while the Maxwellian distribution models a fully stable thermodynamic state. For the simulations having kappa velocity distributions, it is likely that some non-linear wave-particle interaction drives the plasma to a more stable equilibrium state, through the reduction of high energy electrons. This can occur via the enhanced thermal fluctuations and discrete particle noise associated with the kappa distribution (Mace et al., 1998). No changes in the ion velocity distributions were observed in any of the simulations runs.

We performed Fourier analysis, in space and time, of the total electromagnetic (wave) energy density $(U_{\delta E} + U_{\delta B})/(n_{0e}T_e/\epsilon_0)$ in each simulation. The parameters $U_{\delta E} = 1/2\epsilon_0(\delta \boldsymbol{E})^2$ and $U_{\delta B} = 1/(2\mu_0)(\delta \boldsymbol{B})^2$ are the energies of the fluctuating electric and magnetic fields, respectively, with total magnetic field being $\boldsymbol{B} = \boldsymbol{B}_0 + \delta \boldsymbol{B}$. The resulting spectrum of wave intensities is displayed as a function of ω/ω_{ce} and $|k|c/\omega_{pe}$ in Figures 4.6 to 4.8.

The wave intensity spectrum for the $\kappa_{i,e} = 2$ simulation is displayed in Figure 4.6, the $\kappa_{i,e} = 4$ case is displayed in Figure 4.7 and the Maxwellian case is displayed in Figure 4.8. In each of the figures, we use panel (a) to illustrate wave propagation parallel to $\boldsymbol{B}_0$ (0°), panel (b) illustrates wave propagation at 26.6°, panel (c) illustrates wave propagation at 45°, panel (d) illustrates wave propagation at 63.4°, and panels (e) and (f) illustrate wave propagation perpendicular to $\boldsymbol{B}_0$. The intensity spectra of panels (a) to (e) of each figure are displayed over the high frequency range $0 \leq \omega/\omega_{ce} \leq 5.5$, and are produced through temporal Fourier analysis of the electromagnetic fields over the time range $4000 \leq \omega_{pe}t \leq 4300$. In order to adequately resolve the low frequency range, $0 \leq \omega/\omega_{ce} \leq 0.2$, used in the display of panel (f) of each figure, the temporal Fourier analysis was carried out for the entire simulation run, i.e., for the time $0 \leq \omega_{pe}t \leq 7000$.

To display the wave intensity spectra in panels (a) to (e) in each figure, we use white colouring to represent the most intense fluctuations, i.e., those having $(U_{\delta E} + U_{\delta B})/(n_{0e}T_e/\epsilon_0) \geq 10^{8.7}$. We use yellow to represent the next intensity range $10^{8.3} \leq (U_{\delta E} + U_{\delta B})/(n_{0e}T_e/\epsilon_0) \leq 10^{8.7}$. This is followed by orange which represents the range $10^{7.7} \leq (U_{\delta E} + U_{\delta B})/(n_{0e}T_e/\epsilon_0) \leq 10^{8.3}$

(a) Slices through the electron velocity distribution ($\kappa_{i,e} = 2$ case)

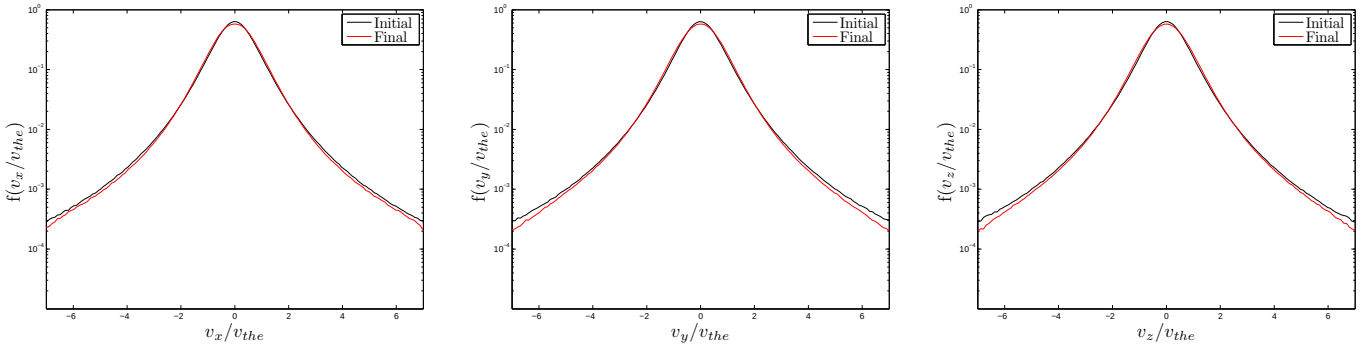

(b) Slices through the electron velocity distribution ($\kappa_{i,e} = 4$ case)

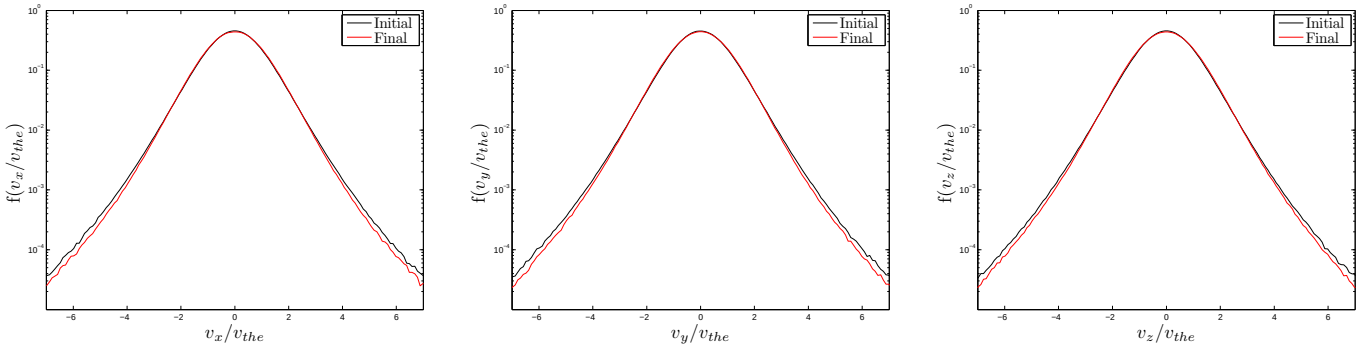

(c) Slices through the electron velocity distribution (Maxwellian case)

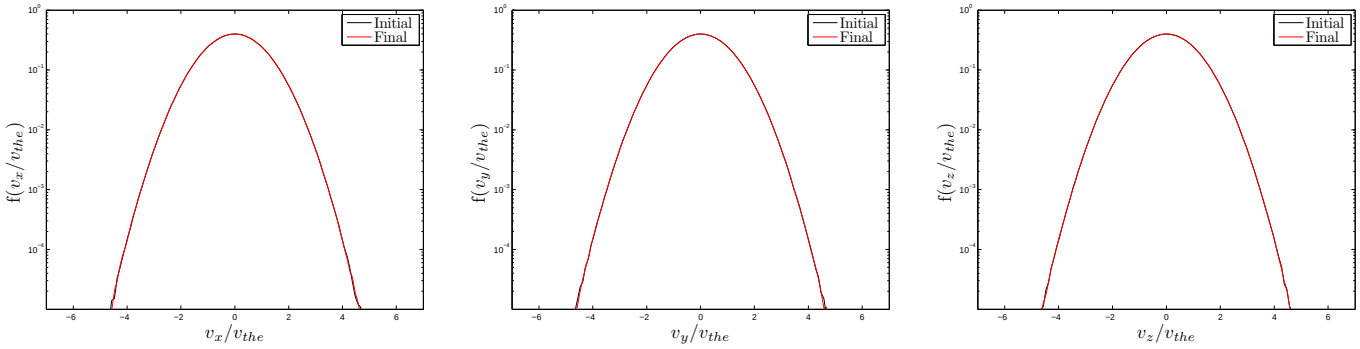

Figure 4.5: A comparison of the slices in the v_x, v_y and v_z directions, through the electron initial (black curve) and final (red curve) velocity distribution in each simulation. Panel (a) presents results for the $\kappa_{i,e} = 2$ simulation, panel (b) for the $\kappa_{i,e} = 4$ simulation and panel (c) for the Maxwellian simulation.

and red which represents $10^{6.7} \leq (U_{\delta E} + U_{\delta B})/(n_{0e}T_e/\epsilon_0) \leq 10^{7.7}$. Since panel (f) in each figure is taken over a longer time interval, the wave intensities are higher. However, white still represents the highest intensities, having $(U_{\delta E} + U_{\delta B})/(n_{0e}T_e/\epsilon_0) \geq 10^{10.3}$, followed by yellow which represents $10^{9.7} \leq (U_{\delta E} + U_{\delta B})/(n_{0e}T_e/\epsilon_0) \leq 10^{10.3}$, orange which represents $10^{9.3} \leq (U_{\delta E} + U_{\delta B})/(n_{0e}T_e/\epsilon_0) \leq 10^{9.7}$ and red which represents $10^{8.7} \leq (U_{\delta E} + U_{\delta B})/(n_{0e}T_e/\epsilon_0) \leq 10^{9.3}$.

In our discussion of the intensity spectra displayed Figures 4.6 to 4.8, a comparison is made between the regions of intense field fluctuations and the relevant linear dispersion relations of Section 4.2, which are over-plotted as dashed lines in each panel. For parallel wave propagation, i.e., panel (a) of each figure, we obtain the linear dispersion relations by solving Equation (4.20) using the software package MATHEMATICA. Equations (4.21) and (4.22) are solved to obtain the linear dispersion relations for perpendicular wave propagation [panels (e) and (f) of each figure]. While Equations (4.20) to (4.22) are for plasmas having kappa velocity distributions, we can approximate the Maxwellian dispersion relations using high values of κ. To approximate the Maxwellian dispersion relations we use $\kappa_{i,e} = 30$ in Equations (4.20) to (4.22). At the oblique angles, i.e., panels (b) to (d), the cold plasma dispersion relations are obtained for the required angles, by solving Equation (4.36).

The intensity spectra for simulation Run 1 ($\kappa_{i,e} = 2$ case) is illustrated in Figure 4.6. In all panels of Figure 4.6, good agreement is observed between the regions of high fluctuation intensities, i.e., the white, yellow, orange and red colouring, representing the intensities $(U_{\delta E} + U_{\delta B})/(n_{0e}T_e/\epsilon_0) \geq 10^{6.7}$, and the respective linear dispersion relations, depicted by the dashed lines. Diffuse field fluctuations are also observed outside the regions predicted by linear theory, as expected in a stable plasma. The agreement between the linear dispersion relations and the regions of intense field fluctuations confirms the validity of our simulation techniques, and also allows for the identification of the wave modes responsible for producing the enhanced field fluctuations.

As seen in panel (a) of Figure 4.6, for parallel propagation we identify the high and low frequency R-modes as well as the L-mode. The linear dispersion relations for these modes were obtained by solving Equation (4.20) and are displayed as the dashed lines. Since the electron oscillations are unaffected by the magnetic field in the parallel direction, Langmuir waves are also observed. We over-plotted as the dashed line, the linear dispersion relation for Langmuir waves, which is (Chen, 1984)

$$\omega^2 = \omega_{pe}^2 + \frac{3}{2}k^2 v_{th,e}^2. \tag{4.42}$$

For the parallel propagating waves in panel (a) of Figure 4.6, the most intense field fluctuations. i.e., the orange, yellow and white colouring having $(U_{\delta E} + U_{\delta B})/(n_{0e}T_e/\epsilon_0) \geq 10^{7.7}$, occur in the low frequency R-mode and Langmuir wave branches. A broad region of enhanced diffuse field fluctuations, displayed as the brighter red colouring with $10^{7.0} \leq (U_{\delta E} + U_{\delta B})/(n_{0e}T_e/\epsilon_0) \leq 10^{7.7}$, also appears for the Langmuir branch at frequencies $2.0 \leq \omega/\omega_{ce} \leq 3.5$ and wave numbers $k_\parallel c/\omega_{pe} \geq 1.2$. The maximum intensity of the Langmuir wave fluctuations had $(U_{\delta E} + U_{\delta B})/(n_{0e}T_e/\epsilon_0) \approx 10^{8.6}$. The Langmuir wave produced the overall highest fluctuation intensity of all the wave modes for the $\kappa_{i,e} = 2$ case. The most intense Langmuir fluctuations (yellow colouring) occur for a narrow band of frequencies around $\omega/\omega_{ce} \approx 2.5$, i.e, the electron plasma frequency, at $0.6 \leq k_\parallel c/\omega_{pe} \leq 1.0$ and $1.4 \leq k_\parallel c/\omega_{pe} \leq 2.7$. We note again that no sources of free energy are available in the plasma, hence, the waves are formed through the natural random motions of the plasma particles. Therefore, the highest wave activity is expected to occur at the natural oscillation frequencies of the plasma particles.

In panel (a) of Figure 4.6, the next mode having high fluctuation intensity, i.e., orange and yellow colouring, is the low frequency R-mode. The dominant wave activity in the low frequency R-mode branch is observed for wave numbers $0.4 \leq k_\parallel c/\omega_{pe} \leq 1.2$ and at frequencies $\omega/\omega_{ce} \leq 0.6$, with lower intensity fluctuations (red colouring) being observed up to $k_\parallel c/\omega_{pe} \leq 2.8$. The maximum intensity of the low frequency R-mode fluctuations had $(U_{\delta E} + U_{\delta B})/(n_{0e}T_e/\epsilon_0) \approx 10^{8.3}$. The high intensity fluctuations at the low frequency R-mode indicates that there is an abundance of electrons with velocities $\boldsymbol{v}_\parallel$, directed parallel to $\boldsymbol{B}_0$, which satisfy the cyclotron resonance condition (Tsurutani and Lakhina, 1997)

$$\omega - \boldsymbol{k}_\parallel \cdot \boldsymbol{v}_{\parallel res} = n|\omega_c|, \tag{4.43}$$

where ω and $\boldsymbol{k}_\parallel$ are the wave frequency and parallel wave vector, respectively, n is a positive integer and ω_c is the cyclotron frequency of the particle. When a particle has a velocity $\boldsymbol{v}_\parallel$ equal to the $\boldsymbol{v}_{\parallel res}$ defined in Equation (4.43), it will experience a Doppler shifted wave frequency $\omega' = \omega - \boldsymbol{k}_\parallel \cdot \boldsymbol{v}_{\parallel res}$ in its guiding centre frame that equals to a multiple n of its own cyclotron frequency ω_c. When this occurs, there is strong cyclotron wave-particle interaction, and the particle either loses or gains energy from the wave. We provide a detailed discussion of the resonance condition, Equation (4.43), in Chapter 5, where we investigate the whistler

instability.

For the L-mode and high frequency R-mode branches displayed in panel (a) of Figure 4.6, enhanced wave activity (red colouring) is observed to lie within close proximity to the respective linear dispersion relations. The field fluctuations for the high frequency R-mode had a higher maximum intensity, $(U_{\delta E} + U_{\delta B})/(n_{0e}T_e/\epsilon_0) \approx 10^{7.3}$, compared to that of the L-mode which had $(U_{\delta E} + U_{\delta B})/(n_{0e}T_e/\epsilon_0) \approx 10^{7.1}$. The intensities of both the L-mode and high frequency R-mode are observed to decrease as frequency increases. This decrease in intensity is due to a lack of particles having $\boldsymbol{v}_{\parallel}$ high enough to produce the necessary Doppler shift, $\omega^{'} = \omega - \boldsymbol{k}_{\parallel} \cdot \boldsymbol{v}_{\parallel res}$, in wave frequency required for strong cyclotron wave-particle interaction.

We now turn our attention to the oblique modes where linear theory is lacking. The oblique modes for the $\kappa_{i,e} = 2$ simulation are displayed in panels (b) to (d) of Figure 4.6. Here, the waves responsible for the enhanced field fluctuations are the oblique R-, X-, L-O and R-X modes, which are identified in panels (b) to (d). When moving from parallel to oblique propagation angles, the parallel L-mode branch becomes the oblique L-O mode, which occupies a different frequency range. Where the parallel L-mode [seen in panel (a)] produces high intensity field fluctuations at frequencies down to $\omega/\omega_{ce} \approx 2.0$ at vanishing wave numbers, the oblique L-O mode produces high intensity field fluctuations down to $\omega/\omega_{ce} \approx 2.5$ [see panels (b) to (d)]. The oblique X-mode, not seen previously, is present in the plasma at the oblique angles.

Before we continue with our discussion of the electromagnetic field intensity spectra at the oblique angles, it should be noted that the resolution of the figures in panels (b) and (d) are lower than the others. This is due to our plotting routine which uses a different number of data points depending on the angle. The electromagnetic field data is stored on a 2D grid. To illustrate our plotting routine we define variable j to index the column of a particular field value and k to index the row of the field value. For N_x columns and N_y rows, $j = 1 \rightarrow N_x$ and $k = 1 \rightarrow N_y$. For parallel propagation, we take field values at the grid points corresponding to $j = 1 \rightarrow N_x$ with $k = 1$. For perpendicular propagation, we take field values at points $j = 1$ with $k = 1 \rightarrow N_y$, and for 45° propagation, we require fields stored at $j = k$. Since we use $Nx = Ny$ in our simulations, these plots will use the same number of data points, i.e., the number of grid points per dimension. At 26.6° and 63.4°, however, we require field data at the grid indices $2j = k$ and $j = 2k$, respectively, which is half the number of field data points than the previous cases. However, as seen on panels (b) to (d) of Figure 4.6, good agreement is still observed between the cold plasma dispersion relations, Equation (4.36), and the regions of high wave activity (red, orange and yellow colouring).

By comparing panels (b) to (d) for the $\kappa_{i,e} = 2$ case shown in Figure 4.6, we observe that an increase in obliquity yields a greater change in the intensity spectra at lower frequencies, $\omega/\omega_{ce} \leq 1.5$, i.e., the oblique R-mode branch, than for higher frequencies. The region of enhanced field fluctuations (red and orange colouring) associated with the oblique R-mode, change in frequency and wave number extent as the angle to $\boldsymbol{B}_0$ increases. The fluctuations associated with the remaining oblique modes occupy a similar range of frequencies and wave numbers with increasing angle of propagation [see panels (b) to (d) of Figure 4.6]. The enhanced field fluctuations for the oblique R-mode branch occupy a diminishing range of frequencies, in accordance with the linear dispersion relation, and increase in wave number extent with increasing propagation angles. As seen in panel (b) for 26.6° propagation, the oblique R-mode fluctuations have frequencies $\omega/\omega_{ce} \leq 1.0$ and wave numbers $|k|c/\omega_{pe} \leq 3.0$. At 63.4° propagation [panel (d)], however, this frequency range diminishes to $\omega/\omega_{ce} \leq 0.6$, with enhanced wave activity observed for the full range of wave numbers shown in panel (d). The maximum wave intensity of the oblique R-mode was not observed to change significantly with an increase in obliquity, having $(U_{\delta E} + U_{\delta B})/(n_{0e}T_e/\epsilon_0) \approx 10^{7.9}$, which is less intense than its parallel propagating counterpart.

A comparison of panels (a) to (d) of Figure 4.6, i.e., propagation from 0° to 63.4°, reveals a similar region of diffuse field fluctuations, i.e., brighter red colouring having $10^{7.0} \leq (U_{\delta E} + U_{\delta B})/(n_{0e}T_e/\epsilon_0) \approx 10^{7.7}$, at frequencies centred around the electron plasma frequency, i.e., $1.5 \leq \omega/\omega_{ce} \leq 3.5$, and wave numbers $|k|c/\omega_{pe} \geq 0.5$.

The region of most intense field fluctuations (orange and yellow colouring) at the oblique angles, is again observed near the electron plasma frequency, $\omega_{pe}/\omega_{ce} = 2.5$, which now forms part of the oblique X-mode branch, as seen in panels (b) to (d). This high wave intensity region seen in panels (b) to (d) is narrow band in frequency extent and occurs for $0.5 \leq |k|c/\omega_{pe} \leq 3.0$. The maximum fluctuation intensity at oblique angles had $(U_{\delta E} + U_{\delta B})/(n_{0e}T_e/\epsilon_0) \approx 10^{8.4}$, and was not observed to change in magnitude with an increase in obliquity.

In the low wave number region of the oblique X-mode, i.e., $|k|c/\omega_{pe} \leq 0.5$, an increase in propagation angle results in an increase in the wave intensities over the frequency range $2 \leq \omega_{pe}/\omega_{ce} \leq 2.5$. As a consequence of this, we observe more orange and red colouring in this region when moving from panel (b) to (d).

For the oblique L-O and R-X mode branches, an increase in the angle of propagation from 26.6° [panel (b)] to 63.4° [panel (d)] results in an apparent increase in wave activity, i.e.,

we observe more orange and brighter red colouring. It should be noted that an increase in obliquity results in the linear dispersion relations for the *L*-*O* and *R*-*X* modes moving closer to each other. Here, the enhanced field fluctuations from each of these modes will be excited in close proximity to the other, and wave coupling can occur.

Finally, for wave propagation perpendicular to $\boldsymbol{B}_0$ in the $\kappa_{i,e} = 2$ simulation, the fluctuation spectra are displayed in panels (e) and (f). In panel (e) of Figure 4.6, the regions of high wave activity, depicted by the red and orange colouring, are due to the 5 lowest order electron Bernstein waves, which propagate in frequency bands bounded by harmonics n of the electron cyclotron frequency, i.e., $n\omega_{ce}$. The perpendicular *X*- and *O*-modes are also responsible for the high field fluctuation intensities seen in panel (e). The intense fluctuations below the lowest order electron Bernstein mode, i.e., at frequencies $\omega/\omega_{ce} < 1$, are due to the ion Bernstein waves, which we display in panel (f). We defer discussion of the ion Bernstein waves to later.

The upper hybrid frequency, for the parameters used in the simulation, is $\omega_{uh}/\omega_{ce} = 2.7$. Since our simulations are fully electromagnetic, the electron Bernstein wave propagating in the upper hybrid frequency band couples to the low frequency cold plasma *X*-mode (Puri et al., 1973; Mace, 2004), i.e., the perpendicularly propagating counterpart of the oblique *X*-mode observed in panels (b) to (d). As a result, for wave numbers $k_\perp c/\omega_{pe} \to 0$, the frequency of the upper hybrid electron Bernstein wave approaches the harmonic below ($\omega/\omega_{ce} = 2$ in this case) instead of approaching the upper hybrid frequency as it does for electrostatic Bernstein waves.

Unlike the wave intensity spectra observed in panels (a) to (d) of Figure 4.6, no broad regions of enhanced field fluctuations are observed for perpendicular propagation, displayed in panel (e). Instead, the intense field fluctuations in panel (e), occur for frequencies and wave numbers in close proximity to those predicted by the linear dispersion relations of Equations (4.21) and (4.22). This is likely due to the magnetic field restricting the motion of the plasma particles, where particles perform gyrations about the magnetic field lines here. The region of most intense wave activity in panel (e), depicted by the orange colouring, is observed in the wave number range $1.0 \leq k_\perp c/\omega_{pe} \leq 1.7$ for the electron Bernstein wave propagating in the upper hybrid frequency band. The maximum wave intensity of the upper hybrid mode had $(U_{\delta E} + U_{\delta B})/(n_{0e}T_e/\epsilon_0) \approx 10^{8.1}$. For the remaining electron Bernstein waves in panel (e), we observe a decrease in wave intensity as the order of the wave increases above the upper hybrid mode. On the other hand, for both the *X*- and *O*-modes in panel (e), the maximum wave intensities had $(U_{\delta E} + U_{\delta B})/(n_{0e}T_e/\epsilon_0) \approx 10^{7.3}$, and we observed no change

in the intensities for the range of frequencies and wave numbers shown in panel (e).

The fluctuation spectra displayed in panel (f) of Figure 4.6 are due to ion Bernstein waves. We emphasize again that both the electron and ion Bernstein waves are resolved within the same simulation run. However, to generate the low frequency fluctuation spectrum displayed in panel (f), we use data from the entire simulation run, i.e., data is taken for the time interval $0 \leq \omega_{pe}t \leq 7000$. The high frequency fluctuation spectra displayed in panels (a) to (e) of this figure were generated using field data taken over the shorter time interval $4000 \leq \omega_{pe}t \leq 4300$. As a result, the waves seen in panel (f) appear to be more intense than those previously discussed.

The intense field fluctuations in panel (f), i.e., the yellow, orange and brighter red colouring having $(U_{\delta E} + U_{\delta B})/(n_{0e}T_e/\epsilon_0) \geq 10^{9.0}$, are observed to follow the linear dispersion relations for the ion Bernstein wave, Equation (4.22). The ion Bernstein waves propagate within frequency bands bounded by harmonics of the ion cyclotron frequency ω_{ci}. The high intensity area below the lowest order ion Bernstein mode, at frequencies $\omega/\omega_{ce} < 0.01$, is due to the zero-frequency mode which is believed to cause particle diffusion in the plasma (Okuda and Dawson, 1973). The zero frequency mode is not predicted by linear theory and was also observed in the simulations of Kamimura et al. (1978) and Abdul and Mace (2014).

The dispersion curves for the ion Bernstein modes in panel (f) of Figure 4.6 are all observed to have frequencies which increase as $k_\perp c/\omega_{pe}$ decreases, reaching a maximum frequency at some value of $k_\perp c/\omega_{pe}$, and following this, the frequencies decrease to the harmonic below as wave number decreases further, i.e., $k_\perp c/\omega_{pe} \to 0$. This is in contrast to the behaviour of electrostatic ion Bernstein waves, where the modes below the lower hybrid frequency exhibit different behaviour. A more detailed discussion of the ion Bernstein wave dispersion relation is given later, when we discuss the curves of Figure 4.10. The most intense field fluctuations for the ion Bernstein waves, i.e., white, yellow and orange colouring having intensities $10^{9.5} \leq (U_{\delta E} + U_{\delta B})/(n_{0e}T_e/\epsilon_0) \leq 10^{10.6}$, are observed up to the tenth order ion Bernstein mode. In particular, the most intense field fluctuations are observed for wave numbers around the area of positive group velocity of the ion Bernstein wave dispersion relations, i.e., where $d\omega/dk > 0$. In general, as the order of the ion Bernstein waves increase, the wave intensities decrease. However, enhanced field fluctuations (red colouring) is observed to extend to higher wave numbers, as the order of the ion Bernstein waves increase.

As a final note for the $\kappa_{i,e} = 2$ case, we remind the reader that the maximum wave intensity for parallel propagating waves occurred for the Langmuir branch at the electron plasma

frequency, and had $(U_{\delta E} + U_{\delta B})/(n_{0e}T_e/\epsilon_0) \approx 10^{8.6}$. For oblique propagation, the maximum wave intensity occurred again at the electron plasma frequency, now forming part of the oblique X-mode, and had intensity $(U_{\delta E} + U_{\delta B})/(n_{0e}T_e/\epsilon_0) \approx 10^{8.4}$. For the high frequency perpendicularly propagating waves, the maximum wave intensity occurred for the electron Bernstein mode in the upper hybrid frequency band, which had $(U_{\delta E} + U_{\delta B})/(n_{0e}T_e/\epsilon_0) \approx 10^{8.1}$. At lower frequencies, the maximum wave intensity for the ion Bernstein waves had $10^{9.5} \leq (U_{\delta E} + U_{\delta B})/(n_{0e}T_e/\epsilon_0) \leq 10^{10.6}$. In our discussion of the results from the simulations for the $\kappa_{i,e} = 4$ and Maxwellian cases given next, a comparison is made to these maximum fluctuation intensities.

The Fourier spectra for simulation Run 2 are displayed in Figure 4.7. This case corresponds to a plasma having velocity distributions modelled by higher spectral indices than the previous case, i.e., $\kappa_e = \kappa_i = 4$, representing a softer energy spectrum for the electrons and ions. When comparing the panels of Figure 4.6 ($\kappa_{i,e} = 2$ case), to those of Figure 4.7 ($\kappa_{i,e} = 4$ case), we observe qualitatively similar fluctuation spectra. However, quantitative differences arise as a result of using higher kappa values. In general, Figure 4.7 illustrates lower intensities for the waves in simulation Run 2, as seen by the reduction in the brightness (intensities) of the panels when compared to those of Figure 4.6. In particular, we observe less orange and yellow colouring, representing intensities $(U_{\delta E} + U_{\delta B})/(n_{0e}T_e/\epsilon_0) \geq 10^{7.7}$ in the panels of Figure 4.7. The orange and yellow colouring in panels (a) to (e) of Figure 4.7 is also more narrow band in frequencies, and occur for a smaller wave number range than seen previously.

To be more quantitative, in panel (a) of Figure 4.7, the maximum wave intensity is again observed for the Langmuir wave branch at the electron plasma frequency. However, the wave intensity is lower than the previous case, i.e., $(U_{\delta E} + U_{\delta B})/(n_{0e}T_e/\epsilon_0) \approx 10^{8.2}$ here. At the oblique angles displayed in panels (b) to (d), the maximum fluctuation intensity had $(U_{\delta E} + U_{\delta B})/(n_{0e}T_e/\epsilon_0) \approx 10^{7.9}$, and is again observed for the oblique X-mode at the electron plasma frequency $\omega_{pe}/\omega_{ce} = 2.5$. In addition to a reduction in wave intensities, the broad diffuse fluctuations (red colouring) in panels (a) to (d) of Figure 4.7 appear less intense as well. As seen in panels (a) to (d) of Figure 4.7, at higher frequencies, $\omega/\omega_{ce} \geq 1.5$, these diffuse fluctuations appear more strongly only at higher wave numbers, $|k|c/\omega_{pe} \geq 1.3$, than seen for the previous case. While for lower frequencies, $\omega/\omega_{ce} \leq 1.5$, we observe an increase in low intensity diffuse fluctuations at $|k|c/\omega_{pe} \geq 3.0$ for the $\kappa_{i,e} = 4$ case, than was seen for the $\kappa_{i,e} = 2$ case displayed in Figure 4.6.

In panel (e) of Figure 4.7, the electron Bernstein mode in the upper hybrid frequency band is still observed to have the highest intensity of the electron Bernstein waves, hav-

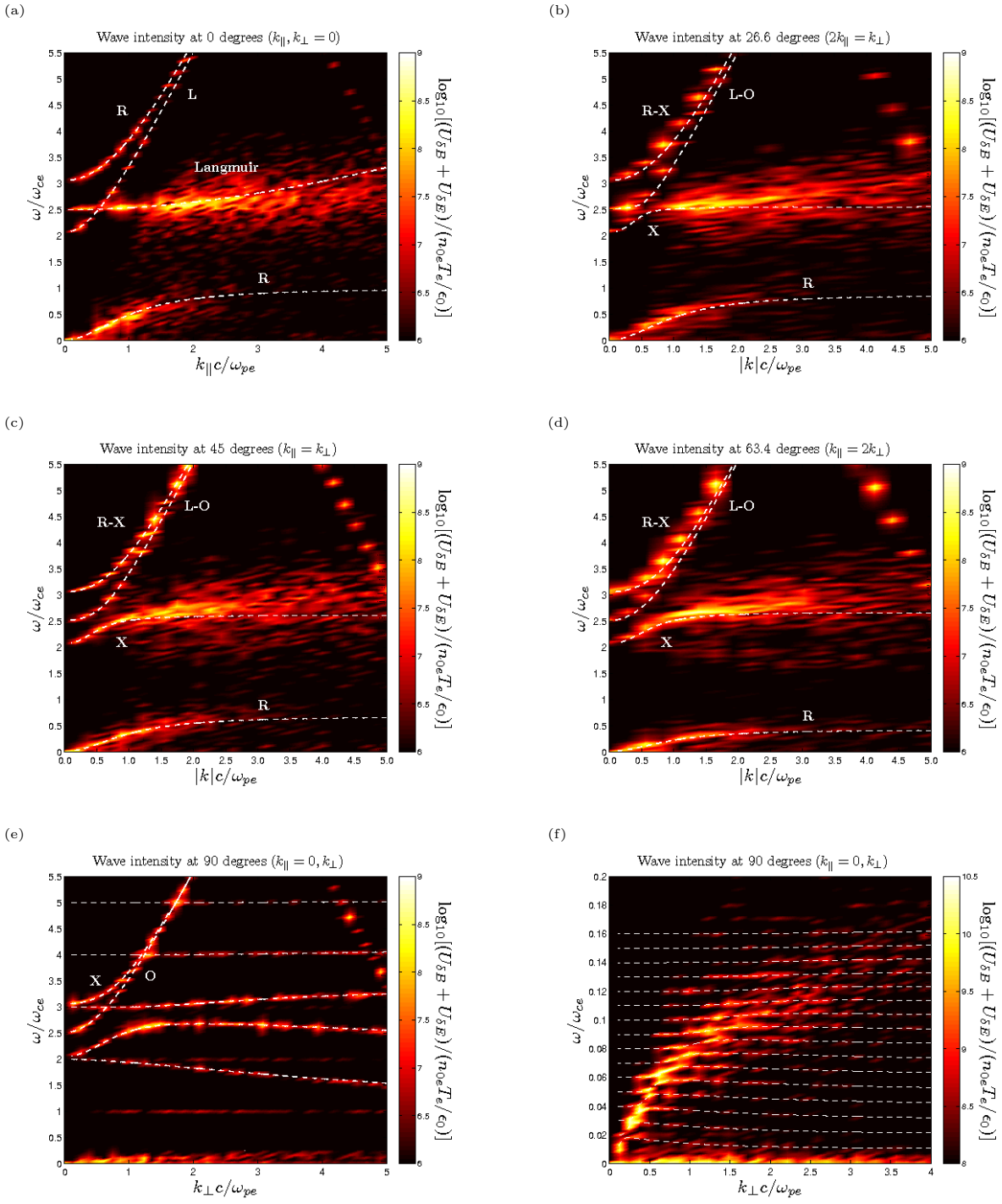

Figure 4.6: The intensity spectrum of the electromagnetic fields as a function of ω/ω_{ce} and $|k|c/\omega_{pe}$ for Run 1, i.e., the $\kappa_{i,e} = 2$ simulation. The spectrum is taken for wave propagation at angles (a) 0°, (b) 26.6°, (c) 45°, (d) 63.4° and (e)-(f) 90° to the magnetic $\boldsymbol{B}_0$, respectively. The relevant dispersion relations are over-plotted as dashed lines in each panel.

ing a lower intensity of $(U_{\delta E} + U_{\delta B})/(n_{0e}T_e/\epsilon_0) \approx 10^{7.9}$. However, unlike the $\kappa_{i,e} = 2$ case discussed previously, the X- and O-modes for the $\kappa_{i,e} = 4$ case had the same maximum intensity as the upper hybrid electron Bernstein mode. For the ion Bernstein waves displayed in panel (f) of Figure 4.7, we also observe lower peak wave intensities, having $10^{9.7} \leq (U_{\delta E} + U_{\delta B})/(n_{0e}T_e/\epsilon_0) \leq 10^{10.3}$. Intense ion Bernstein fluctuations here do not penetrate to lower wave numbers like it did in the previous case. However, there are more low intensity fluctuations at higher wave numbers $0.5 \leq k_\perp c/\omega_{pe} \leq 3.0$ for frequencies $\omega/\omega_{ce} \leq 0.1$, than seen previously.

The intensity spectra for simulation Run 3, i.e, the Maxwellian case, is displayed in Figure 4.8. We again observe qualitatively similar spectra to those discussed previously. In addition, the trends observed for increasing the spectral indices from $\kappa_i = \kappa_e = 2$ to $\kappa_i = \kappa_e = 4$ are again evident here. Significantly, all panels of Figure 4.8 display the lowest field fluctuation intensities of all the cases considered [compare Figure 4.8 to Figures 4.6 and 4.7]. This remains true for both the wave intensities and diffuse field fluctuations. In particular, the Langmuir wave displayed in panel (a) of Figure 4.8 had a maximum intensity of $(U_{\delta E} + U_{\delta B})/(n_{0e}T_e/\epsilon_0) \approx 10^{7.8}$. The oblique X-mode in panels (b) to (d) had a maximum fluctuation intensity of $(U_{\delta E} + U_{\delta B})/(n_{0e}T_e/\epsilon_0) \approx 10^{7.5}$. As discussed for the $\kappa_{i,e} = 4$ simulation results, we again observe an increase in the low intensity field fluctuations in panels (a) to (d) for low frequencies, $\omega/\omega_{ce} \leq 1.5$, and high wave numbers, $|k|c/\omega_{pe} \geq 3.0$, where at higher frequencies, $\omega/\omega_{ce} \geq 1.5$, the diffuse field fluctuations shift to higher wave numbers.

For perpendicular propagation [panel (e)], the electron Bernstein wave in the upper hybrid band had $(U_{\delta E} + U_{\delta B})/(n_{0e}T_e/\epsilon_0) \approx 10^{7.5}$. The ion Bernstein waves had maximums in the range $10^{9.7} \leq (U_{\delta E} + U_{\delta B})/(n_{0e}T_e/\epsilon_0) \leq 10^{10.0}$, occurring for a greatly reduced range of frequencies and wave numbers than seen previously. While the ion Bernstein wave intensities here are the lowest of the three cases [compare panel (f) of Figures 4.6 to 4.8], we again observe more low intensity field fluctuations at higher wave numbers, $k_\perp c/\omega_{pe} \geq 1.5$, for the low frequency range $\omega/\omega_{ce} \leq 0.1$, compared to the $\kappa_{i,e} = 2$ case.

Since the Debye length in a kappa plasma is smaller than its Maxwellian counterpart (Bryant, 1996; Mace et al., 1998), particle discreteness effects are more pronounced in plasmas modelled by low values of κ, than for an equivalent Maxwellian plasma (Mace et al., 1998). As was seen in Figures 4.6 to 4.8, decreasing the spectral indices of the electrons κ_e and ions κ_i enhances the random thermal fluctuations of the plasma particles, resulting in higher wave intensities. The energy associated with diffuse field fluctuations is also seen to be influenced by the kappa distribution, where, we generally observed higher intensity diffuse fluctuations

at lower wave numbers for decreasing $\kappa_{i,e}$. Conversely, increasing $\kappa_{i,e}$ yielded an increase in low intensity diffuse fluctuations at lower frequencies and higher wave numbers.

While it is not evident in the intensity spectra of Figures 4.6 to 4.8, the kappa distribution also affects the linear dispersion relations of the waves. To highlight these differences, we compare in Figures 4.9 and 4.10, the dispersion curves for the electron and ion Bernstein waves, respectively. For the parameters used in our simulations, the kappa distribution was found to not change the linear dispersion relations for the parallel propagating R- and L-modes as well as the perpendicular X- and O-modes, to within graphical accuracy of the plots. As such, we focus on the linear dispersion relations for the electron and ion Bernstein waves, which exhibit a greater dependence on the spectral index of the kappa distribution.

The dispersion curves displayed in Figures 4.9 and 4.10 were obtained by numerically solving Equation (4.22) using $\kappa_i = \kappa_e = 2$ (pink curve), $\kappa_i = \kappa_e = 4$ (green curve) and $\kappa_i = \kappa_e = 30$, which was used to approximate the Maxwellian dispersion relation (black curve). Figure 4.9 displays the numerical solutions for the high frequency range $0 \leq \omega/\omega_{ce} \leq 6.0$, corresponding to the electron Bernstein waves. In Figure 4.10, we display the numerical solutions for the frequency range $0 \leq \omega/\omega_{ce} \leq 0.18$, which corresponds to the ion Bernstein waves.

The effect of the kappa distribution on the electron Bernstein wave dispersion relation has been discussed in detail by Mace (2003, 2004). Therefore, we provide only a brief discussion here. For the electron Bernstein waves displayed in Figure 4.9, the single mode below the lower hybrid frequency band, i.e., the mode with frequencies $1 \leq \omega/\omega_{ce} \leq 2$, displays a slower fall off to the harmonic below as $\kappa_{i,e}$ decreases. On the other hand, the modes propagating within, and above the upper hybrid frequency band, are observed to exhibit a reduced frequency span above the nearest electron cyclotron harmonic as $\kappa_{i,e}$ decreases. Furthermore, the location of the peak frequencies for these modes is observed to shift to higher values of $k_\perp c/\omega_{pe}$ as $\kappa_{i,e}$ decreases.

A comparison of the ion Bernstein wave dispersion relations is given in Figure 4.10. By comparing Figures 4.9 and 4.10, we observe different electron and ion Bernstein dispersion behaviour. Unlike the electron Bernstein wave below the upper hybrid frequency, the ion Bernstein modes below the lower hybrid frequency ($\omega_{lh}/\omega_{ce} = 0.093$ here) do not approach the harmonic above for vanishing wave numbers (as they do in the electrostatic case). They instead have frequencies that increase with decreasing wave number, reaching a peak at a particular wave number $k_\perp c/\omega_{pe}$, and after reaching the peak frequency, they decrease in frequencies as wave number decreases further, $k_\perp c/\omega_{pe} \to 0$. We note that similar dispersion

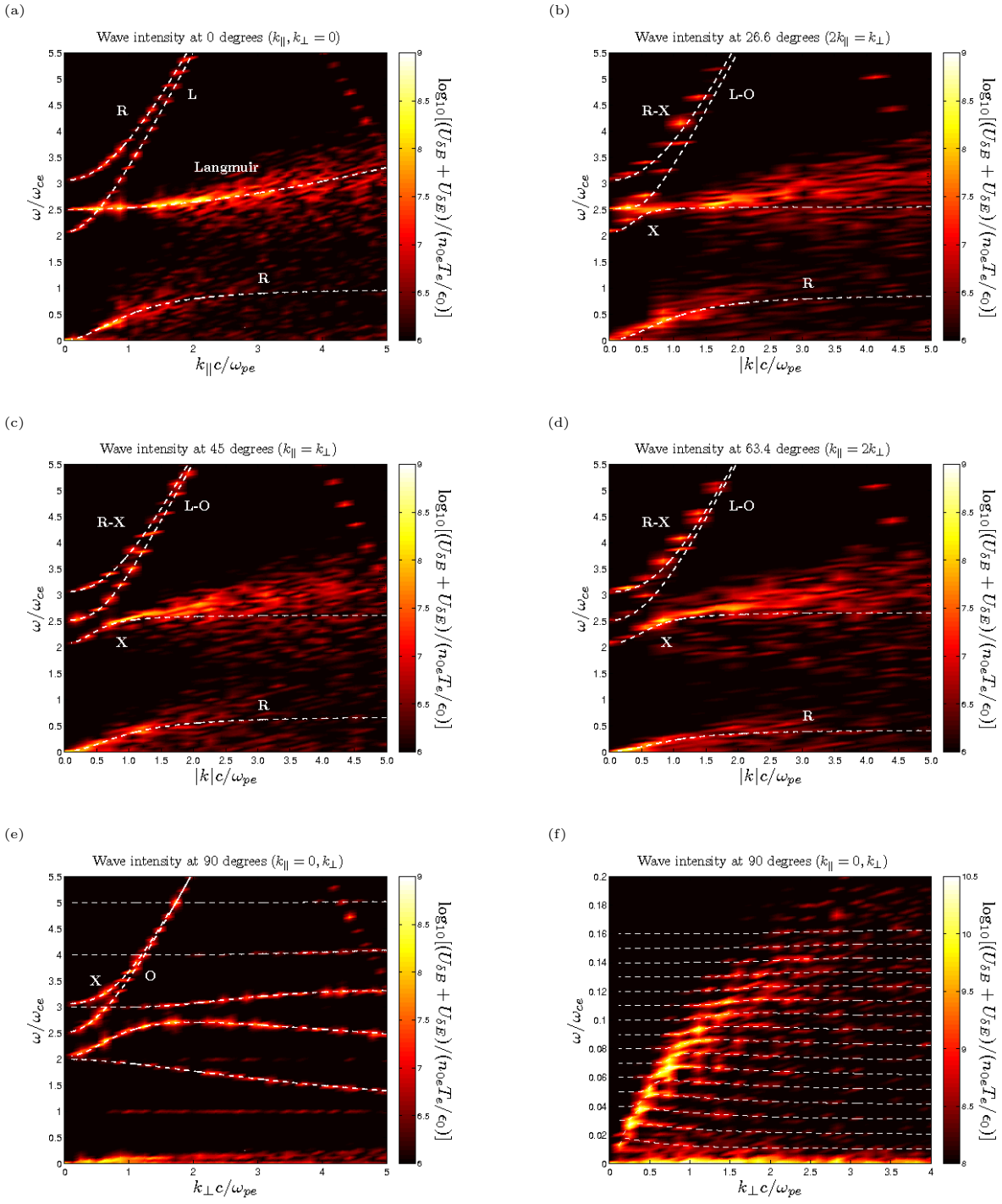

Figure 4.7: The intensity spectrum of the electromagnetic fields as a function of ω/ω_{ce} and $|k|c/\omega_{pe}$ for Run 2, i.e., the $\kappa_{i,e} = 4$ case. The spectrum is taken for wave propagation at angles (a) 0°, (b) 26.6°, (c) 45°, (d) 63.4° and (e)-(f) 90° to the magnetic $\boldsymbol{B}_0$, respectively. The relevant dispersion relations are over-plotted as dashed lines in each panel.

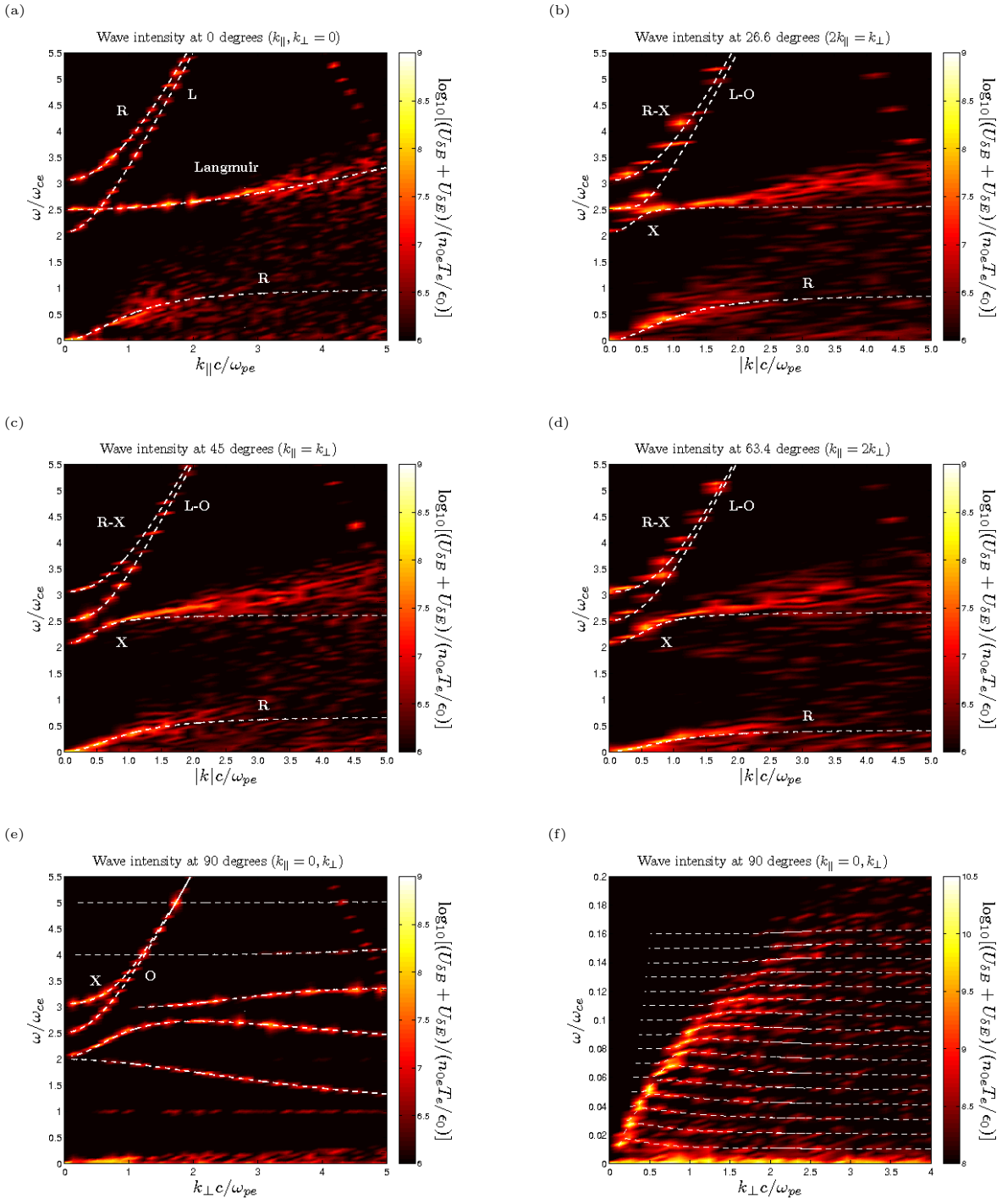

Figure 4.8: The intensity spectrum of the electromagnetic fields as a function of ω/ω_{ce} and $|k|c/\omega_{pe}$ for Run 3, i.e., the Maxwellian case. The spectrum is taken for wave propagation at angles (a) 0°, (b) 26.6°, (c) 45°, (d) 63.4° and (e)-(f) 90° to the magnetic $\boldsymbol{B}_0$, respectively. The relevant dispersion relations are over-plotted as dashed lines in each panel.

curves were found by Puri et al. (1973). The ion Bernstein waves were shown by Puri et al. (1973) to couple to a fast electromagnetic wave below the lower hybrid frequency, resulting in the dispersion behaviour displayed in Figure 4.10.

For the ion Bernstein waves propagating within, and above the lower hybrid frequency band, decreasing $\kappa_{i,e}$ results in the frequency peaks moving to higher wave numbers, and a reduction in the frequency span of these modes (similar to the electron Bernstein waves).

The peak frequencies of the ion Bernstein waves propagating below the lower hybrid frequency band are also observed to move to higher wave numbers for decreasing $\kappa_{i,e}$. However, the kappa distribution has a different effect on the frequency span of each of these modes. For the two lowest order ion Bernstein waves, decreasing $\kappa_{i,e}$ results in an increase in the frequency span of these modes, while it decreases the frequency span of the ion Bernstein modes above.

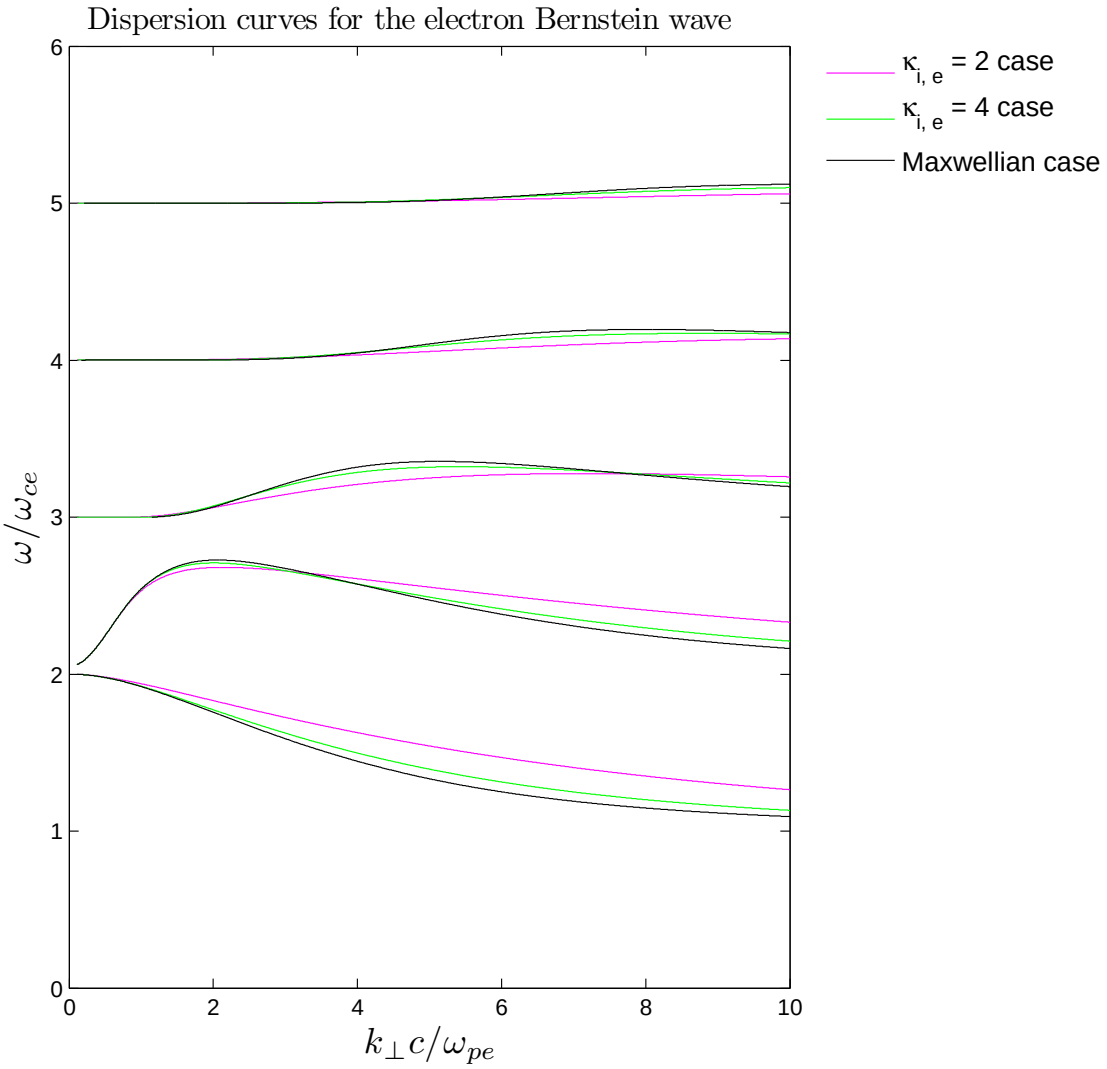

Figure 4.9: A comparison of the electron Bernstein wave dispersion relations, obtained by solving Equation (4.22) over the high frequency range $0 \leq \omega/\omega_{ce} \leq 5.5$. The pink curve illustrates the dispersion relation for $\kappa_{i,e} = 2$, green curve illustrates the dispersion relation for $\kappa_{i,e} = 4$ and the black curve illustrates the dispersion relation for the Maxwellian case.

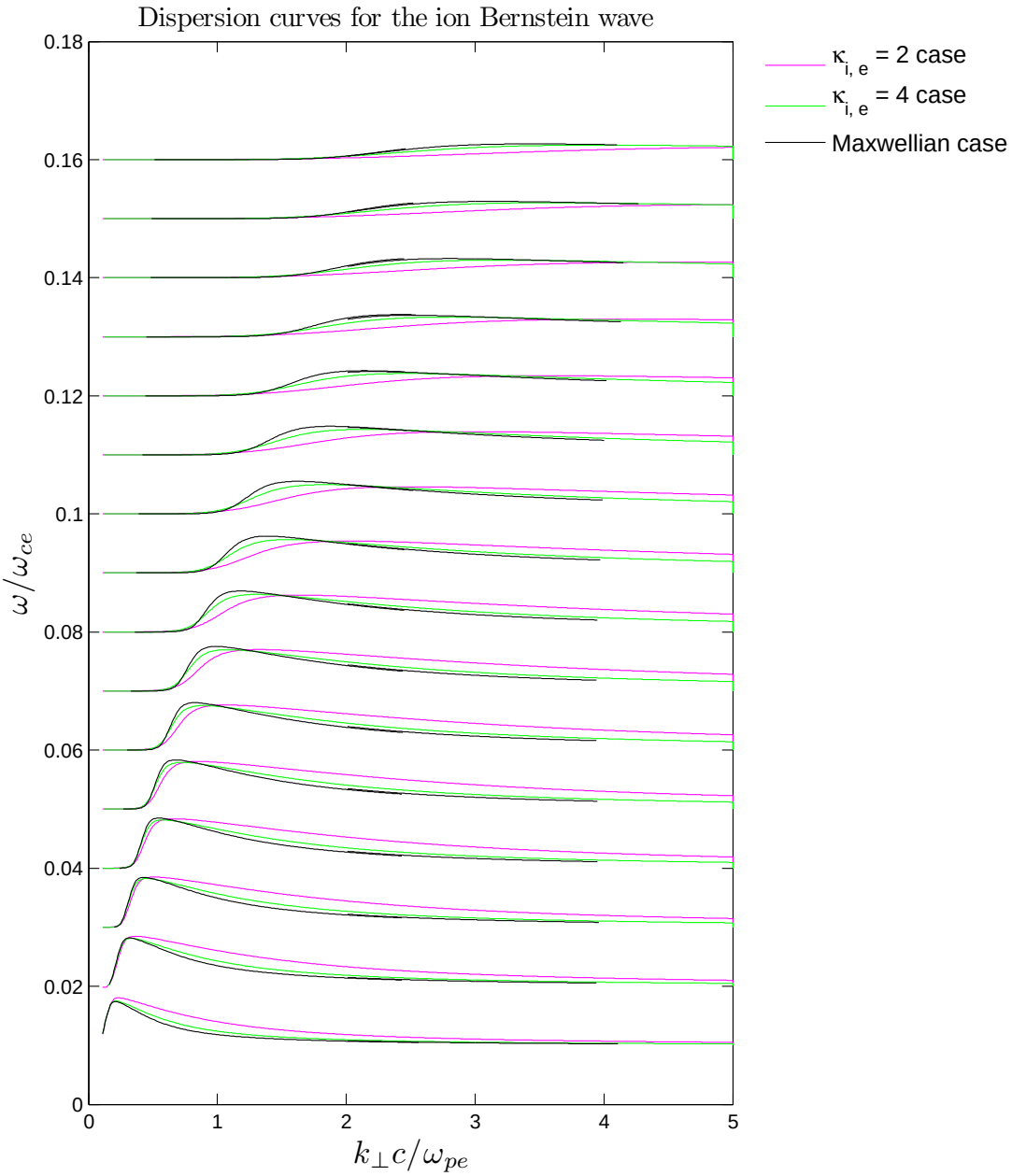

Figure 4.10: A comparison of the ion Bernstein wave dispersion relations, obtained by solving Equation (4.22) over the low frequency range $0 \leq \omega/\omega_{ce} \leq 0.18$. The pink curve illustrates the dispersion relation for $\kappa_{i,e} = 2$, green curve illustrates the dispersion relation for $\kappa_{i,e} = 4$ and the black curve illustrates the dispersion relation for the Maxwellian case.

Chapter 5

Simulation study of the whistler instability

Waves and instabilities in space plasmas are affected by a number of kinetic-scale plasma parameters. One of the parameter sets which affects the behaviour of the plasma is the thermal velocity of each species. The velocity distribution $f(\boldsymbol{v})$ of a plasma species can provide a source of free energy for the generation of micro-instabilities and the rapid growth of waves in the plasma. In this section we apply our code to the study of an electron-ion plasma immersed in a constant, uniform magnetic field $\boldsymbol{B}_0$, where the electrons have thermal anisotropy. In particular, the perpendicular component of the electron thermal energy is set greater than the parallel component, $T_{\perp e} > T_{\parallel e}$, where the directions $\perp$ and $\parallel$ are given with respect to the ambient magnetic field $\boldsymbol{B}_0$. This plasma configuration is known to destabilise the whistler mode. We present results of 2D3V electromagnetic particle-in-cell (PIC) simulations of the whistler instability propagating in (a) kappa and (b) Maxwellian plasmas. The dependence of the wave dynamics and instability growth rates on the spectral index of the electron population κ_e is discussed.

5.1 Introduction

Whistler waves are electromagnetic cyclotron waves which propagate parallel to the ambient magnetic field $\boldsymbol{B}_0$, at frequencies between the ion and electron cyclotron frequencies $\omega_{ci} \leq \omega \leq \omega_{ce}$ (Tsurutani and Lakhina, 1997; Eliasson and Lazar, 2015; Camporeale and

Zimbardo, 2015; Stansby et al., 2016). As the frequency of the wave nears the electron cyclotron frequency ω_{ce}, the wave experiences heavy cyclotron damping and ceases to exist (Stenzel, 1999). Whistler waves are dispersive, i.e., the group and phase velocities of the wave depend on the wave frequency. During the propagation of cyclotron waves, the component of the electric field vector directed perpendicular to the magnetic field $\boldsymbol{B}_0$ will rotate about the magnetic field lines (Treumann and Baumjohann, 1997; Gurnett and Bhattacharjee, 2005). For the whistler wave (R-mode), the direction of rotation of the electric field corresponds to the direction that electrons gyrate about the magnetic field lines (Treumann and Baumjohann, 1997), i.e., whistler waves are right-hand circularly polarised, where polarisation is expressed relative to the background magnetic field $\boldsymbol{B}_0$.

During early investigations of radio emissions from the ionosphere, various whistling sounds in the audio frequency range were detected (Storey, 1953). These sounds were characterised by tones descending in frequency with time and were attributed to waves which came to be known as whistler waves (Storey, 1953; Chen, 1984; Stenzel, 1999). The whistling tones were proposed to result from the dispersive propagation of the wave, with the higher frequencies travelling faster than the lower frequencies (Storey, 1953; Stenzel, 1999; Bellan, 2013). Before the satellite measurement of space plasmas was possible, passive ground observation and study of the dynamics and dispersion of whistler waves provided a means for measuring the average ionospheric electron densities and temperatures (Chen, 1984; Stenzel, 1999; Gurnett and Bhattacharjee, 2005). Whistler waves are known to be excited by lightning bolts (Storey, 1953; Gurnett and Bhattacharjee, 2005) and the unstable whistler modes can be triggered by anisotropic electron plasma populations, such as electron beams, loss cones, rings and temperature anisotropies (Kennel and Petschek, 1966; Tsurutani and Lakhina, 1997; Stenzel, 1999; Nishimura et al., 2002). Kennel and Petschek (1966) were among the first to conduct a comprehensive investigation into the effect of anisotropic electron distributions on the whistler wave stability in the magnetosphere. Kennel and Petschek (1966) showed how the whistler wave interacts with energetic particles and reduces the anisotropy through pitch angle scattering, where a particle's pitch angle defines the angle between the particle's instantaneous velocity and the ambient magnetic field.

Since particle-particle collisions in space plasmas are rare, it is the resonant interaction between plasma waves and particles which serves as the dominant mechanism for energy diffusion and loss of energetic particles in the magnetosphere (Kennel and Petschek, 1966; Cattell et al., 2008; Schriver et al., 2010; Watt et al., 2012) and solar wind (Chen, 1984; Gary et al., 1994; Lacombe et al., 2014). Whistler waves are common naturally occurring waves and exist in a diverse range of space plasma conditions, making them one of the candidate

waves responsible for this wave-particle interaction (Kennel and Petschek, 1966; Watt et al., 2012; Fu et al., 2014).

The whistler instability driven by electron temperature anisotropy produces enhanced magnetic field fluctuations in the plasma. The enhanced field fluctuations are able to resonate with a broad range of energetic electrons, exchanging energy and momentum with the plasma (Watt et al., 2012; Fu et al., 2014). During the evolution of the whistler instability, the excited field fluctuations enhance pitch angle diffusion of electrons which reduces their temperature anisotropy, depleting the resonant particles until a state of marginal stability is reached (Treumann and Baumjohann, 1997; Camporeale, 2015). In space, whistler waves can scatter energetic electrons reducing their pitch angles so that they fall within the loss cone, leading to their precipitation into the ionosphere, producing diffuse aurora (Ossakow et al., 1972a; Tsurutani and Lakhina, 1997; Treumann and Baumjohann, 1997). This pitch angle scattering places limits on the density of stably trapped particles in the magnetosphere, leading to ring current decay during the recovery phase of geomagnetic storms (Ossakow et al., 1972a; Tsurutani and Lakhina, 1997; Treumann and Baumjohann, 1997; Watt et al., 2012; Camporeale and Zimbardo, 2015). Whistlers may also be responsible for the energisation of relativistic electrons in the outer radiation belt during geomagnetic storms, which can negatively impact spacecraft (Lu et al., 2010; Camporeale, 2015). This further reinforces the need to investigate the dispersive characteristics of the whistler instability, as well as investigate the electron distribution function details that influence wave growth and eventual saturation.

The characteristics of whistler waves propagating in plasmas having by Maxwellian velocity distributions is well understood and extensively covered in the literature (Ossakow et al., 1972b; Gary and Wang, 1996; Stenzel, 1999; Gary et al., 1994; Gary and Cairns, 1999; Nishimura et al., 2002; Schriver et al., 2010). As stated previously, however, the family of kappa distributions have increasingly been accepted as providing a better fit to observed space plasma velocity distributions than the Maxwellian distribution. Furthermore, superthermal particle populations are frequently observed in the space plasma environments in which whistler waves are found, such as the solar wind (Maksimovic et al., 1997; Marsch, 2006) and planetary magnetospheres (Scudder et al., 1981; Divine and Garrett, 1983; Christon, 1987; Schippers et al., 2008). The kappa distribution is known to alter the statistics of microphysical plasma processes, affecting the growth and damping of plasma instabilities as well as producing changes in the dispersion relations of purely kinetic plasma waves (Summers and Thorne, 1991; Mace and Hellberg, 1995; Mace et al., 1998; Hellberg et al., 2000, 2005). An increasing body of research has been conducted to investigate the effect the superthermal electron population has on the behaviour of whistler waves.

Mace (1998) investigated the temperature anisotropy driven whistler instability using parameters relevant to the Earth's foreshock region. The study of Mace (1998) was restricted to parallel propagating waves and results were used to explain the nearly field aligned waves in this region, classified as "1 Hz" whistlers (Hoppe et al., 1981, 1982). A plasma composed of a single ion and single electron component was used, where both species were modelled by a loss cone bi-Lorentzian (bi-kappa) velocity distribution (Summers and Thorne, 1991). Mace (1998) found the presence of the superthermal tail to accentuate the growth of waves at smaller wave numbers than those expected for the bi-Maxwellian case and caused an increase in the growth rate of the instability, exceeding that of the bi-Maxwellian plasma with a similar anisotropy. The wave numbers corresponding to the peak in the growth rates were also found to shift to smaller values as the hardness of the electron distribution increased, i.e., as the spectral index κ_e of the electron velocity distribution decreased.

Xioa et al. (2006) investigated the parallel whistler instability threshold condition, defined here as the minimum electron temperature anisotropy required to for a particular instability growth rate. The instability threshold was investigated for a plasma containing an electron population modelled by a bi-kappa velocity distribution as well as a cold population of isotropic ions and electrons. Xioa et al. (2006) investigated the effect of the spectral index κ_e and parallel electron beta $\beta_{\|e}$, i.e., the ratio of parallel electron pressure to magnetic pressure, on the instability threshold. The instability threshold conditions were found to be strongly influenced by the high energy tail of the kappa distribution, where the minimum temperature anisotropy required for the instability was found to decrease for increasing κ_e, and lowest threshold values were obtained for the bi-Maxwellian distribution ($\kappa_e \to \infty$). Xioa et al. (2006) argued that the this is due to maximum growth rates being smaller in plasmas with velocity distributions modelled by decreasing spectral indices.

Mace and Sydora (2010) extended the previous work of Mace (1998). Where Mace (1998) used plasma parameters typical of those found in the foreshock, Mace and Sydora (2010) conducted an extensive parameter survey of the whistler instability propagating in a plasma having an electron species modelled by a bi-kappa velocity distribution. Mace and Sydora (2010) found that the instability maximum growth rates were affected by the spectral index κ_e, as well as the value of electron temperature anisotropy and parallel electron beta $\beta_{\|e}$. For small temperature anisotropies, the instability peak maximum growth rate was found to be enhanced for decreasing κ_e; however, at large temperature anisotropies, the power law tail was found to be deleterious to the instability, decreasing the peak growth rate with decreasing κ_e. At intermediate anisotropies, the growth rate was found to maximise for a particular κ_e value, i.e., the relationship between the instability peak maximum growth rate

and spectral index κ_e is non-monotonic. For a fixed temperature anisotropy, the instability growth rate was found to increase for increasing parallel electron beta $\beta_{\|e}$, and vice versa. Mace and Sydora (2010) also found that it is the parallel electron beta that governs the value of temperature anisotropy at which the relationship between peak growth rate and decreasing κ_e exhibits the monotonic and non-monotonic behaviour.

Eliasson and Lazar (2015) numerically investigated the linear growth rate and non-linear saturation of the whistler instability in a plasma composed of an electron species modelled by the bi-kappa velocity distribution. Eliasson and Lazar (2015) employed parameters typically found in the solar wind as well as in the solar corona and solar flares. Good agreement between the results of their Vlasov simulations and theoretical predictions was found for the instability growth rates and dispersion relations. The instability was found to be dependent on the shape of the velocity distribution as well as the temperature anisotropy of the electrons. The peak growth rates were found to increase with increasing electron kappa values, for the high temperature anisotropy used in their study. The instability was found to saturate by magnetic trapping of electrons, leading to increased saturation wave amplitudes for higher growth rates of the instability.

Linear theory assumes plasma waves have small amplitudes and informs a small window of the plasma dynamics and characteristics. When plasma wave amplitudes become large, a number of physical effects are introduced which are unaccounted for through linear analysis alone. These include non-linear wave-particle interaction, leading to the saturation of instabilities, and plasma wave-wave interaction, leading to plasma turbulence. Kinetic plasma simulation is useful in the non-linear regime of plasma dynamics and is used to extend linear theory. By virtue of its fundamental approach in describing the plasma, particle-in-cell (PIC) simulations provide a kinetic description of the plasma. PIC simulations have the capability to detail the effect the velocity distribution has on the behaviour of the system, both in the linear growth region and in the non-linear regime. A number of authors have used PIC simulations to study the whistler instability.

Devine and Chapman (1995) performed 1D and 2D electromagnetic particle-in-cell simulations of the electron temperature anisotropy driven whistler instability. They used parameters pertaining to the near-Earth night side plasma sheet region, during geomagnetically disturbed times. Devine and Chapman (1995) modelled the electron velocity distribution by a bi-Maxwellian distribution and investigated the dependence of the instability growth rates, non-linear saturation and pitch angle diffusion rates on plasma beta, comparing results from equivalent 1D and 2D simulations. In the simulations of Devine and Chapman (1995), an

electron temperature anisotropy of $T_{\perp e}/T_{\parallel e} = 4$ was required to overcome the noise inherent in their 2D electromagnetic simulations. The instability growth rate was found to be larger in the 1D simulations, leading to higher pitch angle diffusion rates. The instability growth rates were also found to increase with increasing beta values in both the 1D and 2D simulations. During instability growth, the field energy was observed to increase exponentially and temperature anisotropy decreased via wave-particle interaction. During the saturation phase, particle trajectories demonstrated the non-linear trapping of resonant particles in large amplitude waves.

Gary et al. (2000) used 2D electromagnetic PIC simulations to investigate plasma instabilities driven by electron anisotropy. Gary et al. (2000) simulated an electron-ion plasma, where the electron population was modelled by a bi-Maxwellian velocity distribution and the ions were modelled by an isotropic Maxwellian. A strong background magnetic field was imposed in their simulations, yielding $\omega_{pe} \approx \omega_{ce}$, characteristic of plasmas in the auroral and polar magnetosphere. For temperature anisotropies $T_{\perp e}/T_{\parallel e} > 1$, the growth of three modes was observed below the electron cyclotron frequency in their simulations. These were the electrostatic instability, which has maximum growth at oblique propagation angles to the magnetic field, as well as the electromagnetic Z-mode and whistlers, which have maximum growth parallel to the magnetic field. Only the electrostatic mode grows in a plasma with $\beta_e = 0$, while for non-zero plasma beta, the electrostatic mode remains and gains a magnetic component corresponding to the right-hand elliptically polarised Z-mode and whistler mode. The instabilities driven by the electron anisotropy were found to produce enhanced field fluctuations. The electrostatic instability was found to be the dominant contributor to the enhanced field fluctuations at small electron temperatures, while the electromagnetic instabilities dominated for high electron temperatures. The enhanced field fluctuations resulted in wave-particle scattering, which imposes a beta dependent upper bound on the electron temperature anisotropy. The electromagnetic instabilities were found to approximately preserve the bi-Maxwellian character of the electron velocity distribution at low particle energies, while the electrostatic instability produced superthermal enhancement of the electron velocity distribution, at sufficiently low plasma beta.

Lu et al. (2010) ran 1D electromagnetic PIC simulations to investigate the evolution of the whistler instability driven by superthermal electrons. Two electron populations were used in the simulations of Lu et al. (2010) and ion motion was neglected. One of the electron populations was cold, dense and modelled by an isotropic Maxwellian velocity distribution and the other was a tenuous electron population modelled by the bi-kappa distribution, where the accept-reject method was used to generate the kappa distributed deviates in their simulations.

Lu et al. (2010) employed a high electron temperature anisotropy and simulation results indicated an increase in the instability growth rate with increasing electron kappa values κ_e. The threshold condition, defined here as the minimum electron temperature anisotropy required for a particular growth rate, was also found to decrease with increasing κ_e values. The fluctuating magnetic field levels at the saturation phase of the instability were found to increase for decreasing electron kappa, i.e., a harder electron spectrum. Furthermore, the electron velocity distribution was found to fit smaller kappa values than those initially used to model the distribution, after the whistler waves were excited.

Gary et al. (2011) employed 2D PIC simulations to investigated the whistler instability in a low beta plasma, driven by anisotropic electrons. Gary et al. (2011) ran simulations for a plasma composed of a single electron species modelled by a bi-Maxwellian velocity distribution with ions forming a charge neutralising background. Theory predicts that as electron beta decreases to $\beta_e < 0.025$, the maximum wave growth shifts from parallel propagation to oblique angles with respect to the magnetic field. Gary et al. (2011) ran three simulations to investigate the consequences of this change in wave behaviour, as a function of electron beta, using $\beta_e = 0.1, 0.03$ and 0.01, respectively. For the simulations using $\beta_e = 0.1$, the maximum wave growth was found to be directed along the magnetic field and the fluctuating fields were strictly electromagnetic, as predicted by theory. In the simulations using smaller electron beta, the maximum growth displayed a shift to oblique propagation angles, where maximum wave growth was found at the angle $\theta = 48^\circ$ with respect to the magnetic field in the simulation using $\beta_e = 0.01$. The fluctuating fields for low beta plasmas were predominantly electrostatic and were found to heat the electrons, leading to a superthermal component in the parallel electron velocity distribution.

Hughes et al. (2016) ran 2D electromagnetic PIC simulations, which employed the Darwin approximation (Darwin, 1920), to investigate the effect the ratio of electron thermal velocity to the speed of light, $v_{th,e}/c$, has on the temperature anisotropy driven whistler instability. Hughes et al. (2016) used a single electron species in their simulations, where the electron velocity distribution was modelled by the bi-Maxwellian distribution, and ion motion was neglected. PIC simulations usually employ a large value of $v_{th,e}/c$, since it is computationally infeasible to use realistic values, e.g., $v_{th,e}/c = 0.005$ in the solar wind. This is due to simulations needing to satisfy the CFL condition. Hughes et al. (2016) ran simulations using $v_{th,e}/c$ ranging from 0.1 to 0.025 and compared results to theory using realistic $v_{th,e}/c$. Simulation results demonstrated that the linear dispersion relation, saturation amplitudes and pitch angle scattering rates are insensitive to $v_{th,e}/c$ as long as a realistic value of plasma beta is used. Hence, simulations using artificially large $v_{th,e}/c$ can be used to accurately

capture the relevant physics of a cooler plasma, while reducing the computational expense. Hughes et al. (2016) also investigated the numerical noise inherent in electromagnetic PIC simulations and found that larger values of $v_{th,e}/c$ reduce electrostatic noise effects, allowing for a lower number of particles per cell to be used.

Space plasmas often exhibit non-Maxwellian velocity distributions having an abundance of superthermal particles. Consequently, many analytical and numerical studies have been carried out to investigate the whistler instability in plasmas with superthermal electron populations (Mace, 1998; Xioa et al., 2006; Mace and Sydora, 2010). While plasma simulation is an important tool for extending the insights gained through linear theory, few particle-in-cell (PIC) simulations have been carried out to investigate whistlers in plasmas having kappa distributions. In this chapter we present results from 2D3V electromagnetic PIC simulations of the electron temperature anisotropy driven whistler instability in an electron-ion plasma. We model the electron population by (a) the bi-kappa velocity distribution and (b) the bi-Maxwellian velocity distribution. Since we do not confine wave propagation to a single direction, we are also able to glean the properties of the whistler instability at oblique angles in both the kappa and Maxwellian plasmas, by analysing the enhanced field fluctuation spectrum produced by the unstable whistler modes.

5.2 Theory

5.2.1 Cyclotron resonance

Unstable whistler waves grow through cyclotron resonance with an electron population having an excess of particles with a higher momentum than the wave, leading to the enhancement of magnetic field fluctuations (Kennel and Petschek, 1966; Tsurutani and Lakhina, 1997; Treumann and Baumjohann, 1997; Gurnett and Bhattacharjee, 2005). The condition for cyclotron resonance between a whistler wave an the electron is given by

$$\omega^{'} = \omega - \boldsymbol{k}_{\parallel} \cdot \boldsymbol{v}_{\parallel \mathrm{res}} = n|\omega_{ce}|, \tag{5.1}$$

where ω and $\boldsymbol{k}_{\parallel}$ are the wave angular frequency and parallel wave vector, respectively, $\boldsymbol{v}_{\parallel \mathrm{res}}$ defines the velocity necessary for cyclotron resonance and n is a positive integer. When an

electron's guiding centre velocity, i.e., the velocity component $\boldsymbol{v}_{\parallel}$ parallel to the magnetic field, is close to $\boldsymbol{v}_{\parallel \mathrm{res}}$, there will be strong interaction between wave and particle. When the parallel component of the electron velocity equals $\boldsymbol{v}_{\parallel \mathrm{res}}$ defined by Equation (5.1), the electron will experience an electromagnetic wave at frequency $\omega^{'}$ equal to its own cyclotron frequency, or a multiple n of it (Kennel and Petschek, 1966; Tsurutani and Lakhina, 1997). The guiding centre motion along $\boldsymbol{B}_0$ Doppler shifts the original wave frequency ω to a new $\omega^{'} = \omega - \boldsymbol{k}_{\parallel} \cdot \boldsymbol{v}_{\parallel \mathrm{res}}$. Depending on the relative phase of the electron gyration and the rotating perpendicular electric field vector during cyclotron resonance, the electron is subject to continuous acceleration or deceleration by the wave, gaining or losing energy (Chen, 1984).

The parameter n in Equation (5.1) characterises the mechanism of wave-particle resonance. For $n = 0$, the usual Landau resonance occurs. The electrons here do not experience a rapidly fluctuating electric field and the slope of the particle velocity distribution at $\boldsymbol{v}_{\parallel \mathrm{res}}$ dictates whether waves will grow or be damped. If there is an excess number of particles with velocities $\boldsymbol{v}_{\parallel} > \boldsymbol{v}_{\parallel \mathrm{res}}$, i.e., a positive slope of the velocity distribution, then the particles are decelerated and the wave gains energy leading to instability. Conversely, Landau damping occurs for a negative slope of the particle velocity distribution at $\boldsymbol{v}_{\parallel \mathrm{res}}$ (Treumann and Baumjohann, 1997; Tsurutani and Lakhina, 1997).

The case of $n = 1$ in Equation (5.1) corresponds to the phase locking condition between the waves and particles (Treumann and Baumjohann, 1997; Mace et al., 2011). The resonant particles here are at rest in the wave frame and will always see the same phase of the rotating electric field, maximising the wave-particle interaction.

For $n \neq 0$, two types of resonances occur. These are the normal and anomalous resonances. For the normal resonance, the Doppler shifted frequency is positive and the electrons interact with the right-hand circularly polarised wave, i.e., $\boldsymbol{k}_{\parallel} \cdot \boldsymbol{v}_{\parallel \mathrm{res}} < 0$ and wave and particle move in opposite directions. The anomalous resonance occurs when the particle velocity parallel to the magnetic field is greater than the phase velocity of the wave and the particle "overtakes" the wave. The Doppler shift in this case produces a wave frequency in the guiding center frame equal to the negative of the cyclotron frequency, reversing the sense of polarisation of the wave in the guiding centre frame (Tsurutani and Lakhina, 1997).

5.2.2 Plasma model and dispersion Relation

In our simulations, we model the velocity distribution of the electron species by either a bi-kappa or bi-Maxwellian distribution. The bi-kappa distribution is given by (Summers and Thorne, 1991)

$$f(v_\perp, v_\parallel) = \pi^{-3/2} \frac{1}{\theta_\perp^2 \theta_\parallel} \frac{\Gamma(\kappa+1)}{\kappa^{3/2}\Gamma(\kappa-1/2)} \left(1 + \frac{v_\perp^2}{\kappa\theta_\perp^2} + \frac{v_\parallel^2}{\kappa\theta_\parallel^2}\right)^{-(\kappa+1)}, \tag{5.2}$$

where $v_\perp$ and $v_\parallel$ are the velocity components parallel and perpendicular to the magnetic field, respectively, Γ is the gamma function and κ shapes the superthermal tail of the distribution. The generalised thermal speeds $\theta_\parallel$ and $\theta_\perp$, parallel and perpendicular to the magnetic field, respectively, are defined by (Summers and Thorne, 1991)

$$\theta_\parallel = \left[2\left(\frac{\kappa - 3/2}{\kappa}\right)\right]^{1/2} \left(\frac{T_\parallel}{m}\right)^{1/2}, \tag{5.3}$$

$$\theta_\perp = \left[2\left(\frac{\kappa - 3/2}{\kappa}\right)\right]^{1/2} \left(\frac{T_\perp}{m}\right)^{1/2}, \tag{5.4}$$

where $T_\parallel$ and $T_\perp$ are the kinetic temperatures parallel and perpendicular to the magnetic field, and $v_{\parallel\mathrm{th}} = (T_\parallel/m)^{1/2}$ and $v_{\perp\mathrm{th}} = (T_\perp/m)^{1/2}$ are the usual thermal speeds of the plasma species. The bi-kappa distribution reduces to the bi-Maxwellian distribution in the limit $\kappa \to \infty$, which is given by

$$f(v_\perp, v_\parallel) = \frac{1}{(2\pi)^{3/2} v_{th\perp}^2 v_{th\parallel}} \exp\left[-\frac{1}{2}\left(\frac{v_\perp^2}{v_{th\perp}^2} + \frac{v_\parallel^2}{v_{th\parallel}^2}\right)\right]. \tag{5.5}$$

The dispersion relation for whistler waves propagating in a plasma modelled by the bi-kappa distribution, Equation (5.2), is given by (Mace and Sydora, 2010)

$$\begin{aligned}\frac{k^2c^2}{\omega^2} =& 1+\sum_{\alpha}\frac{\omega_{p\alpha}^2}{\omega^2}\left\{A_\alpha+\left[A_\alpha\left(\frac{\omega+\epsilon_\alpha\omega_{c\alpha}}{k\theta_{\|\alpha}}\right)+\frac{\omega}{k\theta_{\|\alpha}}\right]\right.\\ &\left.\times\frac{(\kappa_\alpha-1)^{3/2}}{\kappa_\alpha^{1/2}(\kappa_\alpha-3/2)}\,Z_{\kappa_\alpha-1}\left[\left(\frac{\kappa_\alpha-1}{\kappa_\alpha}\right)^{1/2}\frac{\omega+\epsilon_\alpha\omega_{c\alpha}}{k\theta_{\|\alpha}}\right]\right\},\end{aligned} \tag{5.6}$$

where ω is the complex wave frequency defined by $\omega = \omega_r + i\gamma$, the variable α identifies the different plasma species and the sign of the particle charge is given by $\epsilon_\alpha = q_\alpha/|q_\alpha|$. The plasma frequency of species α and the cyclotron frequency of the particles of species α are given, respectively, by

$$\omega_{p\alpha} = \left(\frac{n_{\alpha 0}q_\alpha^2}{\epsilon_0 m_\alpha}\right)^{1/2}, \qquad \text{and} \qquad \omega_{c\alpha} = \frac{|q_\alpha|B_0}{m_\alpha}.$$

The parameter A_α in Equation (5.6) defines the temperature anisotropy of each species, and is given by

$$A_\alpha = \frac{\theta_{\perp\alpha}^2}{\theta_{\|\alpha}^2} - 1 = \frac{T_{\perp\alpha}}{T_{\|\alpha}} - 1.$$

The symbol Z_κ in the dispersion relation, Equation (5.6), denotes the plasma dispersion function first introduced by Summers and Thorne (1991) (valid only for integer kappa values) and generalised by Mace and Hellberg (1995) (valid for arbitrary real kappa values). Hellberg and Mace (2002) later introduced the plasma dispersion function $Z_{\kappa M}$ for a plasma with a velocity distribution modelled by a 1D kappa distribution along a preferred direction in space and a 2D Maxwellian distribution in the plane perpendicular to that direction (Hellberg and Mace, 2002). Mace and Hellberg (2009) showed that $Z_{\kappa M}$ had wider applicability than first envisaged. They showed that it was equally applicable to wave studies that involve ordinary κ distributions. To eliminate any connotation with the Maxwellian, they introduced an analogous U_κ function, where the function U_κ is given by (Mace and Hellberg, 2009)

$$U_\kappa(\zeta) = i\frac{(\kappa-1/2)}{\kappa^{3/2}}{}_2F_1\left[1, 2\kappa; \kappa+1; \frac{1}{2}\left(1-\frac{\zeta}{i\kappa^{1/2}}\right)\right]. \tag{5.7}$$

The use of the dispersion function U_κ instead of Z_κ frequently produces simpler dispersion relations, and Mace and Sydora (2010) were able to provide a simplified version of the dispersion relation in Equation (5.6), given by

$$\frac{k^2c^2}{\omega^2} = 1 + \sum_\alpha \frac{\omega_{p\alpha}^2}{\omega^2}\left\{A_\alpha + \left[A_\alpha\left(\frac{\omega+\epsilon_\alpha\omega_{c\alpha}}{k\theta_{\|\alpha}}\right) + \frac{\omega}{k\theta_{\|\alpha}}\right]U_{\kappa\alpha}\left(\frac{\omega+\epsilon_\alpha\omega_{c\alpha}}{k\theta_{\|\alpha}}\right)\right\}. \tag{5.8}$$

Looking for waves where ω and k satisfy

$$\left|\frac{\omega+\epsilon_\alpha\omega_{c\alpha}}{k\theta_{\|\alpha}}\right| \gg 1,$$

we can employ the asymptotic form for U_κ (Mace and Hellberg, 2009)

$$U_\kappa(\zeta) = \pi^{1/2}\frac{\Gamma(\kappa)}{\kappa^{1/2}\Gamma(\kappa-1/2)}\left(1+\frac{\zeta^2}{\kappa}\right)^{-\kappa}(i - \tan\kappa\pi) - \frac{1}{\zeta} - \frac{1}{2}\left(\frac{\kappa}{\kappa-3/2}\right)\frac{1}{\zeta^3} + ..., \tag{5.9}$$

to simplify Equation (5.8). This yields the simplified, approximate dispersion relation for an electron-ion plasma [see Mace and Sydora (2010) for further details]

$$\begin{aligned}\frac{k^2c^2}{\omega^2} =& 1 - \frac{\omega_{pe}^2}{\omega(\omega-\omega_{ce})} - \frac{\omega_{pi}^2}{\omega(\omega+\omega_{ci})} + i\pi^{1/2}\frac{\Gamma(\kappa_e)}{\kappa_e^{1/2}\Gamma(\kappa_e-1/2)}\frac{\omega_{pe}^2}{\omega^2} \\ &\times\left[A_e\left(\frac{\omega-\omega_{ce}}{k\theta_{\|e}}\right)+\frac{\omega}{k\theta_{\|e}}\right]\left[1+\frac{1}{\kappa_e}\left(\frac{\omega-\omega_{ce}}{k\theta_{\|e}}\right)^2\right]^{-\kappa_e}.\end{aligned} \tag{5.10}$$

The real part of ω can be obtained from Equation (5.10) by writing $\omega = \omega_r + i\gamma$, taking the Taylor expansion of the equation about some real frequency $\omega = \omega_r$ and ignoring terms $O(\gamma^2)$ and higher, yielding the relation [see Mace and Sydora (2010)]

$$\frac{k^2c^2}{\omega_r^2} = 1 - \frac{\omega_{pe}^2}{\omega_r(\omega_r-\omega_{ce})} - \frac{\omega_{pi}^2}{\omega_r(\omega_r+\omega_{ci})}. \tag{5.11}$$

The damping/ growth rate is given by

$$\frac{\gamma}{\omega_r} = -\pi^{1/2}\frac{\Gamma(\kappa_e)}{\Gamma(\kappa_e - 1/2)}\frac{\omega_{pe}^2}{\omega_r^2}\frac{1}{R(\omega_r)}\left[A_e\left(\frac{\omega_r - \omega_{ce}}{k\theta_{\|e}}\right) + \frac{\omega_r}{k\theta_{\|e}}\right]\left[1 + \frac{1}{\kappa_e}\left(\frac{\omega_r - \omega_{ce}}{k\theta_{\|e}}\right)^2\right]^{-\kappa_e}, \tag{5.12}$$

where the function $R(\omega_r)$ in Equation (5.12) is [see Mace (1998) and Mace and Sydora (2010)]

$$R(\omega_r) = 2 + \frac{\omega_{pe}^2\omega_{ce}}{\omega_r(\omega_r - \omega_{ce})^2} - \frac{\omega_{pi}^2\omega_{ci}}{\omega_r(\omega_r + \omega_{ci})^2}. \tag{5.13}$$

Equation (5.11) is identical to the dispersion relation obtained for a Maxwellian distribution, which shows that superthermal particle effects do not appear at this level of approximation.

As seen from Equation (5.12), for wave growth, i.e., $\gamma > 0$, the following has to be satisfied (Mace and Sydora, 2010)

$$A_e(\omega_r - \omega_{ce}) + \omega_r < 0, \qquad \text{or} \qquad A_e > \frac{\omega_r}{\omega_{ce} - \omega_r}. \tag{5.14}$$

Equation (5.14) implies that for fixed $A_e > 0$, i.e., the condition for whistler instability, there is an upper limit to the interval of growing whistler wave frequencies ω_r, namely

$$\omega_r < \frac{A_e}{A_e + 1}\omega_{ce}. \tag{5.15}$$

5.3 PIC simulations

5.3.1 Simulation parameters

In this section we perform 2D3V electromagnetic particle-in-cell (PIC) simulations of plasmas composed of an electron and singly charged ion species. The simulated plasma is immersed in a uniform, static magnetic field $\boldsymbol{B}_0$ which is directed along the $x-$axis. To guarantee the

whistler instability in our simulations, we impose temperature anisotropy for the electron population with $T_{\perp e} > T_{\parallel e}$, where $T_{\perp e}$ and $T_{\parallel e}$ are the components of electron thermal energy perpendicular and parallel to $\boldsymbol{B}_0$.

Five simulations are run to investigate the whistler instability. In simulation Runs 1 and 2, an electron temperature anisotropy of $T_{\perp e}/T_{\parallel e} = 2.05$ is used. For Run 1, the electron species is modelled by the bi-kappa velocity distribution, Equation (5.2), with $\kappa_e = 3$, while ions are modelled by an isotropic kappa distribution with $\kappa_i = 5$. In Run 2, the electrons are modelled by the bi-Maxwellian velocity distribution, Equation (5.5), with the ions being modelled by an isotropic Maxwellian distribution. We discuss and compare the results from each of these simulations.

For the remaining three simulations, Runs 3 to 5, we impose an electron temperature anisotropy of $T_{\perp e}/T_{\parallel e} = 3.0$. In Runs 3 and 4, we model the electron species by bi-kappa velocity distributions with $\kappa_e = 2$ and $\kappa_e = 3$, respectively, with the ions being modelled by an isotropic kappa distribution with $\kappa_i = 5$ in both of these simulations. In Run 5, the electrons are modelled by a bi-Maxwellian velocity distribution and the ions are modelled by an isotropic Maxwellian velocity distribution. Results from each simulation are compared to linear theory and the effects of the kappa distribution on the whistler instability are discussed. Table 5.1 provides an overview of the above mentioned simulations.

The plasma ions are known to play a negligible role in the generation of the whistler instability due to their lower mobility (Omura, 2007; Mace and Sydora, 2010; Hughes et al., 2016). However, the dynamics of the ions are important to balance the electromagnetic and material stresses in the non-linear whistler wave, hence they are included in our simulations (Dubinin et al., 2003; Mace and Sydora, 2010). The value $\kappa_i = 5$ chosen for the ion species in the plasmas modelled by kappa velocity distributions is indicative of ion velocity distributions in various space plasma regions (Christon et al., 1988, 1989). We employ a cool ion species with a temperature corresponding to $T_{\parallel e}/T_i = 100$, irrespective of whether a kappa or Maxwellian model is used. An ion-electron mass ratio of $m_i/m_e = 100$ is used in all simulations, allowing the dynamics of both plasma species to be resolved within the simulation run. A summary of the plasma species parameters is provided in Table 5.2.

In our simulations, we express all parameters with respect to those from the electron species. As stated above, anisotropic electron populations are used in all simulations of the whistler instability, with $T_{\perp e} > T_{\parallel e}$. Hence, we express the velocities in our simulations as $\boldsymbol{v}' = \boldsymbol{v}/v_{\parallel th,e}$, where the primed variable denotes the simulation parameter and the unprimed

Simulation overview			
	$T_{\perp e}/T_{\parallel e}$	Electron velocity distribution	Ion velocity distribution
Run 1	2.05	bi-kappa ($\kappa_e = 3$)	bi-kappa ($\kappa_i = 5$)
Run 2	2.05	bi-Maxwellian	bi-Maxwellian
Run 3	3.0	bi-kappa ($\kappa_e = 2$)	bi-kappa ($\kappa_i = 5$)
Run 4	3.0	bi-kappa ($\kappa_e = 3$)	bi-kappa ($\kappa_i = 5$)
Run 5	3.0	bi-Maxwellian	bi-Maxwellian

Table 5.1: An overview of the 2D3V electromagnetic PIC simulations performed for the electron temperature anisotropy driven whistler instability. Runs 1 and 2 model the electron species with a temperature anisotropy of $T_{\perp e}/T_{\parallel e} = 2.05$. Runs 3 to 5 model the electron species with a higher temperature anisotropy of $T_{\perp e}/T_{\parallel e} = 3.0$.

variable denotes an ordinary S.I. value, i.e., $v_{\parallel th,e} = (T_{\parallel e}/m_e)^{1/2}$. Similarly, length scales are given by $x^{'} = x/\lambda_{\parallel De}$, where $\lambda_{\parallel De} = v_{\parallel th,e}/\omega_{pe}$, and time scales are give by $t^{'} = \omega_{pe}t$. We employ a time step defined by $\omega_{pe}\Delta t = 0.05$ and a square simulation domain of size $L_x = L_y = 512\lambda_{\parallel De}$, with square cells of size $\Delta x = \Delta y = \lambda_{\parallel De}$. Periodic boundary conditions are used for fields and particles, and all simulations are initialised with 256 particles per cell, per species. In Table 5.3, we provide an overview of the parameters used in each simulation.

The strength of the background magnetic field $\boldsymbol{B}_0$ used in our simulations produces an electron cyclotron frequency given by $\omega_{ce}/\omega_{pe} = 0.447$. The ratio of electron thermal velocity to the speed of light was set to $v_{\parallel th,e}/c = 0.1$. This value of $v_{\parallel th,e}/c$ is known to accurately model the plasma response of a cooler plasma while placing tolerable restrictions on the simulation time steps and cell sizes (Hughes et al., 2016), which are required to satisfy the CFL condition. With ω_{ce}/ω_{pe} and $v_{\parallel th,e}/c$ chosen as above, the parallel electron beta becomes $\beta_{\parallel e} = 2(\omega_{pe}^2/\omega_{ce}^2)/(c^2/v_{\parallel th,e}^2) = 0.1$. The effect of the low pass Fourier space filter discussed in Section 2.8.1 and applied to the current densities in each simulation, was to retain only wave numbers up to $|k|c/\omega_{pe} \leq 15$.

Electron species	**Ion species**
67,108,864 particles	67,108,864 particles
$\omega_{pe} = 1.0$	$\omega_{pi}/\omega_{pe} = 0.1$
$\omega_{ce}/\omega_{pe} = 0.447$	$\omega_{ci}/\omega_{pe} = 0.00447$
$q/m_e = -1.0$	$q/m_i = 0.01$
$v_{th,e} = 1.0$	$v_{th,i}/v_{th,e} = 0.1$

Table 5.2: Plasma species parameters used in each simulation of the electron temperature anisotropy driven whistler instability.

Simulation parameters	
Domain size	$L_x = 512\lambda_{\parallel De}$, $L_y = 512\lambda_{\parallel De}$
Cell size	$\Delta x = \lambda_{\parallel De}$, $\Delta y = \lambda_{\parallel De}$
Time step	$\omega_{pe}\Delta t = 0.05$
Runs 1 and **2** : time steps	100, 000
Runs 3 to **5** : time steps	40, 000

Table 5.3: A list of parameters common to all 2D3V electromagnetic PIC simulations of the whistler instability driven by electron temperature anisotropy.

5.4 Simulation results for $T_{\perp e}/T_{\parallel e} = 2.05$

We provide in this section, results from simulation Runs 1 and 2 of the whistler instability, i.e., those which drive the instability by an electron temperature anisotropy of $T_{\perp e}/T_{\parallel e} = 2.05$ (see Table 5.1). To obtain the linear dispersion relation for whistler waves, we numerically solve Equation (5.8) without approximation, using the software package MATHEMATICA. Equation (5.8) was solved for electron kappa values $\kappa_e = 1.6, 2.0, 3.0, 4.0$ and 30 (Maxwellian case). While Equation (5.8) is valid for plasmas modelled by kappa velocity distributions, we obtain results for a plasma modelled by a Maxwellian velocity distribution by using a high value of kappa, $\kappa_e = 30$, which represents the Maxwellian plasma in Figures 5.1 and 5.2. We used Figures 5.1 and 5.2 as a guide for choosing parameters for the simulations performed in this section.

The linear dispersion relations and companion instability growth rates are displayed in Figures 5.1 and 5.2. The whistler instability is known to depend strongly on electron tempera-

ture anisotropy $T_{\perp e}/T_{\parallel e}$, electron spectral index κ_e and electron parallel beta $\beta_{\parallel e}$ (Mace and Sydora, 2010). For the parameters used in simulation Runs 1 and 2, Figure 5.1 indicates that varying the superthermal electron tail, i.e., varying κ_e, influences the whistler dispersion relations only at wave numbers $k_\parallel c/\omega_{pe} \geq 1.05$. The wave number $k_\parallel c/\omega_{pe} = 1.05$ indicates the point at which electron thermal effects vanish [see discussion in Mace and Sydora (2010)], and as seen in Figure 5.2, it also marks the location where the growth rate vanishes for all whistlers waves, regardless of spectral index.

For our chosen value of parallel electron beta, $\beta_{\parallel e} = 0.1$, and temperature anisotropy, $T_{\perp e}/T_{\parallel e} = 2.05$, Figure 5.2 predicts that the instability growth rate maximises for $\kappa_e = 3$ (see cyan curve of Figure 5.2). Increasing electron kappa from $\kappa_e = 1.6$ to $\kappa_e = 3$, i.e, decreasing the electron tail hardness, results in increasing peak growth rates. Increasing electron kappa further, i.e., $\kappa_e > 3$, results in decreasing peak growth rates. Figure 5.2 also predicts that increasing κ_e results in a decrease in the window of unstable wave numbers. In other words, the harder the electron tail, the greater the instability bandwidth, where the cases of $\kappa_e = 1.6$ (black curve) and $\kappa_e = 2$ (blue curve) have the largest instability bandwidths. This result will be important to the analysis of the fluctuating field spectrum shown later in Figures 5.5 and 5.6.

The reason for the increase in the instability bandwidth for low kappa values can be seen by analysing the linear dispersion relations given in Figure 5.1. As the wave number decreases ($k_\parallel c/\omega_{pe} \to 0$), the frequency ω/ω_{ce} of the whistler waves also decrease. Hence, at smaller wave numbers, the resonance condition given in Equation (5.1) requires a larger Doppler shift, $\omega^{'} = \omega - \boldsymbol{k}_\parallel \cdot \boldsymbol{v}_{\parallel \mathrm{res}} = |\omega_{ce}|$, of the whistler wave frequency up to the electron cyclotron frequency. This necessitates a larger particle resonant velocity $\boldsymbol{v}_{\parallel res}$. Since the kappa distribution models an abundance of higher energy particles compared to the Maxwellian distribution, for the kappa cases, there are many more electrons with high velocities which meet the required $\boldsymbol{v}_{\parallel res}$. Wave-particle resonance is, therefore, achieved at lower wave numbers where whistler waves are now excited.

In the first of two simulations performed and reported on in this section, we chose a value for the electron spectral index κ_e corresponding to the peak maximum growth rate, i.e., $\kappa_e = 3$. For $\kappa_e = 3$, Figure 5.2 predicts a peak growth rate of $\gamma/\omega_{ce} = 0.0076$ at the wave number $k_\parallel c/\omega_{pe} = 0.88$, and a window of wave growth for the range of wave numbers $0.25 \leq k_\parallel c/\omega_{pe} \leq 1.05$. A second simulation was run, which modelled the electrons with a bi-Maxwellian distribution, and results from the two simulations were compared. For the Maxwellian case, Figure 5.2 predicts a peak growth rate of $\gamma/\omega_{ce} = 0.0068$ at wave number

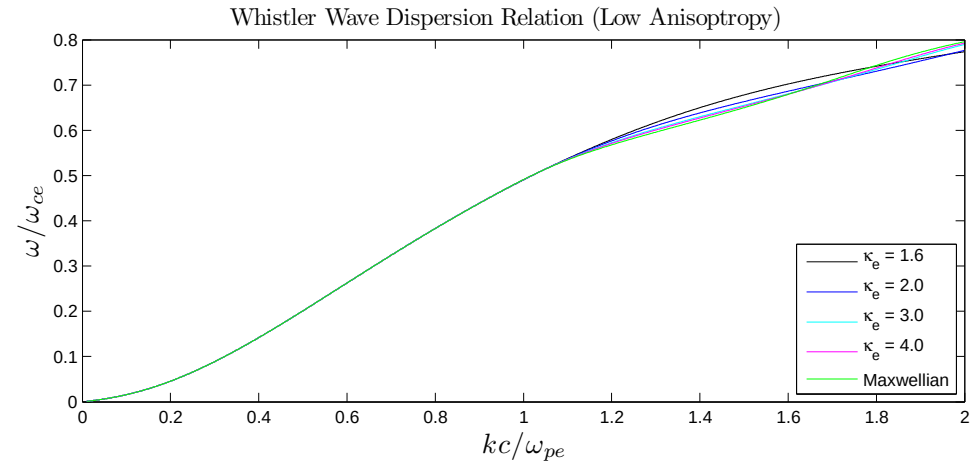

Figure 5.1: The theoretical dispersion relations for the plasmas with $T_{\perp e}/T_{\parallel e} = 2.05$, given for the sequence of electron kappa values $\kappa_e = 1.6, 2.0, 3.0, 4.0$ and 30 (corresponding to the Maxwellian case).

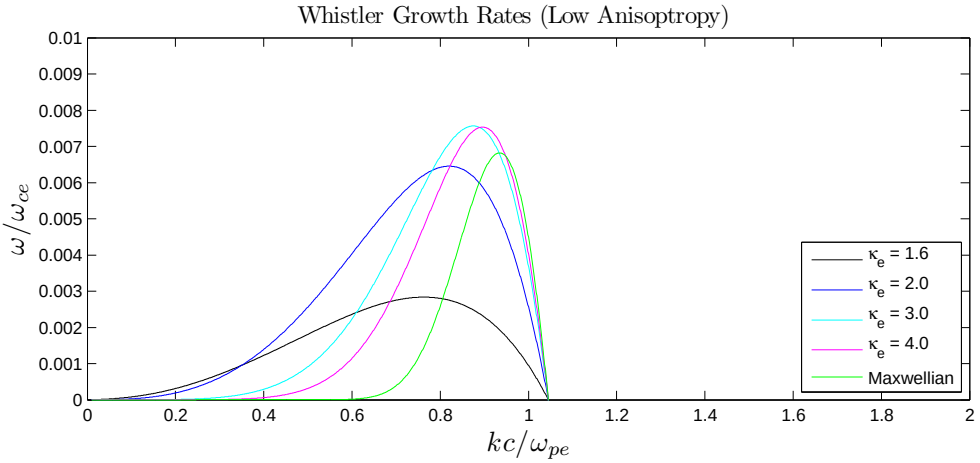

Figure 5.2: The theoretical growth rates for the plasmas with $T_{\perp e}/T_{\parallel e} = 2.05$, given for the sequence of electron kappa values $\kappa_e = 1.6, 2.0, 3.0, 4.0$ and 30 (corresponding to the Maxwellian case).

$k_\parallel c/\omega_{pe} = 0.94$, with a range of unstable wave numbers given by $0.6 \leq k_\parallel c/\omega_{pe} \leq 1.05$.

The temporal evolution of energies in the $\kappa_e = 3$ and Maxwellian simulations are displayed in Figures 5.3 and 5.4, respectively. In each figure, we illustrate the temporal evolution of (a) the fluctuating electric field energy $U_{\delta E} = 1/2\epsilon_0(\delta \boldsymbol{E})^2$, where $\boldsymbol{E} = \delta \boldsymbol{E}$, (b) the fluctuating magnetic field energy $U_{\delta B} = 1/(2\mu_0)(\delta \boldsymbol{B})^2$, where $\boldsymbol{B} = \boldsymbol{B}_0 + \delta \boldsymbol{B}$, (c) the kinetic energy of the electron species $E_e = 1/2m_e|\boldsymbol{v}|^2$, (d) the kinetic energy of the ion species $E_i = 1/2m_i|\boldsymbol{v}|^2$, (e) the sum of the particle and field energies described above E_{total} and (f) displays the percentage deviation of the total energy from its initial value, i.e., $[(E_{\text{total}}(t) - E_{\text{total}}(t = 0))/E_{\text{total}}(t = 0)] \times 100$. To aid in the comparison of the energies in each simulation, all panels in Figures 5.3 and 5.4 are displayed with a y-axis range of $\Delta(E/T_{\parallel e}) = 250$.

The electron temperature anisotropy, $T_{\perp e}/T_{\parallel e} = 2.05$, used in each simulation for Runs 1 and 2 discussed here, produces low instability growth rates, $\gamma/\omega_{ce} \leq 0.0076$, as was seen in Figure 5.2. Consequently, the full evolution of the whistler instability, characterised by exponential wave growth and eventual non-linear wave saturation leading to plasma quasi-equilibrium, is not resolved for either case. In both simulations, the free energy provided by the electron temperature anisotropy resulted in an increase in the fluctuating electric and magnetic field energies, displayed in panels (a) and (b) of Figures 5.3 and 5.4, respectively, indicating wave growth. However, longer simulations are required to observe the full growth of the unstable waves, out of the background thermal fluctuations and noise in the simulated plasma. Nevertheless, important physical observations can still be made from the simulation results for the effect the superthermal tail has on the behaviour of the whistler instability, driven by the temperature anisotropy $T_{\perp e}/T_{\parallel e} = 2.05$.

For the $\kappa_e = 3$ case displayed in Figure 5.3, the electric field energy grows to the value $U_{\delta E}/T_{\parallel e} \approx 59$ by the end of the simulation run, as seen in panel (a). The magnetic field energy displayed in panel (b), on the other hand, grows to $U_{\delta B}/T_{\parallel e} \approx 70$ within the same time frame, indicating that the whistler instability favours the growth of the magnetic field over the electric field. Since the electron species provides the necessary free energy for wave growth, panel (c) of Figure 5.3 displays a decrease in the electron kinetic energy. By taking the difference between the initial and final energies, the electrons in the $\kappa_e = 3$ simulation are observed to lose the energy $\Delta(E_e/T_{\parallel e}) \approx 210$. The ions in the $\kappa_e = 3$ simulation are observed in panel (d) to exhibit an overall increase in energy. The ions likely gain energy from the electron species through the non-linear interaction with growing waves in the plasma. This non-linear coupling between waves and particles is the mechanism by which free energy is redistributed in the plasma, enabling the system to reach a more stable state. As seen in

panel (d), the ion species gains the energy $\Delta(E_i/T_{\|e}) \approx 27$ over the simulation. While all simulations performed for this section were of a closed system, panel (e) of Figure 5.3 indicates that the total energy decreases by $\Delta(E_{total}/T_{\|e}) \approx 79$. This indicates a weakness in the simulation model; however, as seen in panel (f), the deviation is very small, i.e., only 0.013% from the initial value. This small change in total energy gives us a high degree of confidence in the validity of the simulation results.

Figure 5.4 illustrates the energies for the Maxwellian simulation. By comparing panels (a) and (b) of Figure 5.4 to those of Figure 5.3 for the $\kappa_e = 3$ case, the Maxwellian case is observed to exhibit smaller growth in electric and magnetic field (wave) energy. As seen in panels (a) and (b) in Figure 5.4, the electric field energy grows to $U_{\delta E}/T_{\|e} \approx 15$, while the magnetic field energy grows to $U_{\delta B}/T_{\|e} \approx 20$. This is consistent with linear theory, where Equation (5.8) predicted a smaller growth rate for the Maxwellian case (see Figure 5.2). Since whistler waves grow through the free energy provided by the electrons, the smaller growth in field energy observed for the Maxwellian case results in a smaller decrease in the energy of the electron species, compared to the $\kappa_e = 3$ case. Panel (c) of Figure 5.4 indicates that the electrons lose the energy $\Delta(E_e/T_{\|e}) \approx 80$. The ions are again observed to be heated during the simulation, gaining $\Delta(E_i/T_{\|e}) \approx 22$ through the resonant interaction with the waves. The total energy for the Maxwellian case, displayed in panels (e) and (f), is observed to change by an amount corresponding to $\Delta(E_{total}/T_{\|e}) \approx 32$, demonstrating energy conservation up to 0.006%. This small change in the total energy lends validity to our simulation algorithm and results.

For both the $\kappa_e = 3$ and Maxwellian simulations, we perform Fourier analysis of the fluctuating fields $\delta\boldsymbol{E}$ and $\delta\boldsymbol{B}$ in space and time. Analysis of the electromagnetic fluctuation spectrum (not shown here) indicated the presence of the other plasma modes observed in our investigation of the quiet plasma, discussed in Chapter 4, i.e, we observed Bernstein waves, *R*-, *L*-, *X*- and *O*-modes, as well as their oblique counterparts. However, due to the growth of unstable whistler waves, the dominant wave energy was observed to be confined to lower frequencies, $\omega/\omega_{ce} \leq 1$. We shall limit our discussion of the fluctuation spectra in this section to this low frequency range.

The electric and magnetic field energy diagrams displayed in panels (a) and (b) of Figure 5.3 for the $\kappa_e = 3$ simulation, and Figure 5.4 for the Maxwellian simulation, indicated that the magnetic field energy grows larger than the electric field energy during whistler wave growth. This will be shown to be especially true for the $T_{\perp e}/T_{\|e} = 3$ simulations discussed in Section 5.5. The magnetic field, therefore, provides a better representation

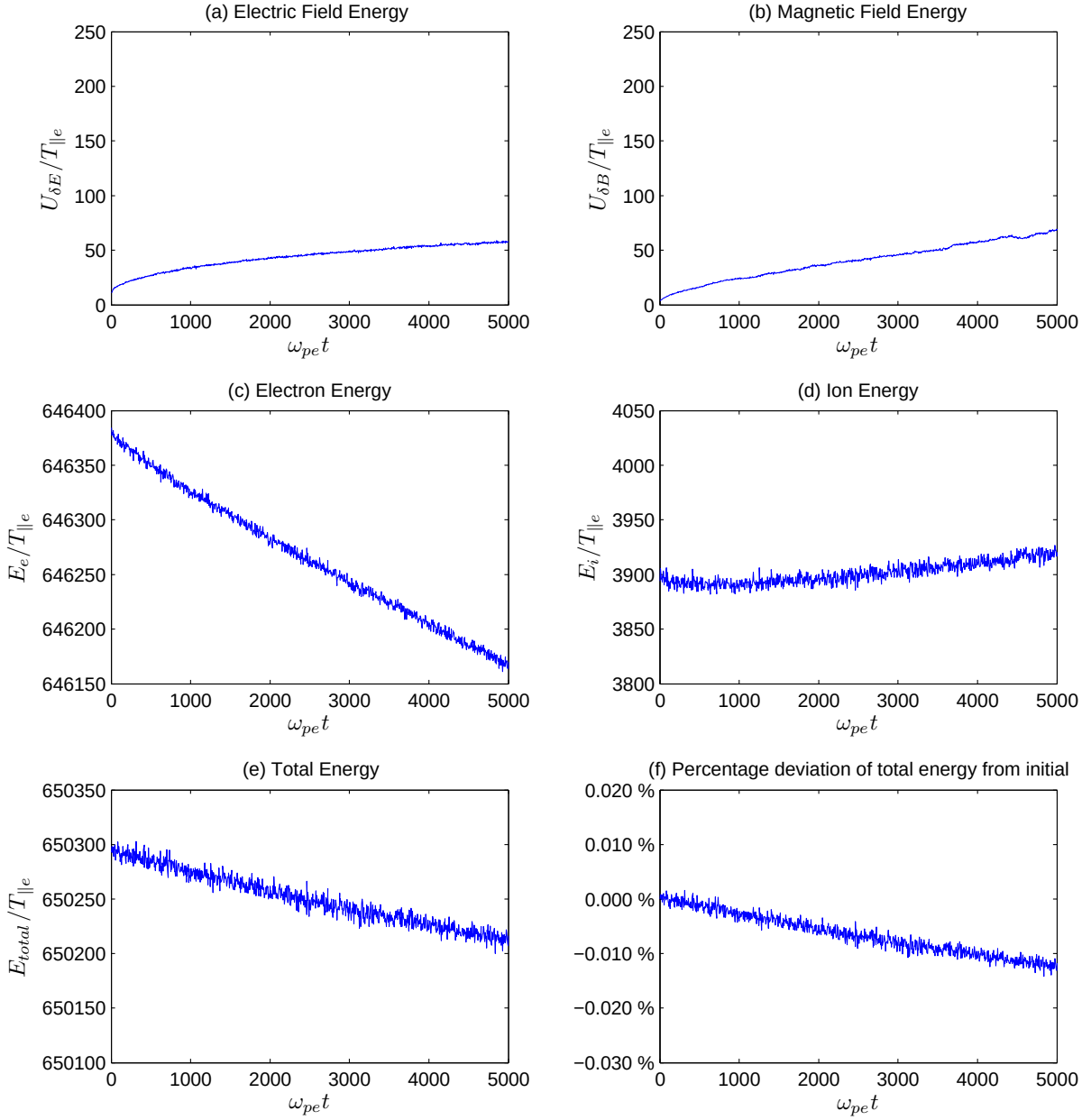

Figure 5.3: The temporal evolution of energies in the $\kappa_e = 3$ simulation, with $T_{\perp e}/T_{\|e} = 2.05$. Panel (a) gives the fluctuating electric field energy, panel (b) the fluctuating magnetic field energy, panel (c) the electron kinetic energy, panel (d) the ion kinetic energy, panel (e) the total energy in the simulation and panel (f) gives the percentage deviation of the total energy from its initial value. All energies are normalised to the parallel component of the electron initial thermal energy $T_{\|e}$.

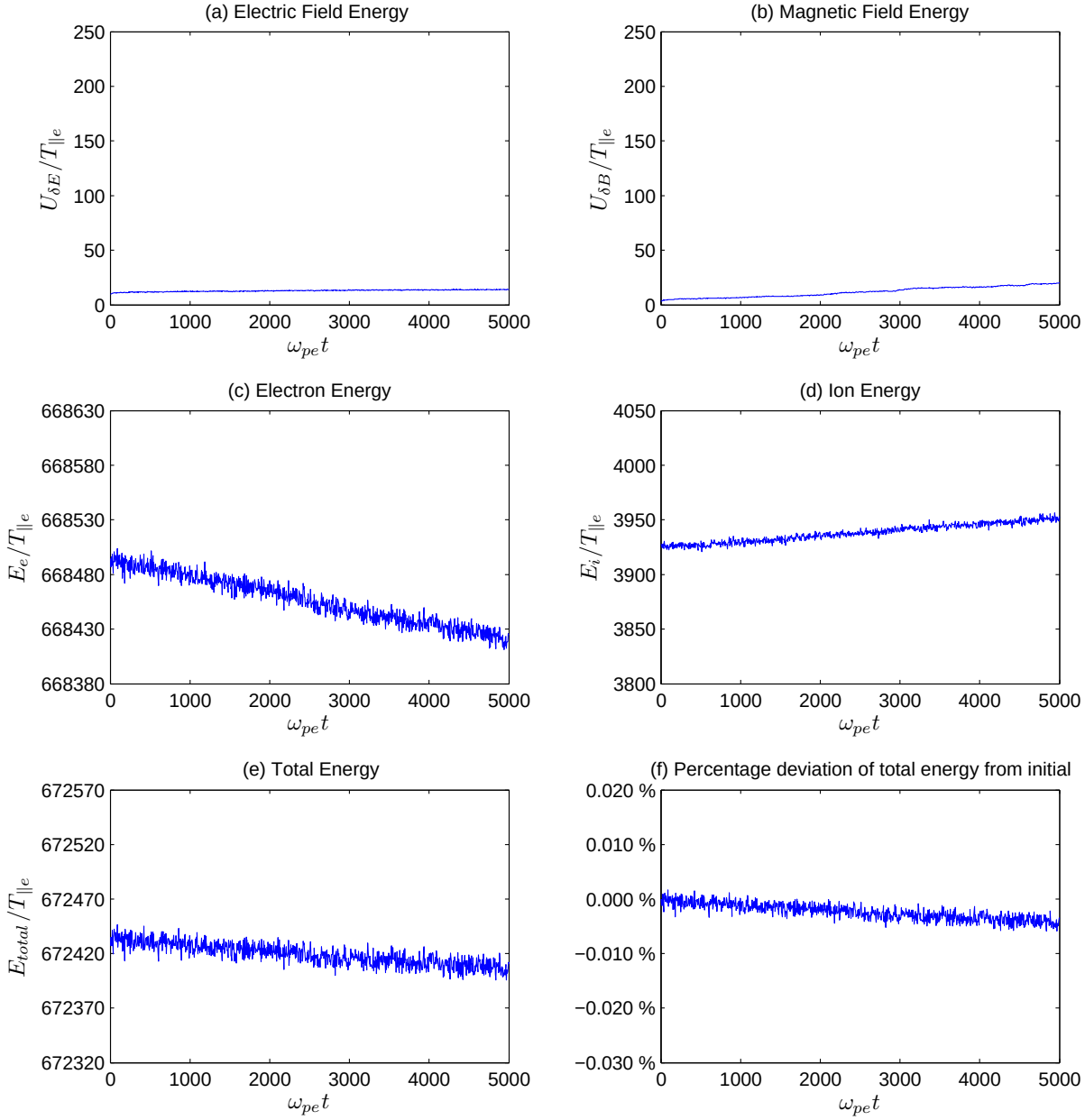

Figure 5.4: The temporal evolution of energies in the Maxwellian simulation, with $T_{\perp e}/T_{\|e} = 2.05$. Panel (a) gives the fluctuating electric field energy, panel (b) the fluctuating magnetic field energy, panel (c) the electron kinetic energy, panel (d) the ion kinetic energy, panel (e) the total energy in the simulation and panel (f) gives the percentage deviation of the total energy from its initial value. All energies are normalised to the parallel component of the electron initial thermal energy $T_{\|e}$.

for the growth of whistler waves. In Figures 5.5 and 5.6 we illustrate the magnetic field intensity spectra $(\delta B)^2/(\omega_{pe}^2 m_e^2/q_e^2)$ as a function of ω/ω_{ce} and $|k|c/\omega_{pe}$, for the $\kappa_e = 3$ and Maxwellian cases, respectively. The fluctuation spectra of Figures 5.5 and 5.6 are displayed for a selection of wave propagation angles, given with respect to $\boldsymbol{B}_0$, and represent a time range $4800 \leq \omega_{pe}t \leq 5000$, i.e., near the end of each simulation. In both figures, these angles are 0° in panel (a), 26.6° in panel (b), 45° in panel (c), 63.4° in panel (d) and 90° in panel (e).

In our discussion of Figures 5.5 and 5.6, we compare the linear dispersion relations for whistler waves to the regions of intense wave activity, i.e., the regions of white representing $(\delta B)^2/(\omega_{pe}^2 m_e^2/q_e^2) \geq 10^{10.5}$, yellow representing $10^{9.5} \leq (\delta B)^2/(\omega_{pe}^2 m_e^2/q_e^2) \leq 10^{10.5}$, orange representing $10^{8.5} \leq (\delta B)^2/(\omega_{pe}^2 m_e^2/q_e^2) \leq 10^{9.5}$ and red representing $10^{6.5} \leq (\delta B)^2/(\omega_{pe}^2 m_e^2/q_e^2) \leq 10^{8.5}$. The dispersion relations are over-plotted as a dashed line in each figure. For parallel propagation, displayed in panel (a) of each figure, we compare the regions of high wave intensity to the linear dispersion relation for whistlers in plasmas having kappa velocity distributions, obtained by numerically solving Equation (5.8) using MATHEMATICA. At oblique angles, displayed in panels (b) to (d) of each figure, we compare the regions of high wave intensity to the cold plasma whistler wave dispersion relation (Bellan, 2013),

$$\frac{c^2k^2}{\omega^2} = 1 - \frac{\omega_{pe}^2/\omega^2}{1 - \dfrac{|\omega_{ce}|}{\omega}\cos\,\phi}, \tag{5.16}$$

where ϕ is the angle of propagation with respect to $\boldsymbol{B}_0$. The cold plasma whistler wave dispersion relation, Equation (5.16), for the angles 26.6°, 45° and 63.4° are plotted as the dashed lines in panels (b) to (d) of Figures 5.5 and 5.6. It should be emphasised that there is presently no adequate theory of oblique wave propagation in plasmas with kappa distributions. Hence, we use Equation (5.16) as a rough guide.

For the $\kappa_e = 3$ case displayed in Figure 5.5, the regions of high wave intensity, i.e., red, orange and yellow colouring, are observed to follow closely the linear dispersion relations in each panel, regardless of propagation angle. This agreement between the linear dispersion relations, displayed as the dashed lines, and the regions of high intensity fluctuations confirms that the enhanced field fluctuations are as a result of whistler wave growth. In panel (a) of Figure 5.5, we observe a broad region of enhanced wave activity, depicted by the red colouring, for the wave number range $0.6 \leq k_\parallel c/\omega_{pe} \leq 0.95$, extending over the full range of frequencies in the figure. This large band of high fluctuation intensity is also observed for the

Maxwellian case; however, we defer discussion of the Maxwellian results to later. While the precise generation mechanism for this band of high magnetic field fluctuations is unknown at present, we note that a very similar high intensity band was seen in the PIC simulations of the whistler instability undertaken by Hughes et al. (2016). In addition to this, the simulations of Hughes et al. (2016) illustrated an area of high intensity field fluctuations at very low wave numbers and frequencies, and this is also observed here in panel (a) at $k_{\parallel}c/\omega_{pe} \leq 0.1$ and $\omega/\omega_{ce} \leq 0.05$.

A comparison of panels (a) to (e) of Figure 5.5 reveals that the parallel propagating whistler wave [panel (a)] is most intense, in agreement with linear theory (Gary et al., 2011). This follows from the fact that broad regions of brighter orange and yellow colouring, representing intensities $(\delta B)^2/(\omega_{pe}^2 m_e^2/q_e^2) \geq 10^{8.5}$, are only observed for parallel wave propagation shown in panel (a). The most intense field fluctuation for the parallel whistler wave observed in panel (a) had $(\delta B)^2/(\omega_{pe}^2 m_e^2/q_e^2) \approx 10^{10.8}$, which occurred at the wave number $k_{\parallel}c/\omega_{pe} \approx 0.84$. This location of maximum wave intensity observed in panel (a) should be compared to the wave number predicted by Figure 5.2 to have peak growth rate for $\kappa_e = 3$, which was $k_{\parallel}c/\omega_{pe} = 0.88$. Figure 5.2 also predicted a range of unstable wave numbers $0.25 \leq k_{\parallel}c/\omega_{pe} \leq 1.05$ for $\kappa_e = 3$. In panel (a) of Figure 5.5, high wave intensity (yellow colouring) is observed for the wave number range $0.46 \leq k_{\parallel}c/\omega_{pe} \leq 0.98$, which is within the limits of this prediction. However, enhanced wave activity, seen as the red colouring, is observed over the full range of wave numbers shown in the figure. Equation (5.15) predicts that wave growth in the linear regime should be confined to frequencies $\omega_r \leq 0.51$, for the electron temperature anisotropy used in our simulations. This theoretical maximum frequency is plotted as the horizontal solid line in panel (a) of Figure 5.5. We observe that the highest wave intensities (yellow colouring) in panel (a) lie below this line, in agreement with Equation (5.15). Enhanced fluctuation intensities (red colouring) is observed above this line, due to non-linear wave effects. A broad region of diffuse field fluctuations is observed in panel (a) for high wave numbers, $k_{\parallel}c/\omega_{pe} \geq 1.0$, at frequencies $0.2 \leq \omega/\omega_{ce} \leq 1.2$. Figure 5.2 predicted vanishing growth rate for wave numbers $k_{\parallel}c/\omega_{pe} \geq 1.05$.

For oblique propagation, where kappa theory is lacking, the wave intensity spectra for the $\kappa_e = 3$ case are displayed in panels (b) to (d) of Figure 5.5. It should be noted that the resolution of panels (b) and (d) is lower than panels (a), (c) and (e). As discussed in Chapter 4 for Figure 4.6, this reduced resolution is due to the plotting routine using fewer data points to generate the spectra in panels (b) and (d). At oblique angles, the areas of enhanced wave activity, i.e., red colouring having $10^{6.5} \leq (\delta B)^2/(\omega_{pe}^2 m_e^2/q_e^2) \leq 10^{8.5}$, are observed to occur near frequencies and wave numbers satisfying the cold plasma dispersion relation, plotted

as the dashed lines. However, as seen in panels (b) to (d), the agreement between the cold plasma dispersion relation, Equation (5.16), and the regions of enhanced wave activity is not perfect. Enhanced wave activity (red colouring) at oblique angles, occurs over the full range of wave numbers displayed in each figure, shifting to lower frequencies with increasing angle to the magnetic field, in accordance with the linear dispersion relation. The maximum field fluctuation intensities at oblique propagation angles are observed to decrease with increasing angle to the magnetic field. At 26.6° in Figure 5.5, the maximum observed fluctuation intensity had $(\delta B)^2/(\omega_{pe}^2 m_e^2/q_e^2) \approx 10^{7.5}$, which decreased to $(\delta B)^2/(\omega_{pe}^2 m_e^2/q_e^2) \approx 10^{7.3}$ at 45°, and $(\delta B)^2/(\omega_{pe}^2 m_e^2/q_e^2) \approx 10^{7.0}$ at 63.4°. For perpendicular wave propagation displayed panel (f), the whistler mode does not exist, and wave activity here is due to other perpendicularly propagating electromagnetic modes, i.e., the electron and ion Bernstein modes discussed in Chapter 4.

Figure 5.6 displays the field fluctuation spectra for the Maxwellian simulation, where on comparison with Figure 5.5, qualitatively similar wave behaviour is observed, as expected (Mace and Sydora, 2010). We shall highlight differences in the behaviour of the plasma due to modelling the electrons by a bi-Maxwellian velocity distribution. In each panel of Figure 5.6, the regions of high wave activity, displayed as the red, orange and yellow colouring, follow closely the linear dispersion relations (dashed lines) of Equation (5.8) for parallel propagation, and Equation (5.16) for oblique propagation. As seen previously, panel (a) of Figure 5.6 also displays a band of enhanced wave activity occurring for the full range of frequencies shown; however, this occurs for a narrower range of wave numbers, i.e., $0.74 \leq k_\parallel c/\omega_{pe} \leq 0.98$, compared to the $\kappa_e = 3$ case. Figure 5.2 predicted a larger peak growth rate for the $\kappa_e = 3$ case compared to the Maxwellian, which was later confirmed by the electric and magnetic field energy diagrams displayed in panels (a) and (b) of Figures 5.3 and 5.4. As a result, the maximum fluctuation intensity in the Maxwellian simulation had $(\delta B)^2/(\omega_{pe}^2 m_e^2/q_e^2) \approx 10^{10.4}$, which is lower than the $\kappa_e = 3$ case, as expected. The maximum fluctuation intensity for the Maxwellian case occurred at the wave number $k_\parallel c/\omega_{pe} \approx 0.88$, which is consistent with the prediction of linear theory for the wave number of peak growth rate, i.e., $k_\parallel c/\omega_{pe} = 0.95$ (seen in Figure 5.2). The region of highest wave intensity in panel (a), i.e., the yellow colouring, is observed for the narrower range of wave numbers, $0.8 \leq k_\parallel c/\omega_{pe} \leq 0.91$, than seen previously for the $\kappa_e = 3$ case. This region, however, is still observed to lie within the limit predicted by Figure 5.2 for the range of unstable wave numbers in the Maxwellian case, i.e., $0.6 \leq k_\parallel c/\omega_{pe} \leq 1.05$. The horizontal line in panel (a) is the maximum frequency predicted by Equation (5.15) for wave growth in the linear regime, where we observe the most intense field fluctuations (yellow colouring) below this line, consistent with linear theory.

In panels (b) to (d) of Figure 5.6 for the Maxwellian case, the regions of enhanced wave activity are again observed near the cold plasma dispersion relation, Equation (5.16), displayed as the dashed lines. The maximum intensities of the field fluctuations at oblique angles are again observed to decrease with increasing angle to $\boldsymbol{B}_0$, as they did for the $\kappa_e = 3$ case. The maximum fluctuation intensities had $(\delta B)^2/(\omega_{pe}^2 m_e^2/q_e^2) \approx 10^{7.3}$ in panel (b), $(\delta B)^2/(\omega_{pe}^2 m_e^2/q_e^2) \approx 10^{7.1}$ in panel (c) and $(\delta B)^2/(\omega_{pe}^2 m_e^2/q_e^2) \approx 10^{6.8}$ in panel (d).

5.5 Simulation results for $T_{\perp e}/T_{\parallel e} = 3$

In this section we discuss results from the simulation Runs 3 to 5 of Table 5.1, i.e, we present results from simulations of the whistler instability driven by the electron temperature anisotropy $T_{\perp e}/T_{\parallel e} = 3$. All other simulation parameters used here are the same as those used in Section 5.4, and are given in Tables 5.2 and 5.3 . Using this new value of $T_{\perp e}/T_{\parallel e} = 3$, we numerically solve Equation (5.8) without approximation using the software package MATHEMATICA, for the kappa values $\kappa_e = 1.6, 2.0, 3.0, 4.0$ and 30 (Maxwellian case), and results are illustrated in Figures 5.7 and 5.8. As before, we use the high value of $\kappa_e = 30$ in Equation (5.8) to represent the Maxwellian plasma in Figures 5.7 and 5.8. The linear dispersion relation curves for parallel propagating whistler waves are displayed in Figure 5.7 and their companion growth rates are displayed in Figure 5.8.

Figure 5.7 shows that the whistler wave linear dispersion relation is influenced by superthermal electrons at high wave numbers, i.e., $k_\parallel c/\omega_{pe} \geq 0.9$, where a small change in dispersion behaviour is observed for varying electron kappa. The linear dispersion relation curves in Figure 5.7 are also observed to meet and cross at the wave number $k_\parallel c/\omega_{pe} = 1.44$, which also corresponds to the wave number of vanishing wave growth seen in Figure 5.8.

As seen by the green curve in Figure 5.8, Equation (5.8) predicts that for $T_{\perp e}/T_{\parallel e} = 3$, the whistler instability peak growth rate maximises for the Maxwellian case, where $\gamma/\omega_{ce} = 0.0815$. This is in contrast to results from Section 5.4 where we employed an electron temperature anisotropy of $T_{e\perp}/T_{e\parallel} = 2.05$. As was seen in Figure 5.2 of Section 5.4, Equation (5.8) predicted a smaller maximum peak growth rate of $\gamma/\omega_{ce} = 0.0076$, which corresponded to the $\kappa_e = 3$ case.

The curves of Figure 5.8 also illustrate that an increase in the electron tail hardness here, i.e., a decrease in the spectral index κ_e, results in a monotonic decrease in the instability peak

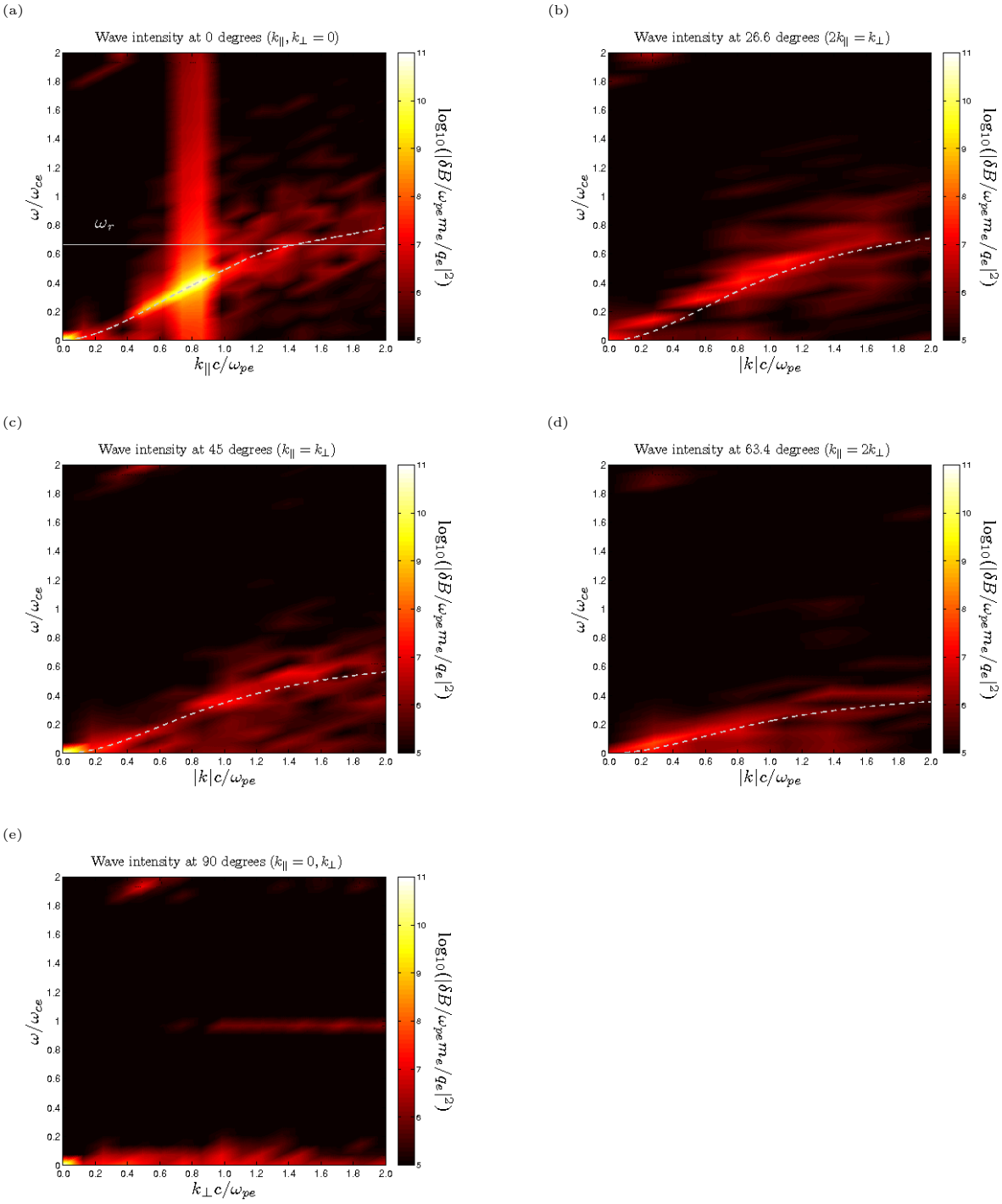

Figure 5.5: The fluctuating magnetic field intensity spectrum in the $\kappa_e = 3$ simulation, given as a function of ω/ω_{ce} and $|k|c/\omega_{pe}$. The fluctuation spectrum is given for waves propagating at angles (a) 0°, (b) 26.6°, (c) 45°, (d) 63.4° and (e) 90° to the magnetic $\boldsymbol{B}_0$, respectively. The dispersion relation for whistler waves, Equation (5.8), is over-plotted as the dashed line in panel (a), while the cold plasma whistler dispersion relation, Equation (5.16), is over-plotted as the dashed line in panels (b) to (d), respectively.

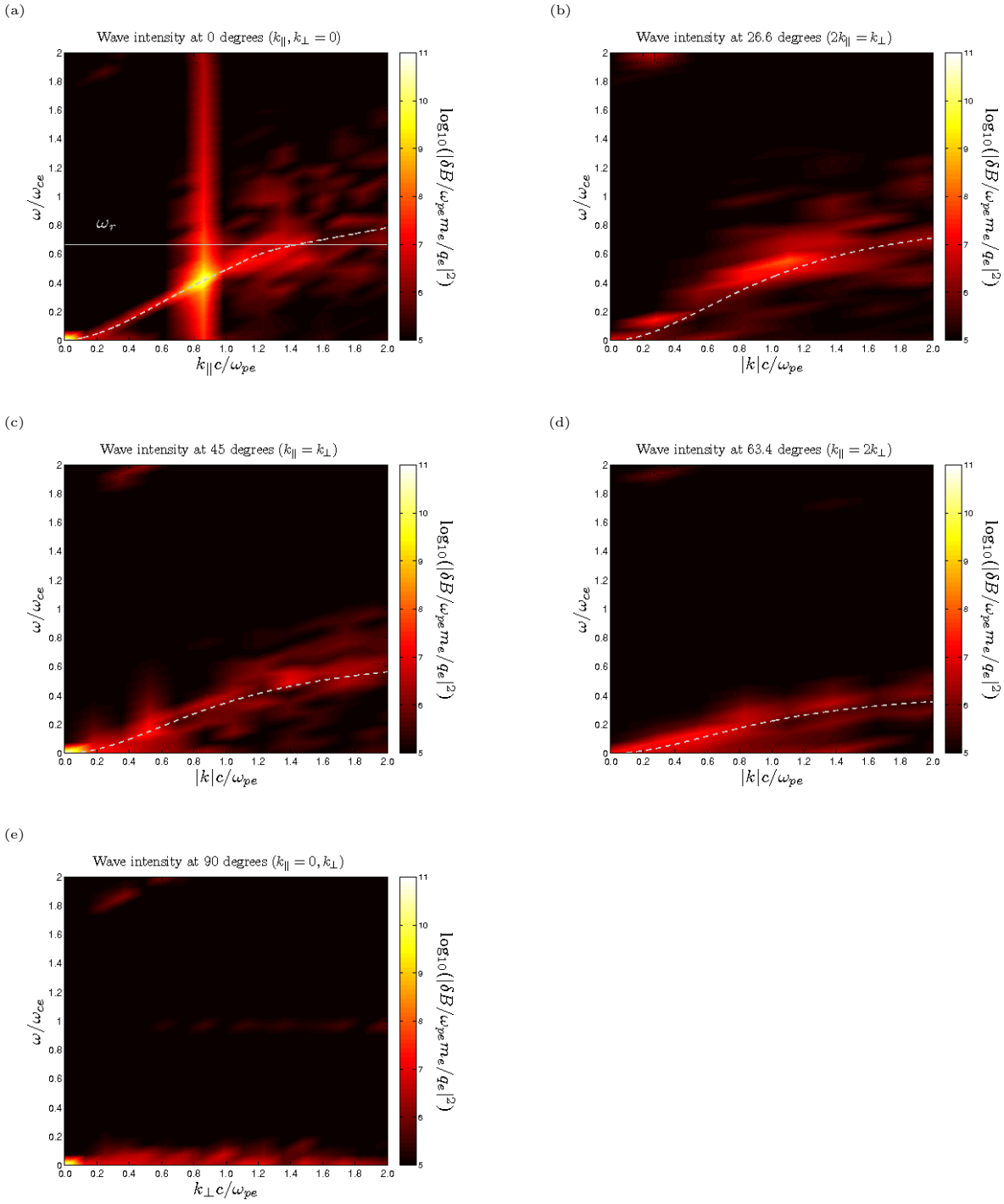

Figure 5.6: The fluctuating magnetic field intensity spectrum in the Maxwellian simulation, given as a function of ω/ω_{ce} and $|k|c/\omega_{pe}$. The fluctuation spectrum is given for waves propagating at angles (a) 0°, (b) 26.6°, (c) 45°, (d) 63.4° and (e) 90° to the magnetic $\boldsymbol{B}_0$, respectively. The dispersion relation for whistler waves, Equation (5.8), is over-plotted as the dashed line in panel (a), while the cold plasma whistler dispersion relation, Equation (5.16), is over-plotted as the dashed line in panels (b) to (d), respectively.

growth rates. This is also contrary to results obtained in Section 5.4 where non-monotonic behaviour was observed when using $T_{e\perp}/T_{e\|} = 2.05$ [see discussion of Figure 5.2]. Similar to the previous study of the whistler instability discussed in Section 5.4, however, increasing κ_e here results in a decrease in the range of unstable wave numbers, i.e., decreasing the electron tail hardness (increasing κ_e) results in a smaller instability bandwidth. This increase in the instability bandwidth for low kappa is due to the kappa distribution proving an abundance of high energy particles, having the required velocities $v_{\|res}$ of Equation (5.1) to produce strong wave-particle interaction at low wave numbers, compared to the Maxwellian. Figures 5.7 and 5.8 were used as a guide for choosing parameters for the simulations performed in this section, which we discuss next.

As was outlined in Table 5.1, to investigate the whistler instability driven by $T_{\perp e}/T_{\|e} = 3.0$ we ran three simulations. In the first simulation the electron velocity distribution was modelled by a bi-kappa distribution, Equation (5.2), with $\kappa_e = 2$. Figure 5.8 predicts that for the case of $\kappa_e = 2$ the peak growth rate will be $\gamma/\omega_{ce} = 0.032$ at $k_\| c/\omega_{pe} = 1.07$, with a range of unstable wave numbers given by $0.19 \leq k_\| c/\omega_{pe} \leq 1.44$. In the second simulation performed for this section, the electrons were modelled by a bi-kappa distribution with $\kappa_e = 3$. For the case of $\kappa_e = 3$, Figure 5.8 predicts a higher peak growth rate of $\gamma/\omega_{ce} = 0.051$ compared to the previous case, which occurs at a slightly higher wave number, $k_\| c/\omega_{pe} = 1.08$. The range of unstable wave numbers is smaller than for the $\kappa_e = 2$ case, i.e., $0.35 \leq k_\| c/\omega_{pe} \leq 1.44$. In the final simulation, the electrons were modelled by the bi-Maxwellian distribution, Equation (5.5), which is observed in Figure 5.8 to have the highest peak growth rate of all the cases, with $\gamma/\omega_{ce} = 0.082$ at the higher value of $k_\| c/\omega_{pe} = 1.09$, along with the smallest range of unstable wave numbers $0.7 \leq k_\| c/\omega_{pe} \leq 1.44$. All simulation runs performed for this section were evolved up to the time $\omega_{pe}t = 2000$ and results from each of the simulations are compared and discussed below.

Figures 5.9 to 5.11 display the temporal evolution of energies in the simulations for the $\kappa_e = 2$, $\kappa_e = 3$ and Maxwellian cases, respectively. As before, we adopt the convention that panel (a) in each figure displays the evolution of the fluctuating electric field energy, $U_{\delta E} = 1/2\epsilon_0(\delta \boldsymbol{E})^2$, panel (b) displays the fluctuating magnetic field energy, $U_{\delta B} = 1/(2\mu_0)(\delta \boldsymbol{B})^2$, panel (c) displays the kinetic energy of the electron species, $E_e = 1/2m_e|\boldsymbol{v}|^2$, panel (d) displays the kinetic energy of the ion species, $E_i = 1/2m_i|\boldsymbol{v}|^2$, panel (e) displays the sum of the particle and field energies described above E_{total}, and panel (f) displays the percentage deviation of the total energy from its initial value. The larger values of linear growth rate predicted for the parameters used in this section (seen in Figure 5.8) lead to more rapid growth in the field energies, coupled with a larger reduction in electron kinetic energy, compared to Runs 1 and

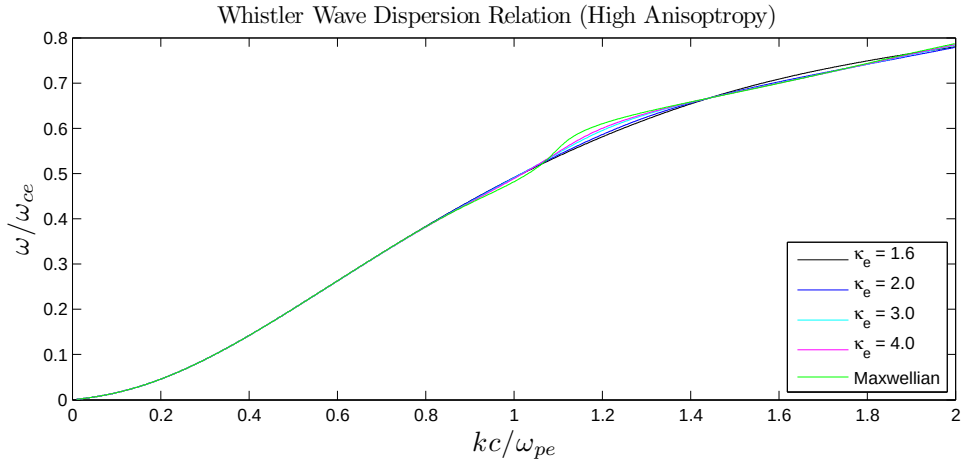

Figure 5.7: The theoretical whistler dispersion relations, i.e., the real frequency obtained from solution of Equation (5.8), for the plasmas with $T_{\perp e}/T_{\parallel e} = 3$, given for the sequence of electron kappa values $\kappa_e = 1.6, 2.0, 3.0, 4.0$ and 30 (corresponding to the Maxwellian case).

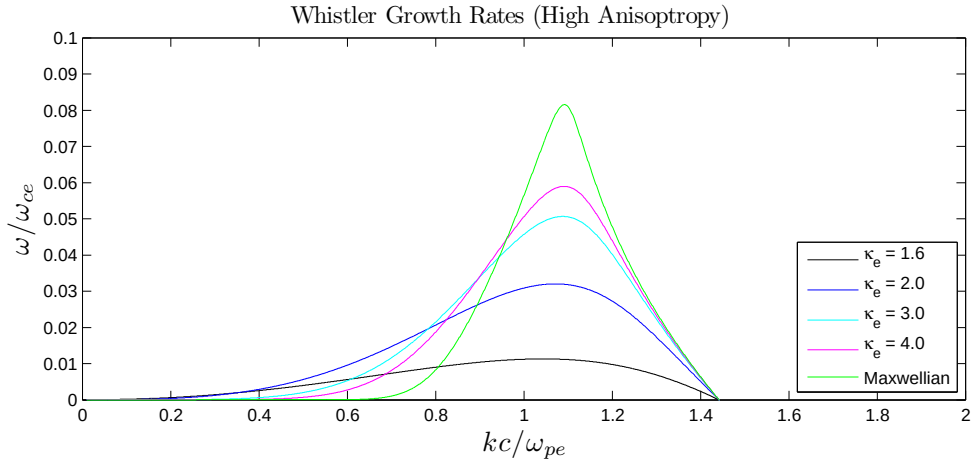

Figure 5.8: The theoretical growth rates for the plasmas with $T_{\perp e}/T_{\parallel e} = 3$, given for the sequence of electron kappa values $\kappa_e = 1.6, 2.0, 3.0, 4.0$ and 30 (corresponding to the Maxwellian case).

2 discussed in Section 5.4. As seen here in panels (a) and (b) of Figures 5.9 to 5.11, respectively, we are now able to resolve the linear growth phase of the instability (characterised by exponential growth in field energies), the non-linear saturation phase (marked by the point at which the field energy ceases to grow) as well as the post-saturation phase marked by constant or slowly varying energies with increasing time.

To aid in the reading and comparison of the energies displayed in Figures 5.9 to 5.11, the magnetic field energy, $U_{\delta B}/T_{\parallel e}$, and electron kinetic energy, $E_e/T_{\parallel e}$, are presented on a $y-$axis scale of $\Delta(E/T_{\parallel e}) = 4500$. To display the electric field energy, $U_{\delta E}/T_{\parallel e}$, and total energy, $E_{\text{total}}/T_{\parallel e}$, we use a $y-$axis scale of $\Delta(E/T_{\parallel e}) = 400$, while the ion kinetic energy, $E_i/T_{\parallel e}$, is displayed using a $y-$axis scale of $\Delta(E/T_{\parallel e}) = 150$.

Panels (a) and (b) of Figure 5.9 for the $\kappa_e = 2$ case, show that the electric and magnetic field energies exhibit an initial phase of exponential growth, followed by a phase of additional (slower) growth, after which the field energies decrease. Specifically, the first phase of field growth in Figure 5.9 is observed to occur over $0 \leq \omega_{pe}t \leq 650$, in which the electric field energy grows to $U_{\delta E}/T_{\parallel e} \approx 185$ and the magnetic field energy grows to $U_{\delta B}/T_{\parallel e} \approx 2021$. Following this, over the interval $650 \leq \omega_{pe}t \leq 1390$, the electric and magnetic fields exhibit further growth in energy up to $U_{\delta E}/T_{\parallel e} \approx 275$ and $U_{\delta B}/T_{\parallel e} \approx 3345$, respectively. By the end of the simulation, the electric field energy reduces slightly to $U_{\delta E}/T_{\parallel e} \approx 265$, while the magnetic field energy reduces to $U_{\delta B}/T_{\parallel e} \approx 3109$. Since the whistler wave grows through its resonant interaction with the electrons, panel (c) of Figure 5.9 shows that the evolution of the electron kinetic energy mirrors that of the field energies, initially losing energy to the growing waves over the two field growth phases, i.e., over $0 \leq \omega_{pe}t \leq 1390$, and gaining back energy for $\omega_{pe}t \geq 1390$. Overall, the electron species for the $\kappa_e = 2$ case loses an amount of energy corresponding to $\Delta(E_e/T_{\parallel e}) = |(E_e(0) - E_e(2000))/T_{\parallel e}| \approx 3780$ for the duration of the simulation. On the other hand, during the simulation, the ion species for the $\kappa_e = 2$ case is observed in panel (d) to have a gain in energy, $\Delta(E_i/T_{\parallel e}) \approx 70$. This is likely due to some non-linear coupling between the ions and the growing waves, which was necessary for energy to equilibrate in the system and for the plasma to reach a quasi-equilibrium state. All simulations performed in this section were of a closed system, requiring total energy to be conserved. However, as seen in panel (e) of Figure 5.9, the total energy decreases by $\Delta(E_{tot}/T_{\parallel e}) \approx 360$ over the entire simulation run. While this numerical artefact indicates a weakness in the simulation model, the deviation is very small, decreasing by only 0.048% from its initial value [see panel (f)]. This gives us a high degree of confidence in the validity of the simulation results.

By comparing Figures 5.9 and 5.10, it is clear that the evolution of the energies for the $\kappa_e = 3$ case are qualitatively similar to that for the $\kappa_e = 2$ case, with a few differences which we shall highlight. Panels (a) and (b) of Figure 5.10 illustrate that the initial growth phase for the $\kappa_e = 3$ case occurs earlier, over the interval $0 \leq \omega_{pe}t \leq 540$, compared to the $\kappa_e = 2$ case. This is in agreement with linear theory (Figure 5.8) which predicts larger growth rates for $\kappa_e = 3$ compared to that for $\kappa_e = 2$, leading to more rapid wave growth. Over the first growth phase, the electric and magnetic field energies in panels (a) and (b) of Figure 5.10 grow to $U_{\delta E}/T_{\parallel e} \approx 217$ and $U_{\delta B}/T_{\parallel e} \approx 2570$, respectively. The second growth phase also occurs earlier, over $540 \leq \omega_{pe}t \leq 980$, in which the electric and magnetic field energies grow further to $U_{\delta E}/T_{\parallel e} \approx 266$ and $U_{\delta B}/T_{\parallel e} \approx 3353$, respectively. The peak electric field energy in the $\kappa_e = 3$ simulation is lower than that for the $\kappa_e = 2$ simulation discussed previously; however, the peak magnetic field energy is higher in the $\kappa_e = 3$ case, consistent with the prediction of larger whistler growth rate. While we observe a longer phase of decreasing field energies here compared to the $\kappa_e = 2$ case, we note that the electric and magnetic field energies here exhibit a more rapid fall off as the simulation progresses, compared to the $\kappa_e = 2$ case. The electric and magnetic field energies decrease to $U_{\delta E}/T_{\parallel e} \approx 216$ and $U_{\delta B}/T_{\parallel e} \approx 2552$, respectively, by the end of the $\kappa_e = 3$ simulation. Similar to the $\kappa_e = 2$ case, the evolution of electron kinetic energy for the $\kappa_e = 3$ case, displayed in panel (c), is observed to mirror that of panels (a) and (b), losing $\Delta(E_e/T_{\parallel e}) \approx 4038$ over $0 \leq \omega_{pe}t \leq 980$ and gaining back $\Delta(E/T_{\parallel e}) \approx 914$ by the end of the simulation run. The non-linear interaction between waves and ions is observed to inject a larger amount of energy into the ion species than was observed for the $\kappa_e = 2$ case, i.e., $\Delta(E_i/T_{\parallel e}) \approx 83$ here, as seen in panel (d) of Figure 5.10. We also observe large amplitude oscillations in the ion kinetic energy at times $530 \leq \omega_{pe}t \leq 2000$, which was not seen previously. This is likely due to the trapping of the ions in ion-scale coherent field structures, leading to the ions performing bounce motion. These ion-scale field structures are often observed in space plasmas along with whistler waves driven by temperature anisotropy (Tenerani et al., 2012, 2013). Panel (e) of Figure 5.10 shows that the total energy for the $\kappa_e = 3$ case decreases over the simulation run; however, panel (f) of this figure shows that this change in total energy is again very small, i.e., at most 0.038%, lending validity to the simulation results.

In panels (a) and (b) of Figure 5.11 (Maxwellian case), the electric and magnetic field energies exhibit only a single phase of exponential field growth, followed by a trend of decreasing field energies at a rate that decreases with increasing time. This is contrary to the $\kappa_e = 2$ and $\kappa_e = 3$ cases discussed previously for Figures 5.9 and 5.10, respectively, where two phases of field growth was observed. This indicates a change in the behaviour of the whistler instability

which is brought about by the presence of a superthermal electron population. While Figure 5.8 predicted growth rate maximising for the Maxwellian case, we observe the smallest growth in electric and magnetic field energies in panels (a) and (b) of Figure 5.11, compared to those seen previously. However, the field energies in panels (a) and (b) of Figure 5.11 reach their maximum values at the earliest time, $\omega_{pe}t = 400$, compared to the previous cases. The larger wave growth rate is likely depleting the free energy required to maintain the exponential growth at a more rapid pace, preventing the field energies from growing to larger values. For the Maxwellian case, panel (a) of Figure 5.11 shows that the electric field energy grows to $U_{\delta E}/T_{\parallel e} \approx 220$, and the magnetic field energy [panel (b)] grows to $U_{\delta B}/T_{\parallel e} \approx 3210$, both occurring over the time interval $0 \leq \omega_{pe}t \leq 400$. Panels (a) and (b) of Figure 5.11 also show that the electric and magnetic field energies for the Maxwellian case have a more rapid fall off than the previous cases. The final electric and magnetic field energies for the Maxwellian case were $U_{\delta E}/T_{\parallel e} \approx 70$ and $U_{\delta B}/T_{\parallel e} \approx 737$, respectively. As seen in panel (c) of Figure 5.11, the evolution of the electron kinetic energy again mirrors that of the magnetic field energy in panel (b). The electron species initially loses $\Delta(E_e/T_{\parallel e}) \approx 3668$ to the growing waves, and thereafter, gains $\Delta(E_e/T_{\parallel e}) \approx 2699$ from the waves. The more rapid wave growth for the Maxwellian case is seen to lead to enhanced trapping of the ions species, where we observe larger amplitude oscillations in the ion kinetic energy than seen for the $\kappa_e = 3$ case, at earlier times $\omega_{pe}t \geq 400$ [compare panel (d) of Figures 5.10 and 5.11]. The ions here gain the energy $\Delta(E_i/T_{\parallel e}) \approx 78$. Panels (e) and (f) indicate that the total energy for the Maxwellian simulation changes by at most 0.023% from its initial value, giving us confidence in these simulation results as well.

The whistler instability is known to grow via cyclotron resonant wave-particle interaction. This resonant interaction scatters electrons, reducing their pitch angles, which in turn decreases the perpendicular component of the electron thermal energy $T_{\perp e}$ and increases the parallel component $T_{\parallel e}$. This decrease in electron temperature anisotropy, $T_{\perp e}/T_{\parallel e}$, leads to the eventual saturation of the instability.

Figures 5.12 to 5.14 display the temporal evolution of the electron temperature anisotropy during the simulations for the $\kappa_e = 2$, $\kappa_e = 3$ and Maxwellian cases, respectively. To calculate the electron temperature anisotropies we use the equipartition of energy theorem, which states that particles have an average energy, per degree of freedom, given by $\langle 1/2mv^2 \rangle = 1/2T$, where temperature is given in units of energy. Although the use of equipartition of energy is more appropriate for particles in thermal equilibrium, it is accepted in practice to use for distributions that diverge from the Maxwellian, such as the kappa distribution [see discussion in Hellberg et al. (2009)]. To calculate the perpendicular and parallel components of the

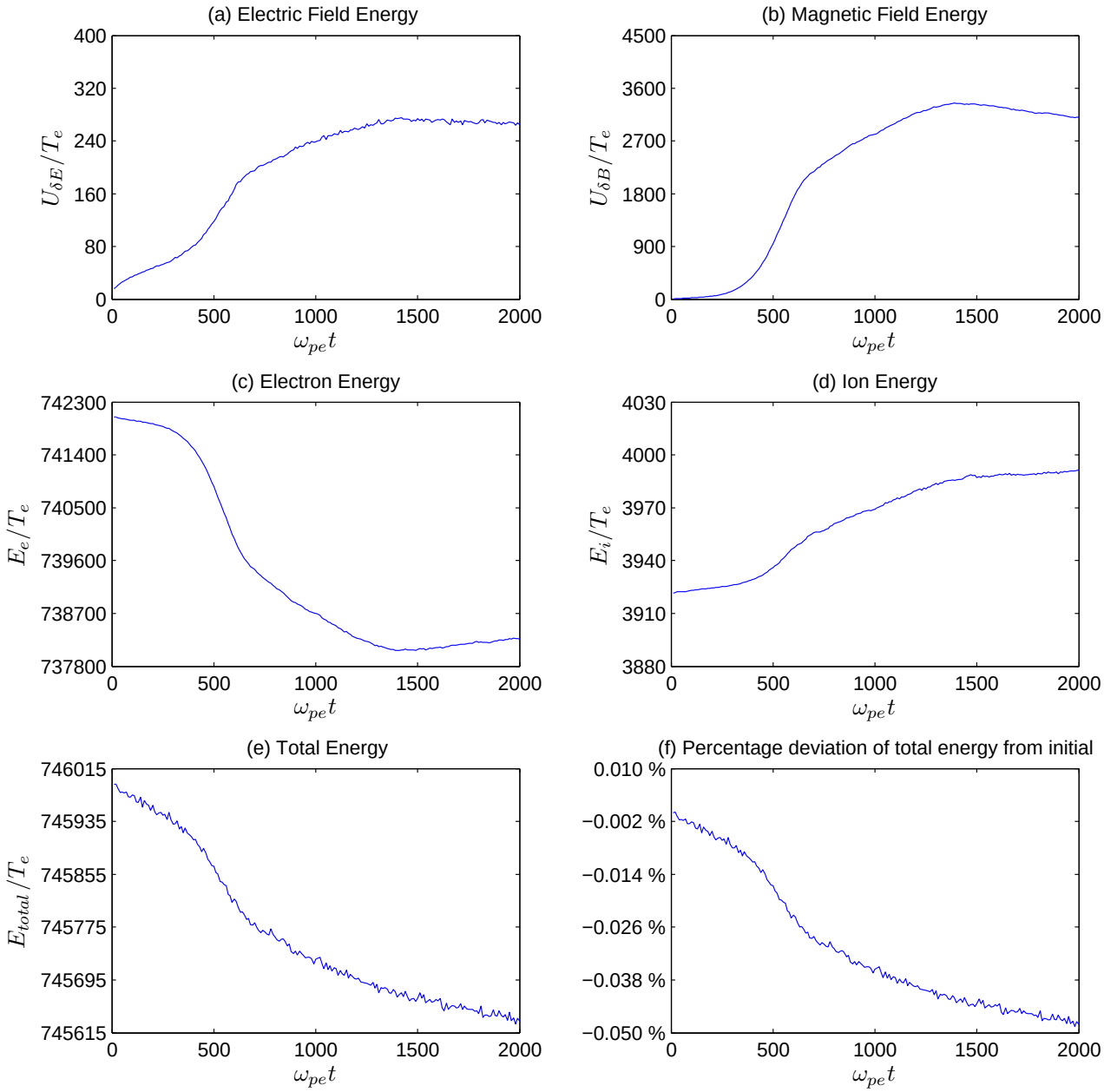

Figure 5.9: The temporal evolution of energies in the $\kappa_e = 2$ simulation, with $T_{\perp e}/T_{\parallel e} = 3$. Panel (a) gives the fluctuating electric field energy, panel (b) the fluctuating magnetic field energy, panel (c) the electron kinetic energy, panel (d) the ion kinetic energy, panel (e) the total energy in the simulation, and panel (f) gives the percentage deviation of the total energy from its initial value. All energies are normalised to the parallel component of the electron initial thermal energy $T_{\parallel e}$.

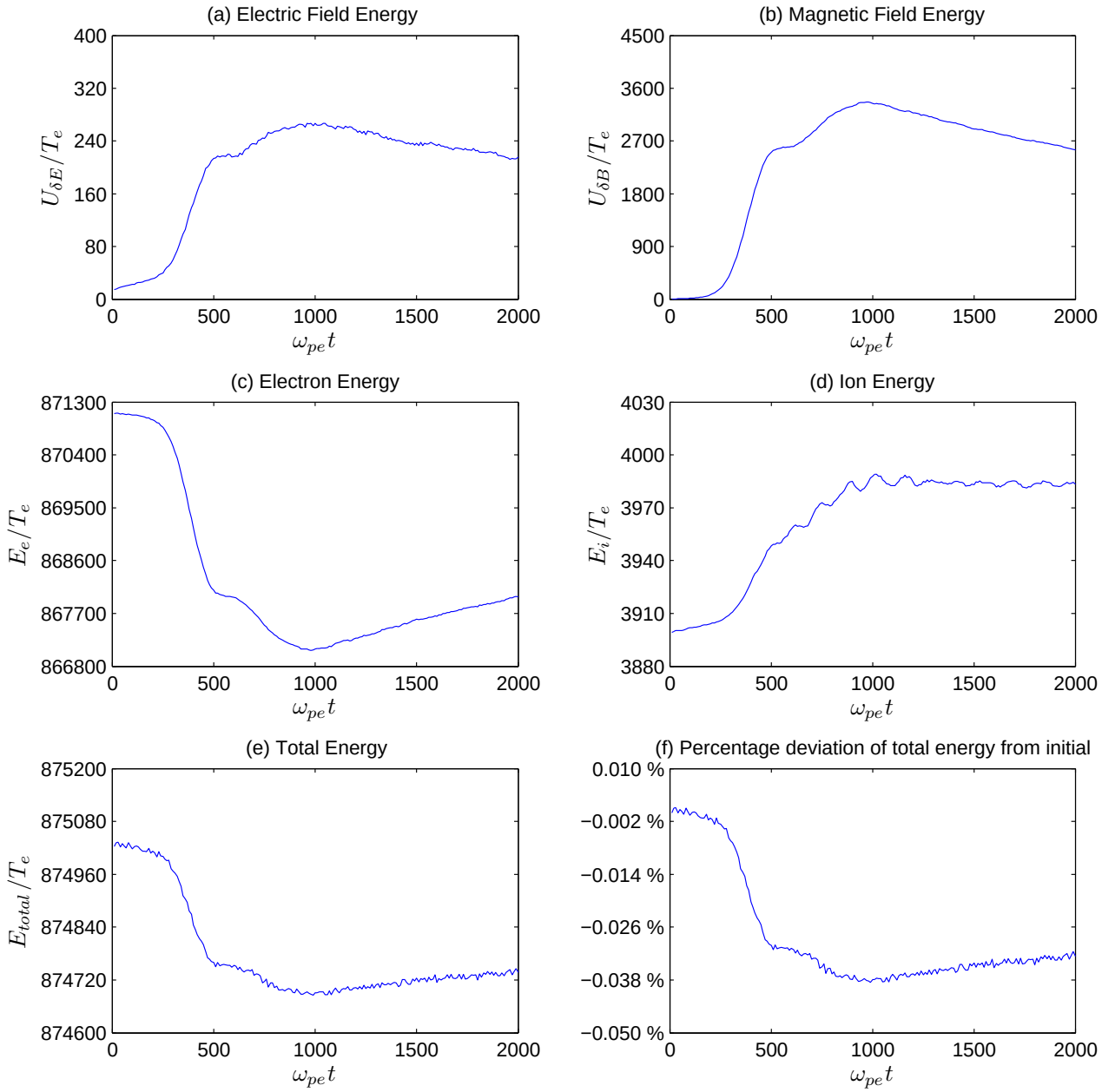

Figure 5.10: The temporal evolution of energies in the $\kappa_e = 3$ simulation, with $T_{\perp e}/T_{\parallel e} = 3$. Panel (a) gives the fluctuating electric field energy, panel (b) the fluctuating magnetic field energy, panel (c) the electron kinetic energy, panel (d) the ion kinetic energy, panel (e) the total energy in the simulation, and panel (f) gives the percentage deviation of the total energy from its initial value. All energies are normalised to the parallel component of the electron initial thermal energy $T_{\parallel e}$.

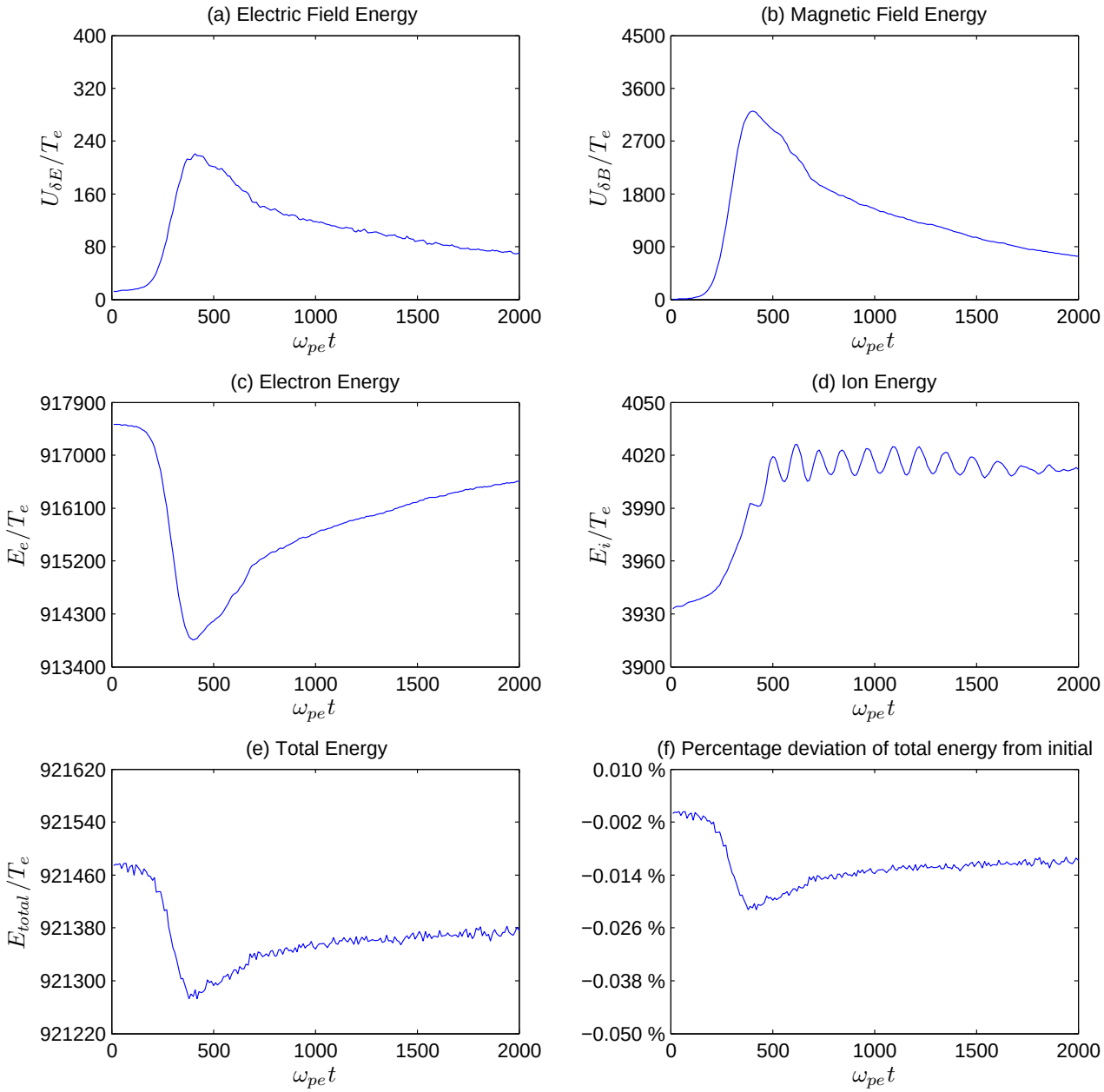

Figure 5.11: The temporal evolution of energies in the Maxwellian simulation, with $T_{\perp e}/T_{\parallel e} = 3$. Panel (a) gives the fluctuating electric field energy, panel (b) the fluctuating magnetic field energy, panel (c) the electron kinetic energy, panel (d) the ion kinetic energy, panel (e) the total energy in the simulation, and panel (f) gives the percentage deviation of the total energy from its initial value. All energies are normalised to the parallel component of the electron initial thermal energy $T_{\parallel e}$.

electron thermal energy, we use

$$\langle \frac{1}{2} m_e v_{\perp e}^2 \rangle = T_{\perp e},$$
$$\langle \frac{1}{2} m_e v_{\parallel e}^2 \rangle = \frac{1}{2} T_{\parallel e}. \tag{5.17}$$

As seen in Figures 5.12 to 5.14, respectively, the electron temperature anisotropy in each case decreases from initial values as the simulation progresses.

For the $\kappa_e = 2$ case displayed in Figure 5.12, the electron temperature anisotropy is observed to exhibit a progressively slower fall off over three stages. Using panels (a) and (b) of Figure 5.9 as a reference, the first stage corresponds to the initial field growth phase and occurs over $0 \leq \omega_{pe} t \leq 650$. The second stage corresponds to the second phase of slower field growth observed in Figure 5.9, and occurs over $650 \leq \omega_{pe} t \leq 1390$. After this, a slower decrease in anisotropy is observed until the end of the simulation. The whistler instability was observed to saturate during the $\kappa_e = 2$ simulation, i.e., field energy stopped growing and began to decrease; however, the electron temperature anisotropy never reaches $T_{\perp e}/T_{\parallel e} = 1$ for the $\kappa_e = 2$ simulation. This indicates that the components of electron thermal energy $T_{\perp e}$ and $T_{\parallel e}$ do not need to be equal for the free energy to be dissipated in the plasma, and for the system to reach a quasi-equilibrium state. At the end of the simulation, Figure 5.12 indicates that $T_{\perp e}/T_{\parallel e} = 2.37$ for the $\kappa_e = 2$ case.

Figure 5.13 displays the temperature anisotropy for the $\kappa_e = 3$ simulation. Similar to the $\kappa_e = 2$ case, the anisotropy here is observed to decrease over three phases, each corresponding to the phases observed in panels (a) and (b) of Figure 5.10. For the interval $0 \leq \omega_{pe} t \leq 540$, the anisotropy in Figure 5.13 decreases rapidly, followed by a slower decrease for $540 \leq \omega_{pe} t \leq 980$. Finally, for $980 \leq \omega_{pe} t \leq 2000$, we observe a slow fall off of the electron temperature anisotropy, where $T_{\perp e}/T_{\parallel e} = 2.33$ at the end of the simulation. The Maxwellian simulation displayed a single phase of field growth in panels (a) and (b) of Figure 5.11. Consequently, we observe a rapid decrease in the electron temperature anisotropy in Figure 5.14 over the times $0 \leq \omega_{pe} t \leq 400$, followed by a slower fall off until the end of the simulation. At the end of the simulation for the Maxwellian case, the electron temperature anisotropy is observed to be $T_{\perp e}/T_{\parallel e} = 2.36$. The larger values of growth rate predicted by Figure 5.8 is observed to produce more rapid wave growth, accompanied by a rapid reduction in electron temperature anisotropy, leading to the instability saturating at earlier times.

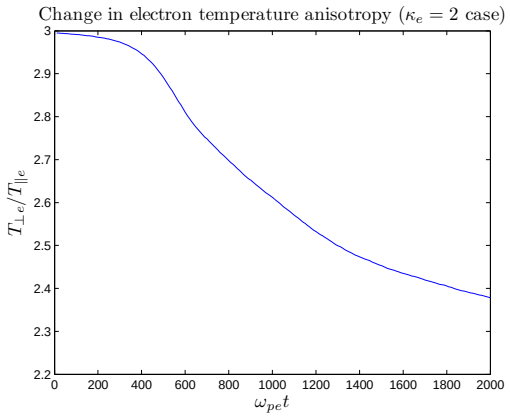

Figure 5.12: The temporal evolution of the electron temperature anisotropy $T_{\perp e}/T_{\parallel e}$ in the $\kappa_e = 2$ simulation, using $T_{\perp e}/T_{\parallel e} = 3$ to drive the whistler instability. At the end of the simulation run $T_{\perp e}/T_{\parallel e} = 2.37$.

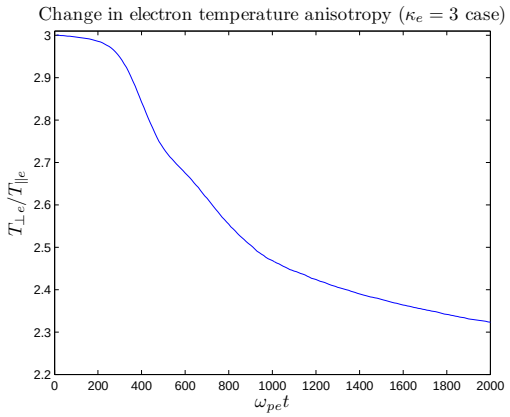

Figure 5.13: The temporal evolution of the electron temperature anisotropy $T_{\perp e}/T_{\parallel e}$ in the $\kappa_e = 3$ simulation, using $T_{\perp e}/T_{\parallel e} = 3$ to drive the whistler instability. At the end of the simulation run $T_{\perp e}/T_{\parallel e} = 2.33$.

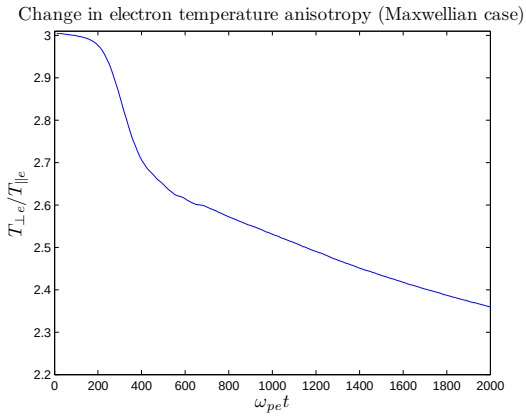

Figure 5.14: The temporal evolution of the electron temperature anisotropy $T_{\perp e}/T_{\parallel e}$ in the Maxwellian simulation, using $T_{\perp e}/T_{\parallel e} = 3$ to drive the whistler instability. At the end of the simulation run $T_{\perp e}/T_{\parallel e} = 2.36$.

Figures 5.15 to 5.17 illustrate slices through the electron velocity distribution in the $v_\parallel$ and $v_\perp$ directions, for the $\kappa_e = 2$, $\kappa_e = 3$ and Maxwellian cases, respectively. In each figure, the left-hand panel displays the slice taken parallel to the magnetic field $\boldsymbol{B}_0$, while the right-hand panel illustrates the slice taken perpendicular to $\boldsymbol{B}_0$. For each of the cases, a comparison is made between the slices of the electron initial velocity distribution (shown by the black curve in each figure) and slices of the electron velocity distribution taken at the end of the simulation run (shown by the red curve in each figure). As discussed in Section 5.2.1, the whistler waves interact strongly with electrons having a particular velocity parallel to the magnetic field $\boldsymbol{B}_0$. This velocity is specified by the cyclotron resonance condition

$$\omega^{'} = \omega - \boldsymbol{k}_\parallel \cdot \boldsymbol{v}_{\parallel \mathrm{res}} = |\omega_{ce}|. \tag{5.18}$$

For the $\kappa_e = 2$ case, the left-hand panel of Figure 5.15 suggests that the whistler wave interacts strongly with electrons whose velocities satisfy $|v_\parallel/v_{th,e}| \geq 2.0$. This is seen in the left-hand panel of Figure 5.15 as the enhancing of the tail of the electron final velocity distribution slice (red curve) for $|v_\parallel/v_{th,e}| \geq 2.0$, compared to the electron initial velocity distribution slice (black curve). Conversely, the right-hand panel of Figure 5.15 shows that the electron velocity distribution slice perpendicular to $\boldsymbol{B}_0$ exhibits a decrease in the tail population at velocities $|v_\perp/v_{th,e}| \geq 4.0$ through the resonant wave-particle interaction. The cooling displayed in the perpendicular slice of the electron velocity distribution, i.e., the reduction in the tail population, combined with the heating displayed in the parallel slice of the electron velocity distribution, i.e., the increase in the tail population, changes the electron pitch angles and reduces the electron temperature anisotropy, reducing free energy in the system. This was shown in Figure 5.12 for the $\kappa_e = 2$ case.

Qualitatively similar results to those described above for the $\kappa_e = 2$ case are observed for both the $\kappa_e = 3$ and Maxwellian cases. The left-hand panel of Figures 5.16 and 5.17 for the $\kappa_e = 3$ and Maxwellian cases, respectively, display an increase in the tail population for velocities $|v_\parallel/v_{th,e}| \geq 2.0$, while the right-hand panel of both figures indicate a decrease in the tail population for $|v_\perp/v_{th,e}| \geq 4.0$.

We note here that the wave number and wave angular frequency corresponding to peak growth rate seen in Figures 5.7 and 5.8 was $k_\parallel c/\omega_{pe} = 1.07$ and $\omega/\omega_{ce} = 0.03$ for $\kappa_e = 2$, $k_\parallel c/\omega_{pe} = 1.08$ and $\omega/\omega_{ce} = 0.05$ for $\kappa_e = 3$, and $k_\parallel c/\omega_{pe} = 1.09$ and $\omega/\omega_{ce} = 0.08$ for the Maxwellian case. Substituting these wave number and frequency pairs into the cyclotron resonance

condition, Equation (5.18), yields a resonant velocity of $v_{\parallel \mathrm{res}} = 2.0$ for the $\kappa_e = 2$ case, $v_{\parallel \mathrm{res}} = 1.98$ for the $\kappa_e = 3$ case and $v_{\parallel \mathrm{res}} = 1.97$ for the Maxwellian case. These calculated resonant velocities approximately coincide with those minimum values of $|\boldsymbol{v}_\parallel / v_{th,e}|$ in each respective figure, at the point where the parallel slices of the electron velocity distribution deviates from the initial loadings [see left-hand panels in Figures 5.15 to 5.17].

We again performed Fourier analysis of the fluctuating magnetic fields for the simulation Runs 3 to 5. Figures 5.18 to 5.20 illustrate the resulting magnetic field intensity spectrum for the $\kappa_e = 2$, $\kappa_e = 3$ and Maxwellian cases, respectively. In each case, the intensity spectrum is given as a function of ω/ω_{ce} and $|k|c/\omega_{pe}$ for a selection of propagation angles taken with respect to $\boldsymbol{B}_0$. Panel (a) in each figure depicts parallel wave propagation (0°), panel (b) depicts wave propagation at 26.6°, panel (c) depicts wave propagation at 45°, panel (d) depicts wave propagation at 63.4° and panel (e) depicts perpendicular wave propagation (90°).

For the $\kappa_e = 2$ case, the temporal Fourier analysis of Figure 5.18 was carried out for the time range corresponding to $1190 \leq \omega_{pe} t \leq 1390$. A time range given by $780 \leq \omega_{pe} t \leq 980$ was used for the $\kappa_e = 3$ case shown in Figure 5.19, and the range $200 \leq \omega_{pe} t \leq 400$ was used for the Maxwellian case shown in Figure 5.20. These time ranges correspond to the maximum field growth in each case, i.e., just before the non-linear saturation of the whistler waves.

As was discussed for Figure 5.7, we obtained the linear dispersion relation for the parallel propagating whistler wave in each case by solving Equation (5.8) without approximation using the software package MATHEMATICA. In panel (a) of Figures 5.18 to 5.20, respectively, we over-plotted the corresponding linear dispersion relation for the parallel propagating whistler wave as a dashed line. In panels (b) to (d) of each figure, for oblique propagation angles, we over-plotted the cold plasma whistler dispersion relation, Equation (5.16), as a rough guide. In Figures 5.18 to 5.20, we again compare the linear dispersion relations to the regions of most intense wave activity, where in each figure, the most intense wave activity is seen as the white colouring [representing intensities $(\delta B)^2/(\omega_{pe}^2 m_e^2/q_e^2) \geq 10^{11.3}$], the yellow colouring [representing $10^{10.3} \leq (\delta B)^2/(\omega_{pe}^2 m_e^2/q_e^2) \leq 10^{11.3}$], orange colouring [representing $10^{9.3} \leq (\delta B)^2/(\omega_{pe}^2 m_e^2/q_e^2) \leq 10^{10.3}$], and the red colouring [representing an intensity range corresponding to $10^{8.3} \leq (\delta B)^2/(\omega_{pe}^2 m_e^2/q_e^2) \leq 10^{9.3}$]. The frequency upper bound for the growing whistler waves, ω_r defined in Equation (5.15), is over-plotted as the horizontal line in panel (a) of Figures 5.18 to 5.20, respectively. As was also seen in panel (a) of Figures 5.5 and 5.6 in Section 5.4, we again observe here a band of high fluctuation intensity extending over the full range of frequencies displayed in each figure, and a high wave intensity region

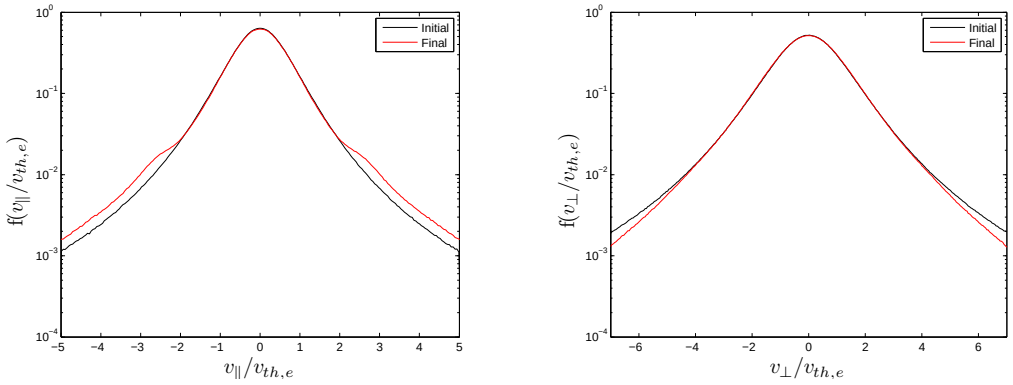

Figure 5.15: Slices parallel and perpendicular to $\boldsymbol{B}_0$ of the electron velocity distribution for the $\kappa_e = 2$ simulation. The black curves in each figure illustrate the slices through the electron initial velocity distribution, while the red curves illustrate the slices through the electron final velocity distribution.

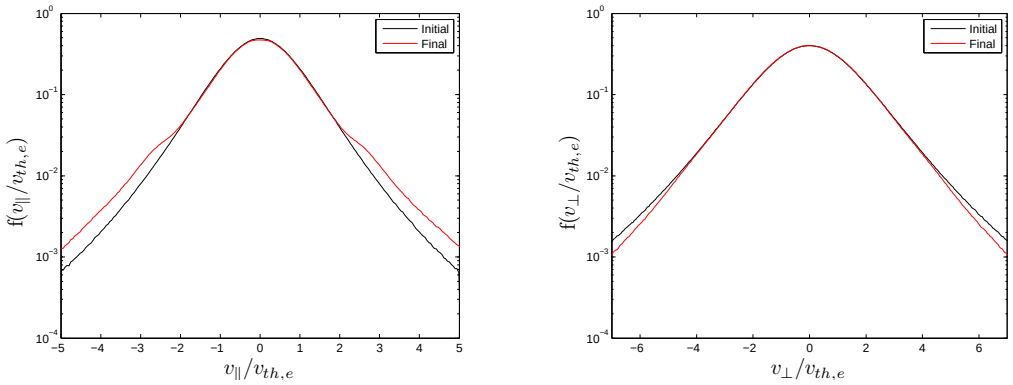

Figure 5.16: Slices parallel and perpendicular to $\boldsymbol{B}_0$ of the electron velocity distribution in the $\kappa_e = 3$ simulation. The black curves in each figure illustrate the slices through the electron initial velocity distribution, while the red curves illustrate the slices through the electron final velocity distribution.

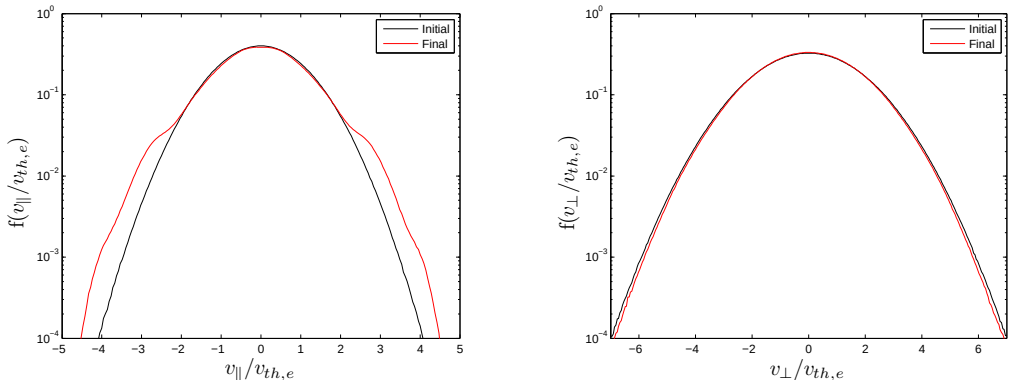

Figure 5.17: Slices parallel and perpendicular to $\boldsymbol{B}_0$ of the electron velocity distribution in the Maxwellian simulation. The black curves in each figure illustrate the slices through the electron initial velocity distribution, while the red curves illustrate the slices through the electron final velocity distribution.

at low frequencies and wave numbers [see panel (a) of Figures 5.18 to 5.20]. Similar results were obtained by Hughes et al. (2016).

For the $\kappa_e = 2$ case displayed in Figure 5.18, panel (a) is observed to exhibit the broadest regions of high wave activity (white, yellow and orange colouring) compared to the other panels. This indicates that the dominant wave energy lies in the parallel propagating whistler mode, as linear theory predicts. As seen in each panel of Figure 5.18, good agreement between the regions of highest wave activity (seen as the brighter colouring of red, orange, yellow and white) and the linear dispersion relations (dashed lines) at each angle is observed. This confirms that the high magnetic field fluctuations are produced as a result of whistler waves. In panel (a) of Figure 5.18, the most intense wave activity, displayed as the yellow and white colouring, is concentrated over the range $0.59 \leq k_{\parallel}c/\omega_{pe} \leq 1.42$, and at frequencies given by $0.22 \leq \omega/\omega_{pe} \leq 0.78$. This is within the linear theory prediction for the range of unstable wave numbers, i.e., $0.2 \leq k_{\parallel}c/\omega_{pe} \leq 1.44$, as was seen in Figure 5.8. Enhanced wave intensity (seen as the red colouring) in panel (a) of Figure 5.18 is observed for wave numbers $0.4 \leq k_{\parallel}c/\omega_{pe} \leq 1.6$. At $0.6 \leq k_{\parallel}c/\omega_{pe} \leq 1.2$, panel (a) displays the broad band of high wave intensities, extending over the full range of frequencies in the figure, similar to that seen before in Figures 5.5 and 5.6. While Figure 5.8 predicted a single wave number corresponding to peak growth rate for the $\kappa_e = 2$ case at $k_{\parallel}c/\omega_{pe} = 1.07$, panel (a) of Figure 5.18 displays two points of intense field fluctuations at wave numbers $k_{\parallel}c/\omega_{pe} \approx 0.86$ and $k_{\parallel}c/\omega_{pe} \approx 1.1$, respectively. These two points of high intensity field fluctuations have intensities $(\delta B)^2/(\omega_{pe}^2 m_e^2/q_e^2) \approx 10^{11.53}$ and $(\delta B)^2/(\omega_{pe}^2 m_e^2/q_e^2) \approx 10^{11.51}$, and may be due to the presence of banded whistler waves. We discuss the banded whistler waves later, for Figures 5.21 and 5.24. The regions if high wave intensity in panel (a), i.e., the yellow colouring, is observed at frequencies slightly higher than that predicted by Equation (5.15), due to the non-linear evolution of the whistler instability, and exceeds ω_r for wave numbers $0.81 \leq k_{\parallel}c/\omega_{pe} \leq 0.91$ and $1.05 \leq k_{\parallel}c/\omega_{pe} \leq 1.42$.

In comparing panels (b) to (d) of Figure 5.18 for oblique wave propagation, the mode propagating closest to parallel propagation, i.e., the mode propagating at 26.6°, is observed to have the highest wave intensity, $(\delta B)^2/(\omega_{pe}^2 m_e^2/q_e^2) \approx 10^{10.1}$. The highest intensities (orange colouring) in panel (b) occur for wave numbers $0.5 \leq |k|c/\omega_{pe} \leq 1.2$ and frequencies $0.2 \leq \omega/\omega_{ce} \leq 0.6$, which is within a smaller range of wave numbers and frequencies than seen for parallel propagation [see panel (a)]. While this region of orange colouring in panel (b) of Figure 5.18 is observed at frequencies higher than those predicted by the cold plasma dispersion relation, indicated by the dashed line, the agreement between the dispersion relation and the regions of high wave intensity is still fairly good.

As obliquity increases, the wave intensities decrease. This is seen as the reduction in the brightness of the intensity spectra when moving from panels (b) to (d) of Figure 5.18. An increase in obliquity also results in a decrease in the frequency span of the high wave intensity regions, and these regions shift to lower frequencies. High wave activity, seen as the orange and red colouring, occurs for frequencies $\omega/\omega_{ce} \leq 1.4$ in panel (b), $\omega/\omega_{ce} \leq 0.6$ in panel (c), and $\omega/\omega_{ce} \leq 0.27$ in panel (d). For wave propagation at 63.4°, enhanced field fluctuations are only observed at wave numbers $|k|c/\omega_{pe} \leq 1.0$. This further confirms that most of the free energy in the system goes into the parallel propagating whistler wave. At perpendicular propagation [panel (e) of Figure 5.18], low wave activity is observed, except for frequencies $\omega/\omega_{ce} \leq 0.1$, implying that very little wave energy resides in the perpendicularly propagating wave modes. We note again, as before, that the resolution of the panels at oblique angles, i.e., panels (b) and (d), are lower than the remaining panels.

Comparing each panel in Figure 5.18 for the $\kappa_e = 2$ case, to those of Figures 5.19 and 5.20 for the $\kappa_e = 3$ and Maxwellian cases, respectively, we observe a similar distribution of wave intensities in all simulations, with a few notable differences.

For the $\kappa_e = 3$ case, the parallel propagating mode displayed in panel (a) of Figure 5.19 is again observed to contain the dominant wave activity, compared to the other panels in Figure 5.19. Good agreement between the regions of high wave activity and the respective linear dispersion relations in each panel of Figure 5.19 is also observed. Similar to the $\kappa_e = 2$ case discussed previously, for $\kappa_e = 3$ we again observe two different points of most intense field fluctuations, at the wave numbers $k_\parallel c/\omega_{pe} \approx 0.75$ and $k_\parallel c/\omega_{pe} \approx 1.1$. These are again attributed to the presence of banded whistler waves, which are discussed in Figures 5.22 and 5.25 for the $\kappa_e = 3$ case. Since the $\kappa_e = 3$ simulation displayed a higher peak magnetic field energy compared to the $\kappa_e = 2$ case [see discussion of Figures 5.9 and 5.10], the most intense field fluctuations for the $\kappa_e = 3$ simulation had slightly higher values, i.e., $(\delta B)^2/(\omega_{pe}^2 m_e^2/q_e^2) \approx 10^{11.54}$ and $(\delta B)^2/(\omega_{pe}^2 m_e^2/q_e^2) \approx 10^{11.53}$.

As was seen for the $\kappa_e = 2$ case, panel (a) of Figure 5.19 shows a similar band of high intensity fluctuations extending over the entire frequency range. The wave number range corresponding to this high intensity band is larger here, i.e., $0.59 \leq k_\parallel c/\omega_{pe} \leq 1.3$, compared to the $\kappa_e = 2$ case. This is likely due to the maximum magnetic field intensities being higher in the $\kappa_e = 3$ simulation. The yellow and red colouring in panel (a) of Figure 5.19, however, occur for a smaller range of wave numbers, $0.55 \leq k_\parallel c/\omega_{pe} \leq 1.56$, than for the $\kappa_e = 2$ case. This reduction in wave number extent of the high intensity field fluctuations is consistent with the linear theory prediction of a smaller instability bandwidth for increasing kappa

values (see Figure 5.8). The regions of highest wave activity in panel (a), corresponding to the yellow colouring, occur for the wave numbers $0.6 \leq k_{\parallel}c/\omega_{pe} \leq 1.4$, which is within the linear theory prediction for the range of unstable wave numbers, i.e., $0.35 \leq k_{\parallel}c/\omega_{pe} \leq 1.44$. The yellow colouring in panel (a) is observed at frequencies higher than that predicted by Equation (5.15), indicated by the horizontal line, for wave numbers $1.0 \leq k_{\parallel}c/\omega_{pe} \leq 1.4$. For the mode propagating at 26.6° in panel (b) of Figure 5.19, we observe a narrower region of high wave intensities (orange colouring) in both wave number and frequency extent, compared to $\kappa_e = 2$ case shown in panel (b) of Figure 5.18. This indicates that high intensity waves are not excited at large propagation angles in the $\kappa_e = 3$ simulation, like they were for the $\kappa_e = 2$ simulation.

The Maxwellian case displayed in Figure 5.20 exhibits the smallest range of wave numbers corresponding to high intensity field fluctuations for the parallel propagating whistler wave, compared to the $\kappa_e = 2$ and $\kappa_e = 3$ cases, as predicted by Figure 5.8. Panel (a) of Figure 5.20 depicts yellow and red colouring for the wave numbers $0.63 \leq k_{\parallel}c/\omega_{pe} \leq 1.5$. Since the peak magnetic field energy for the Maxwellian simulation was the lowest of the three cases [see panel (a) of Figure 5.11], the most intense field fluctuation in panel (a) of Figure 5.20 had the lowest value of $(\delta B)^2/(\omega_{pe}^2 m_e^2/q_e^2) \approx 10^{11.5}$, which occurred for the single wave number $k_{\parallel}c/\omega_{pe} \approx 1.1$. This wave number of highest fluctuation intensity agrees well with the linear theory prediction of the wave number corresponding to peak growth rate, i.e., $k_{\parallel}c/\omega_{pe} = 1.09$. Although the Maxwellian case has lowest peak intensity and the narrowest region of high wave activity (yellow colouring) for the parallel mode, at 26.6° propagation, shown in panel (b) of Figure 5.20, the Maxwellian case exhibits the highest wave intensities of the three cases considered. In panel (b) of Figure 5.20, we observe a large region of high magnetic field intensity (yellow and orange colouring), having $10^{9.3} \leq (\delta B)^2/(\omega_{pe}^2 m_e^2/q_e^2) \leq 10^{10.5}$, indicating that the Maxwellian plasma excites high intensity waves for larger propagation angles. The wave intensities for the Maxwellian case are again observed to decrease with an increase in the angle of propagation, as was seen in the previous two cases, with very little wave activity observed for propagation at 63.4° [see panel (d)].

An alternate representation of the fluctuation spectra for the simulations is presented in Figures 5.21 to 5.23 for the $\kappa_e = 2$, $\kappa_e = 3$ and Maxwellian cases, respectively. Here, the fluctuating magnetic field intensity spectrum is given as a function of $k_{\parallel}c/\omega_{pe}$ and $k_{\perp}c/\omega_{pe}$ for each case. In each panel of Figures 5.21 to 5.23, the propagation angles made with respect to the magnetic field $\boldsymbol{B}_0$ from Figures 5.18 to 5.20 discussed previously, are shown. In comparing the panels in Figures 5.21 to 5.23, we observe that the presence of a superthermal electron population results in an increase in the intensity of diffuse field fluctuations over a

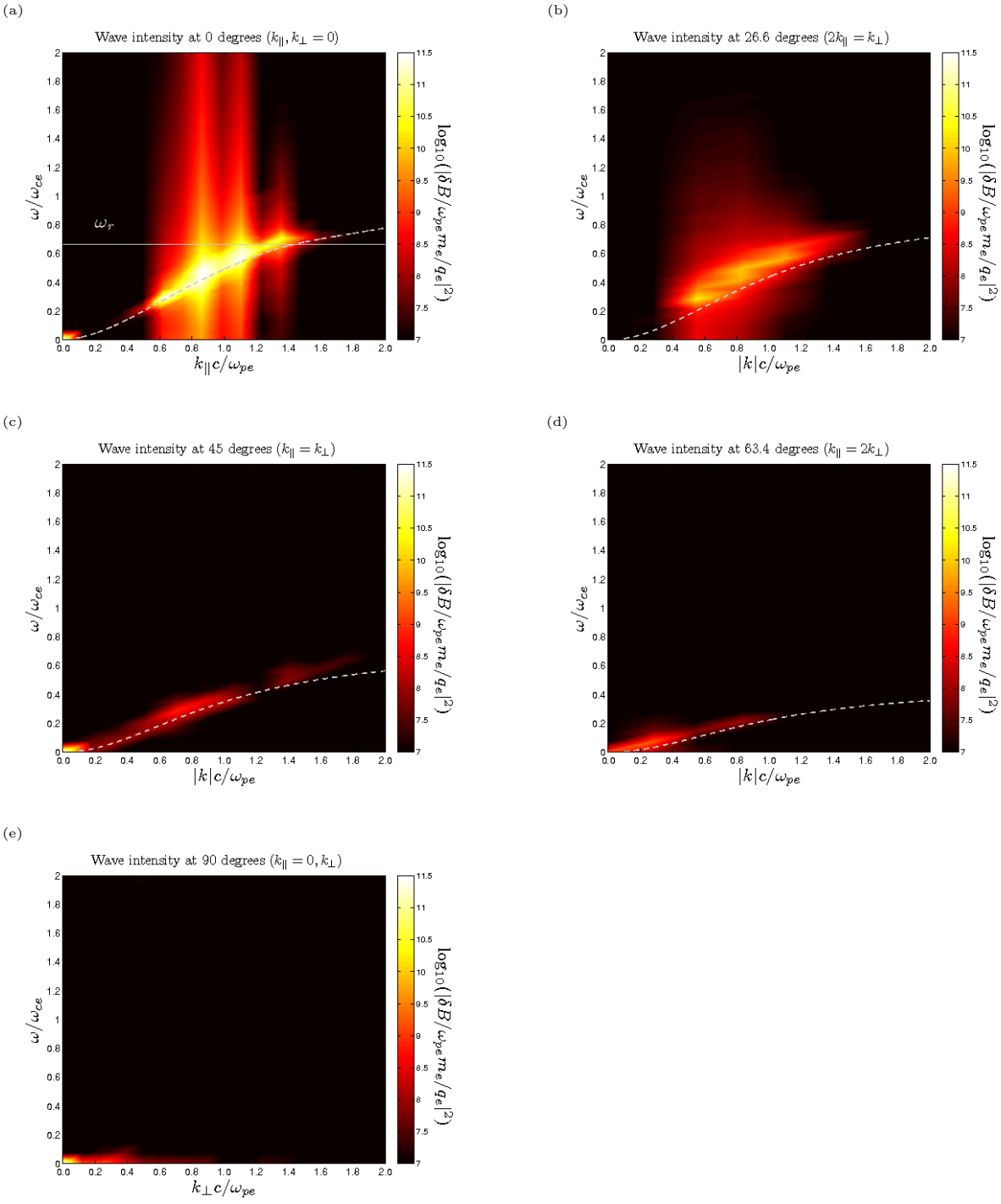

Figure 5.18: The fluctuating magnetic field intensity spectrum in the $\kappa_e = 2$ simulation, given as a function of ω/ω_{ce} and $|k|c/\omega_{pe}$. The fluctuation spectrum is given for waves propagating at angles (a) 0°, (b) 26.6°, (c) 45°, (d) 63.4° and (e) 90° to the magnetic $\boldsymbol{B}_0$, respectively. The dispersion relation for whistler waves, Equation (5.8), is over-plot as the dashed line in panel (a), while the cold plasma dispersion relation, Equation (5.16), is over-plot as the dashed lines in panels (b) to (d), respectively.

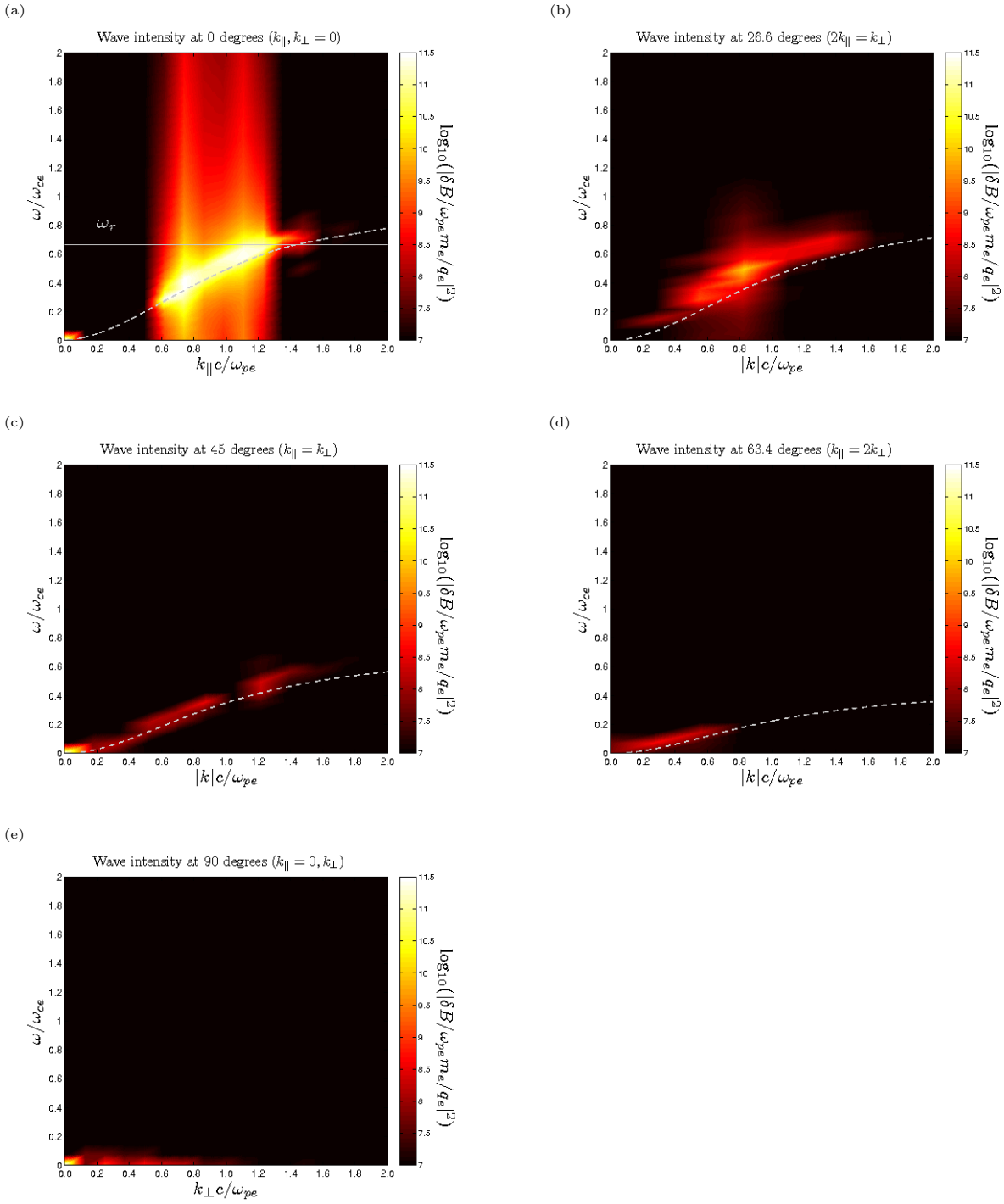

Figure 5.19: The fluctuating magnetic field intensity spectrum in the $\kappa_e = 3$ simulation, given as a function of ω/ω_{ce} and $|k|c/\omega_{pe}$. The fluctuation spectrum is given for waves propagating at angles (a) 0°, (b) 26.6°, (c) 45°, (d) 63.4° and (e) 90° to the magnetic $\boldsymbol{B}_0$, respectively. The dispersion relation for whistler waves, Equation (5.8), is over-plot as the dashed line in panel (a), while the cold plasma dispersion relation, Equation (5.16), is over-plot as the dashed lines in panels (b) to (d), respectively.

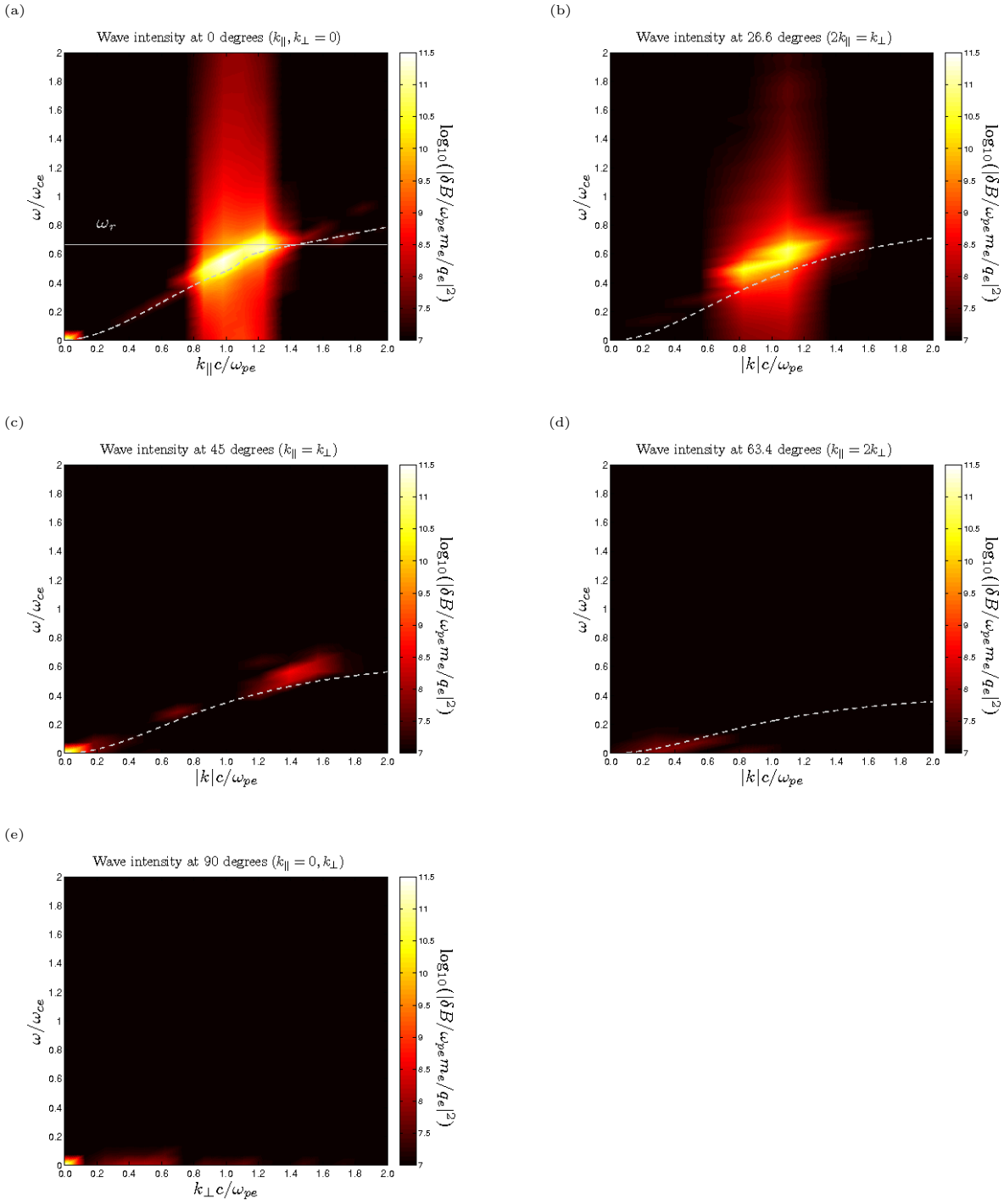

Figure 5.20: The fluctuating magnetic field intensity spectrum in the Maxwellian simulation, given as a function of ω/ω_{ce} and $|k|c/\omega_{pe}$. The fluctuation spectrum is given for waves propagating at angles (a) 0°, (b) 26.6°, (c) 45°, (d) 63.4° and (e) 90° to the magnetic $\boldsymbol{B}_0$, respectively. The dispersion relation for whistler waves, Equation (5.8), is over-plot as the dashed line in panel (a), while the cold plasma dispersion relation, Equation (5.16), is over-plot as the dashed lines in panels (b) to (d), respectively.

broad range of $k_{\parallel}c/\omega_{pe}$ and $k_{\perp}c/\omega_{pe}$. This is seen as the broader region of light blue colouring [corresponding to the intensities $10^{3.5} \leq (\delta B)^2/(\omega_{pe}^2 m_e^2/q_e^2) \leq 10^{4.5}$] covering the panels in Figures 5.21 and 5.22, for the $\kappa_e = 2$ and $\kappa_e = 3$ cases, compared to the panels of Figure 5.23 for the Maxwellian case. A likely reason for this is that low kappa values are believed to enhance the role of particle discreteness effects, leading to enhanced thermal fluctuations and increased noise in the plasma (Mace et al., 1998; Hellberg et al., 2005).

The spectra in panel (a) of Figures 5.21 to 5.23, respectively, are taken at a time given by $\omega_{pe}t = 100$. As was seen in the energy plots given in Figures 5.9 to 5.11, a softer electron tail, i.e., increasing κ_e values, resulted in large exponential field growth at earlier times during the simulation run. This also follows from Figure 5.8 which predicted increasing growth rates for increasing κ_e values. Consequently, panel (a) of each figure shows higher wave activity for the $\kappa_e = 3$ and Maxwellian cases. This is seen as an increasing region of cyan and green colouring, which corresponds to the intensities $10^{4.5} \leq (\delta B)^2/(\omega_{pe}^2 m_e^2/q_e^2) \leq 10^{5.5}$, when comparing panel (a) for each case. The Maxwellian case shown in panel (a) of Figure 5.23 is observed to have the largest region of intense field fluctuations at this time. Furthermore, intense whistler waves are seen to be excited in the Maxwellian case for a cone of propagation angles slightly less than 26.6° with respect to $\boldsymbol{B}_0$.

Panel (b) of Figures 5.21 to 5.23, respectively, displays the field fluctuation spectra taken at a time corresponding to the peak magnetic field energy for each case, i.e., at a time $\omega_{pe}t = 1390$ for the $\kappa_e = 2$ case, at $\omega_{pe}t = 980$ for the $\kappa_e = 3$ case and $\omega_{pe}t = 400$ for the Maxwellian case. The extent of the enhanced field fluctuations (cyan, yellow and red colouring) along the $k_{\parallel}c/\omega_{pe}$ axis in each figure has been discussed previously for each case [see discussion of the parallel mode in panel (a) of Figures 5.18 to 5.20, respectively], and was shown to approximately agree with the range of unstable wave numbers predicted by linear theory, seen in Figure 5.8. The regions of enhanced wave activity are observed here to extend in the $k_{\perp}c/\omega_{pe}$ direction in all simulations, with the intensity of the fluctuations decreasing, i.e, colouring moving from darker red to blue, with increasing angle of propagation with respect to the magnetic field $\boldsymbol{B}_0$, as was also seen in the panels of Figures 5.18 to 5.20.

For the kappa cases, enhanced fluctuation intensities (red to cyan colouring) are observed for a cone of angles below 45° propagation, with the Maxwellian plasma exciting intense waves slightly above 45° [see panel (b) of Figure 5.23]. High wave intensities (orange and yellow colouring) are observed for angles up to 26.6° for the $\kappa_e = 2$ case, and below 26.6° for the $\kappa_e = 3$ case [see panel (b) of Figures 5.21 and 5.22]. While the high wave intensity region for the Maxwellian case occurs for the smallest range of wave numbers along $k_{\parallel}c/\omega_{pe}$, intense

waves (red colouring) are observed pass 26.6° propagation [see panel (b) of Figure 5.23], as was also seen in panel (b) of Figure 5.20.

Panel (c) in Figures 5.21 to 5.23, respectively, illustrates the fluctuation spectra at the end of each simulation. The fluctuation spectra here show regions of high wave activity (red to cyan colouring) at slightly lower propagation angles than observed at earlier times, shown in panel (b) of each figure. We also observe two separate regions of highest wave activity (orange and red colouring) for all three cases, where the regions are separated by a low fluctuation intensity region at the wave number $k_{\parallel}c/\omega_{pe} \approx 1$. A likely cause of this separation will be discussed below.

Figures 5.24 to 5.26 illustrate the magnetic field intensity spectra, displayed as a function of ω/ω_{ce} and $k_{\parallel}c/\omega_{pe}$, for parallel wave propagation. Figure 5.24 displays the spectra for the $\kappa_e = 2$ simulation, Figure 5.25 displays the $\kappa_e = 3$ spectra, and Figure 5.26 displays the Maxwellian spectra. These figures represent temporal Fourier analysis of the magnetic field taken over a time interval near the end of each simulation run, i.e., $1800 \leq \omega_{pe}t \leq 2000$. We observe here the two separate regions of high wave intensity (orange, yellow and red colouring) separated in wave number by a region of less intense fluctuations. The two regions are separated at a wave number given by $k_{\parallel}c/\omega_{pe} \approx 1$ for the each case.

Reading the frequency corresponding to this wave number of separation from the respective linear dispersion relations yields $\omega/\omega_{ce} \approx 0.5$ in each case. The two separate regions of high wave intensity may be related to banded whistler waves (Lui et al., 2011). These are whistler waves which show a banded spectra, having an upper and lower component with minimum wave power near the frequency $0.5\omega_{ce}$ (Tsurutani and Smith, 1974). These waves are observed in the terrestrial magnetosphere and are responsible for banded chorus (Tsurutani and Smith, 1974; Bell et al., 2009) and plasmaspheric hiss (Lui et al., 2011). Banded chorus emissions are produced by intense electromagnetic plasma waves, and diffuse energy in the plasma by accelerating electrons (Bell et al., 2009; Gao et al., 2014). Hiss emissions also exhibit a banded spectra, where the lower band waves tend to be field aligned and are stronger than the upper band waves, which are quasi-electrostatic and propagate at oblique angles to the magnetic field (Lui et al., 2011).

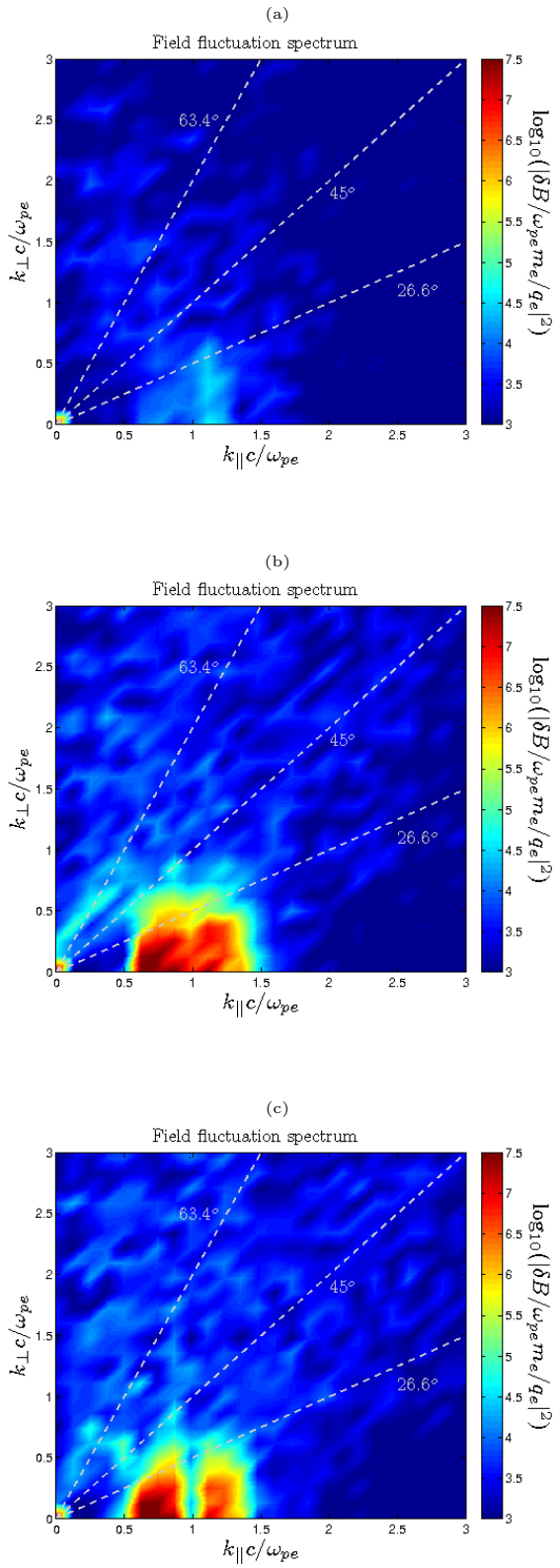

Figure 5.21: The fluctuating magnetic field intensity spectrum in the $\kappa_e = 2$ simulation, given as a function of $k_\parallel c/\omega_{pe}$ and $k_\perp c/\omega_{pe}$. The fluctuation spectrum is given for the times (a) $\omega_{pe}t = 100$, (b) $\omega_{pe}t = 1390$ and (c) $\omega_{pe}t = 2000$.

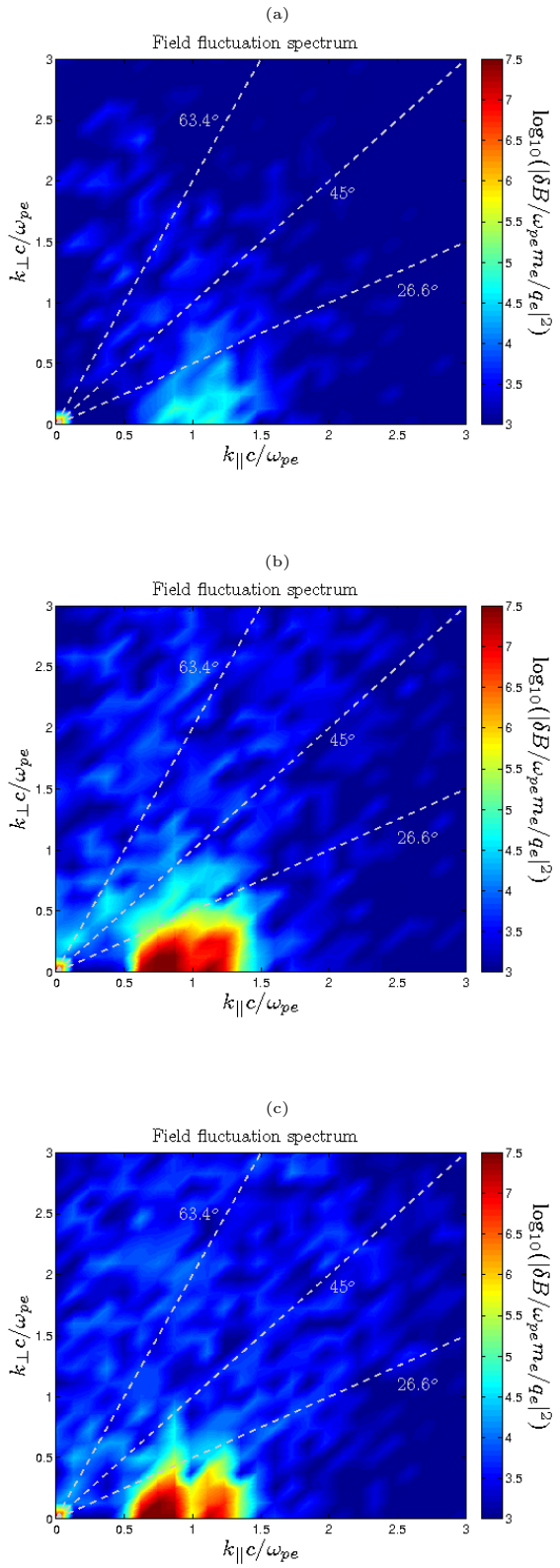

Figure 5.22: The fluctuating magnetic field intensity spectrum in the $\kappa_e = 3$ simulation, given as a function of $k_\parallel c/\omega_{pe}$ and $k_\perp c/\omega_{pe}$. The fluctuation spectrum is given for the times (a) $\omega_{pe}t = 100$, (b) $\omega_{pe}t = 980$ and (c) $\omega_{pe}t = 2000$.

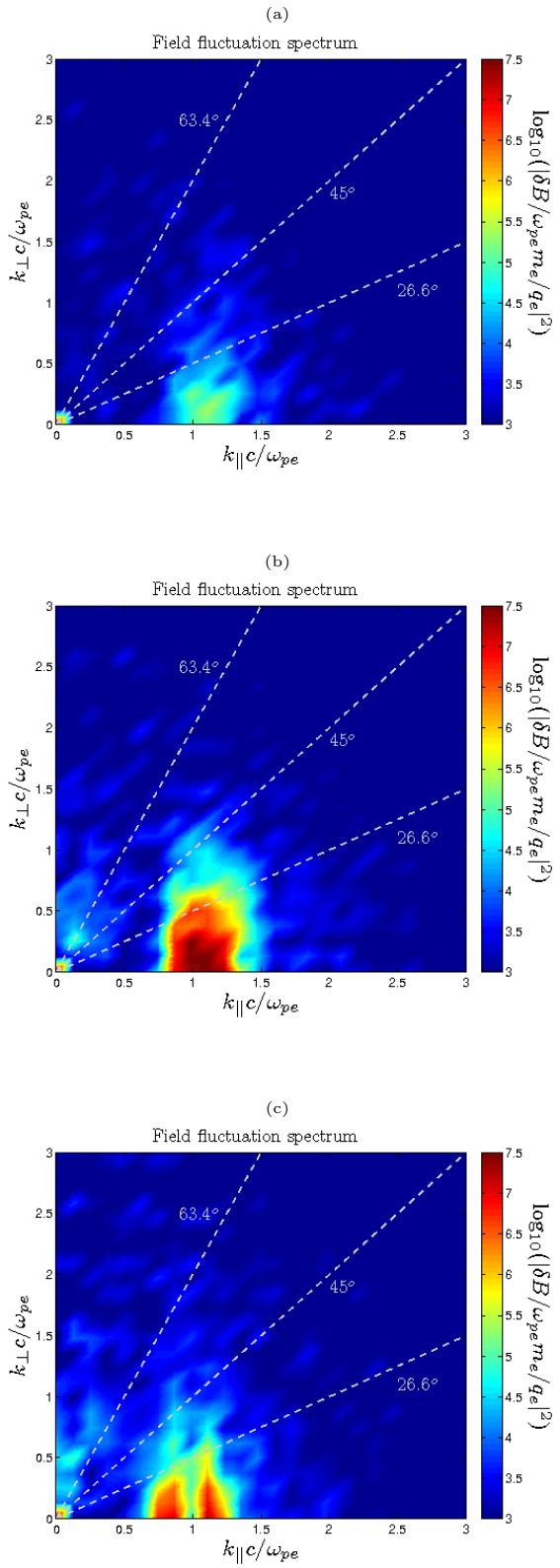

Figure 5.23: The fluctuating magnetic field intensity spectrum in the Maxwellian plasma, given as a function of $k_\parallel c/\omega_{pe}$ and $k_\perp c/\omega_{pe}$. The fluctuation spectrum is given for the times (a) $\omega_{pe}t = 100$, (b) $\omega_{pe}t = 400$ and (c) $\omega_{pe}t = 2000$.

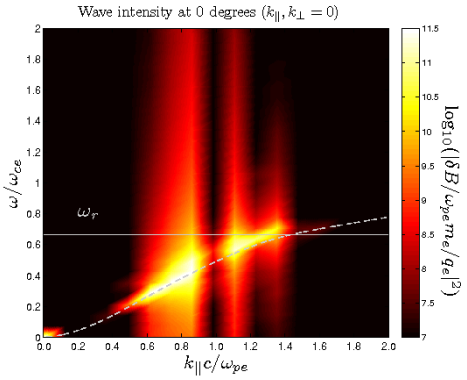

Figure 5.24: The fluctuating magnetic field intensity spectrum for the parallel propagating mode in the $\kappa_e = 2$ simulation, taken for a time corresponding to $1800 \leq \omega_{pe}t \leq 2000$.

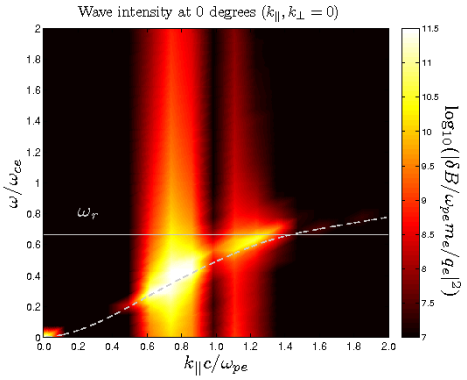

Figure 5.25: The fluctuating magnetic field intensity spectrum for the parallel propagating mode in the $\kappa_e = 3$ simulation, taken for a time corresponding to $1800 \leq \omega_{pe}t \leq 2000$.

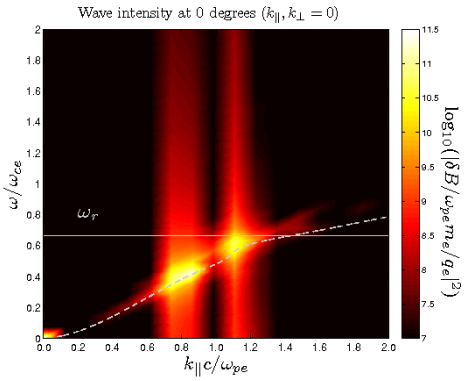

Figure 5.26: The fluctuating magnetic field intensity spectrum for the parallel propagating mode in the Maxwellian simulation, taken for a time corresponding to $1800 \leq \omega_{pe}t \leq 2000$.

Chapter 6

Summary and conclusions

The aim of this research project was to develop multi-dimensional, electromagnetic particle-in-cell (PIC) simulation codes using the C programming language. The codes would then be used to investigate the non-linear evolution of waves and instabilities in space plasmas, specifically those having kappa velocity distributions. The use of kappa velocity distributions in our simulations was motivated by the growing acceptance that the kappa distribution provides a more realistic model for particle velocity distributions in space, than the Maxwellian distribution (Hellberg et al., 2000; Livadiotis and McComas, 2009; Pierrard and Lazar, 2010).

To load the particle species into the simulation with the necessary 3D kappa velocity distribution, we generalised a previously devised method which sampled from the one-dimensional kappa distribution (Abdul and Mace, 2014). Similar to the kappa loader of Abdul and Mace (2014), the 3D kappa velocity loader developed for this thesis relied on the known method of sampling deviates from the closely related Student t distribution (Hofert, 2013). The equivalence of the 3D kappa and 3D Student t distributions was demonstrated in Section 2.3, after making the variable identifications in Equations 2.9 and 2.10 [see p. 26]. Our method is more efficient than the popular accept-reject method, since no deviates are rejected, and is also accurate and easy to implement. To the best of our knowledge, this method has not been used before.

To allow for the execution of large scale simulations, using many millions of plasma particles, the simulation code was made to run entirely on graphics processing units (GPUs) using CUDA (Compute Unified Device Architecture) C. This enabled the computational workload to be shared among available GPU cores, which reduced the simulation execution

times through concurrent computation of the simulation equations. While GPUs offer vast computing capabilities, a redesign of the PIC simulation algorithm was required (Decyk and Singh, 2011; Abreu et al., 2011; Kong et al., 2011) for the efficient GPU computation of our PIC code. Our GPU implementation of the PIC algorithm is discussed in Chapter 2.

Numerical noise remains a persistent problem for electromagnetic PIC simulations (Dawson, 1983). Noise in simulations arise due to the discrete particle nature of the PIC technique, as well as by virtue of having fewer particles in a Debye volume than physical plasmas. While adding more particles in a cell can reduce numerical noise, the total number of particles that can be used in a simulation is limited by the computer resources available. Alternatively, noise in PIC simulations can be reduced by using higher order particle shapes and weighting schemes (Birdsall and Langdon, 1985; Haugbølle et al., 2013; May et al., 2014).

In Chapter 3 we investigated the noise and energy conservation properties of our simulation code when varying the order of the weighting scheme used. The employed weighting schemes were chosen from the family of B-splines, which are often used in PIC simulations. The properties of the four lowest order B-splines was first discussed. The shape of the weighting functions provided by each B-spline was displayed in Figure 3.1 (p. 48). As discussed in Chapter 3, higher order splines produce wider weighting functions, resulting in the particle charge and current density being shared among more grid points [see Figure 3.1, p. 48]. This has the effect of reducing the high frequency fluctuations in the charge and current densities accumulated on the grid. Simulations were performed to investigate the impact of each weighting scheme on the noise and energy conservation of our code. Simulations were run for the first, second and third order B-splines. For each B-spline used, simulations were run using 16, 32 and 128 particles per cell, per species, while all other simulation parameters were kept identical.

Results were obtained for the temporal evolution of total energy, i.e., the sum of particle and field energies, for each simulation [see Figures 3.3 to 3.5, p. 53]. For simulations having an identical number of particles per cell, increasing the order of the spline resulted in a reduction in the deviation of total energy from its initial value, i.e., simulations exhibited better energy conservation when increasing the order of the weighting scheme. The order of the weighting scheme used, however, was not observed to influence the peak-to-peak fluctuations in total energy. When increasing the number of particles used per cell, a reduction in the peak-to-peak fluctuations in total energy was observed, and simulations displayed better energy conservation compared to equivalent simulations using fewer particles per cell.

While increasing both the order of the weighting scheme and the number of particles in a cell improved the accuracy of the simulation, it came at the cost of an increase in computational complexity. In Figure 3.6 (p. 54) we displayed the execution times for each of the simulations performed in Chapter 3. As was seen in Figure 3.6 (p. 54), the execution times of the simulations using the third order B-spline were approximately 1.8 times longer than those for the first order B-spline. The second order B-spline simulations ran approximately 1.4 times longer than the first order simulations. To balance accuracy and execution times, we opted to use the Triangular shaped cloud scheme (second order B-spline) for all simulations performed and discussed in this thesis.

In our first case study, discussed in Chapter 4, we applied our simulation code to the investigation of stable plasma waves propagating in plasmas having (a) isotropic kappa and (b) isotropic Maxwellian velocity distributions. Simulations were run for a plasma composed of an electron and singly charged ion species, immersed in a uniform, constant magnetic field. Three simulations were performed. In the first, both plasma species were modelled by a strongly non-thermal velocity distribution, i.e., both plasma species had isotropic kappa velocity distributions with $\kappa_e = \kappa_i = 2$. In the second simulation, the plasma was moderately non-thermal, i.e., the electrons and ions were modelled by isotropic kappa velocity distributions with $\kappa_e = \kappa_i = 4$. In the final simulation, both plasma species were modelled by isotropic Maxwellian velocity distributions, representing a plasma in thermodynamic equilibrium.

We measured the surface iso-contours of the electron and ion initial velocity distributions in each simulation, and compared them to the surface iso-contours of the 3D theoretical distribution functions used to model the particle velocity distributions [see Figures 4.2 to 4.4, pp. 76 - 78]. In all simulations, the surface iso-contours of the particle velocity distributions coincided with the theoretical distribution functions, Equations 4.40 and 4.41 (p. 73), respectively. This agreement served to confirm the correctness of our particle velocity loading algorithm, discussed in Section 2.3.

While the plasma configuration used in the simulations of Chapter 4 was expected to remain stable, slices through the electron initial and final velocity distribution in the v_x-, v_y- and v_z-directions indicated a deviation from initial loadings for the kappa simulations [see panels (a) and (b) of Figure 4.5, p. 80]. This deviation indicated that the kappa plasmas settled to a more stable equilibrium state than their initialised state, via the reduction of high energy electrons, i.e., thermalisation of the electron species occurred in the simulations using kappa distributions. This is consistent with the theory of the kappa distributions, which model a

metastable plasma state.

Fourier analysis of the electromagnetic (wave) intensities was performed in all simulations. The resulting fluctuation intensity spectra were displayed in Figures 4.6 to 4.8 (pp. 88 - 91), for the $\kappa_{i,e} = 2$, $\kappa_{i,e} = 4$ and Maxwellian simulations, respectively. A comparison was made between the regions of high wave intensity and the linear dispersion relations discussed in Section 4.2. For parallel and perpendicular wave propagation, the dispersion relations for waves propagating in kappa plasmas was used (see Section 4.2.1, p. 62). On the other hand, we used the cold plasma dispersion relations of Section 4.2.2 (p. 68) for waves propagating at oblique angles. In all simulations, the regions of intense field fluctuations were found to follow the curves satisfying the linear dispersion relations. This agreement between simulation results and linear theory provided validation of our simulation code, and also allowed for the identification of the wave modes responsible for producing the enhanced field fluctuations.

In all simulations, analysis of the field fluctuation spectra for parallel wave propagation [panel (a) in Figures 4.6 to 4.8] revealed the presence of the R- and L-modes, as well as Langmuir waves in the simulation. For oblique propagation [panels (b) to (d) of Figures 4.6 to 4.8], we observed the oblique R-, X-, L-O and R-X modes. At perpendicular propagation [panels (e) and (f) of Figures 4.6 to 4.8], we observed the X- and O-modes, as well as the electron and ion Bernstein waves. Since no sources of free energy were available in any of the simulations, the waves were produced through the random thermal motion of the particles in the presence of a magnetic field. As a consequence, for propagation from 0° to 63.4° in each simulation, the most intense field fluctuations were found in the vicinity of the electron plasma frequency. At perpendicular propagation, the magnetic field limited the motion of the plasma particles and particles performed gyrations about the magnetic field lines, introducing finite Larmor orbit effects. The parallel propagating Langmuir wave was found to produce the overall highest field fluctuation intensities, in the vicinity of the electron plasma frequency, in all simulations [see panel (a) of Figures 4.6 to 4.8, pp. 88 - 91].

A similar broad diffuse region of enhanced field fluctuations was observed at the propagation angles 0° to 63.4° in each simulation, centred around the electron plasma frequency. As the angle of propagation to the magnetic field increased from 0° to 63.4°, the regions of intense field fluctuations caused by the low frequency R-mode, were observed to shift to lower frequencies and extend to higher wave numbers. An increase in obliquity from 26.4° to 63.4° was also observed to increase the intensity of the field fluctuations produced by the oblique X-mode, at frequencies $2 \leq \omega/\omega_{ce} \leq 2.5$ and wave numbers $0 \leq |k|c/\omega_{pe} \leq 0.5$.

For perpendicular propagation, the regions of high wave intensity were observed to lie in close proximity to the linear dispersion relations of the Bernstein waves as well as the X- and O-modes. The most intense field fluctuations observed for perpendicular wave propagation occurred, in general, for the electron Bernstein mode propagating in the upper hybrid frequency band. The intensities of the electron Bernstein wave fluctuations decreased as the order of the modes increased above the upper hybrid mode. Ion Bernstein waves were also observed in each simulation, owing to the ion-electron mass ratio used, i.e., $m_i/m_e = 100$. For the ion Bernstein waves, the highest wave intensities were observed around the wave numbers at which the linear dispersion relations exhibited positive group velocity, i.e., $d\omega/dk > 0$. Similar to the electron Bernstein waves, as the order of the ion Bernstein waves increased, the intensities of the field fluctuations decreased; however, low intensity fluctuations were observed to extend to higher wave numbers for higher order ion Bernstein waves.

Varying the kappa values of the electrons, κ_e, and ions, κ_i, was observed to produce qualitatively similar intensity spectra, as expected. Increasing κ_e and κ_i, however, resulted in a reduction in the intensities of the field fluctuations, with the high intensity regions becoming more narrow band in frequency and wave number extent. For propagation angles from 0° to 63.4° [panels (a) to (d) in Figures 4.6 to 4.8, pp. 88 - 91], increasing electron and ion kappa yielded a reduction in the intensity of the diffuse field fluctuations, accompanied by a shift to higher wave numbers of the diffuse fluctuations for frequencies, $\omega/\omega_{ce} > 1.5$. At lower frequencies, $\omega/\omega_{ce} < 1.5$, increasing kappa produced more diffuse field fluctuations at high wave numbers $|k|c/\omega_{pe} \geq 3.0$ [compare Figures 4.6 to 4.8, pp. 88 - 91]. For the ion Bernstein waves, increasing κ_e and κ_i resulted in the high wave intensity regions shifting to higher wave numbers. We also observed an increase in low intensity field fluctuations at high wave numbers, $0.5 \leq |k|c/\omega_{pe} \leq 2.0$, and low frequencies, $\omega/\omega_{ce} \leq 0.1$, with increasing kappa values.

As discussed by Mace et al. (1998), the high energy tail of the kappa distribution enhances the role of single particle behaviour, leading to the increase in thermal fluctuations in the plasma. As a result, the simulations using low kappa values produced higher intensity field fluctuations. The kappa distribution also affected the electron and ion Bernstein wave dispersion relations, in a manner predicted by linear theory [see Figures 4.9 and 4.10, pp. 94 - 95]. The fluctuation spectra and intensities of the field fluctuations, however, is something not predicted by linear theory.

In our second case study, we applied our simulation code to the investigation of an electron-ion plasma immersed in a constant uniform magnetic field, where the electrons had thermal

anisotropy. We set the perpendicular component of the electron thermal energy to be greater than the parallel component, $T_{\perp e} > T_{\parallel e}$, to guarantee the whistler instability.

Whistler waves are electromagnetic cyclotron waves which propagate parallel to the ambient magnetic field at frequencies between the ion and electron cyclotron frequencies. Whistler waves grow through the cyclotron resonant interaction with an electron population having an excess of particles with a higher momentum than the wave [see discussion in Section 5.2, p. 104]. During cyclotron resonance, the unstable whistler waves reduce the electron pitch angles, depleting the resonant particles until a state of marginal stability is reached.

Five simulations were run to investigate the temperature anisotropy driven whistler instability. In the first two simulations, we imposed an electron temperature anisotropy of $T_{\perp e}/T_{\parallel e} = 2.05$. For the next three simulations, a higher electron temperature anisotropy of $T_{\perp e}/T_{\parallel e} = 3.0$ was used [see Table 5.1, p. 111].

For the first simulation having $T_{\perp e}/T_{\parallel e} = 2.05$, the electrons were modelled by a bi-kappa velocity distribution, with spectral index $\kappa_e = 3$. This value of κ_e corresponded to the peak maximum growth rate of the whistler instability driven by $T_{\perp e}/T_{\parallel e} = 2.05$. Simulation results were then compared to a simulation which modelled the electron species by a bi-Maxwellian velocity distribution. As was seen in Figure 5.2 (p. 114), for $T_{\perp e}/T_{\parallel e} = 2.05$, the instability growth rate displayed non-monotonic behaviour when varying electron kappa κ_e; however, decreasing κ_e resulted in an increase in the instability bandwidth. This increase in the range of unstable wave numbers for low κ_e is due to the kappa distribution having more electrons with a high enough velocity $\boldsymbol{v}_{\parallel}$ to produce the necessary Doppler shift in wave frequency required for strong wave-particle interaction.

The electron temperature anisotropy $T_{\perp e}/T_{\parallel e} = 2.05$ was found to not produce significant wave growth during both simulation runs [see Figures 5.3 and 5.4, pp. 117 - 118], and the full evolution of the whistler instability was not observed. Nevertheless, we performed spectral analysis of the magnetic field fluctuations to establish the presence of the whistler waves, and to compared results to theory.

In each case, the parallel propagating whistler wave was found to be the most intense, as expected from linear theory. The intensities of the whistler wave were observed to decrease with increasing angle to the magnetic field. The simulation using $\kappa_e = 3$ was found to produce more intense field fluctuations than the Maxwellian simulation, consistent with the linear theory prediction of higher growth rate for $\kappa_e = 3$ [see Figure 5.2, p. 114]. For parallel

propagation, both the wave number corresponding to the most intense field fluctuation, as well as the range of wave numbers of high fluctuation intensities, were found to agree well with the linear theory predictions of Figure 5.2, in both simulations.

We employed the linear dispersion relation for whistler waves in kappa plasmas [Equation (5.8), p. 108] for parallel propagation, while using the cold plasma dispersion relation [Equation (5.16), p. 119] at the oblique angles. In both simulations, the regions of high wave activity were observed to agree with the linear dispersion relations.

The simulations having $T_{\perp e}/T_{\parallel e} = 3$ produced larger growth rates than those with $T_{\perp e}/T_{\parallel e} = 2.05$ [see Figure 5.8, p. 126]. In contrast to the simulations using $T_{\perp e}/T_{\parallel e} = 2.05$ to drive the whistler instability, for this value of electron temperature anisotropy, the peak growth rate was found to maximise for the Maxwellian case, with growth rates decreasing monotonically for decreasing κ_e. Two simulations were run which modelled the electron species by a bi-kappa velocity distribution, using $\kappa_e = 2$ and $\kappa_e = 3$, respectively. Results were compared to a simulation which modelled the electron species with a bi-Maxwellian velocity distribution [see Table 5.1, p. 111].

Figures 5.9 to 5.11 (pp. 130 - 132), displayed the temporal evolution of the field and particle energies for the simulations having $T_{\perp e}/T_{\parallel e} = 3$. Due to the higher growth rates associated with the anositropy $T_{\perp e}/T_{\parallel e} = 3$, we were able to resolve the linear growth phase of the whistler instability (characterised by exponential growth in the field energies), the non-linear saturation phase (marked by the point at which the field energy stopped growing) as well as the post-saturation phase (marked by slowly varying energies). The presence of the superthermal electron population was found to change the behaviour of the whistler instability, where two phases of field growth were observed in the kappa simulations, with only a single growth phase observed for the Maxwellian simulation [see panels (a) and (b) of Figures 5.9 to 5.11, pp. 130 - 132].

While the peak growth rate maximised for the Maxwellian case, the field energies in the Maxwellian simulation demonstrated the smallest growth of the three cases [see panels (a) and (b) of Figure 5.11, p. 132]. This was likely due to the free energy in the Maxwellian simulation being depleted quicker, preventing the energies from growing to higher values. Consistent with the linear theory prediction of increased growth rates for increasing electron kappa, however, simulations having higher values of κ_e displayed exponential growth in field energies at earlier times, coupled with the instability saturating sooner. After instability saturation, the field energies exhibited a slower fall off as κ_e decreased.

Since the whistler waves grew in each simulation through the resonant interaction with the electron species, the electron kinetic energy in each simulation was observed to mirror that of the field energies, losing energy to the growing waves [see panel (c) of Figures 5.9 to 5.11, pp. 130 - 132]. In all simulations, energy was injected into the ion species through non-linear wave-particle interaction, and for the $\kappa_e = 3$ and Maxwellian cases, ion trapping was observed [see panel (d) of Figures 5.9 and 5.11, pp. 130 - 132]. Panel (f) of Figure 5.9 (p. 130) indicated that the simulations conserved energy to within 0.048% of its initial value, giving us confidence in the simulation results.

The cyclotron resonant interaction between the whistler wave and electrons decreases the perpendicular component of electron thermal energy $T_{\perp e}$, and increases the parallel component $T_{\parallel e}$. This leads to the eventual saturation of the instability. In Figures 5.12 to 5.14 (p. 134) we displayed the temporal evolution of the electron temperature anisotropy for each simulation. We observed a rapid decrease in the electron temperature anisotropy during the exponential growth phase for each case, and a slower fall off after the instability saturated. The electron temperature anisotropy never reached $T_{\perp e}/T_{\parallel e} = 1$ in any of the simulations, indicating that a quasi-equilibrium state was reached while the electrons still had $T_{\perp e} > T_{\parallel e}$.

The slices through the electron velocity distribution in the $v_\perp$ and $v_\parallel$ directions indicated an increase in the high energy electrons in the $v_\parallel$ direction, with a decrease in the high energy electrons in the $v_\perp$ direction [see Figures 5.15 to 5.17, p. 137]. This had the effect of reducing the electron temperature anisotropy, which was displayed in Figures 5.12 to 5.14 (p. 134). For the $v_\parallel$ slice in each case, we observed a deviation of the velocities from the initial loading, at a minimum velocity $|v_\parallel/v_{th,e}|$, which corresponded to the $v_{\parallel\mathrm{res}}$ predicted by Equation (5.18) (p. 135) for the wave number and frequency of peak growth rate.

Fourier analysis of the magnetic field (wave) intensities was carried out, where we again observed good agreement between the regions of intense fluctuations and the whistler dispersion relations, in all cases. The regions of highest fluctuation intensity (yellow colouring) for the parallel wave in all cases, was found to agree with the linear theory predictions of Figure 5.8 for the range of unstable wave numbers. A decrease of this region in wave number extent was also observed for increasing κ_e [compare panel (a) of Figures 5.18 to 5.20, pp. 141 - 143].

As obliquity increased, we observed a drastic reduction in the wave intensities in all simulations, with enhanced field fluctuations occurring for a narrower band of frequencies, which shifted to lower wave numbers with an increase in propagation angle [compare panels (b) to (d), respectively, of Figures 5.18 to 5.20, pp. 141 - 143]. While the Maxwellian plasma

displayed the smallest wave number range of high intensity fluctuations and the lowest peak fluctuation intensity for parallel wave, intense field fluctuations were observed up to the highest propagation angle of the three cases.

In Figures 5.21 to 5.23, we displayed the fluctuation spectra as a function of $k_{\parallel}c/\omega_{pe}$ and $k_{\perp}c/\omega_{pe}$. Low values of electron kappa were shown to enhance thermal fluctuations, increasing the diffuse field fluctuations in the figures [compare Figures 5.21 to 5.23, pp. 146 - 148]. On the other hand, increasing electron kappa was found to produce high intensity field fluctuations at earlier times, due to the higher growth rates. As the angle of propagation increased, the intensity of the field fluctuations decreased. The Maxwellian simulation was shown to excite intense wave fluctuations up to the highest propagation angles with respect to the magnetic field, as was seen previously in Figure 5.20 (p. 143).

At the end of each simulation, the fluctuation spectra displayed whistler waves with a wave number gap between regions of high intensity field fluctuations. These regions could be related to banded whistler waves which are observed in the terrestrial magnetosphere and are responsible for banded chorus (Bell et al., 2009) and plasmaspheric hiss (Lui et al., 2011).

The agreement between our simulation results and theory lends validity to our simulation code as well as confirms the correctness of the kappa velocity loader we devised. Our results also motivate the use of simulations in the study of plasma waves, where the non-linear regime of wave evolution can be investigated. It is especially useful for the study of waves in plasmas having kappa velocity distributions, where the evaluation of the dielectric tensor elements becomes mathematically difficult at oblique angles, due to the non-separable nature of the kappa distribution.

Appendix A

In Section 2.6, a discussion of the method used to update the electromagnetic fields in our simulation was given. During each time step, Maxwell's equations are evaluated in Fourier space and the electromagnetic fields in the simulation are found. Particle-in-cell simulations employ a discretisation of the spatial domain by creating a grid on which field values, as well as their sources, are sampled. Since the fields are only known and evaluated at discrete locations, a discretised version of Maxwell's equations is used and finite difference techniques are employed to approximate the spatial derivatives. In this Appendix, we derive the centred difference forms of the difference operators in Fourier space, i.e., we derive the finite difference forms of $\boldsymbol{\nabla} \rightarrow i\boldsymbol{k}$ and $\nabla^2 \rightarrow -k^2$.

The full set of Maxwell's equations, in S.I. units, are

$$\boldsymbol{\nabla}\cdot\boldsymbol{E}(\boldsymbol{r},t) = \frac{\rho(\boldsymbol{r},t)}{\epsilon_0}, \tag{A.1}$$

$$\boldsymbol{\nabla}\cdot\boldsymbol{B}(\boldsymbol{r},t) = 0, \tag{A.2}$$

$$\boldsymbol{\nabla}\times\boldsymbol{E}(\boldsymbol{r},t) = -\frac{\partial\boldsymbol{B}(\boldsymbol{r},t)}{\partial t}, \tag{A.3}$$

$$\boldsymbol{\nabla}\times\boldsymbol{B}(\boldsymbol{r},t) = \mu_0\boldsymbol{J}(\boldsymbol{r},t) + \frac{1}{c^2}\frac{\partial\boldsymbol{E}(\boldsymbol{r},t)}{\partial t}, \tag{A.4}$$

with $\boldsymbol{r} = (x, y)$, ϵ_0 and μ_0 are the permittivity and permeability of free space, respectively, and c is the speed of light. As discussed in Section 2.6, to aid in the evaluation of Maxwell's equations, the electromagnetic fields are expressed as the sum of a curl-free component (the longitudinal component, L) and a divergenceless component (the transverse component, T), defined for an arbitrary vector $\boldsymbol{A} = \boldsymbol{A}_L + \boldsymbol{A}_T$ as (Sydora, 1999)

$$\boldsymbol{\nabla} \times \boldsymbol{A}_L = 0, \tag{A.5}$$

$$\boldsymbol{\nabla} \cdot \boldsymbol{A}_T = 0. \tag{A.6}$$

To calculate the longitudinal electric field $\boldsymbol{E}_L(x, y)$, where we omit the time parameter for clarity, we use

$$\begin{aligned} \boldsymbol{\nabla} \cdot \boldsymbol{E}(x, y) &= \frac{\rho(x, y)}{\epsilon_0}, \\ \boldsymbol{\nabla} \cdot (\boldsymbol{E}_L(x, y) + \boldsymbol{E}_T(x, y)) &= \frac{\rho(x, y)}{\epsilon_0}, \\ \boldsymbol{\nabla} \cdot \boldsymbol{E}_L(x, y) &= \frac{\rho(x, y)}{\epsilon_0}. \end{aligned}$$

Since $\boldsymbol{\nabla} \times \boldsymbol{E}_L(x, y) = 0$, we define a scalar potential $\phi(x, y)$, such that

$$\boldsymbol{E}_L(x, y) = -\boldsymbol{\nabla} \phi(x, y), \tag{A.7}$$

where $\boldsymbol{\nabla} \times (-\boldsymbol{\nabla} \phi(x, y)) = 0$, follows identically. Thus, using Equation (A.1), we have

$$\boldsymbol{\nabla} \cdot \boldsymbol{\nabla} \phi(x, y) = -\frac{\rho(x, y)}{\epsilon_0}. \tag{A.8}$$

We now write the Fourier transforms of the real space quantities $\boldsymbol{E}_L(x, y), \phi(x, y)$ and $\rho(x, y)$ as $\boldsymbol{E}_L(k_x, k_y), \phi(k_x, k_y)$ and $\rho(k_x, k_y)$, respectively. Hence in Fourier space, Equations (A.7) and (A.8) are given, respectively, as

$$\boldsymbol{E}_L(k_x, k_y) = -ik_x \phi(k_x, k_y)\hat{x} - ik_y \phi(k_x, k_y)\hat{y}, \tag{A.9}$$

$$\phi(k_x, k_y) = \frac{\rho(k_x, k_y)}{\epsilon_0 (k_x^2 + k_y^2)}. \tag{A.10}$$

After discretisation in space, Equations (A.9) and (A.10) are used to calculate the longitudinal electric field in the simulation.

We now turn to a discussion of these equations in their discrete form. We adopt the convention that $X_j \pm \Delta x \equiv X_{j\pm1}$ and $Y_k \pm \Delta y \equiv Y_{k\pm1}$ denote the locations of the grid points, where $(X_j, Y_k) = (j\Delta x, k\Delta y)$. The centred difference forms of Equations (A.7) and (A.8) are

$$\begin{aligned} \boldsymbol{E}_L(X_j, Y_k) = &- \frac{\phi(X_{j+1}, Y_k) - \phi(X_{j-1}, Y_k)}{2\Delta x}\hat{x} \\ &- \frac{\phi(X_j, Y_{k+1}) - \phi(X_j, Y_{k-1})}{2\Delta y}\hat{y}, \end{aligned} \tag{A.11}$$

and

$$\begin{aligned} -\frac{\rho(X_j, Y_k)}{\epsilon_0} = &\left[\frac{\phi(X_{j+1}, Y_k) - 2\phi(X_j, Y_k) + \phi(X_{j-1}, Y_k)}{\Delta x^2}\right] \\ &+ \left[\frac{\phi(X_j, Y_{k+1}) - 2\phi(X_j, Y_k) + \phi(X_j, Y_{k-1})}{\Delta y^2}\right]. \end{aligned} \tag{A.12}$$

We now assume all quantities vary in Fourier space as $\propto f(k_x, k_y)\ \exp(ik_xX_j)\ \ \exp(ik_yY_k)$ and separate Equation (A.12) as $I_1 = I_2 + I_3$ for clarity. The Fourier representation of Equation (A.12) is

$$I_1 = -\frac{\rho(k_x, k_y)\ \exp(ik_xX_j)\ \exp(ik_yY_k)}{\epsilon_0}, \tag{A.13}$$

the first bracket on the right hand side of Equation (A.12) becomes

$$\begin{aligned} I_2 =&\frac{\phi(k_x, k_y)\ \exp[ik_x(X_k + \Delta x)]\ \exp(ik_yY_k)}{\Delta x^2} - \frac{2\phi(k_x, k_y)\ \exp(ik_xX_j)\ \exp(ik_yY_k)}{\Delta x^2} \\ &+ \frac{\phi(k_x, k_y)\ \exp[ik_x(X_j - \Delta x)]\ \exp(ik_yY_k)}{\Delta x^2}, \\ =&\frac{\phi(k_x, k_y)\ \exp(ik_xX_j)\ \exp(ik_yY_k)\ [\ \exp(ik_x\Delta x) - 2 + \ \exp(-ik_x\Delta x)]}{\Delta x^2}, \end{aligned} \tag{A.14}$$

and similarly the second bracket is given as

$$I_3 = \frac{\phi(k_x, k_y)\ \exp(ik_x X_j)\ \exp(ik_y Y_k)\,[\ \exp(ik_y \Delta y) - 2 + \ \exp(-ik_y \Delta y)]}{\Delta y^2}. \tag{A.15}$$

After factoring out the terms containing, $\exp(ik_x X_j)\ \exp(ik_y Y_k)$, Equations (A.13) to (A.15), become

$$\begin{aligned} -\frac{\rho(k_x, k_y)}{\epsilon_0} =& \phi(k_x, k_y) \left[\frac{\exp(ik_x \Delta x) - 2 + \ \exp(-ik_x \Delta x)}{\Delta x^2} \right. \\ & \left. + \ \frac{\exp(ik_y \Delta y) - 2 + \ \exp(-ik_y \Delta y)}{\Delta y^2} \right], \\ =& \phi(k_x, k_y) \left[\frac{-2 + 2\ \cos(k_x \Delta x)}{\Delta x^2} + \frac{-2 + 2\ \cos(k_y \Delta y)}{\Delta y^2} \right], \end{aligned} \tag{A.16}$$

where we used the following identity in the last step of Equation (A.16) (Stewart, 2003)

$$\cos(\theta) = \frac{\exp(i\theta) + \exp(-i\theta)}{2}.$$

Equation (A.16) can be further simplified using (Stewart, 2003)

$$\sin^2(\theta) = \frac{1 - \cos\ (2\theta)}{2}, \tag{A.17}$$

which results in

$$\frac{\rho(k_x, k_y)}{\epsilon_0} = \phi(k_x, k_y) \left[\frac{4\ \sin^2(k_x \Delta x/2)}{\Delta x^2} + \frac{4\ \sin^2(k_y \Delta y/2)}{\Delta y^2} \right]. \tag{A.18}$$

We now make the following variable identifications

$$\begin{aligned} \tilde{K}_x^2 &= \frac{4\,\sin^2(k_x\Delta x/2)}{\Delta x^2}, \\ \tilde{K}_y^2 &= \frac{4\,\sin^2(k_y\Delta y/2)}{\Delta y^2}, \end{aligned} \tag{A.19}$$

and write Equation (A.18) as

$$\phi(k_x, k_y) = \frac{\rho(k_x, k_y)}{\epsilon_0\left(\tilde{K}_x^2 + \tilde{K}_y^2\right)}. \tag{A.20}$$

Comparing Equation (A.20) to Equation (A.10), we see that the quantities $\tilde{K}_x$ and $\tilde{K}_y$ act as the centred difference forms of the Fourier space difference operators k_x^2 and k_y^2. Following a similar procedure, it can be shown that Equation (A.11) reduces to

$$\boldsymbol{E}_L(k_x, k_y) = -i\tilde{k}_x\phi(k_x, k_y)\hat{x} - i\tilde{k}_y\phi(k_x, k_y)\hat{y}, \tag{A.21}$$

where

$$\begin{aligned} i\tilde{k}_x &= ik_x\left[\frac{\sin(k_x\Delta x)}{k_x\Delta x}\right], \\ i\tilde{k}_y &= ik_y\left[\frac{\sin(k_y\Delta y)}{k_y\Delta y}\right], \end{aligned} \tag{A.22}$$

and on comparison with Equation (A.9) we see that these act as the centred difference forms of ik_x and ik_y. Hence, as a consequence of moving from continuous space to one in which we employ a discrete sampling, the effect of the grid is to change the continuous space operators $\boldsymbol{\nabla} \rightarrow i\boldsymbol{k}$ and $\nabla^2 \rightarrow -k^2$ to those defined by Equations (A.19) and (A.22) (Birdsall and Langdon, 1985; Tajima, 1989). The definitions in Equations (A.19) and (A.22) hold for the operator $i\boldsymbol{k}$, which appears in the Fourier space form of Equations (A.3) and (A.4), and can be derived by following a similar procedure to that outlined above. During our simulations, to calculate the electromagnetic fields using a discretised version of Maxwell's equations in Fourier space, we employ the definitions given in Equations (A.19) and (A.22).

Bibliography

Abdul, R. F. and Mace, R. L. (2014). A method to generate kappa distributed random deviates for particle-in-cell simulations. *Comput. Phys. Comm.*, 185(10):2383 – 2386.

Abreu, P., Fonseca, R. A., Pereira, J. M., and Silva, L. O. (2011). PIC codes in new processors: A full relativistic PIC code in CUDA-enabled hardware with direct visualization. *IEEE Trans. Plas. Sci.*, 39(2):675 – 685.

Albert, J. M. and Bortnik, J. (2009). Nonlinear interaction of radiation belt electrons with electromagnetic ion cyclotron waves. *Geophys. Res. Let.*, 36(12):L12110.

Anderson, B. J. and Fuselier, S. A. (1994). Response of thermal ions to electromagnetic ion cyclotron waves. *J. Geophys. Res.*, 99(A10):19413 – 19425.

Aydemir, A. Y. (1994). A unified Monte Carlo interpretation of particle simulations and applications to non-neutral plasmas. *Phys. Plas.*, 1(4):822.

Bell, T. F., Inan, U. S., Haque, N., and Pickett, J. S. (2009). Source regions of banded chorus. *Geophys. Res. Lett.*, 36:L11101.

Bellan, P. M. (2013). Circular polarization of obliquely propagating whistler wave magnetic field. *Phys. Plas.*, 20(8):082113.

Benson, F. R., Osherovich, V. A., Fainberg, J., Viñas, A. F., and Rupert, D. R. (2001). An interpretation of banded magnetospheric radio emissions. *J. Geophys. Res.*, 106(A7):13179 – 13190.

Benson, F. R., Viñas, A. F., Osherovich, V. A., Fainberg, J., Purser, C. M., Adrian, M. L., Galkin, I. A., and Reinisch, B. W. (2013). Magnetospheric electron-velocity-distribution function information from wave observations. *J. Geophys. Res.*, 118(8):5039 – 5049.

Bernstein, I. B. (1958). Waves in a plasma in a magnetic field. *Phys. Rev.*, 109:10 – 21.

Bertrand, P. (2005). Vlasov code applications. In *Proceedings of ISSS-7*.

Birdsall, C. K. (1991). Particle-in-cell charged-particle simulations, plus monte carlo collisions with neutral atoms, PIC-MCC. *IEEE Trans. Plas. Sci.*, 19(2):65 – 85.

Birdsall, C. K. and Fuss, D. (1969). Clouds-in-clouds, clouds-in-cells physics for many body plasmas. *J. Comput. Phys.*, 3:494 – 511.

Birdsall, C. K. and Langdon, A. B. (1985). *Plasma Physics via Computer Simulation*. McGraw-Hill Book Company.

Blandford, R. and Eichler, D. (1987). Particle acceleration at astrophysical shocks: A theory of cosmic ray origin. *Phy. Reports*, 154(1):1 – 75.

Boris, J. P. (1970). Relativistic plasma simulation-optimization of a hybrid code. In *Proceedings of the Fourth Conference on Numerical Simulation of Plasmas*, page 3.

Box, G. E. P. and Muller, M. E. (1958). A note on the generation of random normal deviates. *Ann. Math. Stat.*, 29(2):610 – 611.

Brecht, S. H., Lyon, J. G., Fedder, J. A., and Hain, K. (1981). A simulation study of the east-west IMF effects on the magnetosphere. *Geophys. Res. Lett.*, 8(4):397 – 400.

Bryant, D. A. (1996). Debye length in a kappa-distributed plasma. *J. Plas. Phys.*, 56(1):87 – 93.

Büchner, J. (2007). Vlasov-code simulation. In *Advanced methods for space simulations*, pages 23 – 46. Terra Scientific Publishing Co.

Buneman, O. (1959). Dissipation of currents in ionized media. *Phys. Rev.*, 115(3):503 – 517.

Buneman, O., Barnes, C. W., Green, J. C., and Nielson, D. E. (1980). Principles and capabilities of 3D, E-M particle simulations. *J. Comput. Phys.*, 38:1 – 44.

Burau, H., Widera, R., Hönig, W., Juckeland, G., Debus, A., Klunge, T., Schramm, U., Cowan, T. E., Sauerbrey, R., and Bussmann, M. (2010). PIConGPU: A fully relativistic particle-in-cell code for a gpu cluster. *IEEE Trans. Plas. Sci.*, 38(10):2831 – 2839.

Burger, P. (1967). Elastic collisions in simulating one-dimensional plasma diodes on the computer. *Phys. Fluids*, 10:658 – 666.

Burgess, D. (2006). Interpreting multipoint observations of substructure at the quasi-perpendicular bow shock: Simulations. *J. Geophys. Res.*, 111:A10210.

Camporeale, E. (2015). Resonant and nonresonant whistlers-particle interaction in the radiation belts. *Geophys. Res. Let.*, 42(9):3114 – 3121.

Camporeale, E. and Zimbardo, G. (2015). Wave-particle interactions with parallel whistler waves: Nonlinear and time-dependent effects revealed by particle-in-cell simulations. *Phys. Plas.*, 22(9):092104.

Cattaert, T., Hellberg, M. A., and Mace, R. L. (2007). Oblique propagation of electromagnetic waves in a kappa-Maxwellian plasma. *Phys. Plas.*, 14(8):082111.

Cattell, C., Wygant, J. R., Goetz, K., Kersten, K., Kellogg, P. J., von Rosenvinge, T., Bale, S. D., Roth, I., Temerin, M., Hudson, M. K., Mewaldt, R. A., Wiedenbeck, M., Maksimovic, M., Ergun, R., Acuna, M., and Russell, C. T. (2008). Discovery of very large amplitude whistler-mode waves in earth's radiation belts. *Geophys. Res. Let.*, 35(1):L01105.

Chen, F. F. (1984). *Introduction to plasma physics and Controlled Fusion*. Plenum Publishing Corporation, second edition.

Chen, G., Chacón, L., and Barnes, D. C. (2012). An efficient mixed-precision, hybrid CPU-GPU implementation of a nonlinearly implicit one-dimensional particle-in-cell algorithm. *J. Comput. Phys.*, 231(16):5374 – 5388.

Cheng, C. Z. and Knorr, G. (1976). The integration of the Vlasov equation in configuration space. *J. Comput. Phys.*, 22(3):330 – 351.

Christon, S. P. (1987). A comparison of the Mercury and Earth magnetospheres: Electron measurements and substorm time scales. *Icarus*, 71(3):448 – 471.

Christon, S. P., Mitchell, D. G., Williams, D. J., Frank, L. A., Huang, C. Y., and Eastman, T. E. (1988). Energy spectra of plasma sheet ions and electrons from ≈ 50 ev/e to ≈ 1 mev during plasma temperature transitions. *J. Geophys. Res.*, 93(A4):2562 – 2572.

Christon, S. P., Williams, D. J., Mitchell, D. J., Frank, L. A., and Huang, C. Y. (1989). Spectral characteristics of plasma sheet ion and electron populations during undisturbed geomagnetic conditions. *J. Geophys. Res.*, 94(A10):13409 – 13424.

Collier, M. R. (1993). On generating kappa-like distribution functions using velocity space Lévy flights. *Geophys. Res. Lett.*, 20(15):1531 – 1534.

Collier, M. R. and Hamilton, D. C. (1995). The relationship between kappa and temperature in energetic ion spectra at Jupiter. *Geophys. Res. Lett.*, 22(3):303 – 306.

Cooley, J. W. and Turkey, J. W. (1965). An algorithm for the machine calculation of complex fourier series. *Math. Comput.*, 19:297 – 301.

Crawford, F. W. (1965). A review of cyclotron harmonic phenomena in plasmas. *Nucl. Fusion*, 5(1):73 – 84.

Darwin, C. G. (1920). The dynamical motions of charged particles. *Philos. Mag.*, 39(233):537 – 551.

Dawson, J. M. (1962). One-dimensional plasma model. *Phys. Fluids*, 5(4):445 – 459.

Dawson, J. M. (1964). Thermal relaxation in a one-species, one-dimensional plasma. *Phys. Fluids*, 7(3):419 – 425.

Dawson, J. M. (1983). Particle simulation of plasmas. *Rev. Mod. Phys*, 55(2):403 – 447.

Dawson, J. M., Decyk, V. K., Sydora, R., and Liewer, P. (1993). High-performance computing and plasma physics. In *Physics Today*, pages 64 – 70.

Decyk, V. K. and Singh, T. V. (2011). Adaptable particle-in-cell algorithms for graphical processing units. *Comput. Phys. Comm.*, 182:641 – 648.

Denton, R. and Kotschenreuther, M. (1995). δf algorithm. *J. Comput. Phys.*, 119(2):283 – 294.

Devine, P. E. and Chapman, S. C. (1995). One- and two-dimensional simulations of whistler mode waves in an anisotropic plasma. *J. Geophys. Res.*, 100:17189 – 17203.

Divine, N. and Garrett, H. B. (1983). Charged particle distributions in Jupiter's magnetosphere. *J. Geophys. Res.*, 88(A9):6889 – 6903.

Dougherty, J. P. and Monaghan, J. J. (1966). The theory of resonances observed in ionograms taken by sounders above the ionosphere. *Proc. R. Soc. London Ser. A*, 289(1417):214 – 234.

Drury, L. O. (1983). An introduction to the theory of diffusive shock acceleration of energetic particles in tenuous plasmas. *Rep. Prog. Phys.*, 46:973 – 1027.

Dubinin, E., k. Sauer, and Mckenzie, J. F. (2003). Nonlinear stationary whistler waves and whistler solitons (oscillitons). exact solutions. *J. Plas. Phys.*, 69(4):305 – 330.

Dum, C. T. (1984). Simulation models for space plasmas and boundary conditions as a key to their design and analysis. In *Computer Simulation of Plasmas*, pages 303 – 375. Terra Scientific Publishing Co.

Eliasson, B. and Lazar, M. (2015). Nonlinear evolution of the electromagnetic electron-cyclotron instability in bi-kappa distributed plasma. *Phys. Plas.*, 22(6):062109.

Erlandson, R. E. and Ukhorskiy, A. J. (2001). Observations of electromagnetic ion cyclotron waves during geomagnetic storms: Wave occurrence and pitch angle scattering. *J. Geophys. Res.*, 106(A3):3883 – 3895.

Forslund, D. W. (1985). Fundamentals of plasma simulation. *Space Sci. Rev.*, 42:3 – 16.

Fredricks, R. W. (1968). Structure of the Bernstein modes for large values of the plasma parameter. *J. Plas. Phys.*, 2:197 – 206.

Fried, B. D. and Conte, S. D. (1961). *The plasma dispersion function.* Academic, New York.

Fu, X. R., Cowee, M. M., Liu, K., Gary, S. P., and Winske, D. (2014). Particle-in-cell simulations of velocity scattering of an anisotropic electron beam by electrostatic and electromagnetic instabilities. *Phys. Plas.*, 21(4):042108.

Gao, X., Thorne, R. M., Bortnik, J., Angelopoulos, V., Lu, Q., Tao, X., and Wang, S. (2014). Statistical results describing the bandwidth and coherence coefficient of whistler mode waves using THEMIS waveform data. *J. Geophys. Res. Space Phys.*, 119:8992 – 9003.

Gary, S. P. and Cairns, I. H. (1999). Electron temperature anisotropy instabilities: Whistler, electrostatic and z mode. *J. Geophys. Res.*, 104(A9):19835 – 19842.

Gary, S. P., E.McKean, M., Winske, D., Anderson, B. J., Denton, R. E., and Fuselier, S. A. (1994). The proton cyclotron instability and the anisotropy β inverse correlation. *J. Geophys. Res.*, 99(A4):5903 – 5914.

Gary, S. P., Liu, K., and Winske, D. (2011). Whistler anisotropy instability at low electron β: Particle-in-cell simulations. *Phys. Plas.*, 18(8):082902.

Gary, S. P., Liu, K., Winske, D., and Denton, R. E. (2010). Ion Bernstein instability in the terrestrial magnetosphere: Linear dispersion theory. *J. Geophys. Res.*, 115:A12209.

Gary, S. P. and Wang, J. (1996). Whistler instability: Electron anisotropy upper bound. *J. Geophys. Res.*, 101(A5):10749 – 10754.

Gary, S. P., Winske, D., and Hesse, M. (2000). Electron temperature anisotropy instabilities: Computer simulations. *J. Geophys. Res.*, 105(A5):10751 – 10759.

Gendrin, R. (1975). Waves and wave-particle interactions in the magnetosphere: A review. *Space Sci. Rev.*, 18(2):145 – 200.

Gloeckler, G. and Hamilton, D. C. (1987). AMPTE ion composition results. *Phys. Scripta*, T18:73.

Godfrey, B. B. (1974). Numerical Cherenkov instabilities in electromagnetic particle codes. *J. Comput. Phys.*, 15:504 – 521.

Gómez, D. O., Mininni, P. D., and Dmitruk, P. (2005). MHD simulations and astrophysical applications. *Adv. Space Res.*, 35:899 – 907.

Gradshteyn, I. S. and Ryzhik, I. M. (2007). *Table of Integrals, Series and Products*. Elsevier Inc., seventh edition.

Groth, C. P. T., Zeeuw, D. L. D., Gombosi, T. I., and Powell, K. G. (2000). Global three-dimensional MHD simulation of a space weather event: CME formation, interplanetary propagation, and interaction with the magnetosphere. *J. Comput. Phys.*, 105:25 053.

Gurnett, D. A. and Bhattacharjee, A. (2005). *Introduction to plasma physics, with space and laboratory applications*. Cambridge university press.

Hasegawa, A., Mima, K., and Duong-van, M. (1985). Plasma distribution function in a superthermal radiation field. *Phys. Rev. Lett.*, 54(24):2608 – 2610.

Haugbølle, T., Frederiksen, J. T., and Å. Nordlund (2013). Photon-plasma: A modern high-order particle-in-cell code. *Phys. Plas.*, 20:062904–1 – 062904–24.

Hellberg, M. A. and Mace, R. L. (2002). Generalised plasma dispersion function for a plasma with kappa-Maxwellian velocity distribution. *Phys. Plas.*, 9(5):1495 – 1504.

Hellberg, M. A., Mace, R. L., Baluku, T. K., Kourakis, I., and Saini, S. (2009). Comment on " mathematical and physical aspects of kappa velocity distribution" [phys. plasma 14, 110702 (2007)]. *Phys. Plas.*, 16:094701.

Hellberg, M. A., Mace, R. L., and Cattaert, T. (2005). Effects of superthermal particles on waves in magnetized space plasmas. *Space Sci. Rev.*, 121:127 – 139.

Hellberg, M. A., Mace, R. L., and Verheest, F. (2000). Waves in non-Maxwellian plasmas with excess superthermal particles. *Waves in Dusty, Solar and Space Plasmas*, 537:348 – 355.

Henning, F. D., Mace, R. L., and Pillay, S. R. (2011). Electrostatic Bernstein waves in plasmas whose electrons have a dual kappa distribution: Applications to the Saturnian magnetosphere. *J. Geophys. Res.*, 116.

Hockney, R. W. (1965). A fast direct solution of poisson's equation using Fourier analysis. *J. Assoc. Comput. Mach.*, 12:95 – 113.

Hockney, R. W. and Eastwood, J. W. (1981). *Computer Simulation Using Particles*. New York: McGraw-Hill.

Hofert, M. (2013). On sampling from the multivariate t distribution. *The R Journal*, 5(2):129 – 136.

Hoppe, M. M., Russell, C. T., Eastman, T. E., and Frank, L. A. (1982). Characteristics of the ULF waves associated with upstream ion beams. *J. Geophys. Res.*, 87(A2):643 – 650.

Hoppe, M. M., Russell, C. T., Frank, L. A., Eastman, T. E., and Greenstadt, E. W. (1981). Upstream hydromagnetic waves and their association with backstreaming ion populations: ISEE 1 and 2 observations. *J. Geophys. Res.*, 86(A6):4471 – 4492.

Huff, R. W., Dawson, J. M., and Culler, G. (1982). Computer modeling in plasma physics on the parallel-architecture CHI computer. In *Parallel Computations*, page 365. Academic Press.

Hughes, R. S., Wang, J., Decyk, V. K., and Gary, S. P. (2016). Effects of variations in electron thermal velocity on the whistler anisotropy instability: Particle-in-cell simulations. *Phys. Plas.*, 23(4):042106.

Ichimaru, S. (1973). *Basic Principles of Plasma Physics: A statistical Approach*. Westview Press.

Ishihara, A. (1971). *Statistical Physics*. Academic Press, Inc.

Janhunen, P., Olsson, A., Vaivads, A., and Peterson, W. K. (2003). Generation of Bernstein waves by ion shell distributions in the auroral region. *Ann. Geophys.*, 21:881 – 891.

Jones, F. C. and Ellison, D. C. (1991). The plasma physics of shock acceleration. *Space Sci. Rev.*, 58(1):259 – 346.

Kamimura, T., Wagner, T., and Dawson, J. M. (1978). Simulation study of Bernstein modes. *Phys. Fluids*, 21(7):1151 – 1167.

Kennel, C. F. and Ashour-Abdalla, M. (1982). Electrostatic waves and the strong diffusion of magnetospheric electrons. In *Magnetospheric Plasma Physics*, pages 244 – 344.

Kennel, C. F. and Petschek, H. E. (1966). Limit on stably trapped particle fluxes. *J. Geophys. Res.*, 71(1):1 – 28.

Koen, E. J., Collier, A. B., and Maharaj, S. K. (2012). Particle-in-cell simulations of beam-driven electrostatic waves in a plasma. *Phys. Plas.*, 19:042101.

Kong, X., Huang, M. C., Ren, C., and Decyk, V. K. (2011). Particle-in-cell simulations with charge-conserving current deposition on graphic processing units. *J. Comput. Phys.*, 230:1676 – 1685.

Kotz, S. and Nadarajah, S. (2004). *Multivariate t Distributions and Their Applications*. Cambridge University Press.

Lacombe, C., Alexandra, O., Matteini, L., Santolk, O., Cornilleau-Wehrlin, N., Mangeney, A., de Conchy, Y., and Maksimovic, M. (2014). Whistler mode waves and the electron heat flux in the solar wind: Cluster observations. *Astrophys. J.*, 796:5.

Langdon, A. B. (1970). Effect of the spatial grid in simulation plasmas. *J. Comput. Phys.*, 6:247 – 267.

Langdon, A. B. and Birdsall, C. K. (1970). Theory of plasma simulation using finite-size particles. *Phys. Fluids*, 13:2115 – 2122.

Langdon, A. B. and Dawson, J. M. (1967). Investigations of a sheet model for a bounded plasma field and radiation. In *Proc. 1st Conf. Num. Sim. Plasmas*, pages 39 – 40.

Langdon, A. B. and Lasinski, B. F. (1976). Electromagnetic and relativistic plasma simulation models. *Meth. Comput. Phys.*, 16:327 – 366.

Lapenta, G. (2012). Particle simulations of space weather. *J. Comput. Phys.*, 231(3):795 – 821.

Leboeuf, J. N., Tajima, T., Kennel, C. F., and Dawson, J. M. (1978). Global simulations of the time-dependent magnetosphere. *Geophys. Res. Lett.*, 5:609.

Leitner, M., Leubner, M. P., and Vörös, Z. (2011). Creating kappa-like distributions from a galton board. *Physica A*, 390:1248 – 1257.

Leubner, M. P. (2002). A nonextensive entropy approach to kappa-distributions. *Astrophys. Space Sci.*, 282:573 – 579.

Liewer, P. C. and Decyk, V. K. (1989). A general concurrent algorithm for plasma particle-in-cell simulation codes. *J. Comput. Phys.*, 85:302 – 322.

Livadiotis, G. (2014). Introduction to special section on origins and properties of kappa distributions: Statistical background and properties of kappa distributions in space plasmas. *J. Geophys. Res*, 120:1607 – 1619.

Livadiotis, G. (2017). Statistical origin and properties of kappa distributions. *J. Phys Conf. Series*, 900:012014.

Livadiotis, G. and McComas, D. J. (2009). Beyond kappa distributions: Exploring tsallis statistical mechanics in space plasmas. *J. Geophys.Res.*, 114(A11105):1 – 21.

Livadiotis, G. and McComas, D. J. (2011). Invariant kappa distribution in space plasmas out of equilibrium. *The AstroPhys. Journal*, 741:88.

Livadiotis, G. and McComas, D. J. (2013). Understanding kappa distributions: A toolbox for space science and astrophysics. *Space Sci. Rev*, 175:183 – 214.

Lu, Q., Zhou, L., and Wang, S. (2010). Particle-in-cell simulations of whistler waves excited by an electron κ distributions in space plasma. *J. Geophys.Res.*., 115:A02213.

Lui, K., Gary, S. P., and Winske, D. (2011). Excitation of magnetosonic waves in the terrestrial magnetosphere: Particle-in-cell simulations. *J. Geophys. Res.*, 116:A07212.

Mace, R. L. (1996). A dielectric tensor for a uniform magnetoplasma with a generalised Lorentzian distribution. *J. Plas. Phys.*, 55(3):415 – 429.

Mace, R. L. (1998). Whistler instability enhanced by suprathermal electrons within the earth's foreshock. *J. Geophys. Res.*, 103(A7):14643 – 14654.

Mace, R. L. (2003). A Gordeyev integral for electrostatic waves in a magnetized plasma with a kappa velocity distribution. *Phys. Plas.*, 10(6):2181 – 2193.

Mace, R. L. (2004). Generalized electron Bernstein modes in a plasma with a kappa distribution. *Phys. Plas.*, 11(2):507 – 522.

Mace, R. L. and Hellberg, M. A. (1995). A dispersion function for plasmas containing superthermal particles. *Phys. Plas.*, 2(6):2098 – 2109.

Mace, R. L. and Hellberg, M. A. (2009). A new formulation and simplified derivation of the dispersion function for a plasma with a kappa velocity distribution. *Phys. Plas.*, 16:072113.

Mace, R. L., Hellberg, M. A., and Treumann, R. A. (1998). Electrostatic fluctuations in plasmas containing suprathermal particles. *J. Plas. Phys.*, 59:393 – 416.

Mace, R. L. and Sydora, R. D. (2010). Parallel whistler instability in a plasma with an anisotropic bi-kappa distribution. *J. Geophys. Res.*, 115:A07206.

Mace, R. L., Sydora, R. D., and Silin, I. (2011). Effects of superthermal ring current ion tails on the electromagnetic ion cyclotron instability in multiion magnetospheric plasmas. *J. Geophys. Res.*, 116:A05206,.

Maksimovic, M., Pierrard, V., and Riley, P. (1997). Ulysses electron distributions fitted with kappa functions. *Geophys. Res. Lett.*, 24(9):1151 – 1154.

Marsch, E. (2006). Kinetic physics of the solar corona and solar wind. *Living Rev. Sol. Phys.*, 3:1.

Martino, B. D., Briguglio, S., Vlad, G., and Sguazzero, P. (2001). Parallel pic plasma simulation through particle decomposition techniques. *Parallel Comput.*, 27:295 – 314.

Matsuda, Y. and Okuda, H. (1975). Collisions in mulit-dimensional plasma simulations. *Phys. Fluids*, 18:1740 – 1747.

Matsumoto, H. and Omura, Y. (1984). Particle simulation of electromagnetic waves and its application to space plasmas. In *Computer Simulation of Space Plasmas*, pages 43 – 102. Terra Scientific Publishing Co., Tokyo.

Matsumoto, H. and Omura, Y. (1993). *Computer Space Plasma Physics: Simulation Techniques and Software*. Terra Scientific Publishing Co.

Mauk, B. H. and McPherron, R. L. (1980). An experimental test of the electromagnetic ion cyclotron instability with the Earth's magnetosphere. *Phys. Fluids*, 23(10):2111 – 2127.

May, J., Tonge, J., Ellis, I., Mori, W. B., Fiuza, F., Fonseca, R. A., Silva, L. O., and Ren, C. (2014). Enhanced stopping of macro-particles in particle-in-cell simulations. *Phys. Plas.*, 21:052703–1.

Melrose, D. B. (1986). *Instabilities in space and laboratory plasmas*. Cambridge University press.

Morse, R. L. and Nielson, C. W. (1969). Numerical simulation of warm two-beam plasma. *Phys. Fluids*, 12:2418 – 2425.

Morse, R. L. and Nielson, C. W. (1971). Numerical simulation of the weibel instability in one and two dimensions. *Phys. Fluids*, 14:830.

Nicholson, D. R. (1983). *Introduction to Plasma Theory*. John Wiley & Sons, Inc.

Nishimura, K., Gary, S. P., and Li, H. (2002). Whistler anisotropy instability: Wave-particle scattering rate. *J. Geophys. Res.*, 107(A11):18–1.

Nsengiyumva, F., Mace, R. L., and Hellberg, M. A. (2013). Ion bernstein waves in a plasma with a kappa velocity distribution. *Phys. plas.*, 20:102107.

Nvidia, C. (2015a). *CUDA C Best Practices Guide*.

Nvidia, C. (2015b). *CUDA C Programming Guide*.

Nvidia, C. (2015c). *CuFFT library user's Guide*.

Nvidia, C. (2015d). *Thrust Quick Start Guide*.

Ogino, T. (1993). Two-dimensional MHD code. In Matsumoto, H. and Omura, Y., editors, *Computer space plasma physics: Simulation Techniques and Software*, pages 161 – 207. Terra Scientific Publishing Co., Tokyo.

Ogino, T. A. (1986). A three dimensional MHD simulation of the interaction of the solar wind with the Earth's magnetisphere: The generation of field aligned currents. *J. Geophys. Res.*, 91:6791.

Okuda, H. (1972). Verification of theory for plasma of finite-size particles. *Phys. Fluids*, 15:1268 – 1274.

Okuda, H. and Dawson, J. M. (1973). Theory and numerical simulation on plasma diffusion across a magnetic field. *Phys. Fluids*, 16:408.

Omidi, N. and Winske, D. (1990). Steepening of kinetic magnetosonic waves into shocklets: Simulations and consequences for planetary shocks and comets. *J. Geophys. Res.*, 95:2281.

Omura, Y. (2007). One-dimensional electromagnetic particle code: KEMPO1, A tutorial on microphysics in space plasmas. In Usui, H. and Omura, Y., editors, *Advanced Methods for Space Simulations*, pages 1 – 21. Terra Scientific Publishing Co., Tokyo.

Omura, Y., Ashour-Abdalla, M., Gendrin, R., and Quest, K. (1985). Heating of thermal helium in the equatorial magnetosphere: A simulation study. *J. Geophys. Res.*, 90(A9):8281 – 8292.

Ossakow, S. L., Haber, I., and Ott, E. (1972a). Simulation of whistler instabilities in anisotropic plasmas. *Phys. Fluids*, 15(8):1538.

Ossakow, S. L., Ott, E., and Haber, I. (1972b). Nonlinear evolution of whistler instabilities. *Phys. Fluids*, 15(12):2314.

Parker, E. N. and Tidman, D. A. (1958). Suprathermal particles. *Phys. Rev.*, 111(5):1206 – 1211.

Peiravi, A. (2010). Optimum choice of NGP, CIC, and QS algorithm in one dimensional electrostatic particle simulations. *J. American Sci.*, 6:623 – 628.

Pierrard, V. and Lazar, M. (2010). Kappa distributions: Theory and applications in space plasmas. *Solar Phys.*, 267:153 – 174.

Press, W. H., Teukolsky, S. A., Vetterling, W. T., and Flannery, B. P. (2007). *Numerical Recipes: The Art of Scientific Computing*. Cambridge University Press, third edition.

Puri, S., Leuterer, F., and Tutter, M. (1973). Dispersion curves for the generalised Bernstein modes. *J. Plas. Phys.*, 9:89 – 100.

Quest, K. B. (1988). Theory and simulation of collisionless parallel shocks. *J. Geophys. Res*, 93:9649.

Ryu, C.-M., Rhee, T., Umeda, T., Yoon, P. H., and Omura, Y. (2007). Turbulent acceleration of superthermal electrons. *Phys. Plas.*, 14:100701.

Sanders, J. and Kandrot, E. (2011). *CUDA by example: An Introduction to General-Purpose GPU Programming*. Addison-Wesley.

Schippers, P., Blanc, M., André, N., Dandouras, I., Lewis, G. R., Gilbert, L. K., Persoon, A. M., Krupp, N., Gurnett, D. A., Coates, A. J., Krimigis, S. M., Young, D. T., and Dougherty, M. K. (2008). Multi-instrument analysis of electron populations in Saturn's magnetosphere. *J. Geophys. Res.*, 113.

Schriver, D., Ashour-Abdalla, M., Coroniti, F. V., LeBoeuf, J. N., Decyk, V., Travnicek, P., Santolk, O., Winningham, D., Pickett, J. S., Goldstein, M. L., and Fazakerley, A. N. (2010). Generation of whistler mode emissions in the inner magnetosphere: An event study. *J. Geophys. Res.*, 115(A8):A00F17.

Scudder, J. D., Jr, E. C. S., and Bridge, H. S. (1981). A survey of the plasma electron environment of Jupiter: A view from voyager. *J. Geophys. Res.*, 86(A10):8157 – 8179.

Shaw, W. T. and Lee, K. T. A. (2008). Bivariate student t distributions with variable marginal degrees of freedom and independence. *J. Multivariate Anal.*, 99:1276 – 1287.

Silin, I., Sydora, R. D., Mann, I. R., and Mace, R. L. (2011). Nonlinear evolution of electromagnetic ion cyclotron waves. *Phys. Plas.*, 18:042108.

Smith, P. D. and Sakai, J. I. (2008). Chromospheric magnetic reconnection: two-fluid simulations of coalescing current loops. *Astron. Astrophys.*, 486:569 – 575.

Stansby, D., Horbury, T. S., Chen, C. H. K., and Matteini, L. (2016). Experimental determination of whistler wave dispersion relation in the solar wind. *Astrophys. J. Lett.*, 829(1):L16.

Stantchev, G., Dorland, W., and Gumerov, N. (2008). Fast parallel particle-to-grid interpolation for plasma simulations on the GPU. *J. Parallel Distrib. Comput.*, 68:1339 – 1349.

Stenzel, R. L. (1999). Whistler waves in space and laboratory plasmas. *J. Geophys. Res.*, 104(A7):14379 – 14395.

Stewart, J. (2003). *Calculus*. Thomson Learning, Inc, fifth edition.

Stix, T. H. (1992). *Waves in Plasmas*. AIP Press.

Storey, L. R. O. (1953). An investigation of whistling atmospherics. *Philos. Trans. R. Soc. London A*, 246(908):113 – 141.

Summers, D., Ni, B., and Meredith, N. P. (2007). Timescales for radiation belt electron acceleration and loss due to resonant wave-particle interactions: Theory. *J. Geophys. Res.*, 112:A04206.

Summers, D. and Thorne, R. M. (1991). The modified plasma dispersion function. *Phys. Fluids B*, 3(8):1835 – 1847.

Summers, D. and Thorne, R. M. (2003). Relativistic electron pitch-angle scattering by electromagnetic ion cyclotron waves during geomagnetic storms. *J. Geophys. Res.*, 108:1143.

Swanson, D. G. (2003). *Plasma Waves*. IOP Publishing Ltd, second edition.

Sydora, R. D. (1999). Low-noise electromagnetic and relativistic particle-in-cell plasma simulation models. *J. Comput. and Appl. Math.*, 109:243 – 259.

Sydora, R. D. (2007). δf particle-in-cell plasma simulation model: Properties and applications. In *Advanced Methods for space simulations*, pages 47 – 59. Terra Scientific Publishing Co.

Tajima, T. (1989). *Computational Plasma Physics: With Applications to Fusion and Astrophysics*. Addison-Wesley Publishing Company, Inc.

Tataronis, J. A. and Crawford, F. W. (1970). Cyclotron harmonic wave propagation and instabilities: I. perpendicular propagation. *J. Plas. Phys.*, 4(2):231 – 248.

Tenerani, A., Contel, O. L., Califano, F., Pegoraro, F., Robert, P., Cornilleau-Wehrlin, N., and Sauvaud, J. A. (2012). Coupling between whistler waves and ion-scale solitary waves: Cluster measurements in the magnetotail during a substorm. *Phys. Rev. Lett.*, 109:155005.

Tenerani, A., Contel, O. L., Califano, F., Robert, P., Fontaine, D., Cornilleau-Wehrlin, N., and Sauvaud, J. A. (2013). Cluster observations of whistler waves correlated with ion-scale magnetic structures during the 17 August 2003 substorm event. *J. Geophys. Res.*, 118:6072 – 6089.

Thorne, R. M. and Summers, D. (1991). Landau damping in space plasmas. *Phys. Fluids B*, 3(8):2117 – 2123.

Treumann, R. A. (1999). Generalized-Lorentzian thermodynamics. *Phys. Scripta*, 59:204 – 214.

Treumann, R. A. (2001). Statistical mechanics of stable states far from equilibrium: Thermodynamics of turbulent plasmas. *Astrophys. Space Sci.*, 1:81 – 95.

Treumann, R. A. and Baumjohann, W. (1997). *Advanced Space Plasma Physics*. Imperial College Press.

Treumann, R. A., Jaroschek, C. H., and Scholer, M. (2004). Stationary plasma states far from equilibrium. *Phys. Plas.*, 11(4):1317 – 1325.

Tsallis, C. (1988). Possible generalization of Boltzmann-Gibbs statistics. *J. Stat. Phys.*, 52(1):479 – 487.

Tsurutani, B. T. and Lakhina, G. S. (1997). Some basic concepts of wave-particle interactions in collisionless plasmas. *Rev. Geophys.*, 35(4):491 – 501.

Tsurutani, B. T. and Smith, E. J. (1974). Postmidnight chorus: A substorm phenomenon. *J. Geophys. Res.*, 79(1):118 – 127.

Ueda, H., Omura, Y., Matsumoto, H., and Okuzawa, T. (1994). A study of the numerical heating in electrostatic particle simulations. *Comput. Phys. Comm.*, 79:249 – 259.

Vasyliunas, V. M. (1968). A survey of low-energy electrons in the evening sector of the magnetosphere with OGO 1 and OGO 3. *J. Geophys. Res.*, 73:2839 – 2884.

Verboncoeur, J. P. (2005). Particle simulation of plasmas: Review and advances. *Plasma Phys. Control. Fusion*, 47(5A):A231 – A260.

Viñas, A., Mace, R. L., and Benson, R. F. (2005). Dispersion characteristics for plasma resonances of maxwellian and kappa distribution plasmas and their comparisons to the IMAGE/RPI observations. *J. Geophys. Res.*, 110:A06202.

Watt, C. E. J., Rankin, R., and Degeling, A. W. (2012). Whistler mode wave growth and propagation in the prenoon magnetosphere. *J. Geophys. Res.*, 117(A6):A06205.

Winske, D. (1985). Hybrid simulation codes with application to shocks and upstream waves. *Space Sci. Rev.*, 42:53.

Winske, D. and Omidi, N. (1993). Hybrid codes: Methods and applications. In Matsumoto, H. and Omura, Y., editors, *Computer space plasma physics: Simulation Techniques and Software*, pages 103 – 160. Terra Scientific Publishing Co., Tokyo.

Winske, D. and Omidi, N. (1996). A nonspecialist's guide to kinetic simulations of space plasmas. *J. Geophys. Res*, 101(A8):17 287 – 17 303.

Xioa, F., Zhou, Q., Zheng, H., and Wang, S. (2006). Whistler instability threshold condition of energetic electrons by kappa distribution in space plasmas. *J. Geophys. Res.*, 111(A8):A08208.

Xue, S., Thorne, R. M., and Summers, D. (1996). Parametric study of electromagnetic ion cyclotron instability in the Earth's magnetosphere. *J. Geophys. Res.*, 101(A7):15467 – 15474.

Xue, X., Yu, P., Martins, S. F., Tsung, F. S., Decyk, V. K., Viera, J., Fonseca, R. A., Lu, W., Silva, L. O., and Mori, W. B. (2013). Numerical instability due to relativistic plasma drift in EM-PIC simulations. *Comput. Phys. Comm.*, 184:2503 – 2514.

Yoon, P. H. (2014). Electron kappa distribution and quasi-thermal noise. *J. Geophys. Res. Space Phys.*, 119:7074 – 7087.

Yoon, P. H., Ziebell, L. F., Gaelzer, R., Lin, R. P., and Wang, L. (2012). Langmuir turbulence and suprathermal electrons. *Space Sci. Rev.*, 173:459 – 489.

Yu, S. P., Kooyers, G. P., and Buneman, O. (1965). Time-dependent computer analysis of electron-wave interaction in crossed-fields. *J. Appl. Phys.*, 36:2550 – 2559.

Zhou, Q., Xiao, F., Yang, C., He, Y., and Tang, L. (2013). Observation and modelling of magnetospheric cold electron heating by electromagnetic ion cyclotron waves. *J. Geophys. Res.*, 118(11).